Using Seismic Signals to Forecast Volcanic Processes

Rebecca Olivia Salvage

Submitted in accordance with the requirements for the degree of
Doctor of Philosophy

The University of Leeds
School of Earth and Environment
September 2015

Declaration

The candidate confirms that the work submitted is her own and that appropriate credit has been given within the thesis where reference has been made to the work of others.

This copy has been supplied on the understanding that it is copyright material and that no quotation from the thesis may be published without proper acknowledgement.

The right of Rebecca Olivia Salvage to be identified as Author of this work has been asserted by her in accordance with the Copyright, Designs and Patents act 1988.

Acknowledgements

They say that a thesis should be entirely your own work. However, I for one would not be at the stage of writing my acknowledgements had it not been for many of the people around me. Locko, thank you for sharing your home, your love of wine and your infinite knowledge of volcano seismology with me. Thanks also to Caro and Chloe for the fantastic food that kept us all in top form on many a wine tasting evening at chez Neuberg. Bill, thank you for your rubbish jokes, your kindness and confidence in me, and numerous hot chocolates for which I now definitely owe you.

I am indebted to the past and current staff at MVO, who provided the data for this research and in particular to Paddy Smith, who was always on the other end of an email no matter what the question. In addition, thanks to the staff at the Instituto Geofisico, Ecuador for providing the Chiles-Cerro Negro data and supporting a visit in January 2014. I am particularly grateful to Stephen Hernandez, Daniel Sierra, Patty Mothes and Mario Ruiz for their correspondence and helpful discussions. Thank you also to Alex, Hugo and Juan who carted me up Cotopaxi and introduced me to the delights of eating chicken with only a plastic glove - these are experiences I shall never forget. I am also extremely thankful to Susi Ebmeier, James Wookey, Andy Bell, Anais Boue and Diana Roman for their support with different aspects of this research - you all made my life and this challenge that little bit easier!

To all of the friends that I have made along this incredible journey, and in particular to the staff and students of the Volcano Studies Group here at Leeds - thank you for your encouragement and for your constructive criticism (some of the time!) It has made me into a better researcher (I think!) Special thanks to Mark Thomas, who always had time to answer a question, and who made my day by bringing little Haydn in during the write up stage. Richard Rigby, for always making the impossible possible and for being a total guru in computers - thank you! I promise not to crash too many more MatLab scripts if I can help it. To office mates past and present: Ben, Dave, Holly, Ekbal, David, Karsten, Emma, Amy, Luke and Barbara: thanks for putting up with me and for the numerous laughs 8.153 has given us. I am still particularly proud that my Christmas decorations from 2011 are still up in the office - because we all need a little Christmas cheer no matter the time of year!

To the Geobabes who have come and gone from Leeds: thank you for making these four years unbelievable. Hannah, you always made me feel as though anything was possible, even

if I didn't think so myself. Thank you for being a tornado of dreams. Laura, for your incredible kindness and encouragement, and for your award winning brownies. Katie, for making me laugh in the worst of situations, usually over a drink or two. Sarah, for all your encouragment and making it seem as though getting to the end is possible. Lynz, for your love of gin, what more could a girl possibly need!? Jo, for becoming the office dragon with me, for your friendship, laughter and unrelenting confidence at all times. Sandra, for agreeing to share a room with a stranger called O'Salvage all those years ago, and for sharing a room with me on many an adventure since. Thank you for never giving up on me, and for all your encouragement and understanding of what I was going through. I really couldn't have done any of this without any of you.

Annie, for the constant giggles, messages of encouragements and generally keeping me in the loop about the goings on in London, for understanding exactly how I am feeling without having to tell you, and for trying to make me move to London at every opportunity - thank you. Kari, thank you for making my year abroad the best it could ever be, for keeping me going despite the 6000 odd miles between us and for your constant belief in me. Jess, Lauren and Nat: for the copious glasses (bottles) of wine, the laughter, fun and reminding me that there is far more to life than work. Thank you for being the best housemates and the best of friends, your encouragement got me through.

I would not be where I am today if it were not for my family. Mum, Dad, Helen, Grandad and Grandma: Thank you for your unrelenting love and support, for all your encouragement and belief in me, and for allowing me to follow my dreams and travel the world. This is for you; I hope it makes you proud. Grandma, I miss you and always will. Finally, to Tom, the best thing to happen to me during my four years here in Leeds. Thank you for your love and support, for making me laugh, for encouraging me to be better and for making me feel as though I can achieve anything. Here's to many more adventures together, big and little.

Abstract

One of the ultimate aims in volcanological research is to be able to forecast the timing, location and intensity of a volcanic eruption with confidence. Prior to many volcanic eruptions, an acceleration in geophysical precursors (seismicity, deformation, gas emissions) is observed, suggesting the potential for this as a forecasting tool. The Failure Forecast Method (FFM) relates an accelerating precursor to the timing of failure by an empirical power law, with failure being defined in this context as the onset of an eruption. Previous applications of the FFM have used a wide variety of accelerating time series, often generating questionable forecasts with large misfits between data and the forecast, as well as the generation of a number of different forecasts from the same data series.

This research presents an alternative approach applying the FFM using it in combination with a cross correlation technique which identifies seismicity from the same active source mechanism and location. Isolating a single system at depth avoids additional uncertainties introduced by averaging data over a number of different accelerating phenomena, and consequently reduces the misfit between the data and the forecast. Similar seismic waveforms are identified in the precursory accelerating seismicity to dome collapses at Soufrière Hills volcano, Montserrat in June 1997, July 2003 and February 2010. These events were specifically chosen since they represent a spectrum of collapse scenarios at this volcano. The use of similar seismicity as a forecasting tool for collapses in 1997 and 2003 greatly improved the forecasted timing of the dome collapse, as well as improving the confidence in the forecast, thereby outperforming the classical application of the FFM. The dome collapse event of 2010 could not successfully be forecast using the FFM since no acceleration in seismicity was observed.

Use of the FFM requires the assumption that the accelerating seismicity at depth forms a direct and causal link to the dome collapse at the surface. Collapse triggers can be either internal (e.g. the movement of magma) or external (e.g. rainfall). For the first time within a volcanic environment, the use of grey incidence analysis quantitatively recognised that the most influential parameters for affecting the likelihood of a dome collapse at Soufrière Hills were internal; and particularly important was the effect of low frequency seismicity, which may induce instability through an increase in pore fluid pressures related to the movement of magma and hydrothermal fluids from depth. Finite Element Modelling of the stability of the volcanic dome in the days before the collapses in July 2003 and February 2010 suggested that neither were stable, and should have already collapsed. The errors involved in such a calcu-

lation are large due to the large uncertainties associated with the mechanical properties of the rock masses involved which act as an input to the model. Therefore, in order to develop more accurate dome stability models, it is essential that these uncertainties in mechanical properties are reduced.

Application of this combined methodology of the FFM and a cross correlation technique as a forecasting tool was also applied for the first time to the onset of an unrest scenario at Chiles-Cerro Negro (Ecuador/Colombia) in October 2014, which had previously been assumed to be dormant. At the time of investigation (February 2015) unrest was still ongoing, and there was very little geological or geophysical information regarding this volcano in the past. The number of similar seismic events accelerated and became distinctly organised into separate temporal clusters on 20 October 2014, prior to a Magnitude 5.8 earthquake directly beneath the volcano. Each temporal cluster displayed a distinctly different waveform shape, indicating the activation of a number of different sources (either in mechanism or location) at depth. Application of the FFM to the acceleration in similar seismicity allowed an accurate forecast of the Magnitude 5.8 earthquake beneath the volcano, suggesting a direct relationship. Similar seismicity has not been identified at any of the Ecuadorian volcanoes before, and consequently the computer codes for identifying similar seismicity, and using it as a forecasting tool are currently being tested at the Instituto-Geofisico, Ecuador, for their real time application potential.

Contents

List of Figures

List of Tables

Chapter 1

Introduction

1.1 Monitoring Volcanic Activity

With more than half of the 1300 volcanoes known to have erupted since the Holocene still being considered active (Tilling, 1989), and over $91,500$ people believed to have been killed in the 20^{th} Century alone from volcanic eruptions (Witham, 2005), it is little wonder that scientists still endeavour to research volcanic behaviour and consequences. Volcanic unrest can manifest itself in a number of different ways, but is most simply defined as a deviation from the background level (Phillipson et al., 2013). Since not all volcanoes worldwide are continuously monitored, this background level can often be difficult to define. Current monitoring efforts at volcanoes are fundamentally split into three categories: measuring gas outputs, deformation and seismicity (Table 1.1), which are believed to be associated with the movement of magmatic fluid, and thus are useful indicators of processes at depth which could lead to volcanic eruptions. The methods associated with monitoring are summarised briefly in Table 1.1, which also explains some of the major advantages and disadvantages of each technique.

Gas monitoring provides vital information of changing magmatic conditions at depth, albeit over long time periods. The remote sensing of gas emissions is favoured, either ground based which still requires reasonable proximity to the emissions, or from satellite observations, since it is considered less dangerous. An increase in gas emission rate is associated with an increase in the exsolution of gases from depth, which is often linked to the new emplacement of magma (Edmonds et al., 2003). The most abundant gas emissions from volcanoes are water (H_2O) and carbon dioxide (CO_2), followed by sulphur dioxide (SO_2) (Giggenbach, 1996). One of the main challenges for monitoring gas emissions at volcanoes is to be able to distinguish between

volcanic gases, and those which are simply atmospheric.

Ground deformation is commonly observed within volcanic environments, where inflation is interpreted as increased magma storage within the crust prior to extrusion. Magma movement deforms the subsurface resulting in volume changes. Ground based measurement techniques have the ability to track small scale temporal changes (on the scale of minutes to hours) and therefore can track the deformation with great precision, but often lack spatial coverage (Pinel et al., 2014), since a large amount of human effort is needed to install and maintain such networks.

With huge advances in technology, it is now possible to take deformation readings from space, using synthetic aperture radar interferometry (InSAR), which calculates deformation based on the difference in phase between two radar images (Pinel et al., 2014). One major advantage of InSAR is its ability to monitor volcanic phenomena in remote locations where ground measurements may not be possible (Dzurisin, 2003). For example, Okmok volcano is located on the island of Umnak in the Aleutian arc, with a population of less than 50 people. Despite a low population, eruptions in this area are of importance due to the high volume of air traffic which crosses directly over the Aleutian arc on a daily basis (Buurman et al., 2014). Inflation of a magmatic body beneath the caldera was interpreted as causing a surface uplift of 18 cm between 1992 and 1995, detected only by synthetic aperture radar techniques (Lu et al., 2000).

A combination of both GPS and InSAR allows maximum temporal and spatial resolution to study ground deformation, and the amount of deformation can be verified by each methodology. Studying the deformation patterns can help scientists to determine the potential volume, shape and location of the intruded magma below the surface, which allows forecasts of the onset and evolution of an eruption involving this stored magma (Dzurisin, 2000). However, deformation can occur in volcanic environments which may not be related to the volcanic system, but instead related to, for example, regional tectonics; isostatic readjustment; or a change in the geothermal system (Sparks, 2003). Therefore, deformation alone as a monitoring tool can often lead to ambiguous results and misleading interpretations (Biggs et al., 2014).

Monitoring Tool	**Frequency of measurements**	**Sensors**	**Output**	**Advantages**	**Disadvantages**	**Example Publications**
Volcanic Gases	Campaign - usually monthly	COSPEC (Correlation spectrometer) DOAS (Differential optical absorption spectrometer)	Amount of SO_2	Easily distinguished from background atmosphere	Not continuous, danger to collector	Stoiber and Jepsen (1973), Watson et al. (2000) Galle et al. (2003), McGonigle et al. (2002)
		FITR (Field transportable Fourier transform infra-red)	Footprint of molecules	Differentiation of complex molecules	Not continuous, danger to collector	Oppenheimer et al. (2002), Christopher et al. (2010)
		Multigas	Amount of CO_2		Difficulty distinguishing between atmospheric CO_2	Edmonds et al. (2010)

Deformation	Campaign - weekly, or when required as a supplement to continuous sites	GPS (Global Positioning System)	Ground displacement	Ease of use, inexpensive, high precision	Lack temporal and spatial coverage	Odbert et al. (2014a), Pinel et al. (2014)
		EDM (Electronic Distance Measurements)				Pingue et al. (1998), Matsushima and Takagi (2000)
		InSAR (Synthetic aperture radar)	Phase difference between two radar images to calculate displacement	No danger to collector, large spatial coverage, coverage in inaccessible locations	Temporal resolution dependent on satellite configuration, processing time, coherence distorted by vegetation, steep topography, atmosphere	Pinel et al. (2014), Biggs et al. (2014), Dzurisin (2003)

	Continuous	Strainmeters or Tiltmeters GPS	Change in angle of the slope from the horizontal Ground displacement	Ease of use, inexpensive, high precision	Lack spatial coverage	Linde and Sacks (1995), Voight et al. (2010) Owen et al. (2000)
Seismicity	Continuous - either long or short term campaigns	Short Period	Seismogram in counts	Low cost	Narrow range of frequency observations	Legrand et al. (2015)
		Broadband		Wide range of frequency observations	Expensive	Rodgers et al. (2015), Hidayat et al. (2000), Kawakatsu et al. (1992)

Table 1.1: Monitoring in a volcanic environment using seismicity, deformation and gas emissions

In many cases, monitoring volcanic evolution needs to be done on shorter time scales than gas emissions or deformation studies allow, and therefore seismicity has remained the primary monitoring tool, since seismic events can be registered by automated systems 24 hours a day, and therefore analysed in near real time. Seismicity is also more easily distinguished from the background level, and the number of events and the size of events can be used as monitoring parameters.

1.2 Seismicity in Volcanic Settings

Seismicity in volcanic settings is thought to be related to a number of physical processes at depth, including the migration of magmatic fluids and fracturing of the conduit itself. In addition to this, seismicity can also be generated in relation to surface processes such as pyroclastic flows and rockfall events. The extreme variety of seismic signals generated in volcanic settings is a reflection of the number of different processes and the great structural heterogeneities found in this context (Chouet, 1996a). The characterisation of seismicity can be based upon waveform and spectral similarities, but is most commonly based upon the frequency content of the waveform. Consequently, signals originating from depth are usually split into low frequency and high frequency end-members, with a whole spectrum of event waveforms in between. The major advantage of classifying seismic events in this manner is that it is possible to distinguish different processes that are occurring at depth (Lahr et al., 1994).

As with any emerging science, terminology for volcano-seismology has often relied upon its closest neighbour for direction, in this case tectonic seismology . This has led to much confusion in nomenclature from both parties (Neuberg, 2011) and is exacerbated by the continuum spectrum of seismic events which can be identified within volcanic settings (Chouet and Matoza, 2013). In this chapter the nomenclature that will be used throughout this thesis will be described, as will definitions and characteristics of the signals.

1.2.1 High Frequency events

High frequency seismic signals (volcano-tectonic or VT events) have a clear high frequency onset, dominated by P- and S- phase arrivals, as seen in the upper panel of Figure 1.1, followed by a short broadband coda. VT events show mixed polarities at recording stations, in a similar manner to tectonic earthquakes. They generally have a frequency range of 1-20 Hz, with peak energy between 6 and 8 Hz (Lahr et al., 1994). The generation of VT seismicity is associated

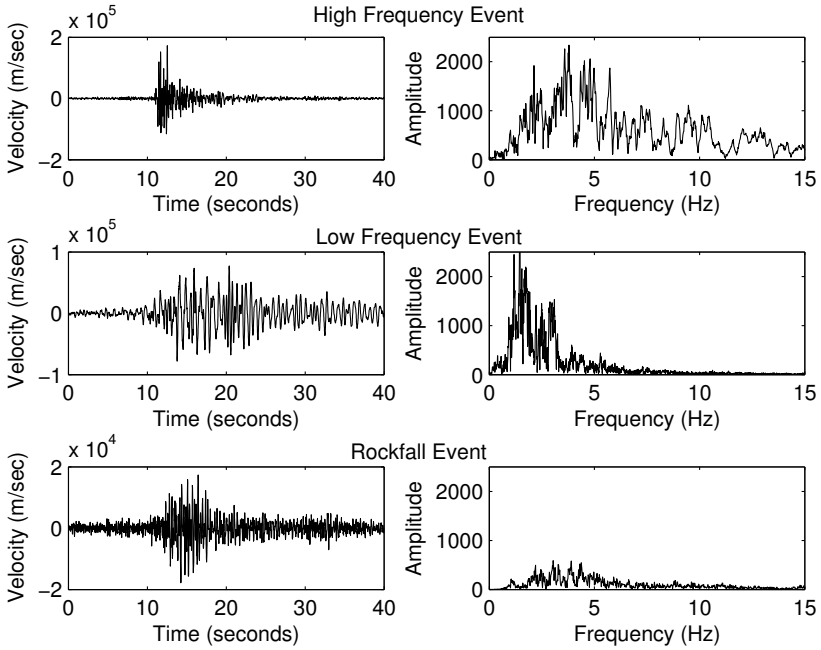

Figure 1.1: Examples of waveforms and their frequency content seen in volcanic environments taken from Soufrière Hills Volcano, Montserrat in 1997. *Upper*: High frequency waveform with clear phase arrivals. *Middle*: Low frequency waveforms with an emergent onset. Waveform filtered between 0.5 and 5 Hz. *Lower*: Rockfall event with classic "cigar" shape.

with brittle failure, when magmatic processes create enough elastic strain within an already regionally stressed field to force the surrounding rock into failure (Arciniega-Ceballos et al., 2003). If the stress produced is great enough, a new magmatic pathway can be created from the coalescence of fractures within the edifice (Kilburn, 2003, 2012). Failure can therefore be associated with the emplacement or removal of magma, or through temperature and pressure changes. For example, they may be generated from the interaction of the magmatic plumbing system with an active hydrothermal system at depth. They differ only from tectonic earthquakes in their patterns of occurrence: VT events occur in swarms (a number of earthquakes which are of a similar magnitude and location), rather than a typical main shock and aftershock sequence that is common for purely tectonic events (McNutt, 2005). VT events are ultimately related to perturbations in the pressurization of the volcanic system (Lahr et al., 1994) and can therefore be used to map the area of deformation and stress change patterns at depth (Chouet, 1996a), despite not mapping the magma chamber itself (Neuberg, 2011).

1.2.2 Low Frequency events

Signals which originate when a fluid is disturbed as it migrates are classed as either long period, low frequency (LP or LF) events or tremor. LF events consist of an emergent P- wave onset followed by a harmonic waveform which occupies the spectral range of 0.2-5 Hz (Chouet, 1996a, Neuberg et al., 2000) as denoted in the middle panel of Figure 1.1. Tremor can be identified as a signal of sustained amplitude lasting from minutes to days in which individual events cannot be distinguished (Arciniega-Ceballos et al., 2003), or may also describe the background noise that occurs in the presence of magmatic activity. Similarity between LF events and tremor in terms of their temporal and spectral characteristics suggests a common source mechanism (Fehler, 1983, Chouet, 1996a), which is why some authors believe tremor may also be simply the merging of many low frequency events within a short space of time (Neuberg, 2011). It is thought that low frequency seismicity originates from the boundary between a fluid (such as magma or gas) and the surrounding volcanic edifice, with seismic energy becoming trapped within the fluid-filled cavity, providing that the width of the cavity is much smaller in relation to the seismic wavelength (Ferrazzini and Aki, 1987, Neuberg et al., 2000). Low frequency tremor has been postulated to be a consequence of unsteady magma or fluid flow at depth (Julian, 1994, Chouet, 1996b). Since low frequency events are intrinsically linked to the movement of fluid at depth and are concentrated within the fluid filled cracks or the conduit, they may be an indirect way of determining magma ascent rates, and consequently could be related to an impending eruption (Cornelius and Voight, 1994, Hammer and Neuberg, 2009, Thomas and Neuberg, 2012).

Observations at active volcanoes also suggest that low frequency seismicity often occur in "swarms", i.e. a number of events, often with similar waveforms, within a short space of time followed by periods of quiescence (Figure 1.2), with typical durations of hours to days (Green and Neuberg, 2006, Buurman et al., 2013). In particular, this has been noted prior to volcanic eruptions where a number of repetitive swarms separated by periods of limited seismic activity have been observed (Miller et al., 1998, Cornelius and Voight, 1994), potentially presenting the capability as a forecasting tool. Rowe et al. (2004), Ottemöller (2008) and Buurman et al. (2013), amongst other authors, suggest that many of the events within a seismic swarm can have very similar waveform shapes and therefore have been exposed to the same path effects en route to the receiver, as well as being generated by the same source mechanism at depth. This suggests that the source mechanism of low frequency seismicity is a stationary, repetitive

and non-destructive source process (Green and Neuberg, 2006).

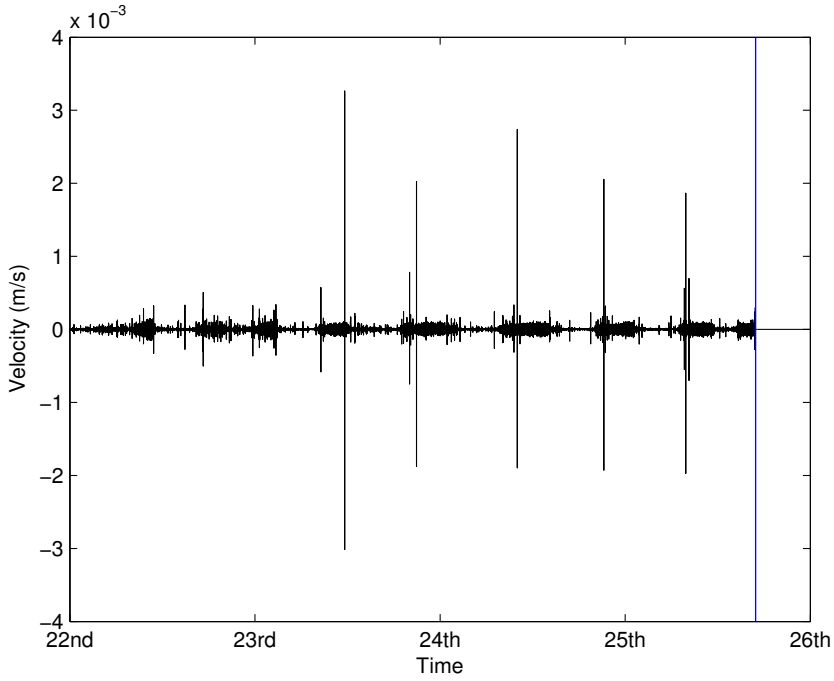

Figure 1.2: Raw continuous seismogram from 22 -25 June 1997 on Montserrat showing temporal swarms of earthquakes prior to dome collapse. The timing of the dome collapse is represented by the vertical line on 25 June.

The Origin of Low Frequency Seismicity

The generation of the low frequency coda of the waveform which makes it so distinctive is usually attributed to the resonance of energy trapped at the interface of a solid and a fluid (Chouet, 1988, Neuberg et al., 2000) and therefore is a consequence of the source process. There is still no consensus on the size or aspect ratios (diameter:length) of such fluid filled bodies (i.e. whether the fluid filled body is a crack or conduit). Models which propose a crack as the resonator have aspect ratios of 1:100-1000, with the crack containing a low viscosity fluid which is highly compressible, such as steam (Chouet et al., 1994) or ash laden gas mixtures (Morrissey and Chouet, 2001). Alternatively, models which suggest that the conduit of the volcanic system can act as the resonating body (with aspect ratios much lower than 1:100), have the conduit or dyke filled with a magma containing crystals, melt and gas (Collier et al., 2006).

This however does not concern the actual triggering mechanism of such energy. A number

of distinct mechanisms have been proposed: (1) A slip-stick mechanism at the conduit walls (e.g. Denlinger and Hoblitt (1999), Iverson et al. (2006)), (2) the brittle failure of the magma itself (e.g. Webb and Dingwell (1990), Goto (1999), Neuberg et al. (2006)), (3) self sustaining oscillations, and (4) the interaction between the magmatic and the hydrothermal system. The first two mechanisms require the movement of fluid (magma, gases, hydrothermal fluids etc.) for the generation of seismicity, whether that be when the flow rate of a compressible (Newtonian) magma through the conduit exceeds a given threshold and therefore evokes a stick-slip mechanism along the conduit walls (Denlinger and Hoblitt, 1999), or by a large magmatic plug which is being forced incrementally upwards and therefore inducing seismicity at the conduit edges (Iverson et al., 2006). The brittle failure of the magma itself is envisaged by an increase in viscosity and strain rates (Lavallée et al., 2008) caused by high ascent rates of magma (Neuberg et al., 2006), changes in crystal and/or bubble concentrations in the magma (Goto, 1999), or by a change in the geometry of the conduit (Thomas and Neuberg, 2012). Julian (1994) suggested that volcanic tremor, and therefore by extension low frequency events, could be generated by self sustained oscillations (roll waves) with an increase in the magma flow velocity, which would cause the channel walls to constrict due to the Bernoulli effect and then expand again due to the fluid pressure. However, it has been suggested that these roll waves could only be maintained if the fluid was very hot, contained highly pressurized H_2O and CO_2 and flowed at speeds of 10 ms^{-1} (Rust et al., 2008). Furthermore, the interaction of magma and water also has the potential to generate low frequency seismicity by boiling and therefore depressurizing shallow groundwater systems (Leet, 1988); the collapse and forcible opening of hydrothermal cracks (Nakano and Kumagai, 2005, Waite et al., 2008); or by the chocking of magmatic steam at depth (Chouet et al., 1994). More recently, Bean et al. (2014) suggested that low frequency earthquakes could be attributed to slow rupture failure in unconsolidated volcanic materials and therefore to deformation within the upper edifice, rather than the movement of fluid.

1.2.3 Hybrid Events

Since volcanoes are complex systems, it is often fairly difficult to distinguish between high and low frequency idealised end-member scenarios of seismicity. Hybrid events have a high frequency onset (smaller in amplitude than a VT event, but still with mixed first motion polarities), followed by a long resonating low frequency coda (similar to a LF event) (Chouet, 1996a, Chouet and Matoza, 2013). Hybrids are thought to involve the shear failure of a brittle plane intersecting a fluid filled crack (Lahr et al., 1994), and therefore relate to the pressurization

of the volcanic system at depth (Neuberg, 2011) since both a shear failure mechanism and a resonance mechanism are involved (Chouet and Matoza, 2013). The high frequency component of hybrid seismicity could also relate to the sudden brittle failure of the melt itself, as has been described for low frequency events. In many cases, hybrid events are simply classed in the same group as low frequency events, primarily because source and path interactions at the seismometers can result in a low frequency event at one seismic station being recorded as a hybrid event at another (De Angelis et al., 2007, Neuberg et al., 2000). This is further evidence of a similar source mechanism between the two types of events.

However, Harrington and Brodsky (2007) have suggested that a hybrid earthquake may be generated in the same way as a VT earthquake through brittle failure, and it is only the path effects to the receiver which cause the low frequency proportion of the waveform. For example, the low frequency element of the waveform could be produced by trapped waves within loosely consolidated soft sediment en route to the receiver (Kedar et al., 1996).

1.2.4 Very Long Period Events

Due to the implementation of broadband seismometers as a monitoring tool at volcanoes rather than simply short period instruments, it is now possible to detect seismicity within a wider frequency band, and in particular at the lower end (up to a 60 second period) (McNutt, 2005). Known as very long period (VLP) events, these have periods greater than 2 seconds, and appear to be intrinsically linked to low frequency events (Arciniega-Ceballos et al., 2003), especially since they appear to occur at very shallow depths beneath volcanoes (McNutt, 2005). It is still not fully understood how such waves could form within small source zones and yet have such long wavelengths. Waveform inversion results from a number of studies have determined the geometrical relationship of such contrasts to be complicated, with suggestions including sill-dyke interactions (Chouet et al., 2005, Dawson et al., 2011), complex intersecting dyke patterns (Chouet et al., 2008) and a number of magma chambers in close proximity connected by narrow carriers (Nishimura et al., 2000). It has also been suggested that these waveforms could be produced in distinct pulses as magma moves past a restriction in its container (sill, dyke, conduit) (Ohminato et al., 1998), or by the sudden removal of a lid capping the pressurized container, which causes viscous magma to ascend rapidly and thus fragment in the process (Ohminato et al., 2006). In either case, VLP signals are typically attributed to inertial forces associated with perturbations in the flow of fluid and gases within a pressurized volcanic conduit

or crack (Chouet and Matoza, 2013).

1.2.5 Surface generated seismicity

Active volcanoes exhibit a variety of associated surface seismicity such as landslide, rockfall, pyroclastic flow signals and lahars. These are particularly dominant during dome building eruptions and at volcanoes with glaciers during the spring and summer due to the partial melting of the ice (McNutt, 2005). Important parameters in determining the frequency content, amplitude and shape of the waveform generated include the rock fragment size involved, the ground surface angle of repose and the physical properties of the surface and the falling material. Typically rockfall events (small free falling rock events) form a "cigar shaped" waveform with an emergent onset (Figure 1.1, lower panel), whereby there is an initial increasing amplitude of the waveform as the amount of material falling down slope increases (Neuberg, 2011). Pyroclastic flow signals are distinguishable from rockfalls since their waveforms are at least an order of magnitude larger and they often occur over a longer duration since larger amounts of material are involved moving down slope (De Angelis et al., 2007), however the two are likely to exist on a continuum.

Volcanoes that appear at high latitudes or high altitudes often host glacial environments. Seismic signals can then be produced at the interface between the moving ice and the underlying bedrock, and since the wave velocity is much lower in ice than in the bedrock, resonance can be set up within the glacier itself, producing low frequency earthquakes (McNutt, 2005). Explosion signals (1-20 Hz) are characterised by two parts: a seismic wave and an air wave, both of which can be detected by a seismometer, microphone or barograph (McNutt, 2005). Explosion signals are associated with the production of an eruption column and can occur during lava effusion, or as single discrete events. In some cases, an ongoing eruption may experience both of these types of explosion signals, as was the case at Fuego volcano, Guatemala from 2005 to 2007 (Lyons et al., 2010).

1.3 Current understanding of Forecasting Volcanic Eruptions

The ability to predict the timing, intensity and type of volcanic eruptions is one of the key issues facing volcanologists today. Increased accuracy in the timing of volcanic hazards, and quantification of forecast uncertainties will allow more effective mitigation of such events (Bell et al., 2011b). The most successful models for forecasting volcanic eruptions have foundations

in first principles and natural laws. However, being dynamic systems, volcanic processes are often non-linear and have many uncertainties associated with the controlling parameters, making them difficult to constrain (Sparks, 2003). That said, almost every currently monitored volcano appears to exhibit increased levels of activity prior to a volcanic eruption, whether that be an increase in seismicity, gas or deformation of the volcano. This allows some comprehension of any systematic evolutionary trends that may occur, and relate these using physical laws. Since these precursors are ultimately linked to the movement of magma and/or fluid towards the surface, larger eruption volumes (e.g. Mt St Helens (1980) and Mt Pinatubo (1991)) are often more easily detected than smaller movements of magma which can easily go unnoticed amongst background noise (McNutt, 2005).

The most notable instances of successful volcanic forecasting are using precursory activity at andesitic-dacitic volcanoes. The cataclysmic eruption of Mt Pinatubo, Philippines on 15 June 1991 was preceded by at least two months of heightened VT seismicity (the first seismometer was installed following phreatic eruptions on 5 April 1991 when there was already increased levels of activity) (Harlow et al., 1996). With sudden increases in LF seismicity and an alarming sudden drop in SO_2, scientists were able to successfully evacuate 45,000 to 50,000 local people and 14,500 military personnel to safety by 14 June, such that less than 300 people were killed in the ensuing pyroclastic flows, lahars and ash fall on 15 June. In addition, the pyroclastic flow and lahar paths were correctly anticipated by hazard maps which had been drawn up when the unrest began a few months before (Punongbayan et al., 1996). More recently, the 2010 eruption of Merapi, Indonesia, on 26 September was preceded by 36 days of precursory activity: rates of VT and hybrid seismicity and SO_2 during this time were comparable to, or higher than, the highest rates observed during previous (smaller) Merapi eruptions (1992-2007), and rapid deformation was observed by EDM. Consequently, one day prior to the explosive eruption, several tens of thousands of people were evacuated from a radius extending 10 km from the volcano, resulting in a greatly lowered death toll of 35 (Surono et al., 2012). Eruptions at basaltic volcanoes can also sometimes be preceded by seismicity (Bell and Kilburn, 2012, Chastin and Main, 2003). In these instances, the eruptions were characterised by the fact that a new pathway for magma to reach the surface was generated. Those eruptions lacking precursory seismicity may simply be related to eruptions in which an open pathway to the surface already exists, resulting in seismic silence.

Monitoring deformation within volcanic environments is intrinsically linked to the instability of volcanic edifices due to the displacement of the surrounding rock at the surface above magmatic intrusions. In some instances, e.g. Mt St Helens in 1980, the size of a volcanic collapse was estimated (Voight, 2000) due to detected movement of the flank by 1.5-2.5 m a day in the 25 days preceding the collapse (Lipman et al., 1981). However, since deformation monitoring requires stable base stations positioned on rocky outcrops (for GPS) or good coherence by exposed rock masses (for SAR acquisitions), it is often impossible to extract the deformation signal. This was the case with the Grimsvøtn eruption in Iceland in 1996 where the deformation signal from the opening of two dykes to allow magma to the surface was obscured by the overlying icecap (Pagli et al., 2007). The use of InSAR as a forecasting and monitoring technique has been limited due to its temporal resolution, since analysis can only be conducted once acquisitions are completed, which is dependent upon the configuration of satellites above the Earth. However, ground based techniques offer increased temporal resolution. Tiltmeters have been used at Sakurajima volcano, Japan to forecast explosion events. Of the 39 explosion events during an investigated period in 1985 (26 days), 27 events occurred following an identified "critical stage" of sustained inflation (Kamo and Ishihara, 1989).

Forecasting volcanic eruptions using gas emissions is almost unheard of, likely because continuous monitoring is problematic and dependent upon clear weather conditions, line of sight, and the ability to actually sample gases being emitted from the volcano, which is obviously not possible during an eruption. Using remote sensing techniques to analyse gas composition within a continuous volcanic plume at Etna, Sicily, Aiuppa et al. (2007) suggested that an increase in the CO_2/SO_2 ratio (5 to 50 times greater than during quiescence degassing periods) prior to explosive activity could be related to the ascent of gas-rich magma within basaltic systems, and consequently used as a forecasting tool. However such evaluations appear to be rare.

1.3.1 The Failure Forecast Method

Volcanic eruptions are often preceded by accelerating geophysical signals (McNutt, 2002), associated with the movement of magma or other fluid towards the surface. Of these precursors, seismicity is at the forefront of forecasting volcanic unrest since it is frequently observed and the change from background level can be observed in real time (Chouet et al., 1994, Cornelius and Voight, 1994, Kilburn, 2003, Ortiz et al., 2003). Since forecasting of volcanic eruptions

relies on the ability to forecast the timing of magma reaching the surface, low frequency seismicity with a spectral range of $0.2-5$ Hz (Lahr et al., 1994) may potentially act as a forecasting tool due to its potential correlation with the movement of magmatic fluid at depth (Chouet et al., 1994, Neuberg et al., 2000).

The relationship between an accelerating geophysical precursor and the timing of failure of the system was first considered for landslides (Fukuzono, 1985) but has since been adapted for the forecasting of volcanic eruptions (Voight, 1988, 1989). The Material Failure Law or the Failure Forecast Method (FFM) as it is referred to in volcanology (Cornelius and Voight, 1995), is an empirical power-law relationship based on first principles associated with failing materials, which relates the acceleration of a precursor ($d^2\Omega/dt^2$) to the rate of that precursor ($d\Omega/dt$) at constant stress and temperature (Voight, 1988) by:

$$\frac{d^2\Omega}{dt^2} = K\left(\frac{d\Omega}{dt}\right)^{\alpha} \tag{1.1}$$

where K and α are empirical constants. Ω can represent a number of different geophysical precursors, for example low frequency seismic event rate (Hammer and Neuberg, 2009), event rate of all recorded seismicity (Kilburn and Voight, 1998), or the amplitude of the events (Ortiz et al., 2003). Throughout this thesis, Ω shall be referred to as the "observable" meaning it is the measured precursory phenomena that shall be used in conjunction with the FFM. The parameter α is thought to range between 1 and 2 in volcanic environments (Voight, 1988, Voight and Cornelius, 1991), or may even evolve from 1 towards 2 as seismicity proceeds (Kilburn, 2003). In this instance, an infinite $d\Omega/dt$ suggests an uncontrolled rate of change or a singularity and is associated with an impending eruption (Figure 1.3: Left panel). The inverse form of $d\Omega/dt$ is linear if α = 2, and therefore the solution to determine the timing of failure is a linear regression of inverse rate against time. The extrapolation to singularity (when $d\Omega/dt$ tends to infinity and is therefore believed to be approaching uncontrolled propagation) is straightforward and the timing of potential failure is determined as being when the linear regression intersects the x-axis (Voight, 1988) (Figure 1.3: Right panel). It is important to note that this forecasted timing of failure is associated with the potential for an eruption, and may not necessarily result in one, since a direct pathway of magma to the surface may not have been generated.

K is thought to be dependent upon the composition of the material, the temperature and the confining pressure at the time (Kilburn, 2012). One method to determine the values of α and

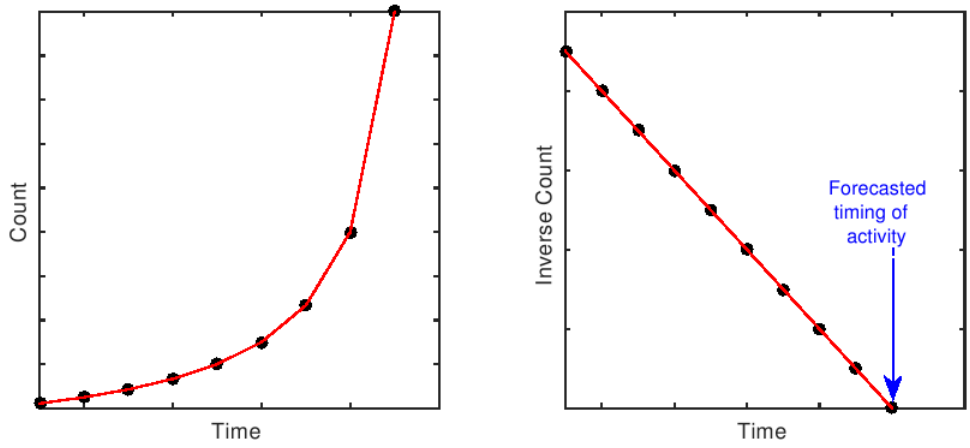

Figure 1.3: Schematic graphical extrapolation of the timing of failure using the Failure Forecast Method. *Left:* Each black dot represents the counts of an accelerating precursor (Ω) at different times (synthetic data). The red line represents a power law best-fit function to the data. It is assumed that once this tends towards infinity, eruption is imminent due to a major change in the system. *Right:* The inverse count of the accelerating precursor is plotted against time. A least squared regression analysis is represented by the red line. The forecasted timing of the eruption is the point at which this linear regression crosses the x-axis, as indicated.

K is the linear form of:

$$\log\left(\frac{d^2\Omega}{dt^2}\right) = \alpha \log\left(\frac{d\Omega}{dt}\right) + \log(K), \tag{1.2}$$

on a log rate vs. log acceleration plot. α can be estimated by the slope and K by taking the exponent of the intercept (Cornelius and Voight, 1995).

The FFM has been applied to material failure scenarios at many different volcanoes. Research suggests that the method would have aided volcanologists in hindsight in the prediction of volcanic eruptions at Mt. St. Helens, USA (1981, 1982, 1985, 1986); Redoubt volcano, Alaska (1989-1990); Mt. Pinatubo, Philippines (1991) (Voight and Cornelius (1991), Cornelius and Voight (1995), and references therein) and Bezymianny, Russia (1959-1961) (Tokarev, 1963). However, since these analyses were conducted in hindsight and this is an empirical technique, appropriate caution must be applied when using the FFM in real-time situations of volcanic unrest. Previous applications of the FFM to volcanic environments shall be discussed further in Section 3.1.

1.4 Instability at Volcanoes

Forecasting volcanic eruptions is therefore reliant upon indirect analysis of processes occurring at depth, since it is impossible to gain direct measurements of magma movement at depth. This research is primarily interested in forecasting dome collapses at Soufrière Hills volcano, Montserrat, since these have proved one of the most destructive phenomenon in this environment. Dome collapses are likely to be affected by a number of internal and external factors, but most significantly a collapse will not occur if there is no dome to collapse or the dome is not unstable. Consequently, dome stability analysis will be used in conjunction with the FFM as a forecasting tool since understanding the processes controlling volcanic dome collapse is essential in order to assess the long and short term hazard potential of a volcano (Reid et al., 2010). Prior to 1980, very little research was extended towards the potential hazards and impacts of collapse at volcanoes. Except for Moore (1964), who reported that two large landslides on the Hawaiian ridge were the result of volcanic instability and Ridley (1971), who reported on volcanic collapse features on Tenerife, there appears to be very little literature on this. The catastrophic lateral blast in 1980 of Mount St Helens, Washington, USA, in which 50 people lost their lives, demonstrated the risks of dome collapse and instability of volcanic edifices (Christiansen and Peterson, 1981).

A more detailed discussion of instability at volcanoes, and in particular at Soufrière Hills Volcano Montserrat, including the driving forces behind dome collapses will be discussed in Chapter 5.

1.4.1 The Mechanics of Slope Failure

The generation of edifice instability is likely to be related to a number of factors which all intertwine, so that at any particular moment, the yield stress within the edifice is lowered significantly enough to generate collapse. In order for a slope to fail, the stresses allowing failure must be greater than those which are resisting failure. In terms of principal stresses, the normal stress resists failure along a sliding plane, and the shear stress promotes it. Within volcanic environments, the normal stress acting upon a potential failure plane is the lithostatic pressure which is a consequence of the overlying rock mass. However, it is more appropriate to determine the effective lithostatic pressure (σ') rather than simply the normal lithostatic pressure, which is defined as the difference between the total normal stress (σ) and the pore water or gas

pressure (u):

$$\sigma' = \sigma - u \tag{1.3}$$

acting on the failure plane, since the effective lithostatic pressure is more encompassing of the fact that the rock overlying the failure plane is made up of an interstitial system of connecting discontinuities and rock pieces, which can allow deformation. Lower values of effective lithostatic pressure are more likely to result in failure (Simons et al., 2001). Equation 1.3 implies that an increase in fluid or gas pressure can lead to a lower effective lithostatic pressure, which can therefore induce instability.

Following equation 1.3, there are a number of ways in which it is possible to induce failure. Either σ must be reduced, or u must be increased (whilst always conserving mass and energy). To reduce the total normal stress σ, the rock mass above the failure plane must be removed, either by small mass wasting events which effectively lower σ over a long period of time, or in large landslide events where the stress field is unable to re-adjust fast enough back to equilibrium. An increase in u could be achieved by an increase in the gas output at a volcano, direct magma intrusions, or dyke intrusions close to the failure plane (Voight and Elsworth, 2000).

1.5 Bridging the gap between science and operational procedures

Benefactors of scientific research are particularly interested in the impact that the science could have, both for society and in economic terms. However, there can often be large discrepancy between academic science and results that are useful for real world applications. Designing complicated models to explain complex geophysical and geochemical signals from a volcano helps to improve our understanding of that volcanic situation and the possible future scenarios associated with it. However, they may not be useful for routine monitoring of a volcano, which is often stressful not only due to potential volcanic unrest, but also due to political, geographical and financial pressures.

This research aims to begin to close the gap between the output of scientific research within academic environments, and the use of this science in an operational environment. Research into forecasting volcanic eruptions, which are inherently complex systems, needs to be per-

formed from an operational point of view: there is little gained from having a hugely complex model for forecasting if it is too expensive, requires too much computational power and is too complicated for those meant to be using the forecasting tools in volcano observatories. Research done in collaboration with volcano observatories, with input from staff in these environments, is much more likely to be successfully implemented. One of the ultimate aims of this research is therefore to develop forecasting tools which can be successfully implemented at volcano observatories. This has partly been successful; at the time of writing the cross correlation forecasting technique (description and applications shown in Chapter 4) developed during this research are being modified to comply with system requirements at the Instituto Geofisico in Quito, Ecuador, who are responsible for the continued monitoring all of the active volcanoes in the country, including Cotopaxi, Tungurahua and Reventador. The implementation of these forecasting codes into day to day monitoring has been explicitly requested by the Director of the Institute.

1.6 Thesis Aims

The primary objective of this research is to develop volcanic dome collapse forecasting tools using seismic signals which: (1) provide accurate forecasts; (2) can be used in real-time scenarios; and (3) are easily implemented at volcano observatories. Much research has been performed into forecasting volcanic eruptions using seismicity and other precursors, however the resulting forecast accuracy is varied. Principally this research aims to further develop forecasting tools by establishing causal relationships between seismicity occurring at depth, and the eruption occurring on the Earth's surface.

More specifically, the aims of this research are:

1. To appreciate and understand the monitoring capacity at the volcanoes where this research is based (Soufrière Hills, Montserrat and Chiles-Cerro Negro, Ecuador/Colombia) in order to develop operational forecasting tools adequate for the needs of these observatories, and compare this with other monitored volcanoes worldwide.

2. To take conventional forecasting techniques and develop them further such that forecasting is based upon one single active system at depth, and does not average across all precursory seismic activity.

3. To investigate volcanic dome stability at Soufrière Hills volcano prior to collapse, and determine the important factors which may enhance this instability.

4. To develop a conceptual model that links the acceleration of seismicity at depth to dome collapses at the surface at Soufrière Hills, Montserrat.

5. To test the newly developed forecasting tools on a developing volcanic unrest scenario at Chiles-Cerro Negro, Ecuador/Colombia.

1.7 Thesis Outline

Chapter 2 introduces the target volcanoes which have been investigated during this research: Soufrière Hill volcano, Montserrat and Chiles-Cerro Negro, Ecuador/Colombia. This includes a brief geological history, and analysis of the past and current monitoring practices. Chapter 3 details previous use of the Failure Forecast Method for forecasting volcanic eruptions, and applies these conventional techniques to a number of dome collapses at Soufrière Hills. Chapter 4 comprises the introduction of a suggested alteration on the FFM whereby similar low frequency seismicity is used as a forecasting tool. A number of assumptions about the FFM are challenged, including the use of a power law exponent, and different types of regression analysis. Volcanic edifice instability, and its importance is assessed in Chapter 5, with Finite Element Modelling suggesting that often the volcanic dome is already inherently unstable before unrest begins. A conceptual model linking the accelerating precursory seismicity at depth and the failure of an unstable volcanic edifice is presented in Chapter 6, based on the movement of magma at depth. Chapter 7 details the use of similar seismicity and forecasting to an unfolding unrest scenario at Chiles-Cerro Negro volcano, Ecuador/Colombia, where previously there was very little geological or geophysical understanding. Finally, Chapter 8 presents the main conclusions of this research, along with some of the limitations of the methods presented, and details of some ideas for further work.

Chapter 2

Target Volcanoes and their Monitoring Capacity

Significant differences are found between the monitoring of different volcanoes around the world. The monitoring capacity of a volcano is not only dependent upon the number of monitoring instruments which can be placed in the vicinity. It is dependent upon numerous political, geographical and financial considerations, which often conflict with one another. Therefore, the monitoring capacity of each volcano is unique, but might be comparable to other volcanoes in similar tectonic and political settings. This chapter provides an overview of the monitoring capacity of a number of volcanoes in different political, geographical and financial situations, which has formed part of Work Package 6 of the collaborative VUELCO (Volcanic Unrest in Europe and Latin America) project (http://www.vuelco.net/). Forecasting tools developed as part of this research will be created on the basis of the monitoring capacity of the target volcanoes, in order for the tools to be applicable immediately in an operational setting.

2.1 The Monitoring Capacity at Target Volcanoes

Since there is no direct way to investigate the magmatic system at depth, an understanding is based upon surface instrumentation and its interpretation. The manifestation of magmatic processes can be measured fundamentally through gas output at the volcano, ground deformation and seismicity. However, political, geographical and financial issues mean that it is impossible to monitor every single volcano on Earth, and different volcanic settings will require different levels of instrumentation. Inevitably, there is a trade off between safety of the proximal population, scientific research and financial implications.

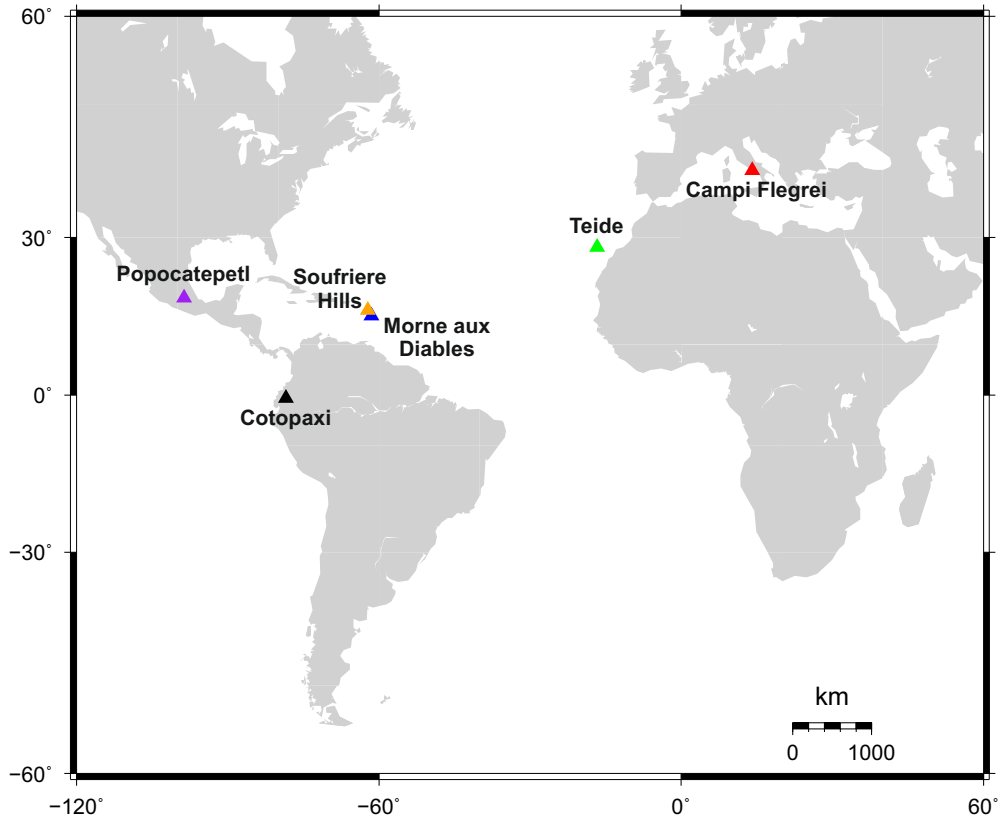

Figure 2.1: Locations of six target volcanoes chosen to investigate their monitoring capacity as part of the VUELCO project

Six andesitic volcanoes within Europe and Latin America were chosen as case studies to investigate the monitoring capacity at different volcanoes around the world (Figure 2.1 and Table 2.1). The chosen volcanoes span a wide range of volcanic settings, in different geographical and political situations, and all have a long history of monitoring using numerous sensors, with at least one documented period of "unrest". Here, unrest is defined as a period of activity above the normal background level (Phillipson et al., 2013). Common themes exist between each of the volcanoes, whether this be in their geographical setting, the type of dominant eruptions, or the longevity of the current phase of eruption. Campi Flegrei and Soufrière Hills are similar in the fact that they have been persistently active for decades. Popocatépetl has also been persistently active for a long time (since 1994), but sits in a very different cultural setting. Morne aux Diables is thought to be a reawakening volcano, since it has had two VT seismic crises in the past decade, after a number of decades of quiescence (Lindsay et al., 2005). However as a Caribbean volcano it is in a similar political and geographical position as Soufrière Hills. Neither Morne aux Diables or Soufrière Hills pose a threat to a large population, both being situated on small Caribbean islands. Campi Flegrei and Popocatépetl sit within highly popu-

Sensor	Campi Flegrei	Cotopaxi	Morne aux Diables	Popocatépetl	Soufrière Hills	Teide
BB Seismometer	17	5	1	4	10	6
SP Seismometer	8	9	5	5	2	3
Gas	3	3	1	4	4	3
EDM	-	6 base sites, 14 reflector points	-	2	8	-
Tiltmeters	-	6	-	3	-	-
Continuous GPS	3	7	2	-	11	8
Campaign GPS	-	22	12	2	-	20
Remote Cameras	-	Yes	-	Yes (3)	Yes	-
Thermal	Yes	Yes	-	Yes	Yes	-

Table 2.1: The monitoring capacity of six volcanoes in Europe and Latin America. BB are Broadband instruments, SP are Short Period and EDM are Electronic Distance Measurements.

lated areas, and thus pose an enormous threat to people. Therefore each volcano offers a unique insight into the monitoring capacity of different volcanoes in different settings, but also allows comparisons to be drawn.

It is evident from Table 2.1 that all of the volcanoes chosen for this case study are well monitored. Observatories responsible for the regular monitoring of the chosen volcanoes appear to place high precedence upon seismic networks for determining unrest. Campi Flegrei has a total of 25 seismometers in its vicinity, not only due to the large spatial area that the caldera occupies, but also because of the high risk to human life if unrest does develop, since over 2 million people live within 5 km of the caldera (Smithsonian Institution, Global Volcanism Program, 2015a). Even those volcanoes which are in more remote locations and so threaten smaller populations have a minimum of 6 seismometers (e.g. Morne aux Diables). Continuous GPS measurements of deformation and gas output measurements are also important, allowing detailed assessment of the volcano over longer timescales. These appear to be particularly valued monitoring tools at Cotopaxi and Teide volcanoes, where steep sided domes could threaten large numbers of the proximal population through over-steepening and collapses.

Monitoring of a volcano is not only important during periods of unrest. During periods of quiescence, it is important to continuously monitor a volcano in order to determine background levels of seismicity, deformation and gas output. Without this information, it is almost impossible to determine the onset of unrest periods, as well as to determine when the volcano has returned to a "normal" state. Ideally, dormant and quiescent volcanoes would be monitored by at least one seismometer, preferably broadband for the greatest frequency detection, and a number of continuous GPS's to detect inflation and deflation. A minimum of three seismometers equally distributed around the volcano allows the determination of hypocentres at depth and therefore allows spatial, as well as temporal, monitoring of seismicity. These should be placed in areas of low anthropogenic and other noise, but where they are easily accessible for maintenance. This, however, is not available in many cases, due to the financial implications of the equipment and maintenance of the monitoring scheme. Another seismic station is needed at greater distance from the volcano ($\geq$ 20 km) in order to easily distinguish between volcano seismicity and regional events (Wassermann, 2002). GPS's are more financially viable and therefore numerous instruments can be placed around the volcano as a monitoring tool for a small cost in comparison to a seismic network.

Two volcanoes were chosen to investigate the development of forecasting tools on active volcanoes: Soufrière Hills volcano, Montserrat and Chiles-Cerro Negro volcano, Ecuador-Colombia. Further details of the geological history and the unrest periods are given in Section 2.2 and 2.3. Chiles-Cerro Negro was chosen as a volcano with limited monitoring and understanding of the volcano's geological history. Sitting within the same volcanic arc as Cotopaxi, this allows a comparison to be drawn to one of Ecuador's most well monitored volcanoes.

Soufrière Hills volcano, Montserrat, is unusual in the fact that it is a persistently active volcano and has been in this state for over 15 years. This consequently means that the volcano is extremely well monitored and there is a wealth of data spanning back to 1995, including seismicity, deformation and gas measurements. Montserrat is also fortunate in the fact that it is a British overseas territory, and therefore benefits from an extensive aid program from the UK. It is estimated that the island has received over $£324$ million between 1997 and 2012 in aid (Tran, 2013), which means that the monitoring network is maintained and upgraded as is deemed appropriate. In addition to this, even 20 years later, an international Scientific Advi-

sory Committee (SAC) meets on the island every 12 months to discuss the previous months volcanic activity, and assess possible future scenarios which may unfold on Montserrat. This is a collaborative effort from UK and US scientists, as well as staff at the Montserrat Volcano Observatory (MVO). It is unusual for international collaboration to remain persistent at an active volcano for such a long time, in particular one which affects such a limited population.

In stark comparison to this, Chiles-Cerro Negro, Ecuador-Colombia has a minimal monitoring network, and sits within an active volcanic chain of the Andes mountains. Unrest was first detected at Chiles-Cerro Negro in 1991 by a single seismometer, however a dramatic increase in VT seismicity in October 2014 led to more recent concern. Chiles-Cerro Negro is unusual, since it sits astride of two countries (Ecuador and Colombia) with very different political agendas. The unrest detected at Chiles-Cerro Negro provides an excellent opportunity to test forecasting tools during ongoing unrest, where there is no benefit of hindsight, and in an environment which completely contrasts to Soufrière Hills. At Chiles-Cerro Negro, possible future scenarios are based only on geological mapping of the area, since there have been no historical eruptions. In addition, the background levels of seismicity, deformation and gas output are not really known, which means any deviations from developing unrest cannot be detected even with the current monitoring endeavours.

2.2 Soufrière Hills Volcano, Montserrat

2.2.1 Geological Background

The Caribbean is geologically complex, due to the variety of plate boundaries within a small area (Figure 2.2). The Caribbean plate itself is thought to be an anomalously thick oceanic plateau, ranging from 3 to 20 km thick (Giunta and Orioli, 2011). GPS measurements suggest that the Caribbean plate is moving approximately 1-2 cm a year to the E-NE (Wadge et al., 2014), with respect to the Americas, resulting in the formation of the subduction zone in the East, and thus the formation of the Lesser Antilles island arc, which extends almost 850 km in a North-South direction (Figure 2.2). The relative E-NE movement of the plate represents both the movement into the subduction zone, but also small amounts of North-South extension in this area, accommodated by East-West normal faulting (Wadge et al., 2014), as shown in the upper right panel of Figure 2.2. The Antilles is described as a “double arc system’. In the

southern half of the archipelago, two arcs have become superimposed on one another to form the islands of Grenada to Martinique. North of Martinique, the two arcs appear separated into the older outer arc to the East and a younger arc to the West, in which the current volcanic activity is paramount (Draper et al., 1994), and where Montserrat is located.

Montserrat (16° 45' N., 62° 10' W.) sits within the western series of islands that form the volcanic arc of the Lesser Antilles. Volcanic activity appears to have occurred intermittently along the arc for approximately 20 to 25 million years. The older, outer arc of volcanic centres (which includes Barbuda and Antigua) is thought to have become extinct and eroded before the late Eocene (55 to 33 million years ago). The first historically recorded eruption in the Caribbean was in St Kitts in 1692. Prior to the current eruption at Soufrière Hills volcano, which began in 1995, there is no evidence of historical eruptions on Montserrat, although seismicity and "unusual soufriere (fumerolic) activity" was noted in 1897 and 1933 (MacGregor, 1938).

The island of Montserrat is made up of adjacent, topographically distinct regions (from North to South: Silver Hills, Centre Hills, Garibaldi Hill, St. George's Hill, Soufrière Hills and South Soufrière Hills - Figure 2.3), each of which represents the remnants of a volcano which has become eroded with time (MacGregor, 1936). The central cores of these volcanic remnants consist of intrusive andesite with eroded deposits of unconsolidated agglomerates, tuffs and volcanic sands (MacGregor, 1936). The youngest volcanic centre on the island is Soufrière Hills, which has been in a state of unrest since 1995 and is still currently active. Although morphologically distinct, evidence from radiometric dating at Soufrière Hills and South Soufrière Hills suggests a near continuous record of volcanism spanning both centres (Smith et al., 2007a), with late stage volcanism at South Soufrière Hills giving way to volcanism at Soufrière Hills by the migration of the magmatic source at depth (Rea, 1974). The petrological and geochemical nature of Silver Hills, Center Hills and Soufrière Hills are broadly similar, with andesitic deposits containing abundant mafic inclusions (Harford et al., 2002), thought to represent the repeated injections of hot material into the cooler magma chamber at depth, which is then rapidly quenched due to a temperature contrast (Murphy et al., 2000). The magmatic evolution of the island is still under debate (Figures 2.4 and 2.5) with MacGregor (1936) and Rea (1974) suggesting that volcanism may have oscillated between the north and south of the island. Harford et al. (2002), using $^{40}\mathrm{Ar}/^{39}\mathrm{Ar}$ dating techniques has suggested that evolution

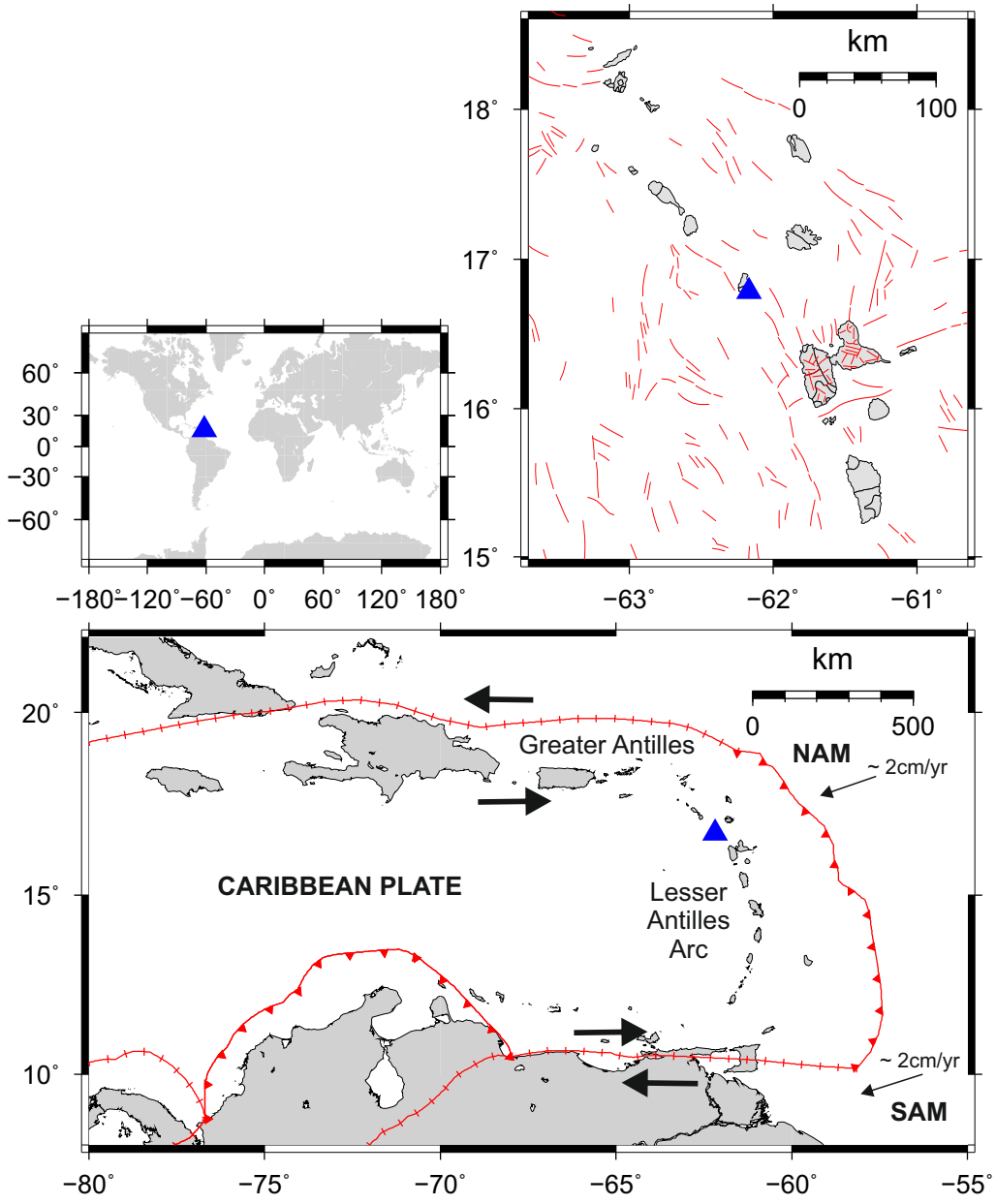

Figure 2.2: *Upper left*: The location of Montserrat. The triangle represents the location of Soufrière Hills volcano. *Upper right:* Faulting in the Lesser Antilles arc close to Montserrat, both in a N-S and E-W direction. Modified from USGS (2013). *Lower:* Major plate boundaries in the vicinity of Montserrat. The subduction zone (red line with triangles) to the East of Montserrat is thought to be responsible for the volcanism. NAM is the North American Plate, SAM is the South American Plate. Relative movement of the large scale transform faults (red) are also shown (after Feuillet et al. (2002) and Bird (2003)).

has been from North to South, with Silver Hills being active 2.5-1.1 Ma, followed by Centre Hills (954-550 ka) and finally Soufrière Hills from 174-24 ka prior to the current eruption.

The Soufrière Hills complex consists of four dome structures (Gage's Mountain, Chance's

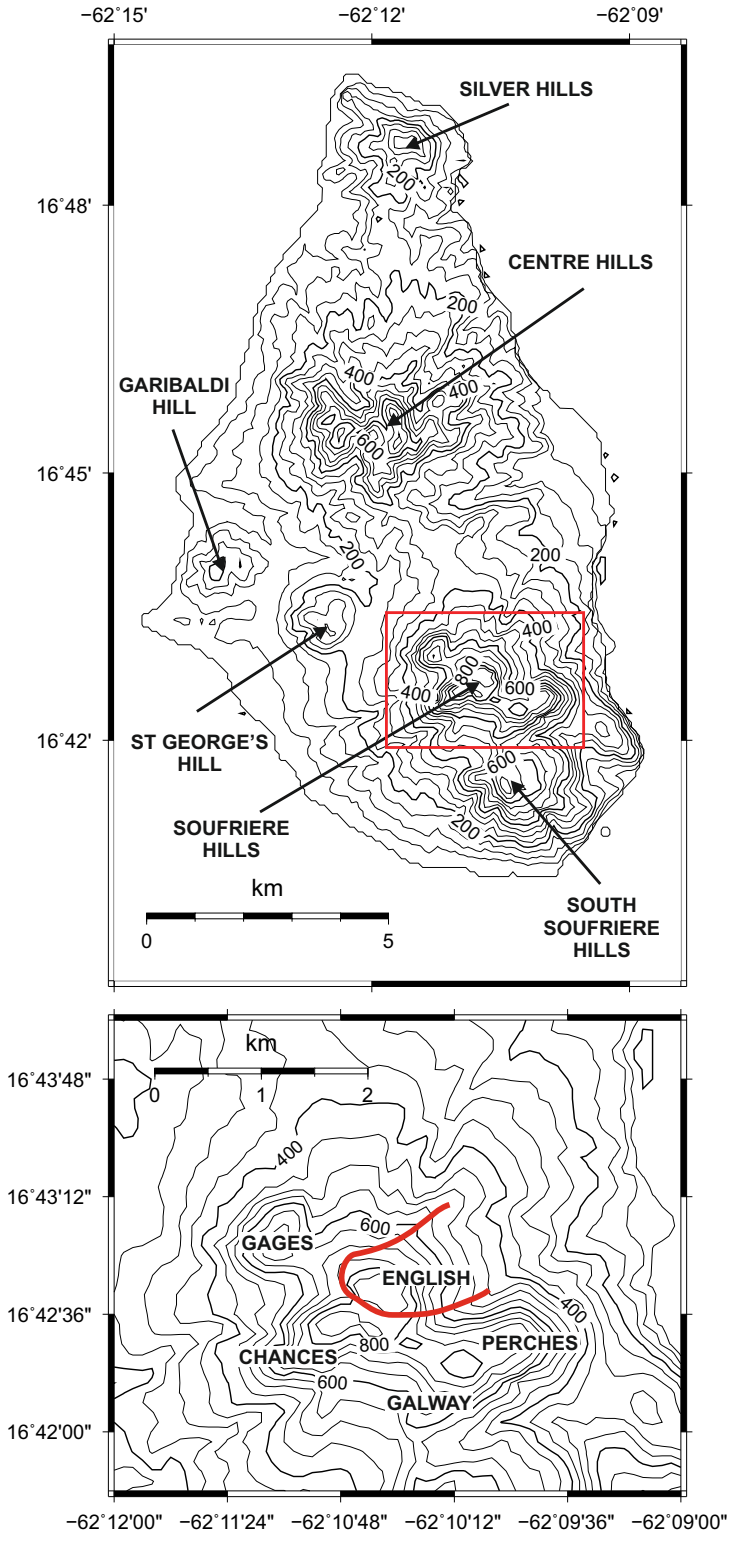

Figure 2.3: Topographic regions on Montserrat. *Upper:* The main topographic regions on Montserrat. The red box denotes the region seen in lower figure. *Lower:* The Soufrière Hills dome complex, with the scar of English's crater, open to the East, depicted in red.

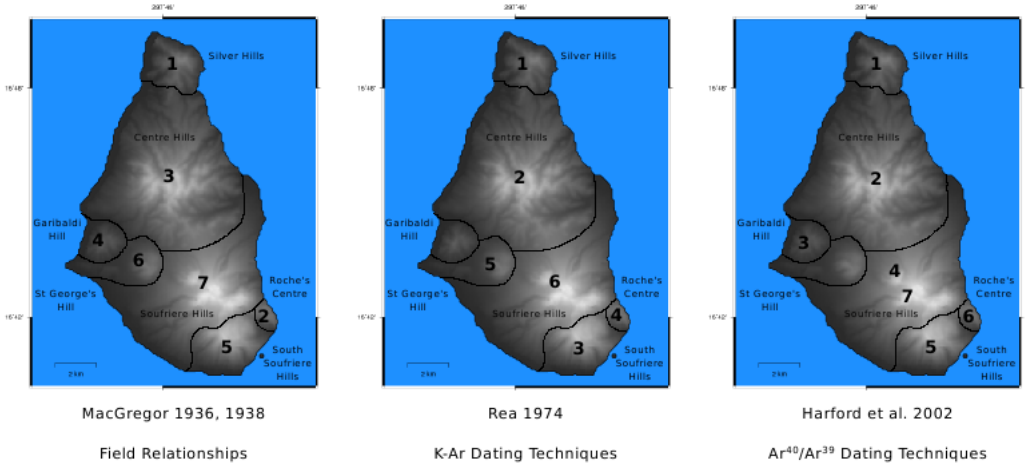

Figure 2.4: The magmatic evolution of the Island of Montserrat. Adapted from Harford et al. (2002). Each section represents a different stage of evolution in terms of age, with 1 being the oldest.

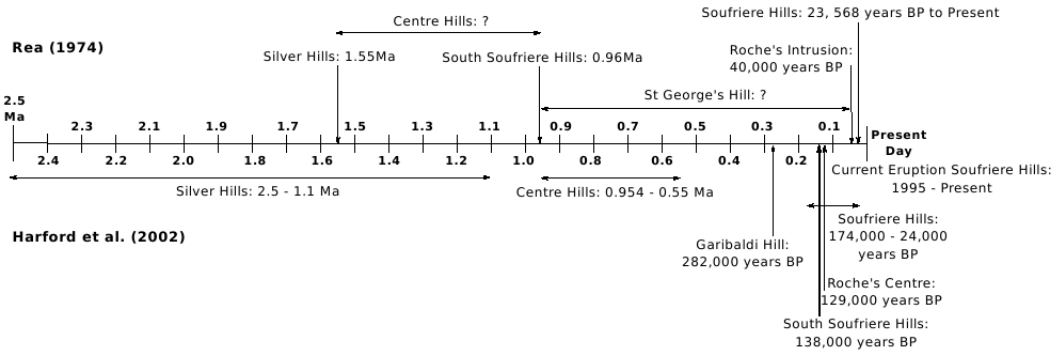

Figure 2.5: The Evolution of Montserrat's volcanic centres according to Rea (1974) and Harford et al. (2002)

Peak, Galway's Mountain and Perche's Mountain), punctured by a dome filled crater (English's crater) holding Castle Peak, which appears to "sit on" loose unconsolidated pyroclastic flow deposits, believed to be from the present eruption (Wadge and Isaacs, 1988) (Figure 2.3). Petrological and physiological differences between each of the four domes suggest that each represents a separate volcanic feature (Rea, 1974, Harford et al., 2002). English's Crater (a collapse sector scar from where the current activity is focused) is believed to be younger than all of the other domes, since it truncates both Galway's and Chance's Peak, and sits open to the East (Rea, 1974). Much of the underlying stratigraphy has now been covered by deposits from the current eruptive phase, but the suggestion is that the eruption style at Soufrière Hills has been cyclic between Peléan and Plinian style. Volcanic activity is believed to have been

largely intermittent, at least over the past 400,000 years, lasting a few thousand years at a time separated by long periods of quiescence. Historical eruptions derived from dating the youngest block and ash flows on the island suggest that Soufrière Hills may have erupted around 1475 and again between 1536 and 1561. These eruptions are likely to have been smaller than the current one, since deposits are only concentrated around the eastern flank of Soufrière Hills volcano within the current sector collapse scar (Smith et al., 2007a).

2.2.2 The current eruptive period: 1995 to Present

The latest eruption of Soufrière Hills Volcano, Montserrat began in July 1995 with a series of phreatic explosions associated with vent openings around the crater. This was the first historical eruption of the complex, although seismic crises had been recorded on the island at approximately 30 year intervals in 1897-98, 1933-37 and 1966-67 (Aspinall et al., 1998). Shepherd et al. (1971) noted that the seismicity in 1966-67 was predominately made up of VT events with clear P- and S- arrivals, located in the south of the island, and related the earthquake activity to the volcano. However, since the activity ranged from shallow to approximately 10 km depth, they concluded that no large sized magmatic body was present at shallow depths, as the presence of S-waves were clearly evident, which would be unable to travel through the liquid magmatic body. Since VT activity is primarily associated with the fracturing of intact rock (Arciniega-Ceballos et al., 2003), these volcano-seismic crises may have been the first indication that the magmatic system at depth was once again becoming active (Wadge et al., 2014).

Since November 1995, Soufrière Hills has undergone a repeated cycle of dome growth and collapse, with the collapse phases resulting in pyroclastic flows, lahars and ash fall. The eruption can be split into five extrusive phases (Table 2.2). Along with the repetitive cycles of dome growth and collapse, Vulcanian explosions have also been a common feature during periods of extrusion, which are often accompanied by ash venting (Donovan et al., 2011). Prior to the current eruption onset in 1995, only two seismic stations (MGHZ and MLGT) existed for the daily monitoring of the volcano, maintained by the University of the West Indies. More seismometers were installed by the USGS Volcano Disaster Assistance Program (Aspinall et al., 1998) in the configuration shown in Figure 2.6 just after the unrest began.

Since 1995 a continuous network of monitoring equipment has existed on Montserrat to ensure the constant and consistent monitoring of the volcano by the Montserrat Volcano Ob-

servatory (MVO). The current configuration of seismometers (shown in figure 2.7(a)) consists of 10 broadband stations and 2 short period stations. All stations are owned by MVO, with the exception of MBWW which is owned by the University of Leeds, with data being passed both to the University and to MVO. This configuration allows detailed locations of hypocentres to be determined. In addition to this, there are 2 sites of continuous gas monitoring, 8 Electronic Distance Measurement (EDM) stations and 11 continuous GPS sites, allowing all three major monitoring techniques of an active volcano to be utilised (Figure 2.7(b)).

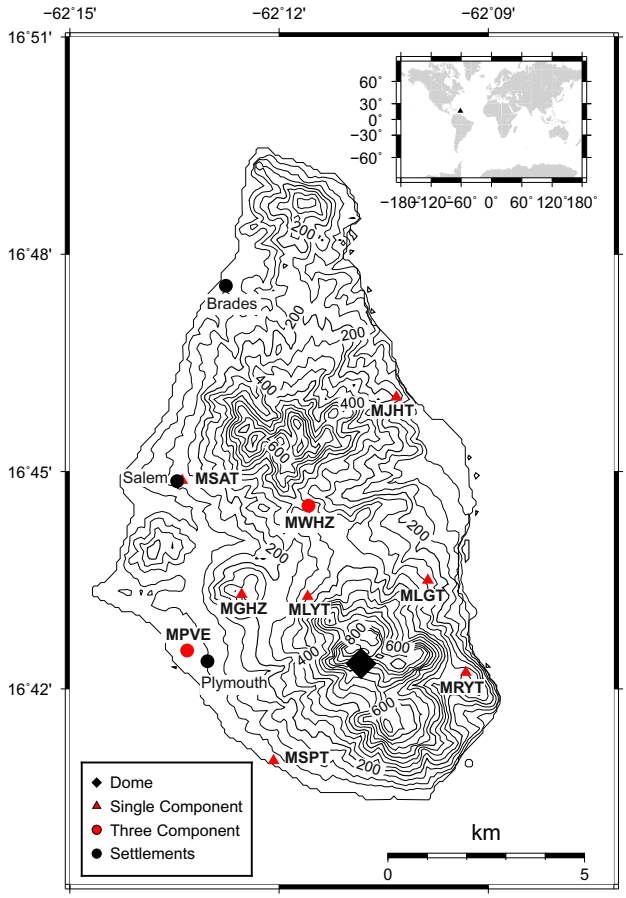

Figure 2.6: Configuration of seismometers on Montserrat in 1995 after the eruption began

Phase	Dates	Average Ex. Rate (m3/sec)	Characteristics	Major Collapse Events	Citations
1	July 1995 - March 1998	4.5	Precursory phreatic episode. Predominantly dome growth and collapse.	25th June 1997. Death toll: 19. Removal of 5.5 million m^3. Plymouth (capital) permanently evacuated.	Loughlin et al. (2002), Calder et al. (2002)
2	November 1999 - August 2003	2.9	Two short intervals of no extrusion. Ended in collapse of $\geq 95\%$ of dome.	12th July 2003. Removal of 210 million m^3. Pyroclastic flows enter the sea, generating a small tsunami and hydrovolcanic explosions	Herd et al. (2005)
3	August 2005 - April 2007	5.3	Precursory phreatomagmatic episode. One major collapse. Episode ends with large dome in place.	20th May 2006. Removal of 97 million m^3	Loughlin et al. (2010)
4a	July 2008 - September 2008	2.9			
4b	December 2008 - January 2009	14	Highest extrusion rate observed.		
5	October 2009 - February 2010	6.8	Ends in large collapse.	11th February 2010. Removal of 50 million m^3	Stinton et al. (2014)

Table 2.2: Extrusive phases on Montserrat, after Wadge et al. (2014)

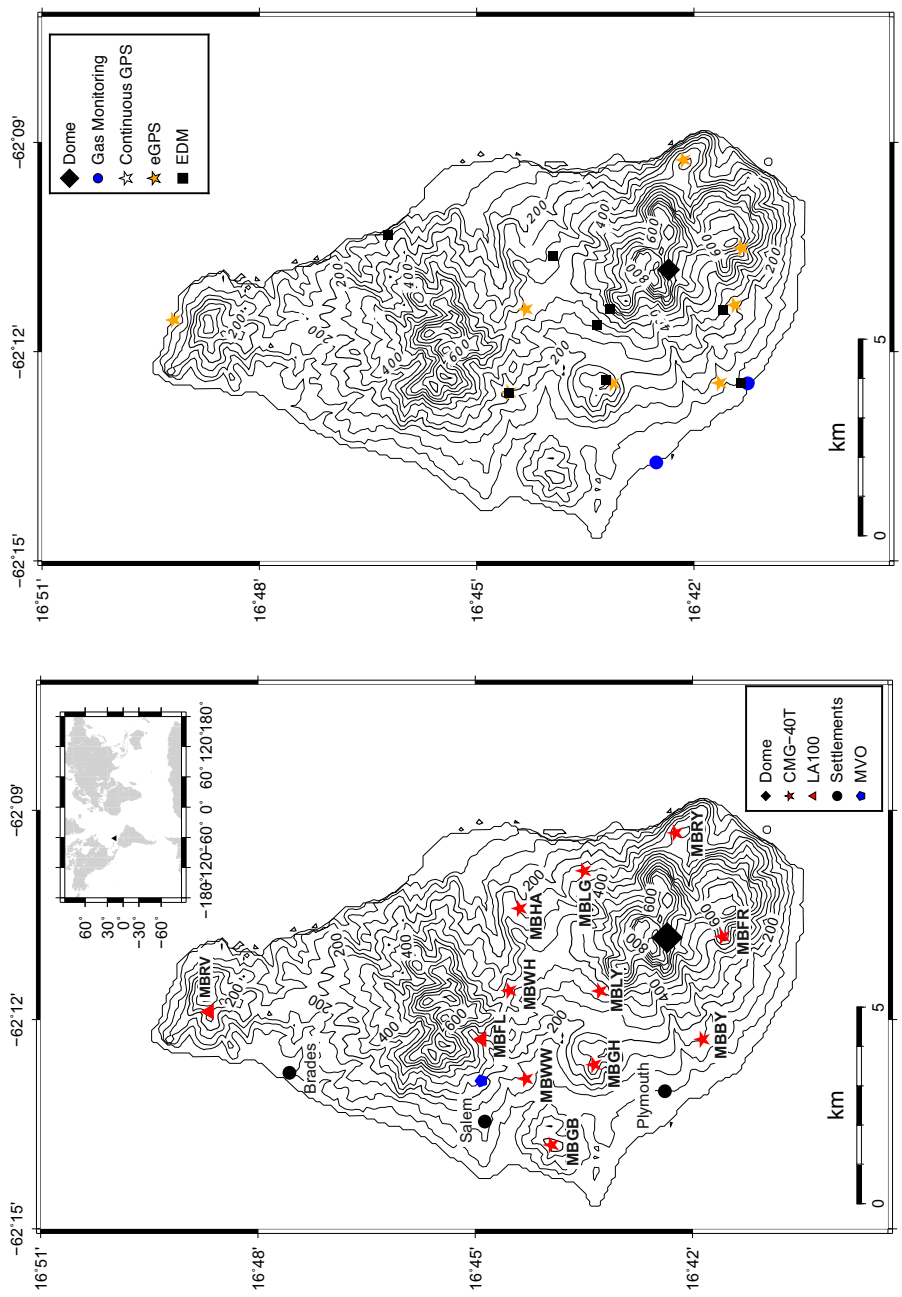

(a) Current configuration of seismometers on Montserrat

(b) Other monitoring tools on Montserrat

Figure 2.7: Current configurations of seismometers and other monitoring tools on Montserrat

2.2.3 Seismicity associated with the current eruption

Seismicity is dominant during phases of extrusion at Soufrière Hills volcano (Table 2.2). During these times, seismicity has fluctuated, potentially due to fluctuating extrusion rates (Wadge et al., 2014). Almost all large dome collapses at Soufrière Hills volcano have been preceded by swarms of low frequency earthquakes, often occurring in cycles of 8-12 hours and lasting from a few hours to several days (Voight et al., 1998, Miller et al., 1998, Green and Neuberg, 2006). However, swarms of low frequency events can also occur without there being any collapse (Neuberg et al., 2006). These swarms are of a periodic nature, which can be well correlated to tilt signals (Green and Neuberg, 2006), suggesting that during times of inflation of the dome, low frequency seismic swarms are extensive, reaching a maximum intensity at the point of the maximum tilt signal (i.e. the maximum inflation of the dome) (Miller et al., 1998). During times of deflation, low frequency event swarms become negligible and other types of seismic signals are more identifiable such as pyroclastic flow signals and rockfalls, which may signify the onset of dome collapse (Voight et al., 1998). This suggests that low frequency events are related to processes of pressurization within the volcanic plumbing system (Neuberg et al., 2006). Neuberg et al. (2000) concluded that only a closed resonating volcanic cavity (such as a conduit) has the ability to sustain resonating low frequency seismic events over time scales that are observed on Montserrat (single events can last up to 10 seconds), since an open system would allow the seismic waves to escape to the surface.

High frequency VT events have also been recorded at Soufrière Hills volcano, although they occur much less frequently. During periods of dome growth, VT earthquake levels have been low and almost always exclusively located at depths between 2 km and 5 km below the dome. This is much deeper than the located low frequency signals, which are focused from the surface down to approximately 3 km depth. VT earthquakes are also far more dominant when low frequency signals are low (Miller et al., 1998). Rockfall signals are common during periods of dome growth and collapse and, combined with visual observations, are caused by the steepening of the talus slopes of loose material on the volcano flanks by the inflation of the dome. Associated with this phenomenon are pyroclastic flow signals, which involve the movement of larger amounts of material. Since 1997, Soufrière Hills has undergone intermittent periods of Vulcanian explosions during eruptive phases, inducing eruptive columns up to 10 km high. These have almost always been preceded by swarms of low frequency seismicity, which often merges into volcanic tremor in the latter stages of the eruption when ash venting

becomes dominant (Neuberg et al., 2000).

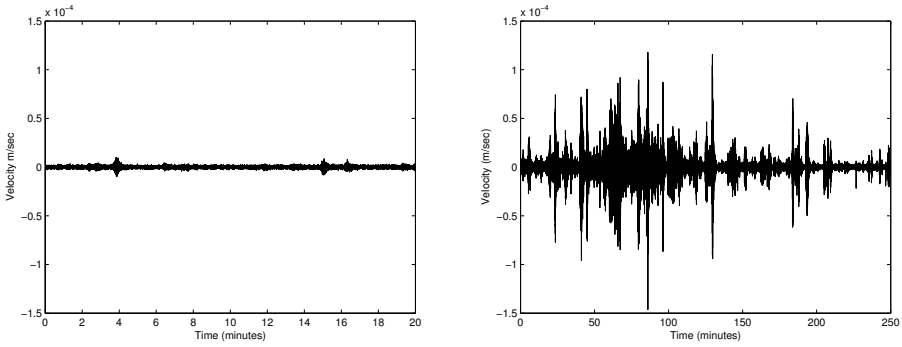

(a) Limited seismicity above background level on 25 December 2006 at station MBLG

(b) High seismic activity on 11 February 2010 at station MBLG, prior to a large scale dome collapse

Figure 2.8: Low and high seismic activity recorded on Montserrat

Examples of different seismic scenarios at Soufrière Hills volcano are shown in Figure 2.8. An example of low seismic activity is seen in Figure 2.8a from 25 December 2006, where almost no fluctuations in seismicity are seen above the background noise level. The seismogram has been Butterworth band pass filtered between 0.5 and 15 Hz, in order to try and amplify any low frequency seismicity present. The example in Figure 2.8b is taken from the day of the large scale dome collapse on 11 February 2010, and is again Butterworth filtered between 0.5 and 15 Hz. Since the dome collapse in February 2010, seismicity at the volcano has remained low, except for a short VT swarm from 22-23 March 2012.

2.3 Chiles-Cerro Negro, Ecuador-Colombia Border

2.3.1 Geological Background

The stratovolcanic complex of Chiles $(00°49'\mathrm{N}, 77°56'\mathrm{W})$ and Cerro Negro de Mayasquer $(00°49'\mathrm{N}, 77°57'\mathrm{W})$, known as Chiles-Cerro Negro, lies directly on the border between Ecuador to the South and Colombia to the North, sitting at heights of 4748 m and 4470 m respectively (Instituto Geofisico EPN, 2015), within the cordillera Occidental (Western cordillera) of the Andes mountain chain. Cerro Negro volcano is located approximately 5 km to the west of Chiles. Besides active fumaroles and hot springs, which is indicative of an active hydrothermal system, there are no confirmed eruptions of the Chiles-Cerro Negro complex. However, there is clear evidence that both of these stratovolcanoes have been very destructive in the past, with

large scale collapse scars on the northern flank of Chiles (approximately 1 km in diameter), and on the western flank of Cerro-Negro (approximately 1.8 km in diameter) (Jimenez and Velasco, 1997). However, very little research has been conducted into these volcanoes and therefore very little is known about them in terms of their geological history.

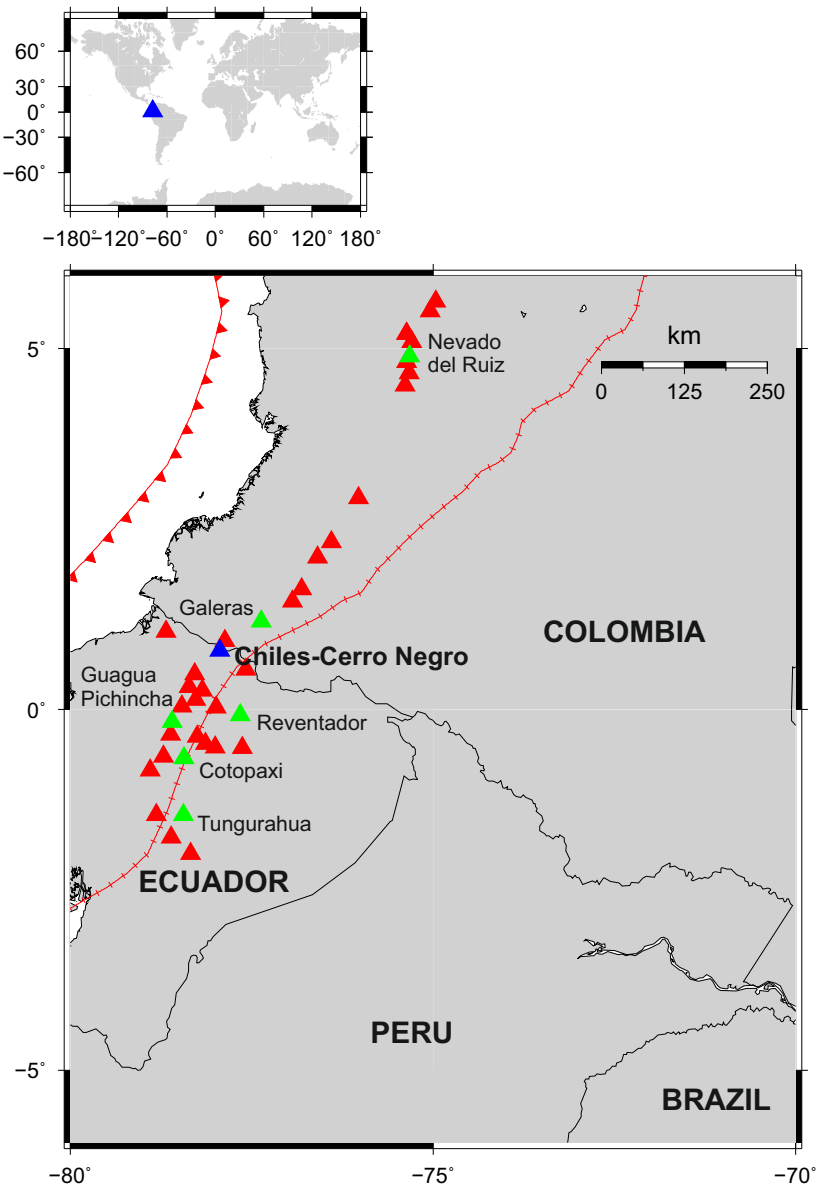

Figure 2.9: Setting of Chiles-Cerro Negro. Blue triangle represents the location of Chiles-Cerro Negro. All other volcanoes within the NVZ are shown in red, with notable ones named and shown in green. Subduction zone to the west (red line with triangles) thought to be responsible for the volcanism. Large scale transform fault (red line) bisects the volcanoes in Ecuador. Boundaries after Bird (2003).

The Northern Volcanic Zone (NVZ) of the Andes extends roughly North-South over 800 km from Romeral in Colombia down to Sangay volcano in Ecuador, and notably includes the

volcanoes of Nevado del Ruiz, Galeras, Cotopaxi and Tungurahua (Figure 2.9). Volcanism in this area is the direct result of the eastward subduction of the Nazca oceanic plate (in the last 20 Ma) beneath the South American continent, at angles of $25°$-$35°$ (Lavenu et al., 1992), with a subduction rate of 6.5 to 9 cm/year. In Colombia, the NVZ is divided into three sub-parallel cordilleras separated by deep inter-Andean valleys known as the Western, Central and Eastern cordilleras. South of the city of Pasto, Colombia, the Central and Eastern cordilleras converge, resulting in the Ecuadorian Andes being characterised by only two chains: the Occidental and Real cordilleras (Droux and Delaloye, 1996). It is thought that the lenses of sediment creating the cordilleras are a result of a number of accretion events from the South-West onto the continental edge of Colombia during the Cretaceous (Grösser, 1989). They are bounded by large scale faults on either side trending in a NNE-SSW direction (see Figure 2.10).

The current geological map produced by the Servicio Geologico de Colombia shows that the composition of the deposits from Chiles and Cerro Negro are primarily andesitic and dacitic, and extend for up to 5 km radially from the volcanoes (Figure 2.10). A number of local faults, known collectively as the El Angel-Guachucal fault system, appear to pass directly through the volcanic centres of Chiles and Cerro Negro, and appear to facilitate a mixture of strike slip and reverse movement (Ruiz et al., 2013a). Only the Tuffino fault (highlighted in red in Figure 2.10 in the East) is believed to still be currently active, although there is evidence that two large magnitude (Mw 6.6 and 7.2) earthquakes in 1868 were also caused by a culmination of movement within this entire fault system (Ruiz et al., 2013a, Beauval et al., 2010).

In 1996, the Observatorio Vulcanologico y Sismologica de Pasto began geochemical studies of the area which included taking water and gas samples of the surrounding hot springs. Besides this, only one operational seismic station (short period) existed in the near vicinity of the volcanoes, sitting on the southern flank of Cerro Negro as a monitoring tool (ECEN in Figure 2.11). The station was installed in 1991 by the Instituto Geofisico de la Escuela Politecnica del Ecuador (IG-EPN), who also analysed the incoming seismic data (Ruiz et al., 2013b, Jimenez and Velasco, 1997). Anomalous VT seismicity was detected in January and February 2000, which was believed to be related to the fault systems in the area, as there was no other evidence of a reactivation of the volcanic complex (Ruiz et al., 2013a).

2.3.2 Current Phase of Unrest: 2014 to Present

Prior to the current phase of unrest, Chiles-Cerro Negro is not known to have had any historic eruptions. The last eruption is thought to have been ≈3400 years ago from Cerro Negro, in the form of a debris avalanche (Ruiz et al., 2013b). There is some confusion as to whether an eruption beginning on 17 July 1936, and with an unknown end date (classed as a VEI 2) is really an eruption of Chiles-Cerro Negro as was reported at the time (Smithsonian Institution, Global Volcanism Program, 2015b). Fieldwork has suggested that none of the younger volcanic deposits on the flanks of Chiles-Cerro Negro are a product of these volcanoes (Jimenez and Velasco, 1997), and are more likely to be deposits of Reventador in Ecuador (Smithsonian Institution, Global Volcanism Program, 2015b).

Month (2013)	ML ≤ 2	ML ≤ 3	ML ≤ 4	ML ≥ 4	**Total**
July	0	7	1	0	**8**
August	2	7	2	0	**11**
September	5	23	9	0	**37**
October	11	21	6	2	**40**

Table 2.3: Number of Events registered at Chiles-Cerro Negro from July to October 2013

Despite a difficult political environment, the unfolding volcanic unrest is being carefully monitored by both the Ecuadorian Instituto Geofisico (IG-EPN) and the Colombian Servicio Geologico de Colombia (SGC), since unrest is unprecedented at this complex. IG-EPN currently has 3 seismometers to the south of the volcanic complex, with SGC having 5 seismometers in the north (Figure 2.11), and both work together to increase the monitoring effort of this volcanic complex.

Detection of "anomalous" VT seismicity around the volcanic complex began in 1991, however this was assumed to be related to the active hydrothermal system and thus became the background seismicity. Generally, there were between five and ten events a month, with a mix of VT and LF events (Ruiz et al., 2013b). The seismic event rate once again increased above this now background level in July 2013 (Table 2.3); some events were felt in the neighbouring settlements due to their magnitude. Seismicity has remained elevated ever since (Pers. Comm. D. Sierra- IG-EPN, April 2015). The events from July to October 2013 were initially classed as a swarm of activity due to movement along faults which dissected the craters of Chiles and

Cerro Negro (Ruiz et al., 2013a). One of the largest events in October 2013 occurred almost directly below the current crater of Chiles volcano on the 16 October, at a depth of approximately 2 km, which sparked an increased awareness of the hazardous nature of this complex. The event registered as a M4.5 on the Richter scale and was felt locally. The event has since been determined as a thrust fault with components of strike slip, similar to the suggested movements along most of the faults in the area (Ruiz et al., 2013a). Following the increased VT seismicity in July 2013, the IG-EPN installed two broadband seismometers in April 2014, which allowed the more accurate determination of hypocentres of seismicity (Pers. Comm. D. Sierra, IG-EPN, April 2015), in particular those which are of small magnitude and could not be picked up on the regional seismometer system.

The number of VT seismic events registered in close proximity to Chiles-Cerro Negro (approximately 10 km radius) dramatically increased in October 2014, from what had become a "background" seismic event rate over the past few months of 10 to 50 events per day, to over 150 events a day. In addition to this, there appears to have been a systematic increase in the magnitude of events, with proportionally more events larger than M2 (Figure 2.12, (Ruiz et al., 2013a,b)). Since the start of the year (January 2015), there appears to have been a general decrease in both the number of events, and their relative magnitude. As shown in Figure 2.13, the seismicity appears to be concentrated to the south of Chiles-Cerro Negro, and within the upper 10 km of the crust. Figure 2.13 however does appear to show many artefacts with respect to the depth of the seismicity, presumably related to the input velocity model used in the location of events, with events appearing, for example, at depths of around 2.5 km, 3 km, 5 km and 10 km consistently across different latitude. No clear migration in seismicity is seen over these time scales, although perhaps the events of January and February 2015 are consistently shallower and more concentrated spatially to the summits of Chiles and Cerro Negro than those before. Location and depth information was generated by the IG-EPN.

Since unrest began at Chiles-Cerro Negro, four large magnitude earthquakes have been detected in the Ecuador-Colombia border region, and two within close proximity to the volcanic complex (Figure 2.13). The largest of these, a M5.8 on 20th October 2014 (Figure 2.12), is shown as the more southerly of the large magnitude earthquakes in Figure 2.13 and occurred at the very shallow depth of 4.6 km (Pers. Comm. D. Sierra, IG-EPN, April 2015). Deformation data from InSAR (Figure 2.14) suggests that the earthquake generated approximately 18 cm

of surface deformation in the region close to the location of the earthquake. The displacement pattern echoes slip of 0.8 m along an oblique thrust fault which is located to the south of Chiles volcano at a shallow depth (1.5-3 km) and orientated in a NNE-SSW direction (Pers. Comm. S. Ebmeier, University of Bristol, April 2015). As shown in Figure 2.12, following this event, the number of higher than usual magnitude events increased.

2.4 Summary

Two volcanoes have been used in this study. Soufrière Hills volcano, Montserrat has been persistently active for almost 20 years (split over 5 phases of extrusion) and appears to be in a continuous cycle of dome building and collapse. The monitoring network is exceptional, with 12 seismometers, plus continuous and campaign GPS, and gas monitoring. Seismicity is particularly persistent during eruptive phases, and almost all large dome collapses have been preceded by swarms of low frequency seismicity. The wealth of data covering many scenarios is excellent for the development of forecasting tools. Chiles-Cerro Negro sits on the border between Ecuador and Colombia and became restless again in July 2013. Prior to this, only one seismometer was active and occasional gas sampling of the active fumaroles were performed. The volcano was believed to be dormant but with an active hydrothermal system at depth which generated background levels of seismicity. This is an excellent opportunity to test forecasting tools which appear to be successful at Soufrière Hills volcano during a developing unrest scenario, where there is very little background information and therefore limited experience to draw upon for the volcano in question.

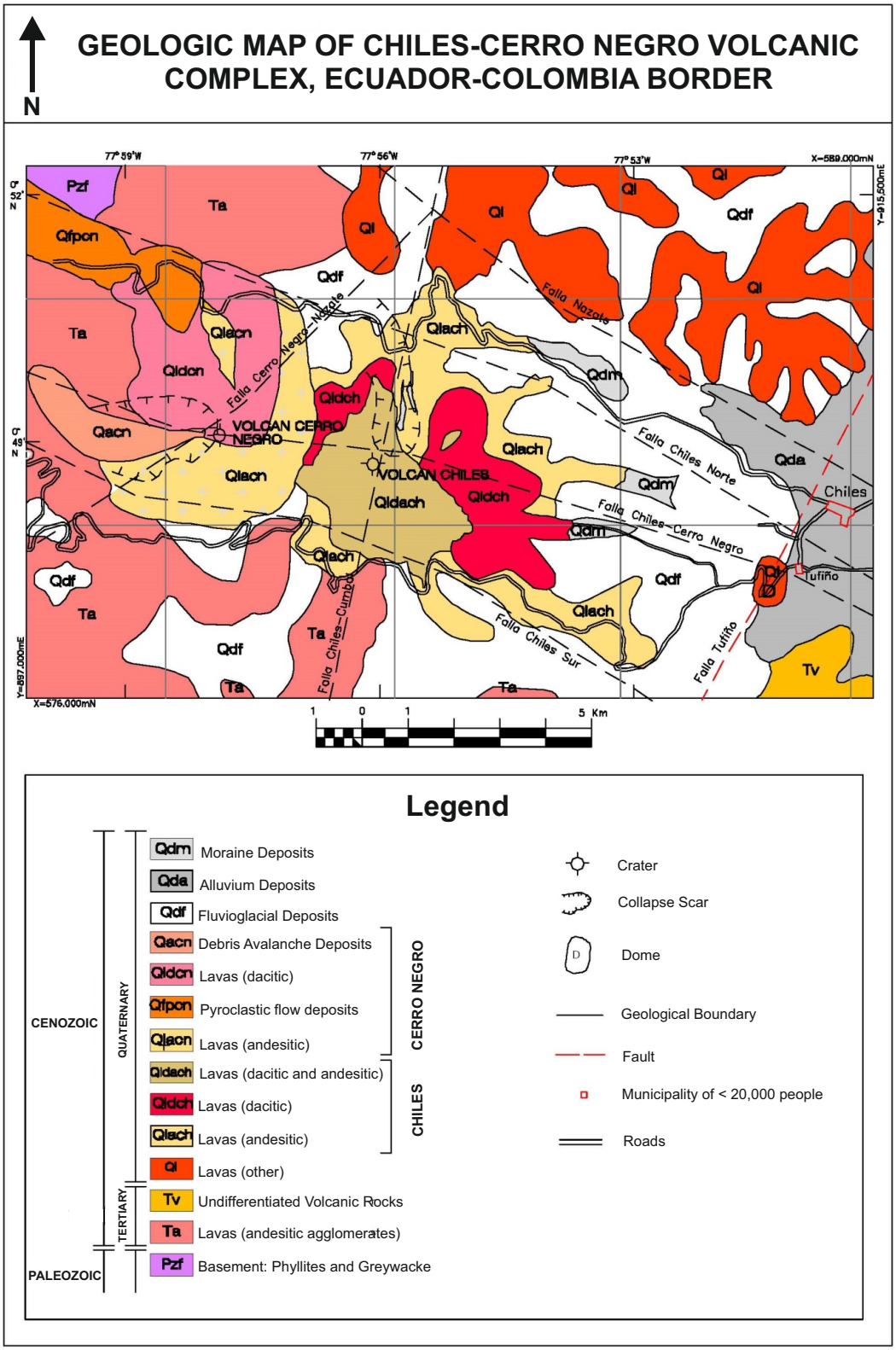

Figure 2.10: Geological map of the Chiles-Cerro Negro volcanic complex showing main deposits and faults in the area. Modified from Servicio Geologico de Colombia.

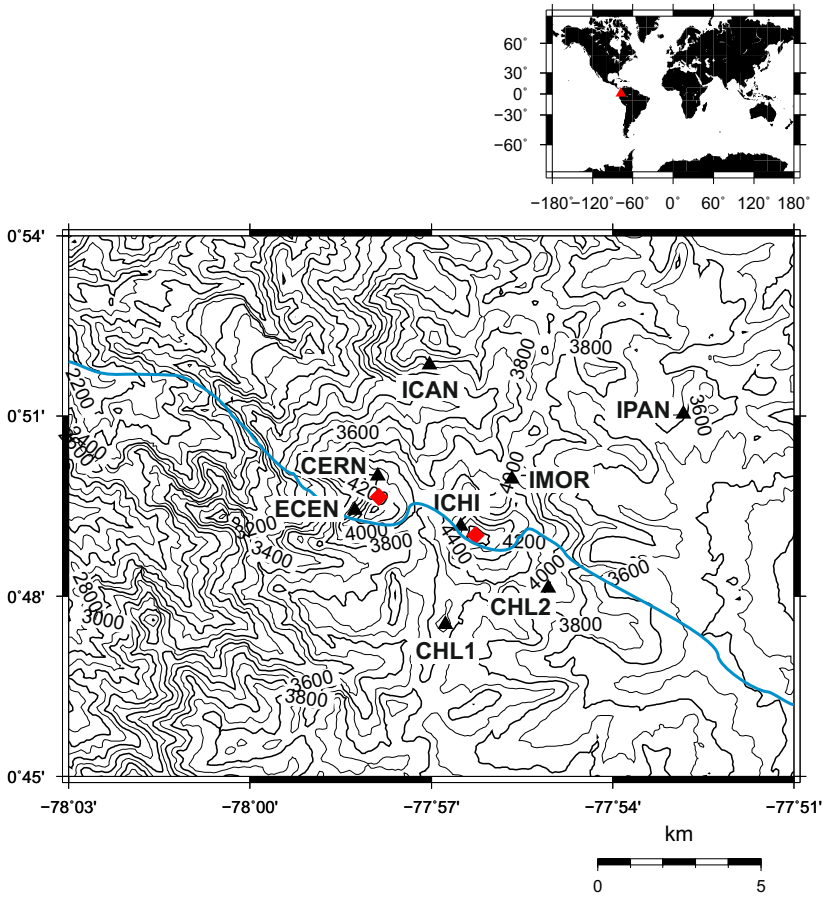

Figure 2.11: Distribution of seismometers currently monitoring Chiles-Cerro Negro. All stations are broadband sensors (Trillium Compact 120), except for ECEN which is a short period station. The approximate border between Ecuador and Colombia is also shown as a solid line passing directly through the craters of both volcanoes.

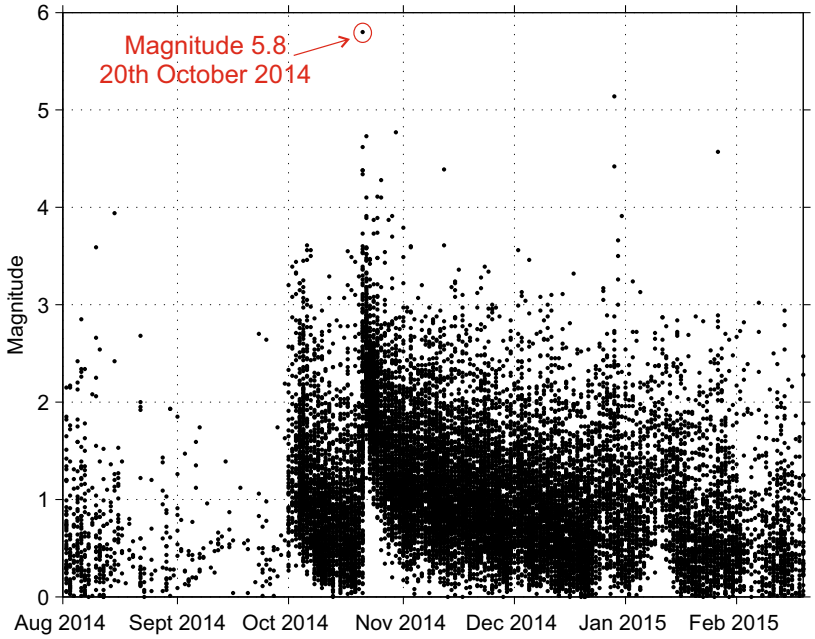

Figure 2.12: The magnitude of events recorded in close proximity to Chiles-Cerro Negro from September 2014 to February 2015. Event magnitudes generated by the Instituto Geofisico.

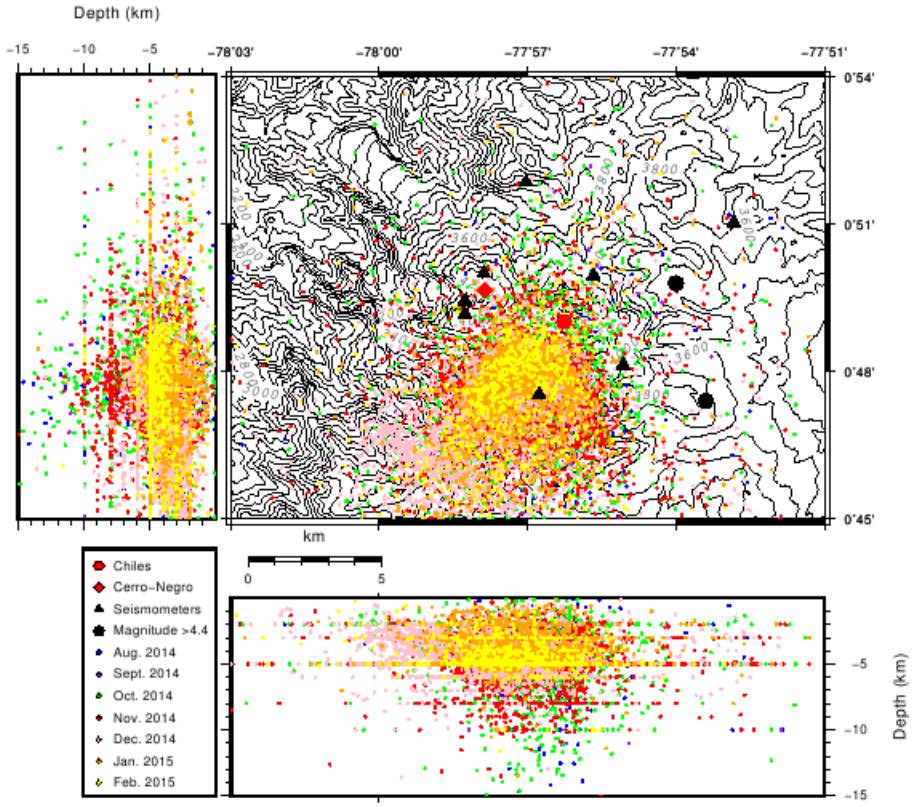

Figure 2.13: Current seismometer configuration and distribution of seismicity at Chiles-Cerro Negro from official catalogue of events as determined by the Instituto Geofisico in Ecuador. The border between Ecuador and Colombia runs directly through the craters of each volcano in a NW-SE orientation on the figure. 16,844 seismic events from August 2014 to February 2015 are plotted which were within approximately 10 km radius of the volcanic complexes and are temporally colour coded.

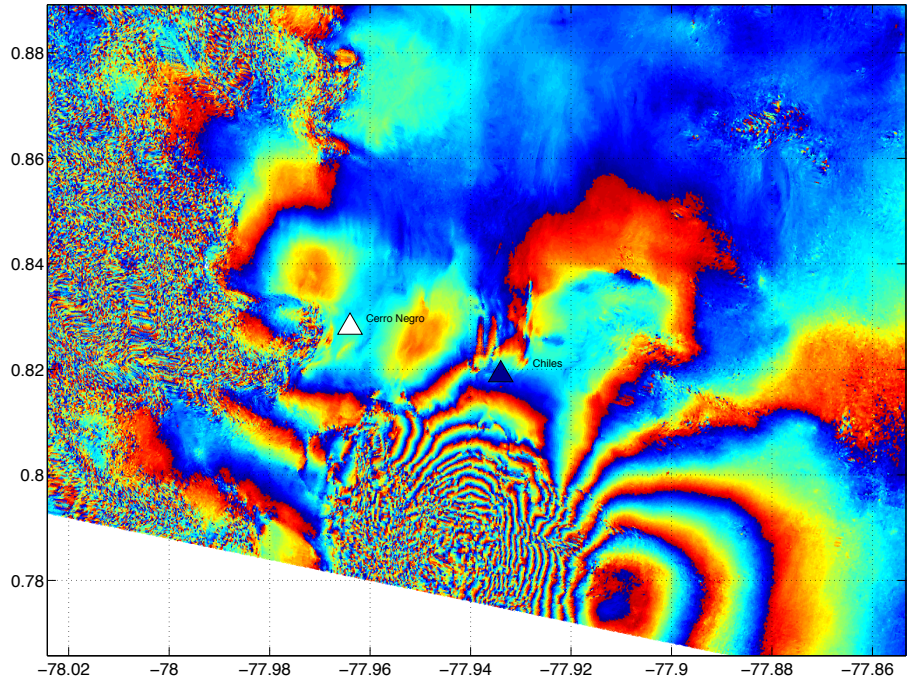

Figure 2.14: Deformation at Chiles-Cerro Negro associated with unrest from 18th to 29th October 2014. Each complete colour cycle represents a 2 pi phase change or 1.55 cm of deformation in the satellite line of sight. One colour cycle ranges from red to yellow to blue. Maximum displacement is towards the satellite to the south of Chiles volcano (apparent displacement of 18 cm). This displacement pattern is well matched by movement on an oblique thrust fault (strike=197, dip=40, rake=143, depth=1.5-3 km) with uniform slip of 0.8 m. *Figure courtesy of S. Ebmeier, University of Bristol.*

Chapter 3

Towards Forecasting Volcanic Processes: The Failure Forecast Method

One increasingly popular method for forecasting volcanic eruptions relies upon the Failure Forecast Method (FFM), which has been outlined in Section 1.3. However, this is mostly done in hindsight and has yet to be tested for its reliability as a forecasting tool on a number of volcanic phenomena at a single volcano. Soufrière Hills offers the unique chance to investigate precursory seismicity prior to a number of large dome collapses due to a long established monitoring effort (Section 2.2.2). This chapter introduces current common forecasting methods using the FFM and investigates their reliability for forecasting three large dome collapses at Soufrière Hills: June 1997, July 2003 and February 2010, amongst others. It is shown that these current practices are not reliable enough to base forecasts upon, because the techniques do not allow the separation of processes at depth, and therefore the FFM is averaging over a larger set of parameters, rather than concentrating on one single process.

3.1 Previous application of the Failure Forecast Method in Volcanic settings

Accelerating rates of geophysical precursors appear to be common in volcanic settings, and in representative laboratory settings prior to material failure (e.g. eruptions, landslides, fracturing). For example accelerations in the number of seismic events were observed prior to the 1989 eruption of Redoubt volcano (Cornelius and Voight, 1994), and the 1982, 1985 and 1986 eruptions at Mt St Helens (Voight, 1988, Voight and Cornelius, 1991, Smith et al., 2007b).

Accelerations in seismic energy prior to the 1994 and 1998 eruption of Colima volcano (De la Cruz-Reyna and Reyes-Dávila, 2001) have also been observed as well as accelerations in seismic amplitude prior to the 2000 eruption of Villarrica volcano (Ortiz et al., 2003). Within the laboratory environment, experiments have been set up to emulate the final moments prior to failure and acoustic emissions measured, mimicking seismicity prior to eruption (Smith et al., 2009). However, very rarely are forecasts made for volcanic phenomena in real time situations.

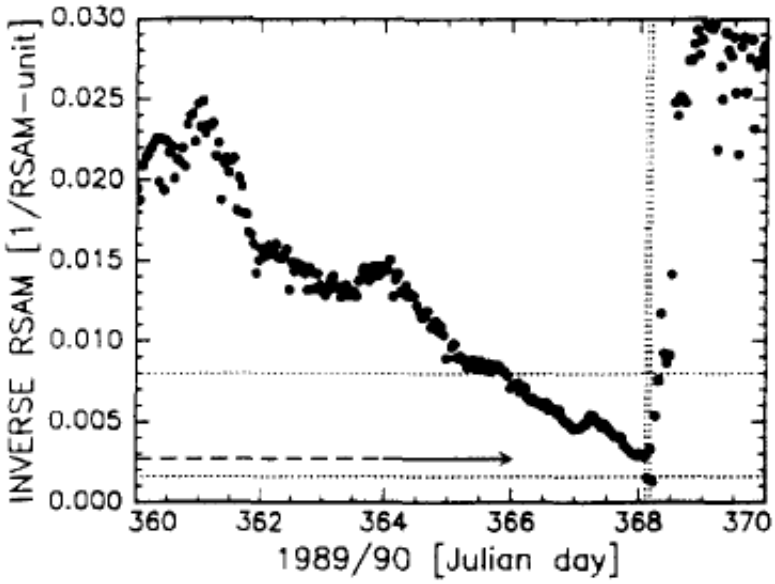

Figure 3.1: Inverse average amplitude measurements (one hour averages) for station RED at Redoubt Volcano prior to the dome destroying eruption on 2 January 1990 (marked by vertical dashed line on Julian day 368). The horizontal arrow represents the mean value (dotted horizontal lines are one standard deviation from this) of the inverse average amplitude measurement of the previous five explosion events at Redoubt volcano. From Cornelius and Voight (1994).

One of the first instances of real time forecasting using the FFM came at Redoubt volcano, when the inverse average amplitude of seismic events followed a linear regression trend for 4 days prior to a dome collapse on 2 January 1990 (Figure 3.1). Due to this trend, and the fact that the seismic intensity was far above background levels, the Alaskan Volcano Observatory issued a "formal warning" of an impending eruptive event on the morning of the 2 January, a few hours before the eruption, although the FFM calculations suggested an eruption was likely within 0.5-2 days. A similar, if not clearer trend, that supported the forecast was found using the same precursory sequence but only using seismic events within the spectral range of 1.3-1.9 Hz (Cornelius and Voight, 1994). These events were thought to be indicative of the volumetric

excitation of fluid filled cracks or the conduit itself (Chouet et al., 1994).

De la Cruz-Reyna and Reyes-Dávila (2001) reported the forecasting of volcanic phenomena at Colima volcano in November 1998 following a rapid accelerating trend in the seismic energy release after a period of relative quiescence. After 12 days of elevated seismic energy release, three forecasts were generated based on alternative curve fitting models to the seismic energy data. Forecasts were produced for possible eruptions beginning late on 16 November, late on 17 November and late on 18 November. A new dome was detected at Colima on the 20 November (although elevated seismicity had resumed on 19 November following a short decrease, which is now believed to have been the onset of the dome building eruption) and pyroclastic flows were first produced on the 21 November. Consequently, the forecast made one week earlier was within 48 hours of the timing of the eruption (Reyes-Dávila and De la Cruz-Reyna, 2002).

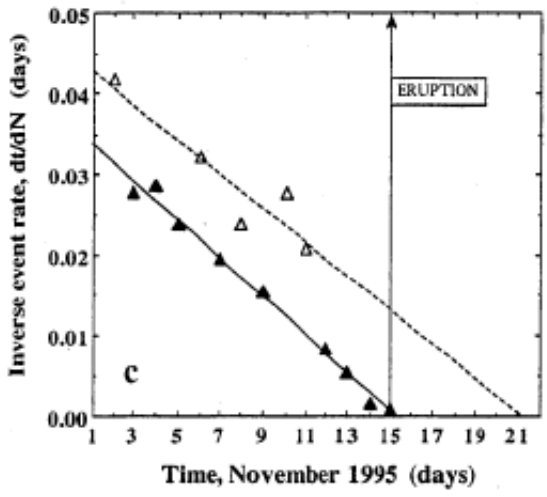

Figure 3.2: Inverse event rate of seismicity from 1 to 21 November 1995 at Soufrière Hills Volcano. Two event populations can clearly be seen (open and closed triangles) which both generate near parallel regression trends. The closed triangle regression forecasts the timing of the eruption in November 1995 very well. Event rate was determined from an array of short period vertical component seismometers with a triggering algorithm counting the number of events above a critical amplitude threshold. From Kilburn and Voight (1998).

Due to the wealth of data, Soufrière Hills volcano has also been previously used as a case study for forecasting volcanic phenomena. This has always been done in hindsight. This is partly why this volcano was chosen as a target volcano, as results developed through this research can be critically compared to previous findings. Kilburn and Voight (1998) showed that

the FFM could be successfully used to forecast an eruption in November 1995, when magma first reached the surface, by using inverse daily seismic event rates (Figure 3.2). They related the accelerating seismicity to accelerated fracture growth controlled by the progressive weakening of the surrounding host rock by hydrothermal fluids, but the forecast was only successful once the seismic events were treated as two distinct populations (i.e. two distinct sources of seismicity). Kilburn and Voight (1998) postulated that the reason for two distinct populations might have been the episodic growth of the magmatic conduit.

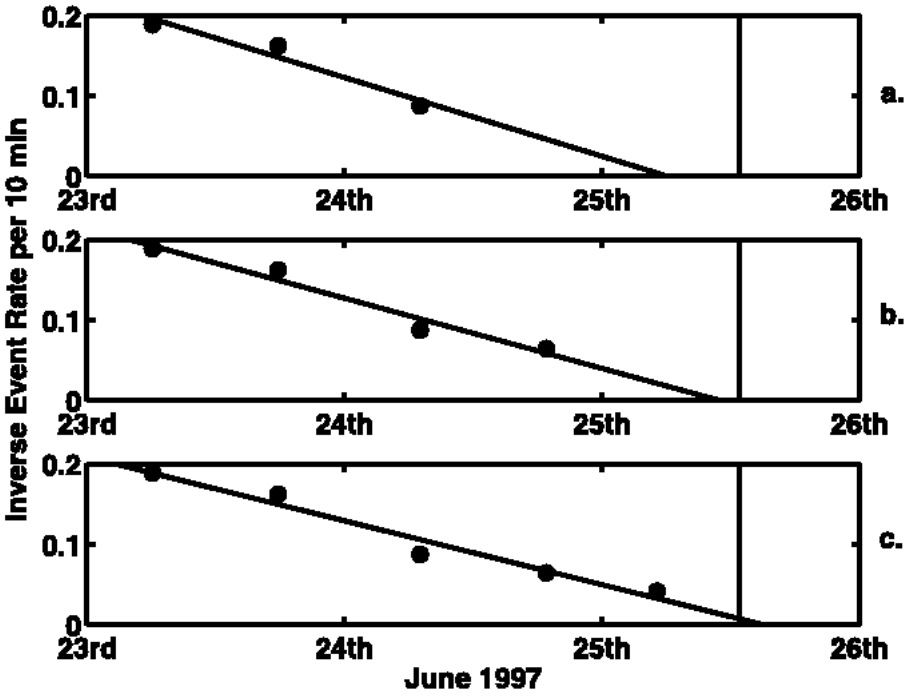

Figure 3.3: Inverse event rate (per 10 minutes) of swarms of seismicity from 23 to 26 June 1997 at Soufrière Hills Volcano. The vertical line marks the onset of the dome collapse on the 25 June 1997. The timings of failure are estimated to (a) 07:00h, (b) 11:15h, and (c) 14:45h on the 25th June (see linear regressions). From Hammer and Neuberg (2009).

Of particular note to this research is the study of Hammer and Neuberg (2009). Using precursory seismicity and the FFM, they successfully forecasted the timing of a dome collapse on 25 June 1997 at Soufrière Hills (Figure 3.3). This was based on accelerating rates of low frequency earthquakes which occurred in swarms, rather than simply the number of low frequency events over the precursory time period. They used the average event rate per swarm which gave a clearer accelerating pattern overall, rather than the traditional method of binning data in units of time. Hammer and Neuberg (2009) used one single waveform family in their

swarm analysis, which shall be emulated in Chapter 4. However, the authors failed to provide details of the waveform family used, its significance above other waveform families found during the same time period (e.g. (Green and Neuberg, 2006)) or report the errors on their results. In addition, only one dome event was investigated which is too little to base a conclusion that the FFM is a successful forecasting tool.

3.2 Seismic Amplitude as the Observable

The amplitude of registered seismicity is important since one large event may facilitate magmatic fluid movement more easily than a number of very small events. However, this is dependent upon seismicity being registered as discrete events, which is not always the case, as precursory seismicity may transition to tremor as the eruption time becomes closer (e.g. at Soufrière Hills volcano in June 1997 prior to a dome collapse (Voight et al., 1998)). Consequently, a method is required which is not reliant upon determining the amplitude of discrete seismic events, but can also measure the amplitude of continuous tremor.

3.2.1 The definition of RSAM and SSAM

The Real-time Seismic Amplitude Measurement (RSAM) is a monitoring tool which calculates the average amplitude of incoming continuous seismicity over a selected time bin (1 minute, 10 minutes, 1 hour etc.) in real time. RSAM therefore determines the accurate relative intensities of eruptive episodes, regardless of the type of seismicity that is occurring (e.g. high frequency, low frequency, discrete events, tremor, rockfalls etc.) (Endo and Murray, 1991). However, RSAM lacks spectral information, and therefore cannot be used to determine the type of activity occurring, since it places all seismic signals regardless of origin into the calculation. In some cases, RSAM has successfully been used to forecast volcanic phenomena e.g. Figure 3.1 at Redoubt volcano (Cornelius and Voight, 1994), however it is difficult to relate the acceleration in RSAM to an individual process at depth which leads to a singularity, and therefore induces failure. In response to this, the Seismic Spectral Amplitude Measurement (SSAM) calculates the average amplitude of continuous seismicity within discrete frequency bands (Stephens et al., 1994), and therefore allows accelerations to be related to distinct processes occurring at depth (see Section 1.2).

RSAM can be directly used in conjunction with the FFM, with the accelerating observable Ω in Equation 1.1 being represented by the average amplitude measurements. The units of

RSAM are consistent with the units of the input seismic data, and therefore can be in counts, volts, or average ground velocity, if the seismic data has been correctly calibrated and converted. All of the continuous seismic data used in RSAM calculations in this research has been velocity calibrated and therefore RSAM is representative of average ground velocity in meters per second. Since the recorded signal frequencies of interest are within the passband of the instruments recording them, full signal restitution is not required. Instead, velocity calibrated signals can be achieved by multiplication with the appropriate calibration factors, which removes the seismometer and digitizer response from the signal.

Originally developed as a monitoring rather than active forecasting tool, Endo and Murray (1991) first suggested a link between the accelerating RSAM and the onset of dome building eruptions at Mt. St. Helens, based on the high correlation between rapid increasing tilt signals for data recorded between 1985 and 1986. Furthermore, RSAM and tilt signals were correlated at Soufrière Hills volcano during the first phase of unrest of the volcano in 1996 and 1997 (Voight et al., 1998). However, the first use of the FFM in conjunction with RSAM and SSAM came from the eruption of Redoubt volcano in 1989-1990, which generated successful forecasts (Cornelius and Voight, 1994) (Figure 3.1).

3.2.2 Application of RSAM and SSAM with the FFM

RSAM and SSAM calculations at Soufrière Hills volcano have utilized vertical component data from station MBLG. From 1995 until 2005, a one component (vertical) short period seismic sensor was present at this site (Figure 2.6). In 2005, this was upgraded to a three component broadband seismometer (Figure 2.7). MBLG was chosen due to its close proximity to the volcanic crater, which means a high signal to noise ratio, which is particularly important for the calculation of RSAM since no information including any unwanted signals (e.g. anthropogenic noise, teleseisms) are filtered out during the calculation. In addition, continuous seismic data and earthquake counts as determined by MVO were made available for the entire precursory periods of interest at MBLG, which was not the case for other proximal stations.

In the SSAM calculation, under the assumption that low frequency seismicity is generated by magmatic fluid movement, and it therefore may be a precursor to volcanic eruptions, all frequencies below 0.5 Hz and above 5 Hz were filtered out. Noise below 0.5 Hz is attributed to oceanic microseisms (Arciniega-Ceballos et al., 2003), and signals with frequencies above

5 Hz are not thought to be typical of volcanic low frequency seismicity (Chouet, 1996a, Neuberg et al., 2000), and instead are associated with the brittle failure of the volcanic edifice (Arciniega-Ceballos et al., 2003), rockfall events or other surface generated seismicity.

For both the RSAM and SSAM calculation, the continuous seismic data is placed into discrete bins from which an average is taken, the length of which are somewhat arbitrary (Bell et al., 2013). Since this research is focused on quickly developing seismic unrest and short-term forecasting tools, and following the example of previous authors (e.g. Cornelius and Voight (1994), Voight et al. (1998)), a moving computing window of 10 minutes was used to calculate the average seismic amplitude of the signals.

June 1997

Described as the first major collapse at Soufrière Hills volcano, although subsequent collapse volumes have been much larger, the 25 June 1997 event removed 6.4 million m^3 of material (Montserrat Volcano Observatory, 2012) and generated the only fatalities of the eruptive period so far, with 19 people losing their lives as pyroclastic flows breached English's crater to the North (Loughlin et al., 2002). The dome collapse was preceded by hybrid earthquake swarms (Figure 3.4), volcanic tremor, and clear inflation and deflation cycles from the 22 June onwards (Montserrat Volcano Observatory, 1997b, Voight et al., 1998).

Figure 3.5 shows the average seismic amplitude in 10 minute bins of the continuous seismic signal prior to a dome collapse on 25 June 1997. The precursory seismic sequence begins on the 22 June, with a large acceleration in the average seismic amplitudes. However, after this event, the RSAM value appears to fluctuate with no clear accelerations which are greater that the event on the 22, up to the time of the dome collapse on the 25 June. The FFM has been applied to the inverse RSAM (Figure 3.6) in circumstances when an inverse regression is registered for over 30 minutes (i.e. for three successive decreasing time bins). The forecast timing and the R^2 value for the linear regression fit to the data are summarized in Table 3.1.

After Barrett (1974), R^2 is defined as:

$$R^2 = \frac{\sum_{i=1}^{n}(y_i - \hat{y}_i)^2}{\sum_{i=1}^{n}(y_i - \bar{y})^2} \tag{3.1}$$

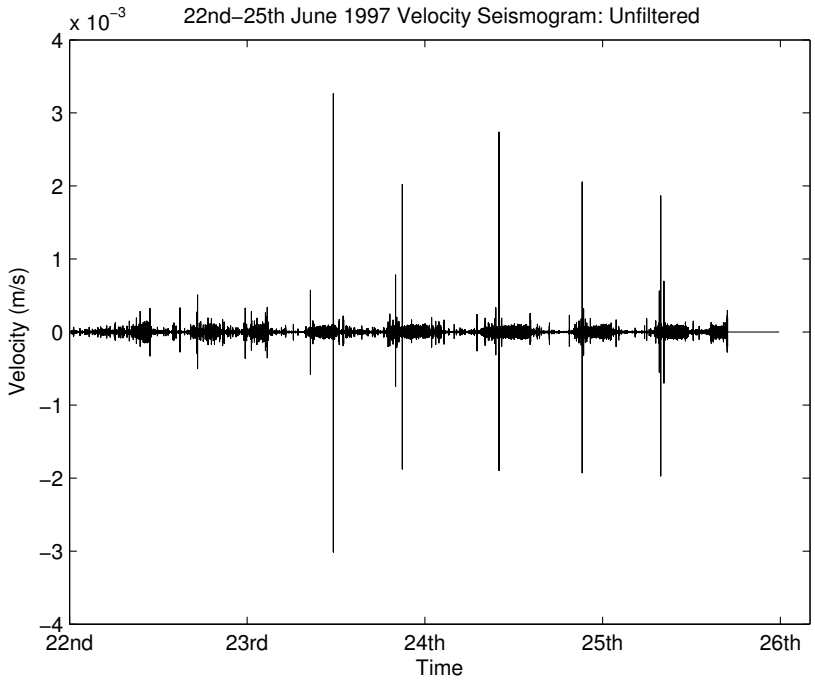

Figure 3.4: Raw continuous seismogram, 22 to 25 June 1997 at Soufrière Hills volcano, station MBLG. The signal has been velocity calibrated by removal of the instrument and digitizer responses, thus the units are in meters per second. The dome collapse on 25 June 1997 can be seen on the seismogram as the point where no data is collected, and the velocity of the signal remains at 0 m/s.

where y_i represents the observed parameter at position i (i.e. the inverse event rate at a given time), $\hat{y}_i$ represents the predicted parameter of y at i (i.e. the FFM linear regression at this time), and $\bar{y}$ represents the mean value of all of the y values. R^2, the coefficient of determination, is the proportion of variability which can be explained by the model, and ranges from a minimum value of 0, which suggests that the model does not explain any part of the data, up to a maximum of 1, which suggests the model perfectly describes the data. In this case, the R^2 value shows how well future outcomes can be predicted by the model (the FFM), and therefore the closer the value is to 1, the more confidence there is in the forecast.

Four forecasts could have been made using RSAM data from the 22 to 26 June 1997, as shown in Figure 3.6 (labelled 1 to 4). All four forecasts have high R^2 values, suggesting that the FFM fits well to the inverse amplitude data, particularly the first forecast made on the 23 June (Table 3.1). However, none of the forecasts are accurate, and RSAM appears to simply fluctuate during the precursory period rather than accelerate towards the time of failure (i.e. eruption). The use of RSAM in June 1997 in real time would not have provided any accurate forecasts, and more likely, would have created confusion as to the fluctuating signals. One

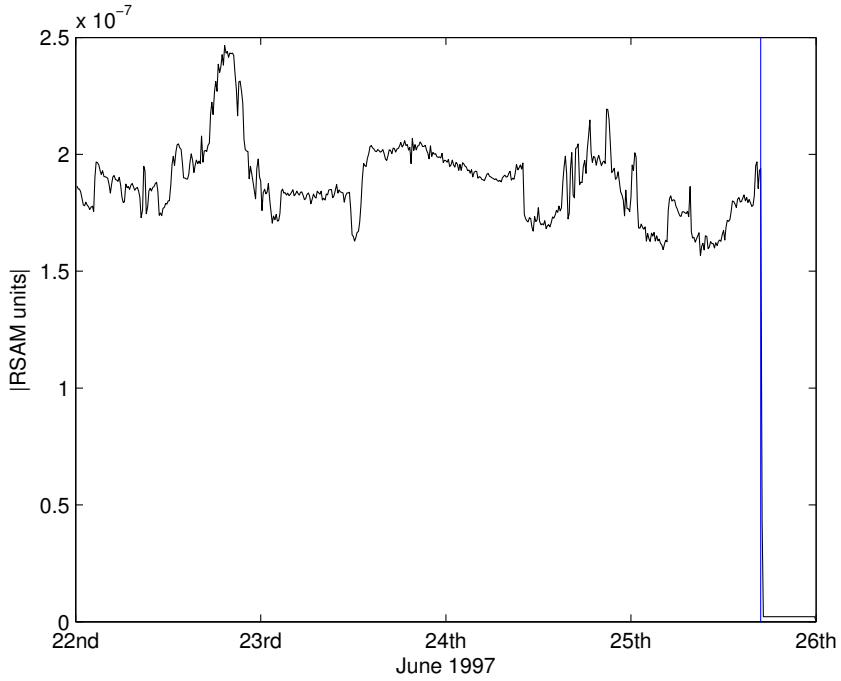

Figure 3.5: RSAM (10 minute averages) at Soufrière Hills volcano, 22 to 25 June 1997, station MBLG. The vertical line represents the known timing of dome collapse, at which point MBLG was disconnected from the seismic network due to a passing pyroclastic flow. RSAM is representative of average ground velocity in meters per second.

potential reason for the generation of false forecasts may be the mixing of different types of seismic signals within one calculation. Therefore, it is unclear as to what process the calculation is actually forecasting if the assumption is that each type of seismic signal is representative of different processes.

Forecast	Time of Forecast	R^2	Minutes used in linear regression
1	23rd June 05:48	0.9206	150
2	23rd June 21:54	0.7835	70
3	26th June 01:31	0.7041	400
4	27th June 07:17	0.7100	290

Table 3.1: Forecasts made with inverse RSAM, 22nd to 28th June 1997

The seismic amplitudes of seismicity within the frequency band of 0.5-5 Hz (SSAM) shows a different pattern to RSAM (Figure 3.7). It is clear that the low frequency seismicity occurs in a regular cyclic patterns of swarms, and the amplitude change within each swarm itself is also cyclic. An initial increase in the amplitude of the events is followed by a decrease in

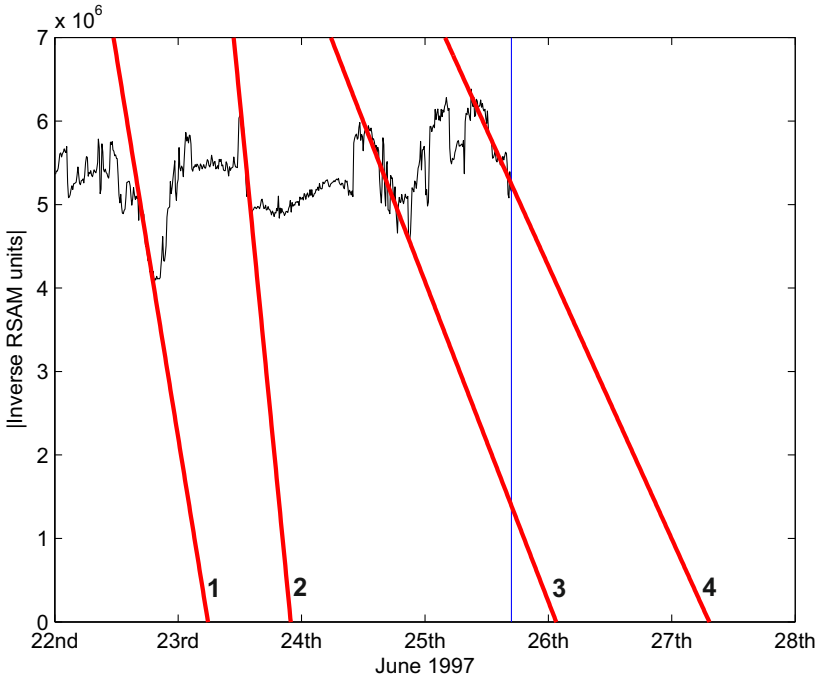

Figure 3.6: Inverse RSAM (10 minute averages) at Soufrière Hills volcano, 22 to 28 June 1997, station MBLG. The vertical line represents the known timing of dome collapse, at which point MBLG was disconnected from the seismic network due to a passing pyroclastic flow. RSAM is representative of average ground velocity in meters per second. Each forecast using the FFM (alpha = 2) is shown by a linear regression and is labelled 1-4. Details of the forecasts can be found in Table 3.1.

amplitude within each swarm. However, the overall amplitude within each swarm appears to increase with time towards the dome collapse. The difference in the RSAM and SSAM (Figures 3.6 and 3.7) can be explained as the low frequency seismic amplitudes are two orders of magnitude smaller than the average amplitude of all of the seismicity, therefore suggesting that the low frequency events, although dominant in number, are much smaller in amplitude. Consequently, when placed into the RSAM calculation with all other types of seismicity, which are larger amplitude signals, the swarm like behaviour is seemingly lost.

July 2003

The dome collapse on 12 July 2003 is the largest of the eruptive period to date, and the largest recorded in historical times at any volcano (Herd et al., 2005). Over 18 hours, 210 million m^3 of material collapsed in a north-westerly direction, with large pyroclastic flows reaching the sea and generating intense hydrovolcanic activity at the shoreline, as well as a small tsunami. 15 cm of ash fall (not compacted) was recorded in Old Towne, to the North of Garibaldi Hill (Figure 2.3). Unlike previous collapses (e.g. June 1997), a pause in extrusion was noted from

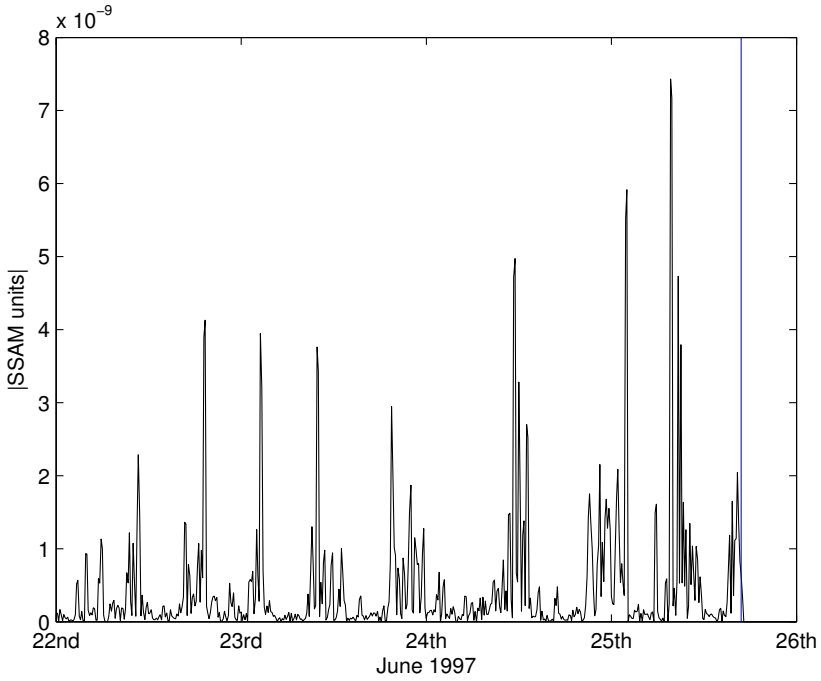

Figure 3.7: SSAM (10 minute averages) at Soufrière Hills volcano, 22 to 25 June 1997, station MBLG. The raw continuous seismogram was filtered between 0.5 and 5 Hz, see text for explanation. The vertical line represents the known timing of dome collapse, at which point MBLG was disconnected from the network due to a passing pyroclastic flow. SSAM is representative of average ground velocity in meters per second, related to the occurrence of low frequency seismicity.

the middle of June 2003 until the dome collapse on the 12 July, although precursory seismic signals began on 9 July (Herd et al., 2005), Figure 3.8.

As shown in Figure 3.9, the RSAM calculation provides very little information about the precursory seismicity, and certainly does not show the same cyclic nature as was observed in June 1997 (Figure 3.5). RSAM in July 2003 provided no opportunity to apply the FFM since no accelerating trends could be identified, and therefore it is not a useful forecasting tool in this instance. The large peaks in RSAM on the 11 and 12 July, prior to the collapse are probably related to rockfall events, since they are not seen in the SSAM (Figure 3.10). Prior removal of these rockfall events is not in keeping with the original execution of RSAM, however if performed does not allow the identification of any precursory sequences. Again, no precursory trends can be identified from the SSAM prior to the collapse, which makes the FFM not applicable for this seismic sequence. Figure 3.10 does show an increase in low frequency seismic amplitudes once the collapse has begun (vertical line in figure), which could be related either to the easier movement of magmatic fluid from depth once the eruption began,

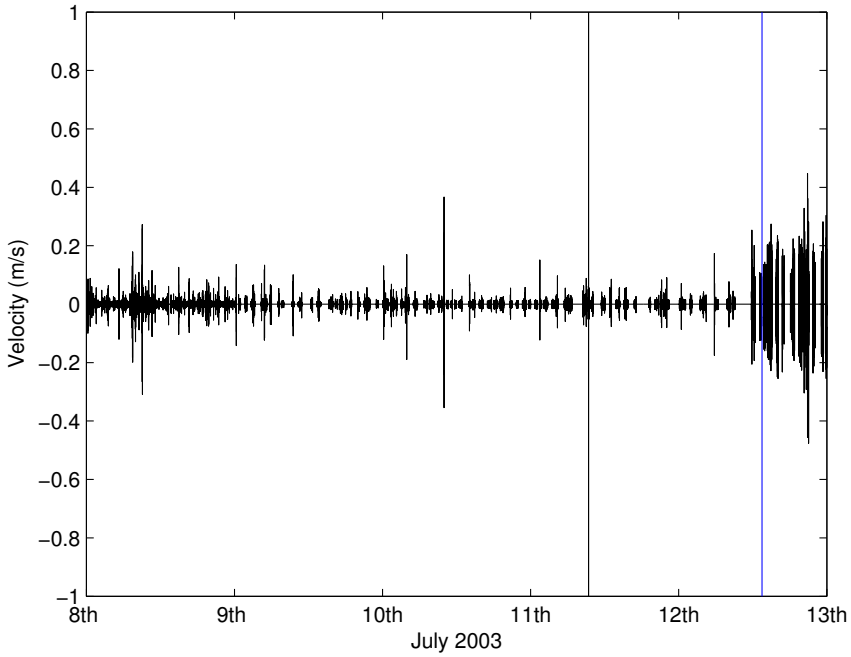

Figure 3.8: Raw continuous seismogram, 8 to 13 July 2003 at Soufrière Hills volcano, station MBLG. The signal has been velocity calibrated by removal of the instrument and digitizer responses, thus the units are in meters per second. The vertical line represents the known timing of a dome collapse on 12 July 2003. Although it may look like swarm like behaviour, the periods of "quiescence" are actually data gaps. The seemingly large event on the 11 July is actually an event which saturated the system.

or due to the low frequency component of pyroclastic flow signals. In either case, the increase in amplitude is partly due to the increase in seismicity which was registered as the collapse unfolded.

February 2010

The most recent significant dome collapse occurred on 11 February 2010 during the latest eruptive episode that Soufrière Hills has seen (Phase 5, Table 2.2). Four months of intensive extrusive and explosive activity culminated in the collapse of 50 million m^3 of material (Figure 3.11). The average extrusion rate for this period was 7 $\mathrm{m}^3\mathrm{s}^{-1}$ although there is some evidence that extrusion rates could have reached as high as 35 $\mathrm{m}^3\mathrm{s}^{-1}$ for short periods of time (Stinton et al., 2014, Odbert et al., 2014b).

It is clear from Figure 3.12 that the seismic amplitudes of events was cyclic in the 9 days prior to the dome collapse on the 11 February, with a period of approximately 24 hours (i.e. one cycle per day). This cyclicity does not appear to be affected by the precursory Vulcanian explosions that occurred on the 5 and 8 February, suggesting the processes generating

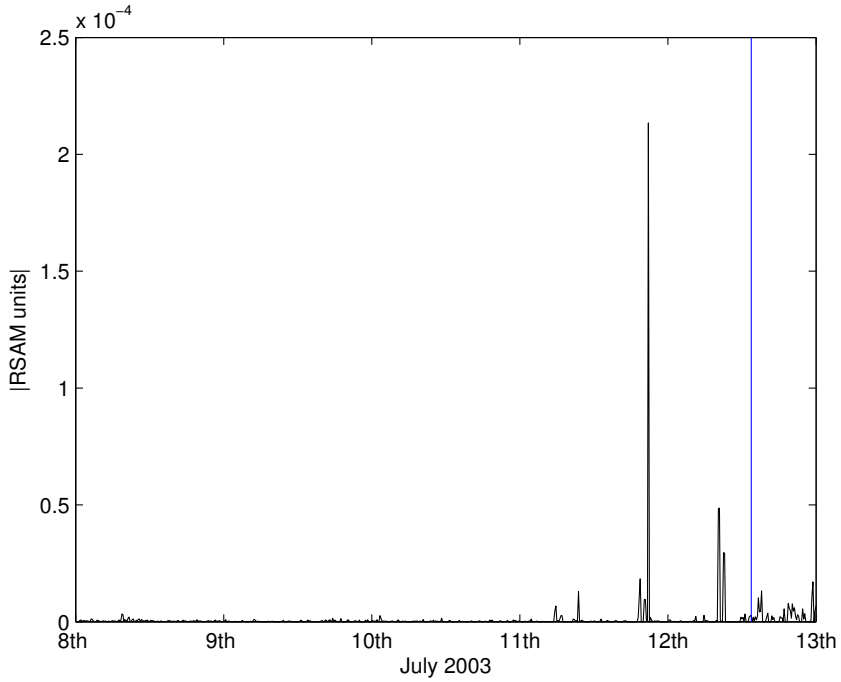

Figure 3.9: RSAM (10 minute averages) at Soufrière Hills volcano, 8 to 13 July 2003, station MBLG. The vertical line represents the known timing of dome collapse on 12 July at ≈1330 local time. RSAM is representative of average ground velocity in meters per second.

the seismic cyclicity is completely separate to the processes involved in the explosion events. Figure 3.12 suggests a slight increase in the range of amplitudes as time progresses, although not significantly. Hammer and Neuberg (2009) also found that the mean amplitude of events prior to the 25 June 1997 dome collapse were almost constant. The cyclic nature of RSAM in February 2010 makes using the FFM in conjunction with the continuous seismicity difficult since it would forecast an eruption every 8 hours, as the RSAM values once again increase in each cycle. Furthermore, there appears to be very little difference in character between the early RSAM cycles and the one preceding the dome collapse, making forecasting the event void using this method.

Figure 3.13 shows the seismic amplitudes of events within the frequency range of 0.5 to 5 Hz, and therefore represents the seismicity associated with the movement of magmatic fluids. No acceleration in seismic amplitude was observed prior to the dome collapse on 11 February, with the peak in seismic amplitude occurring simultaneously with the dome collapse. Therefore, the precursory seismic sequence provided no evidence of a failure event, as would be necessary for application of the FFM.

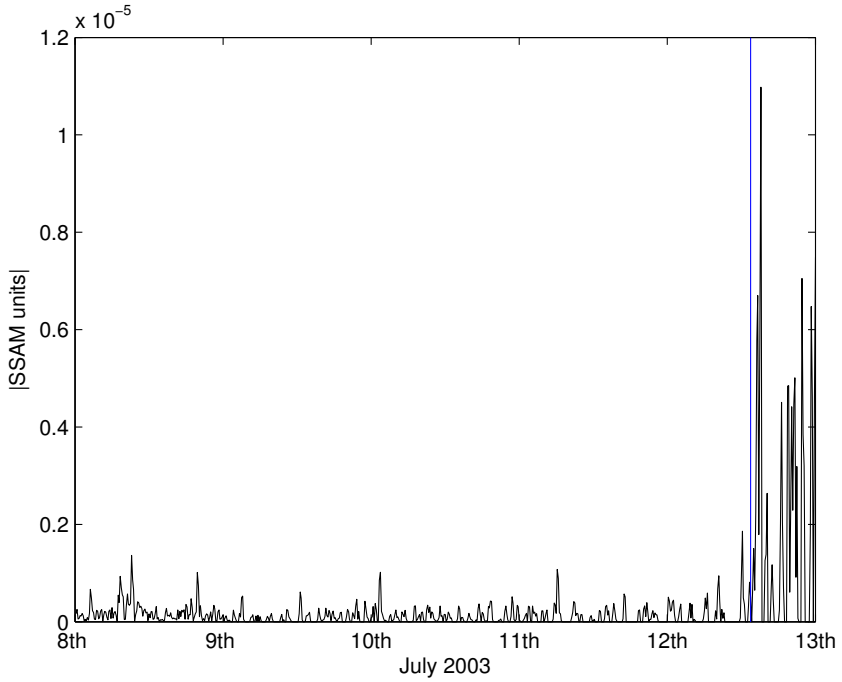

Figure 3.10: SSAM (10 minute averages) at Soufrière Hills volcano, 8 to 13 July 2003, station MBLG. The raw continuous seismogram was filtered between 0.5 and 5 Hz. The vertical line represents the known timing of dome collapse on 12th July at ≈1330 local time. SSAM is representative of average ground velocity in meters per second, related to the occurrence of low frequency seismicity.

3.3 Crude Seismic Energy as the Observable

3.3.1 The Definition of RSEM and SSEM

The energy release from seismicity is directly proportional to the amplitude of the events that have occurred. The Real-time Seismic Energy Measurement (RSEM) monitoring tool was developed at Colima volcano, Mexico, and is proportional to the Root-Mean-Square (RMS) of seismic energy flux arriving at the seismic station being used for the calculation (De la Cruz-Reyna and Reyes-Dávila, 2001). As described by Tárraga et al. (2008), it takes the form of:

$$RSEM = k\sqrt{\frac{1}{N}\sum_{i=1}^{N}(A_i - A_{\text{avg}})^2} \tag{3.2}$$

where *N* is the number of samples, A_i is the amplitude of the seismic signal, A_{avg} is the average of the number of samples and k is a calibration factor which accounts for the analogue-digital conversion and the instrument response characteristics. RSEM was once again calculated in 10 minute windows and therefore *N* was equal to 45000 samples when the signal was digitized at 75 Hz. The seismogram has already been calibrated for the digitizer and seismometer response,

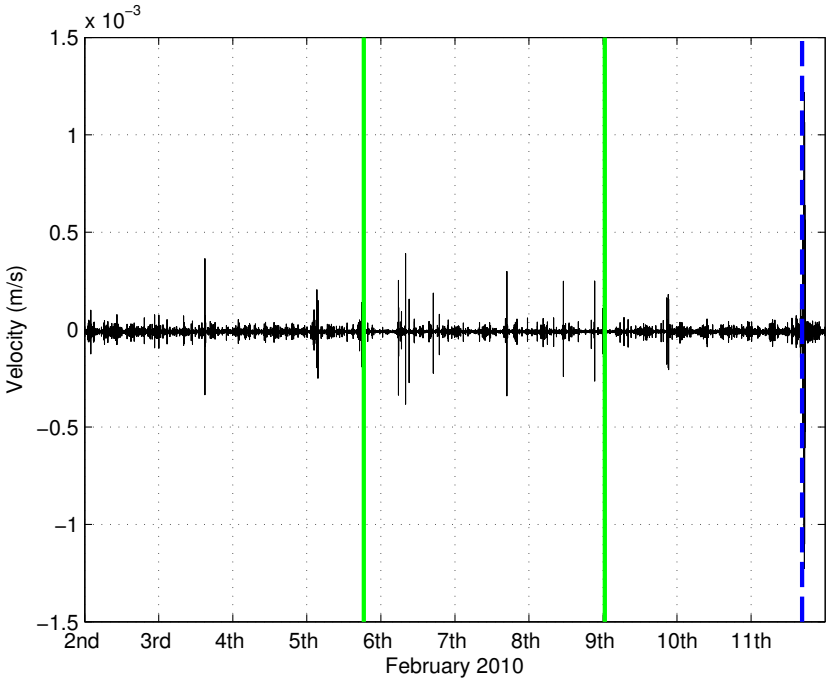

Figure 3.11: Raw continuous seismogram, 2 to 11 February 2010 at Soufrière Hills volcano, station MBLG. The signal has been velocity calibrated by removal of the instrument and digitizer responses, thus the units are in meters per second. The first two vertical lines (green) represent two small Vulcanian explosions, on the 5 and 8 February. The final vertical line (dotted, blue) represents the onset of the dome collapse and associated pyroclastic flows on 11 February. Timings for these events are taken from Stinton et al. (2014).

therefore making k equal to one. RSEM is directly proportional to the rate of strain from seismic processes and therefore is also comparable to the rate of deformation (De la Cruz-Reyna and Reyes-Dávila, 2001, Tárraga et al., 2008). De la Cruz-Reyna and Reyes-Dávila (2001) suggest that an acceleration in the strain rate, as would be needed in order to use the FFM as a forecasting tool, is indicative of accelerating behaviour in fracture formation and extension. Failure is achieved once the volumetric density of fractures overcomes a critical threshold.

Similar to analysis with continuous amplitude measurements, it is important to distinguish between different source mechanisms at depth and relate the ongoing seismicity to distinct processes that may be occurring. Therefore, the SSEM calculation measures the average seismic energy release within a given spectral frequency band, which consequently relates to a single source mechanism. In order for an eruption to occur there must be movement of magmatic fluid from depth to the surface, which is assumed to be accompanied by low frequency seismicity. Accordingly, analysis of the energy release from only low frequency seismicity may aid forecasting of the impending eruption.

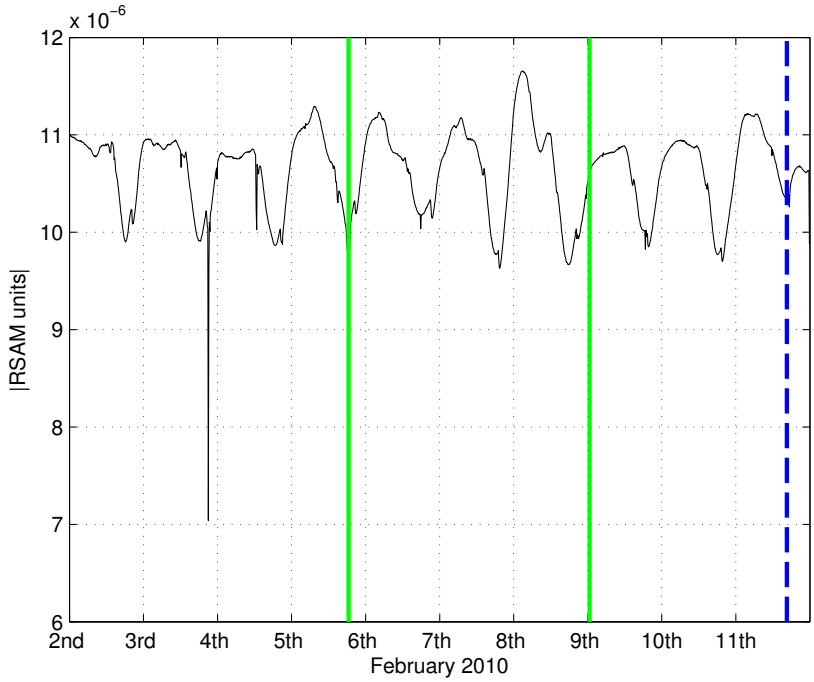

Figure 3.12: RSAM (10 minute averages) at Soufrière Hills volcano, 2 to 11 February 2010, station MBLG. RSAM is representative of average ground velocity in meters per second. The first two vertical lines (green) represent two small Vulcanian explosions, on the 5 and 8 February. The final vertical line (dotted, blue) represents the onset of the dome collapse and associated pyroclastic flows on 11 February.

3.3.2 Application of RSEM and SSEM with the FFM

RSEM and SSEM were attempted for the continuous seismic data available for the periods already studied using RSAM (June 1997, July 2003 and February 2010). For SSEM analysis, the continuous data was filtered between 0.5 and 5 Hz, to remove sources of seismicity not related to the movement of magmatic fluid. Since the continuous seismograms have already been velocity calibrated, the units of RSEM and SSEM are in meters per second.

Figure 3.14 shows the energy release from seismicity from the 22 to 26 June 1997 prior to a large scale dome collapse on 25 June 1997. It is clear that the energy release is cyclic, and that within each cycle the energy release initially increases and then decreases once more. It is interesting to note that large spikes in energy release usually occur during the first half of the cycle, and do not necessarily represent the inflexion point within the cycle from continued increasing to decreasing energy release.

RSEM can also be thought of as reflecting stress changes beneath the volcano, which in

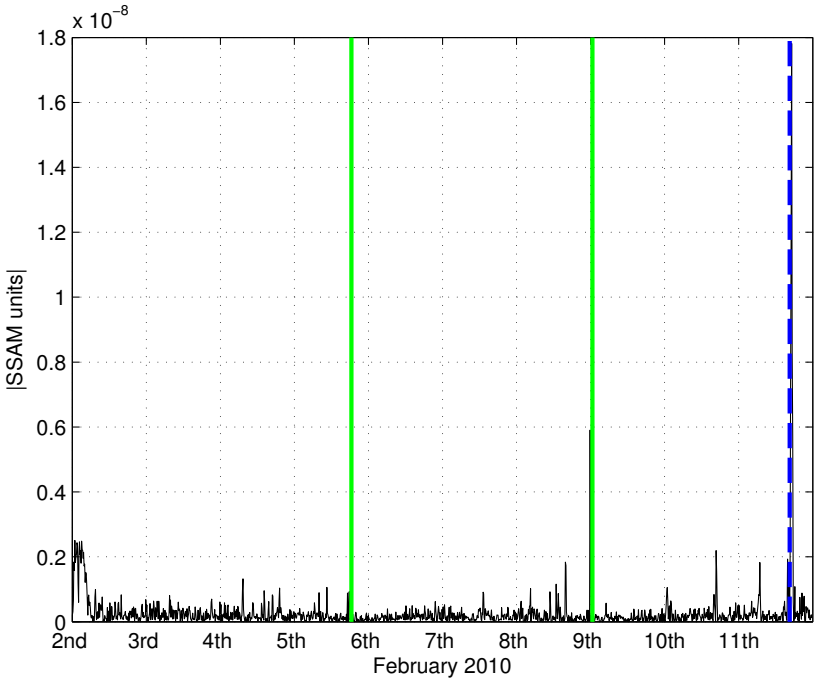

Figure 3.13: SSAM (10 minute averages) at Soufrière Hills volcano, 2 to 11 February 2010, station MBLG. The raw continuous seismogram was filtered between 0.5 and 5 Hz. SSAM is representative of average ground velocity in meters per second, for low frequency seismic events. The first two vertical lines (green) represent two small Vulcanian explosions, on the 5 and 8 February. The final vertical line (dotted, blue) represents the onset of the dome collapse and associated pyroclastic flows.

this precursory sequence is clearly cyclic. This cyclicity is also reflected in tilt cycles (Figure 3.15), representative of high amplitude shallow pressurization cycles approximately every 10 hours. The tilt data suggests that this cyclic behaviour continued after the dome collapse, but with a decrease in the period of the cycles (down to approximately 8 hours) and an increase in the mean amplitude of the cycles, marking a distinct change in the deformation pattern (Green and Neuberg, 2006). This cyclic deformation has been linked at silicic volcanoes to increased magma flow rates inducing a stick slip condition at the conduit walls, thereby periodically reducing the pressure in the system (Denlinger and Hoblitt, 1999), or by magma flow through a lower gas charged conduit of constant viscosity which allows pressure to build up and therefore the flow rate to increase. In this case, the rapid flow of magma into an upper conduit which is actively degassing, causes a decrease in pressure in the lower conduit, allowing a cyclicity to develop (Wylie et al., 1999). On Montserrat, cyclic deformation has also been linked to the development of shear stresses along the conduit wall due to pressure gradients induced by increased magma flow (Green et al., 2006), as well as the pressurization of a dyke which acts as a feeder system to the surface (Hautmann et al., 2009, 2014). Therefore, it is possible for

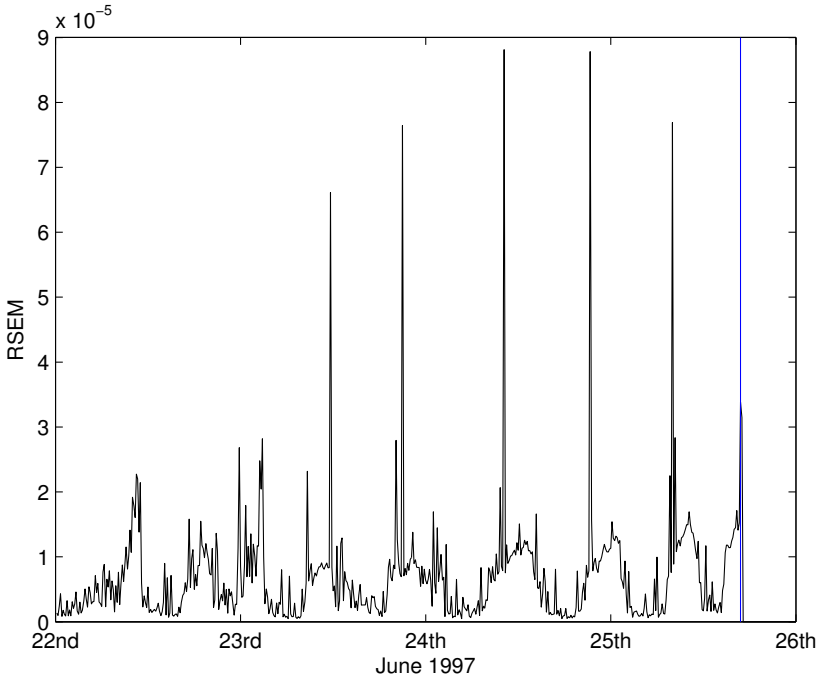

Figure 3.14: RSEM (10 minute averages) at Soufrière Hills volcano, 22 to 26 June 1997, station MBLG. The vertical line represents the known timing of dome collapse, at which point MBLG was disconnected from the seismic network due to a passing pyroclastic flow. RSEM is representative of the average strain release from seismic events.

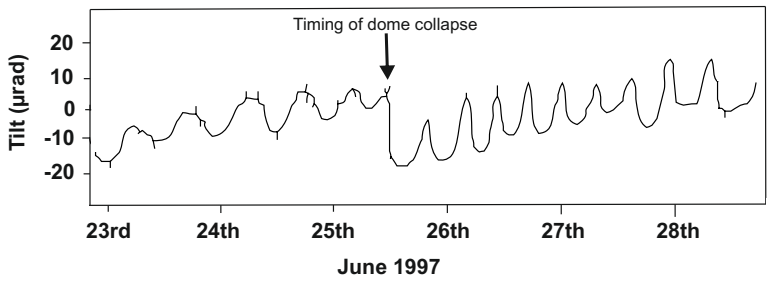

Figure 3.15: Tilt cycles at Soufrière Hills volcano, 23 to 28 June 1997, Station CP2, approximately 1.5 km from the active vent. Modified from (Green and Neuberg, 2006).

seismometers to detect deformation cycles in a similar way to tiltmeters, if these are not available, and provide information on the potential cyclicity of magma movement from depth.

RSEM calculations for July 2003 (Figure 3.16) and February 2010 (Figure 3.17) suggested no accelerating behaviour and therefore could not be used as a forecasting tool. The energy release from 8 to 13 July 2003 shows an increase approximately 30 minutes prior to the collapse, but nothing that would have been alarming given some of the larger increases in energy release in previous days which did not lead to an eruption. Cyclicity is apparent in the RSEM calcula-

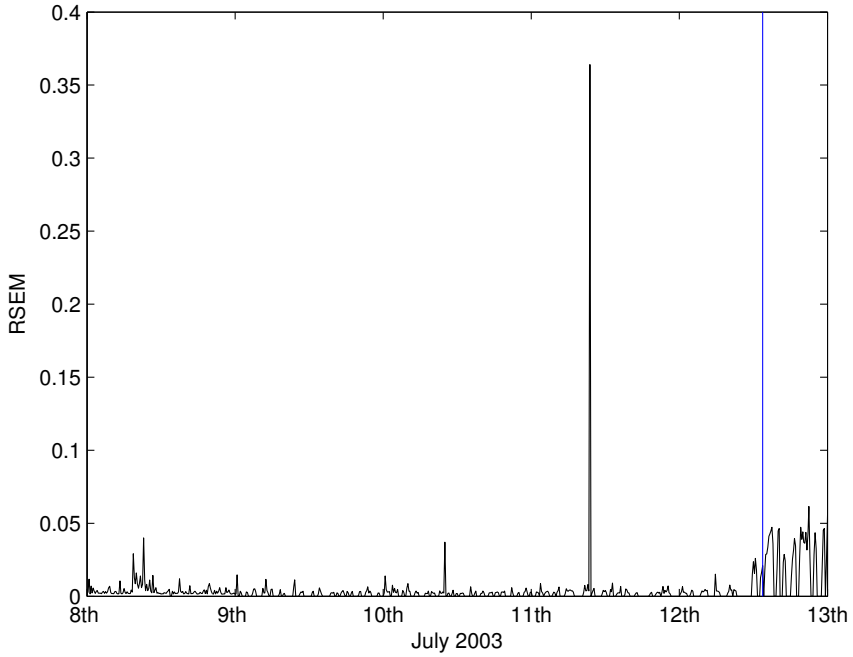

Figure 3.16: RSEM (10 minute averages) at Soufrière Hills volcano, 8 to 13 July 2003, station MBLG. The vertical line represents the known timing of dome collapse. RSEM is representative of the seismic energy flux arriving at the seismic station and is therefore indicative of stress changes in relation to the ongoing seismicity.

tions from the 2 to 13 February 2010 (Figure 3.17), which is unsurprising since cyclicity had already been identified using RSAM (Figure 3.12). However, the periodicity of the cycles appears much shorter, perhaps on six to eight hour cycles. No accelerations can be identified prior to either of the explosion events on the 5 and 8 February 2010, or to the dome collapse on the 11 February. This cyclicity in seismic energy release would have made forecasting the volcanic phenomena using the FFM and accelerating seismicity very difficult since the accelerations are themselves cyclic, and appear to bare limited relevance to whether an eruptive scenario occurs or not. SSEM calculations for the same time periods showed no evidence of accelerating seismicity prior to eruptive events, meaning that forecasting using this methodology was not possible in this instance.

3.4 Event Rate as the Observable

The simplest, and perhaps most basic analysis that a volcano observatory will do is count the number of earthquakes that occur each day. An increase in the number of events is therefore indicative of more restless volcanic behaviour. Like many volcano observatories, MVO uses a STA/LTA (short-term average to long-term average) amplitude ratio triggering algorithm to

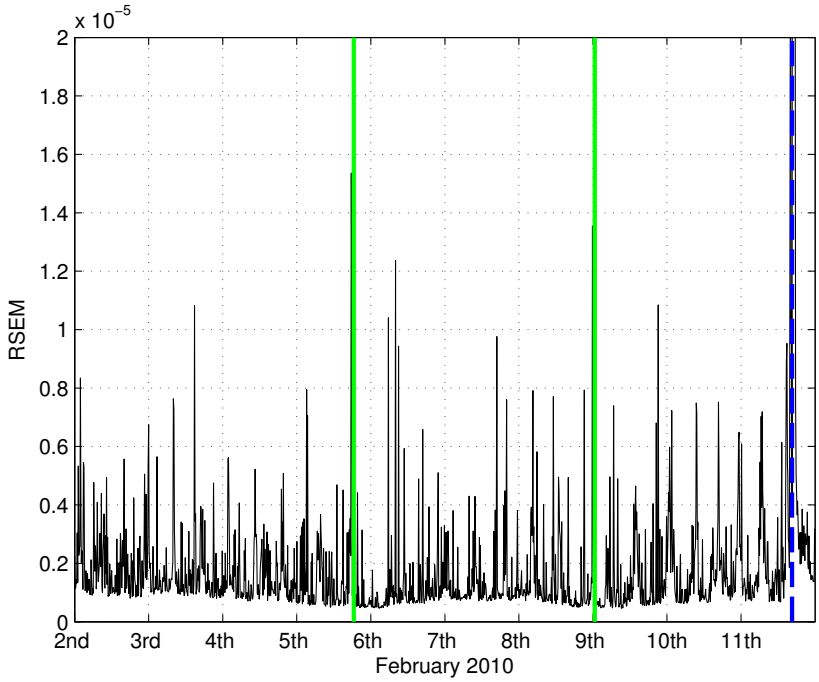

Figure 3.17: RSEM (10 minute averages) at Soufrière Hills volcano, 2 to 11 February 2010, station MBLG. The first two vertical lines (green) represent two small Vulcanian explosions, on the 5 and 8 February. The final vertical line (dotted, blue) represents the onset of the dome collapse and associated pyroclastic flows on 11 February. RSEM is representative of the seismic energy flux arriving at the seismic station and is therefore indicative of stress changes in relation to the ongoing seismicity.

identify individual events from the incoming continuous seismic record. It consists of two sliding windows, one investigating the short term amplitudes and is therefore very sensitive to incoming seismic signals, and one investigating the long term amplitude of the signal, which can provide information about the temporal amplitude of the noise at the site of the seismometer (Withers et al., 1998). Since the trigger is based on the ratio between these two windows, the algorithm is better able to record weak seismicity, compared to a simple amplitude only trigger mechanism (Trnkoczy, 2002). If a trigger (when a critical threshold of this ratio is exceeded) is found on three or more seismic stations simultaneously then an event is declared and registered within the event count catalogue (pers. comm., MVO, P. Smith, 2014).

3.4.1 Identification of individual seismic events

During times of quiescence, less than ten earthquakes are detected each week by this system at Soufrière Hills volcano. A total of 1435 triggered events were placed within the catalogue from the 22 - 25 June 1997, although the exact parameter settings of the STA/LTA algorithm used

are not known. A total of 288 events were placed within the catalogue from 8 - 13 July 2003, again with unknown STA/LTA parameters. Consequently, an STA/LTA algorithm was run on the continuous data for June 1997 and July 2003 as a comparison to the MVO triggers. The parameters used in this analysis are shown in Table 3.2. The sampling interval is the digitization rate based on the instrument being used. The short term and long term averaging windows are the amount of time over which an average amplitude is calculated. This is then converted to a ratio (STA/LTA) and if this value exceeds a given threshold (in this instance a value of 4), then the algorithm declares that a seismic event is occurring. The seismic event ends when the detrigger value is reached again, however an event is only registered by the algorithm if the time between the trigger and detrigger value is at least 10 seconds.

Parameter	**Value given**	**Units**
Sampling Interval	1/75 (before 2005) or 1/100 (after 2005)	Seconds
Beginning time of signal	0	Seconds
End time of signal	Dependent on length of input signal	Seconds
Short term averaging window length	0.333	Seconds
Long term averaging window length	60	Seconds
Value of STA/LTA ratio that triggers	4	
Value of STA/LTA ratio that detriggers	2	
Time buffer added before triggering time	2	Seconds
Time-buffer added after detriggering time	10	Seconds
Minimum window length of any triggered section	10	Seconds
Time between trigger and detrigger that must be exceeded in order for the triggered section to be reported	10	Seconds

Table 3.2: STA LTA parameters

The short term averaging window must be smaller than the shortest seismic event expected to be registered on the seismometer, but must also be longer than a few periods of the expected incoming seismic event (Trnkoczy, 2002). Since this research is aimed at using low frequency seismicity as a forecasting tool for volcanic eruptions due to its relationship to magmatic fluid

movement, the likely periods of an incoming seismic signal will range between 0.2 and 2 seconds. The short term averaging window must be kept small in order to concentrate only on local seismicity. Consequently, a short term averaging window of 0.333 seconds was chosen.

A long term averaging window of 60 seconds was chosen in accordance with Trnkoczy (2002), since it was not necessary to identify distant regional events in this analysis, and since emergent regional events are a high possibility (the waveform shape of a low frequency event can often be emergent). The short term to long term average ratio trigger was set at 4; any higher than this and many events would not have been picked out by the algorithm and registered, and any lower than this and the influence of noise became too great. The detrigger value was set to 2 in order to capture the entire waveform. Using this type of algorithm has many advantages since it can process in near real time, and is easily adapted. However, the automatic trigger recognition system is unlikely to record every single seismic event, in particular when events are not temporally separate or are being influenced by a high degree of noise. In addition, the algorithm does have the capacity to generate false signals, which are not seismic in any way but could still be included within event counts.

Using an STA/LTA algorithm with the parameters set out in Table 3.2, 1817 events were identified form 22 to 25 June 1997, and 520 events from 8 to 13 July 2003. In comparison, MVO's triggered system identified 1435 events in June 1997, and 288 events in July 2003 over the same time periods. Therefore, the parameters chosen for the STA/LTA algorithm for this study cannot be the same input parameters that were used at the time by MVO in order to identify triggered events. Without knowledge of at least some of the parameters which were used by MVO to identify events, it is almost impossible to replicate their identification of events, since so many combinations of the parameters could be used. The parameters most likely to have been changed to produce such a difference in the number of identified events are: the values of the STA/LTA ratio that triggers or detriggers an event; the lengths of both of the averaging windows; and the minimum window length of a triggered section. At MVO it is possible that these parameters changed with time reflecting noise characteristics and other influencing factors, although in this analysis the parameters were kept the same for the 1997 and 2003 analysis.

These parameters were not appropriate for identifying individual seismic events in February 2010. Instead the STA/LTA parameters were changed such that some seismic events were

identified on 11 February 2010 from the continuous seismic record. In particular, the short term averaging window length changed from 0.333 seconds to 2 seconds (the maximum period likely for a low frequency signal between the frequency of 0.5 and 5 Hz), allowing the concentration on temporally longer events. The long term averaging window went from 60 to 120 seconds, again to accommodate for longer events, meaning that very short term events (Figure 4.17) did not get identified as an event. The trigger ratio value, the value at which the algorithm begins to detect an event, was moved from 4 to 8 since large amounts of noise appeared to dominate most of the signal thus many of the previous triggers were simply for noise. A total of 452 events were identified using this method between the 8 and 12 February 2010.

The STA/LTA algorithm only identifies potential seismic events, but it does not classify them in any manner. The most common classification of seismic events is by frequency, as has been outlined in Section 1.2 since it allows an interpretation of the source mechanism to be made. Unless otherwise stated, all seismic analysis done in this and the subsequent chapters refers only to low frequency seismicity, within the spectral band of 0.5 to 5 Hz, which is thought to relate to the movement of magmatic fluid (Chouet, 1996a, Neuberg et al., 2000).

3.4.2 Individual seismic swarms analysed with the FFM: All low frequency seismicity

Although not obvious in the continuous seismic data (Figure 3.8), the RSAM (Figure 3.9) or the RSEM (Figure 3.16), the timings of the incoming triggered events in July 2003 by the MVO detection algorithm at the time, placed the seismicity into a number of "swarms". Analysis of energy release for the precursory seismicity of February 2010 also suggested short cyclic behaviour, which was particularly dominant during the final few days before the dome collapse (Figure 3.17). Therefore these "swarms" were used in the analysis of individual seismic swarms (this section) and consecutive seismic swarms analysis (Subsection 3.4.3), for both 2003 and 2010, even though the swarm like behaviour is not very obvious in the continuous data.

Similar to using RSEM (Figure 3.14), using the number of events every 10 minutes across the entire precursory period from 22 to 25 June as the accelerating observable Ω in equation 1.1 generated swarm like behaviour. Therefore each seismic swarm within the precursory period was investigated individually. All followed a similar pattern, as shown in Figure 3.18, whereby

an initial acceleration in the event rate is seen, but then followed by a deceleration in the event rate. This is the same pattern that has been observed in the RSEM data (Figure 3.14) and the SSAM data (Figure 3.7) and is therefore believed to be a fundamental phenomena observed in precursory seismicity.

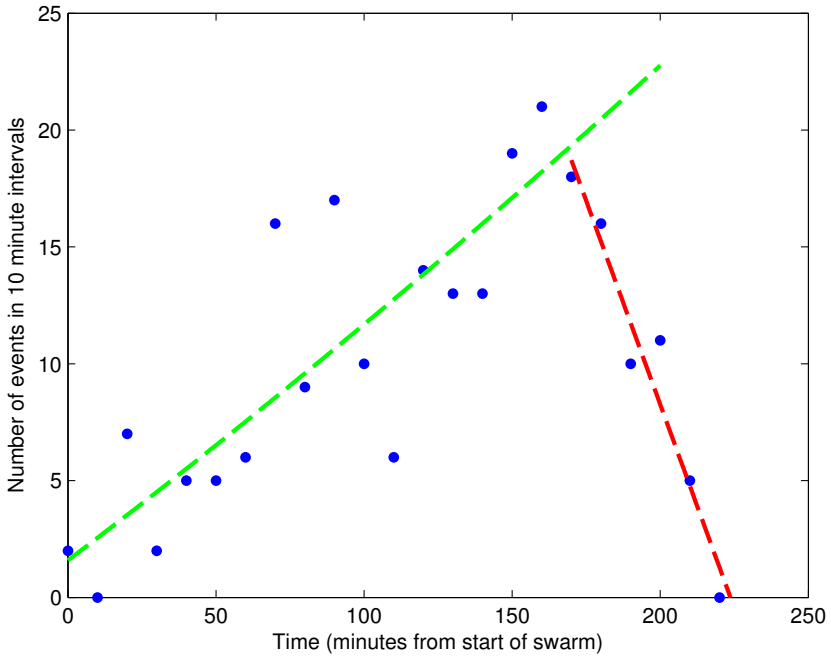

Figure 3.18: The change in rate of seismicity within one single swarm on the 24 June 1997. The green dashed line indicates the acceleration phase, the red dashed line indicates the deceleration phase. Each data point represents the event rate for each 10 minute interval.

The acceleration of event rate can be related to the trigger model proposed by Neuberg et al. (2006), whereby a constriction in the conduit causes an increase in strain rate (Thomas and Neuberg, 2012), leading to the generation of seismicity due to brittle failure within the magma itself. The brittle failure of magma will result in an acceleration in flow through generated fractures, and thus ultimately lead to a de-pressurization within the magma column. This effectively reduces the strain across the column and consequently would lead to a decrease in seismic event rates as seismicity decays relative to the decay in strain (Hammer and Neuberg, 2009).

The FFM assumes that as a geophysical precursor (e.g. event rate) accelerates, a scenario of failure will occur once uncontrolled propagation develops (Voight, 1988). Consequently, the FFM is not applicable to each individual swarm since the acceleration phase is followed by a

deceleration phase, which is not accountable for in the FFM. In addition, if each accelerating period was taken, it would be possible to generate multiple false forecasts for an eruption, due to the cyclic nature of the swarm activity. Cyclic seismicity can therefore be misleading when generating forecasts for volcanic phenomena, since it is unclear as to which accelerating phase will lead to an uncontrolled rate, and therefore to an eruption.

3.4.3 Consecutive Seismic Swarms with the FFM: All LF Seismicity

Hammer and Neuberg (2009) suggested that although individual swarm analysis was not suitable for the FFM, consecutive swarm analysis might be (Figure 3.3). Instead of taking the event rate every 10 minutes from the continuous data, the event rate per 10 minutes is averaged across the entire duration of the seismic swarm, suggesting an overall acceleration in the event rate (i.e. the first swarms have a lower average event rate (per 10 minutes) than the latter swarms which are closer to the known timing of the dome collapse).

June 1997

Figure 3.19 shows the acceleration of consecutive swarm event rates for the precursory period of 22 to 25 June 1997. Initially a clear accelerating trend can be identified from the swarms on the 22 and 23 June, however after this the acceleration appears to slow, despite the average event rate within each swarm remaining higher than previous event rates. Nonetheless, since an overall acceleration in the seismic swarm event rate is identified, it is possible to apply the FFM to the data in order to determine a forecasted timing of collapse (Figure 3.20). It is clear that although the forecasted timing of the dome collapse is extremely good (forecasted to within approximately 2.5 hours of the known timing of the dome collapse), the fit of the linear regression is not good, and there is a wide discrepancy between the observed event rates and the theoretical application of the FFM (R^2 = 0.63, see Section 3.2.2 for details).

July 2003

The acceleration of swarms identified from the triggered catalogue (STA/LTA parameters unknown) determined by MVO is shown in Figure 3.21. There is perhaps a very slight overall accelerating trend (solid green line), although it certainly is not exponential and does not lead to a singularity in the moments prior to the dome collapse (vertical blue line). The dashed green line shows a slightly better accelerating trend since only the accelerating swarms (swarms 2 to 6) are used in the curve fitting. Similar to the precursory seismicity identified in 1997, the

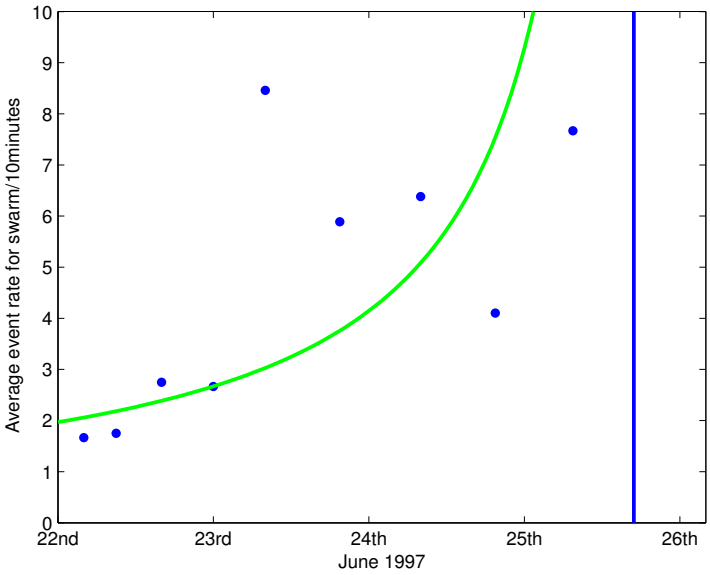

Figure 3.19: Acceleration of consecutive swarms at Soufrière Hills volcano, 22 to 26 June 1997, station MBLG. The vertical line represents the known timing of the dome collapse on 25 June. Each data point represents one individual swarm, and the average event rate per 10 minutes within this swarm. An exponential trend is fitted to the accelerating swarm data (solid green line).

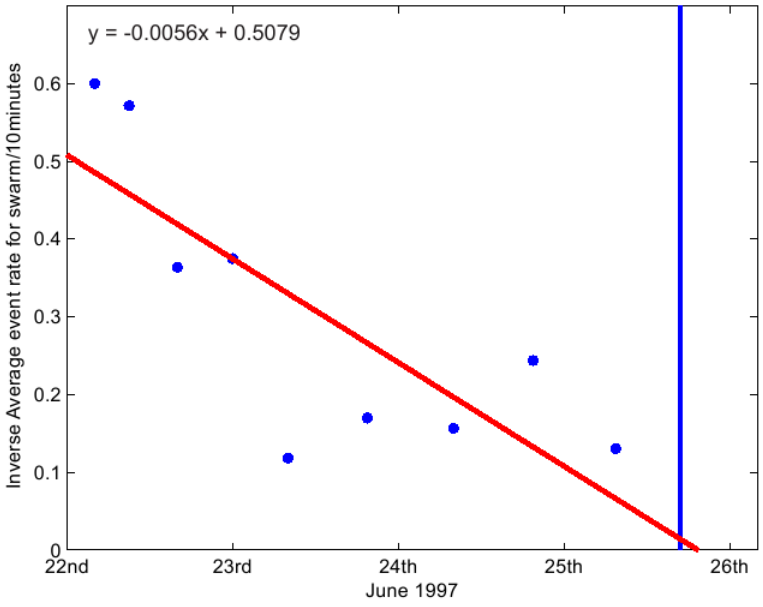

Figure 3.20: Application of the FFM to consecutive swarms at Soufrière Hills volcano, 22 to 26 June 1997, station MBLG. The vertical line represents the known timing of the dome collapse on 25 June. Each data point represents one individual swarm, and the inverse average event rate per 10 minutes within this swarm. A linear regression is fitted to all of the data points (solid red line). Known timing of dome collapse: approximately 12:55 on 25 June. Forecasted timing of dome collapse: 15:25 on 25 June.

acceleration appears to slow towards the onset of the dome collapse.

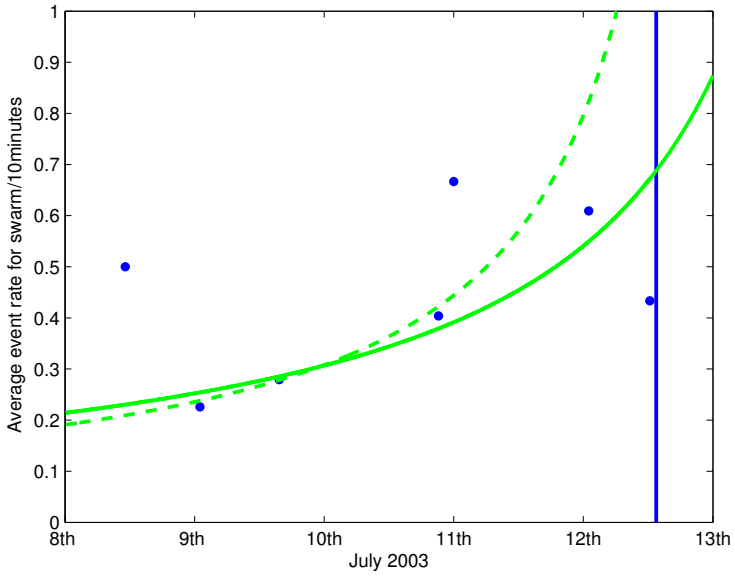

Figure 3.21: Acceleration of consecutive swarms at Soufrière Hills volcano, 8 to 13 July 2003 using triggered MVO data, station MBLG. The vertical line represents the known timing of the dome collapse on 12 July. Each data point represents one individual swarm, and the average event rate per 10 minutes within this swarm. An exponential trend is fitted to all the swarm data (solid green line), and to only the accelerating swarms (dashed green line).

Application of the FFM to the precursory seismic swarms in July 2003 yields a better fit between the FFM model and the data than in June 1997 (Figure 3.22). Using all of the swarms in the analysis (solid red line) demonstrates a forecast on 14 July at approximately 15:00, 49 hours and 30 minutes after the known timing of the collapse. The fit of the linear regression to the data is ambiguous, with an R^2 value of 0.59. However, when generating a forecast using only the accelerating swarms from the precursory seismicity, the fit of the data to the linear regression is good (R^2 = 0.87) allowing confidence in the forecast (dotted red line in Figure 3.22). The forecasted timing of the dome collapse using only the accelerating swarms is 13 July at 06:17, 16 hours and 47 minutes after the known timing of failure.

STA/LTA analysis in this research using known parameters did not identify clear swarm behaviour in July 2003. Therefore, the timing of swarms were taken from the MVO triggered event data, identified in Figure 3.21. Figure 3.23 suggests a fall in the average event rate for each swarm from 11 July onwards, and in fact as the dome collapse approaches the seismicity event rate enters a deceleration phase (solid green line). Application of an exponential trend to

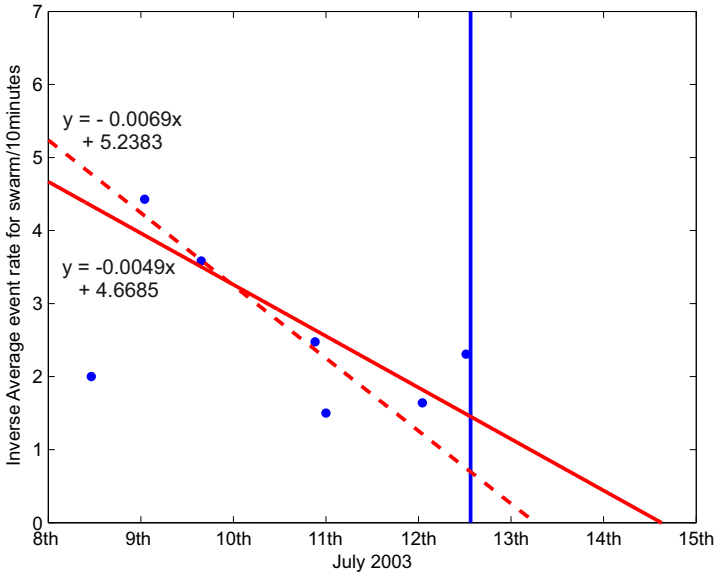

Figure 3.22: Application of the FFM to consecutive swarms at Soufrière Hills volcano, 8 to 13 July 2003 using triggered data, station MBLG. The vertical line represents the known timing of the dome collapse on 12 July. Each data point represents one individual swarm, and the inverse average event rate per 10 minutes within this swarm. A linear regression is fitted to all of the data points (solid red line), and only to those swarms which were accelerating in Figure 3.21 (dashed red line).

only those consecutively accelerating swarms suggests tending towards an uncontrolled event rate as would be expected with application of the FFM (dashed green line). However, the point of singularity although off the figure, would be anticipated much earlier than the known time of the dome collapse on 12 July.

Application of the FFM to all of the swarms identified using known STA/LTA parameters in the precursory seismicity from 8 to 13 July generates a forecast on 11 July at 17:50, 19 hours and 40 minutes before the known timing of the collapse (Figure 3.24). Again, when using all of the swarms in analysis, the fit of the linear regression to the data points is ambiguous (R^2 = 0.54), not generating much confidence in the forecast. When using only the accelerating swarms, a forecast is generated for 10 July at 19:39, 41 hours and 51 minutes before the known collapse and more confidence can be placed in the forecast since the R^2 value is higher at 0.72. However, neither of the forecasts are that accurate, which highlights the issue that not every accelerating seismic swarm (or consecutive swarms) will lead to an eruption immediately. Voight (1988) also suggested that there could be a delay interval between the forecasted timing of a failure event, and the actual timing of the failure event, which shall be discussed thoroughly in Chapter 6. The suggestion is based upon the fact that the FFM is forecasting a phenomena

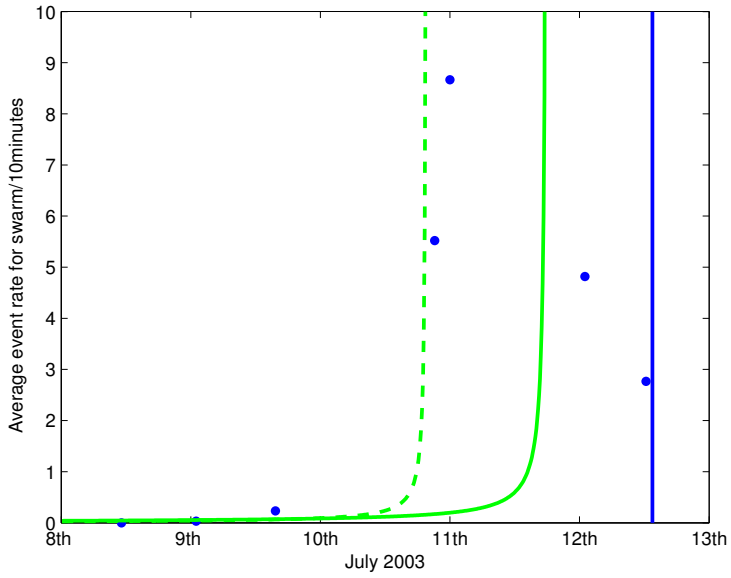

Figure 3.23: Acceleration of consecutive swarms at Soufrière Hills volcano, 8 to 13 July 2003 using events identified from the continuous data using an STA/LTA algorithm, station MBLG. The vertical line represents the known timing of the dome collapse on 12 July. Each data point represents one individual swarm, and the average event rate per 10 minutes within this swarm. An exponential trend is fitted to all the swarm data (solid green line), and to only the accelerating swarms (dashed green line).

related to the seismicity, which is occurring at depth, and therefore a transfer function must exist between the seismicity at depth and the collapse or eruption occurring at the surface.

February 2010

Cyclic behaviour was identified within the precursory seismic sequence from 2 to 11 February, in particular in relation to RSEM (Figure 3.17). Consequently each of these acceleration and deceleration periods were classified as an individual swarm. However, the average event rate across each of these swarms is fairly constant (Figure 3.25). No overall acceleration in the event rate is seen when considering all of the known swarms. This is perhaps not surprising since it might be assumed that all events within these swarms are extremely similar due to the similar amount of energy release (RSEM, Figure 3.17) by each one. When considering only the swarms which accelerate (from 8 to 10 February) a small exponential trend in the data can be identified, however it does not culminate towards a singularity at the known timing of the dome collapse or appear to be trending towards this.

Application of the FFM with all identified swarms from 8 to 12 February generates a forecasted time of dome collapse greater than 2 weeks from the known timing of failure, with an

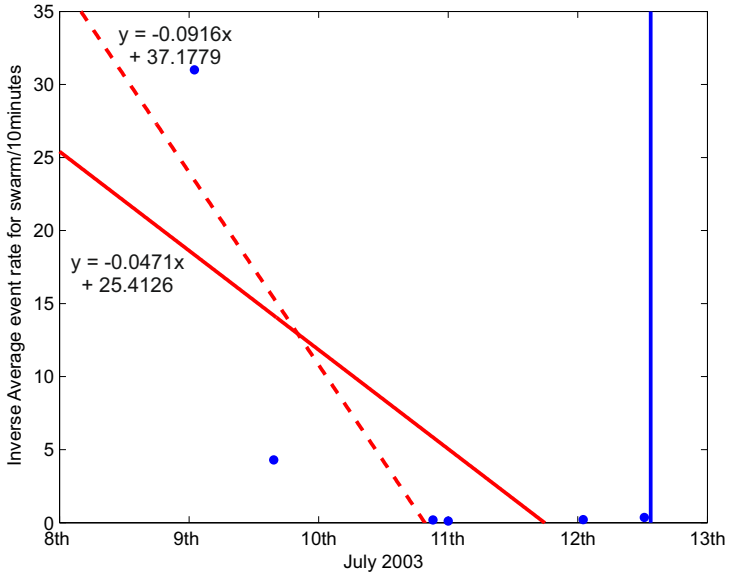

Figure 3.24: Application of the FFM to consecutive swarms at Soufrière Hills volcano, 8 to 13 July 2003 using events identified from the continuous data using an STA/LTA algorithm, station MBLG. The vertical line represents the known timing of the dome collapse on 12 July. Each data point represents one individual swarm, and the inverse average event rate per 10 minutes within this swarm. A linear regression is fitted to all of the data points (solid red line), and only to those swarms which were accelerating in Figure 3.23 (dashed red line).

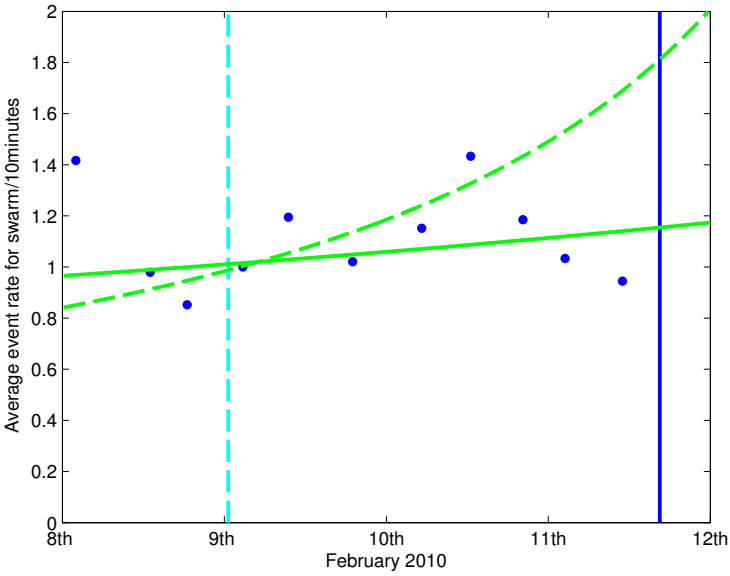

Figure 3.25: Acceleration of consecutive swarms at Soufrière Hills volcano, 8 to 12 February 2010 using events identified from the continuous data using an STA/LTA algorithm, station MBLG. The first vertical line (light blue) represents a small Vulcanian explosion the 8 February. The final vertical line (blue) represents the onset of the dome collapse and associated pyroclastic flows. An exponential trend is fitted to all the swarm data (solid green line), and to only the accelerating swarms (dashed green line).

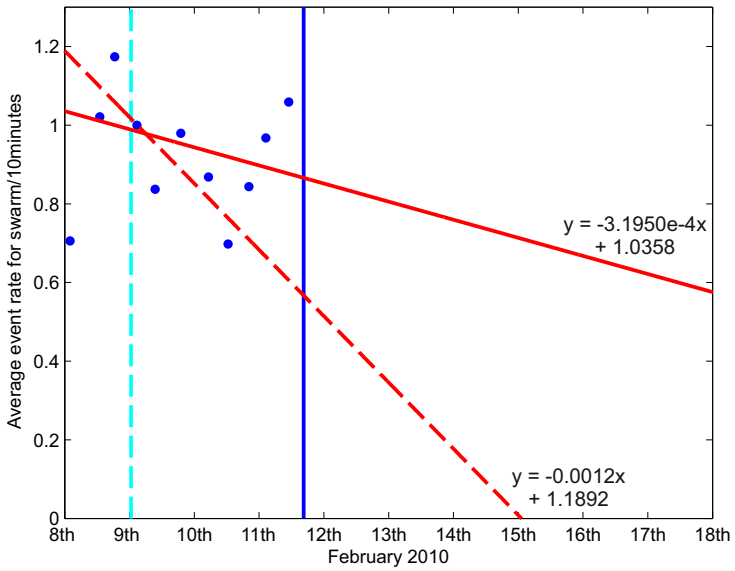

Figure 3.26: Application of the FFM to consecutive swarms at Soufrière Hills volcano, 8 to 12 February 2010 using events identified from the continuous data using an STA/LTA algorithm, station MBLG. The first vertical line (light blue) represents a small Vulcanian explosion the 8 February. The final vertical line (blue) represents the onset of the dome collapse and associated pyroclastic flows. Each data point represents one individual swarm, and the inverse average event rate per 10 minutes within this swarm. A linear regression is fitted to all of the data points (solid red line), and only to those swarms which were accelerating in Figure 3.25 (dashed red line).

R^2 value of 0.12, which is an extremely poor forecast. Using only those swarms which were slightly accelerating (from 8 to 10 February) generates a forecast on 15 February at 01:13, approximately 80 hours after the initiation of the dome collapse on 11 February. Although the R^2 value is significantly higher than when using all swarms in the forecast (R^2 = 0.66), it is still ambiguous and does not allow great confidence in the forecast.

Other time periods of swarm activity

A number of other periods of precursory swarm activity were also investigated, related to the onset of dome collapses (mostly minor in comparison to the 1997, 2003 and 2010 events). In addition, one of the first major eruptive events of the ongoing eruption at Soufrière Hills volcano in December 1996 was investigated.

Consecutive swarm analysis and application of the FFM was inappropriate and unsuccessful in December 1996, since no acceleration in the seismic event rate was observed (Figure 3.27). Instead, the event rate fluctuated around 2.5 to 5 events every 10 minutes during the week preceding the generation of pyroclastic flows. No acceleration in event rate was observed

prior to the minor dome collapse in June 2006, meaning no forecast could be generated (Figure 3.30). This could be related to the fact that the volcanic system was still unstable following a large scale collapse the month before. However, analysis of the major dome collapse in May 2006 suggests that although a linear regression can be fitted to the inverse event rate, the fit of the regression to the data points is poor (Figure 3.30). If the third swarm on 16 May was excluded, no regression could be identified.

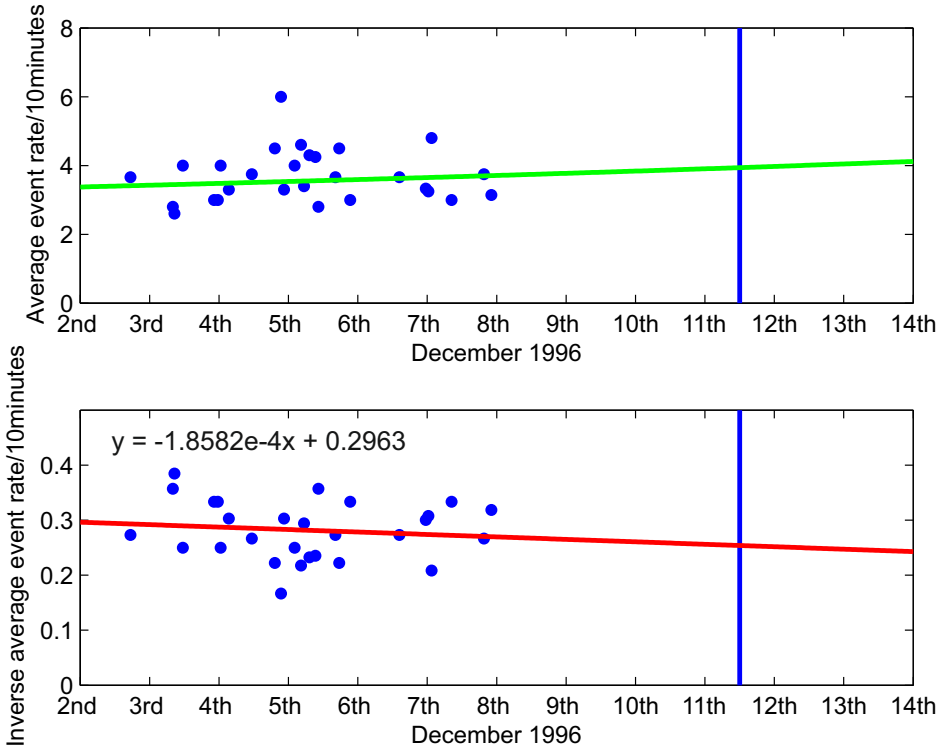

Figure 3.27: Consecutive swarm analysis: December 1996. *Upper:* Consecutive swarms at Soufrière Hills volcano, 2 to 7 December 1996 using events identified from the MVO catalogue, station MBLG. Each data point represents one individual swarm, and the average event rate per 10 minutes within this swarm. Vigorous growth of the dome and pyroclastic flows occurred on 11 December, following a period of quiescence (Young et al., 1998). No exponential trend could be fitted to the data. *Lower:* Application of the FFM. The timing of the onset of the pyroclastic flows is represented by the vertical blue line. Although a linear fit could be fitted to the data (R^2 = 0.01), there was no regression in this. Consequently no forecast could be made for these pyroclastic flows using consecutive swarm analysis.

In March 2004, application of the FFM to precursory seismic swarms may have aided a forecast for a minor dome collapse. A clear linear regression can be plotted (Figure 3.28), which forecasts the timing of the dome collapse to within 24 hours of the known timing of collapse. It is possible that the forecast is even closer than this, since it is unclear as to when the collapse first began due to lack of visual observations.

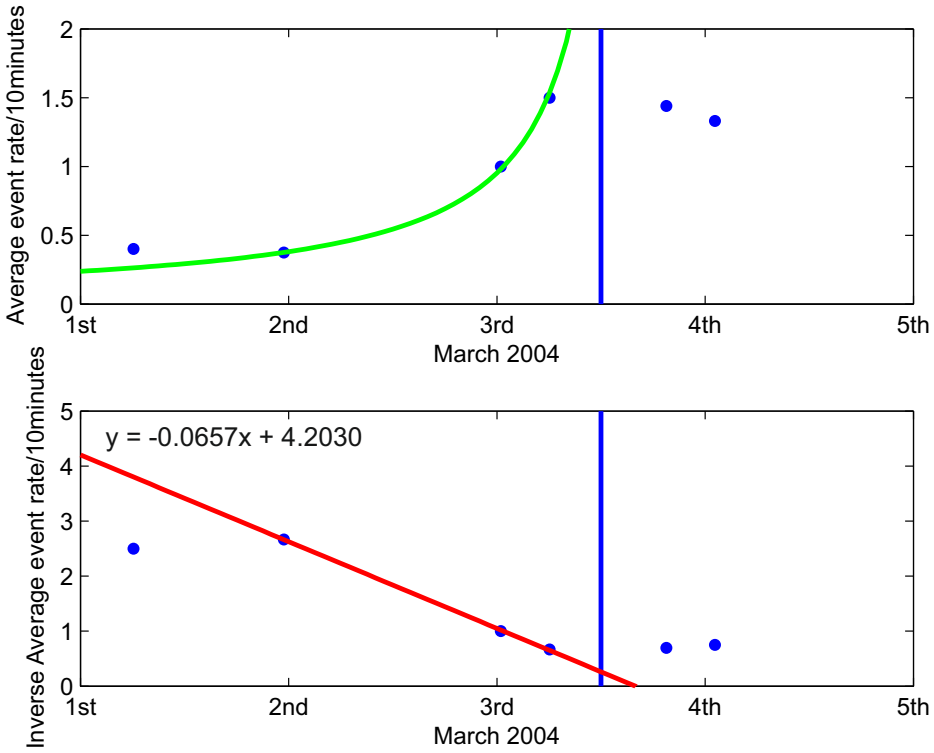

Figure 3.28: Consecutive swarm analysis: March 2004. A small dome collapse occurred on 3 March 2004 and is represented by the vertical blue line, although the actual onset of activity is not known due to poor visual conditions. *Upper:* Consecutive swarms at Soufrière Hills volcano, 1 to 4 March 2004 using events identified from the MVO catalogue, station MBLG. Each data point represents one individual swarm, and the average event rate per 10 minutes within this swarm. A slight exponential trend could be fitted to the data, which appears to decrease again following the onset of collapse. *Lower:* Application of the FFM. A linear regression for the three swarms preceding the dome collapse forecasts the timing of the dome collapse to approximately 16:00 on 3 March (R^2 = 0.99).

3.5 Comparison of different methods for forecasting volcanic processes

Although application of the FFM can, under the right conditions and parameters, provide an accurate forecast of the onset timing of volcanic phenomena, it is clear that on many occasions a forecast simply cannot be made. A successful forecast is one that is made within two to three days of the known timing of the volcanic phenomena trying to be forecast, and is done so with a strong linear regression (i.e. a high R^2 value indicating a higher likelihood that the model (the FFM) is applicable to the data point used). More successful forecasts were made using consecutive swarm event rates of low frequency seismicity than any other method. However in most cases, as exemplified by June 1997 (Figure 3.20), even though the forecast using all of the available swarms in hindsight may be accurate in terms of timing, in reality if this approach

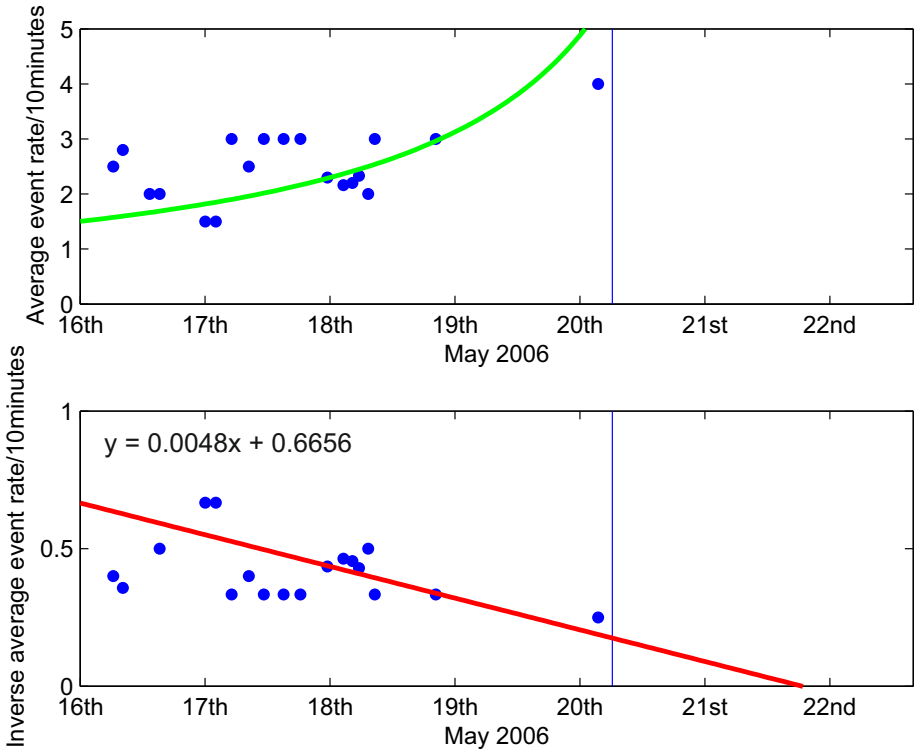

Figure 3.29: Consecutive swarm analysis: May 2006. A major dome collapse occurred on 20 May 2006 and is represented by the vertical blue line. Almost 100% of the dome standing at the time was removed in this event. *Upper:* Consecutive swarms at Soufrière Hills volcano, 16 to 20 May 2006 using events identified from the MVO catalogue, station MBLG. Each data point represents one individual swarm, and the average event rate per 10 minutes within this swarm. Besides a major increase in the event rate just prior to the collapse, event rates in the preceding few days remains fairly constant. *Lower:* Application of the FFM. A linear regression through all of the swarms identified forecasts the dome collapse on 21 May at approximately 19:00, over 37 hours after the known timing of collapse (R^2 = 0.16).

were to be undertaken in real time, there would be limited confidence in the forecast due to the poor fit of the linear regression to the data points. Using only the accelerating swarms in the forecast (e.g. in 2003, Figure 3.22, and in 2010, Figure 3.26) appears to generate a more reliable forecast in terms of the confidence between the linear regression and the data points, if not always in terms of timing. This is unsurprising since the FFM is only really applicable to accelerating systems.

One major advantage of using consecutive swarm analysis in conjunction with the FFM appears to be the lack of false forecasts that it is associated with. Although the trend in consecutive swarm event rates may not give an accurate forecasted timing, it does discourage getting a number of different forecasts within a short space of time, as is the case when using RSAM

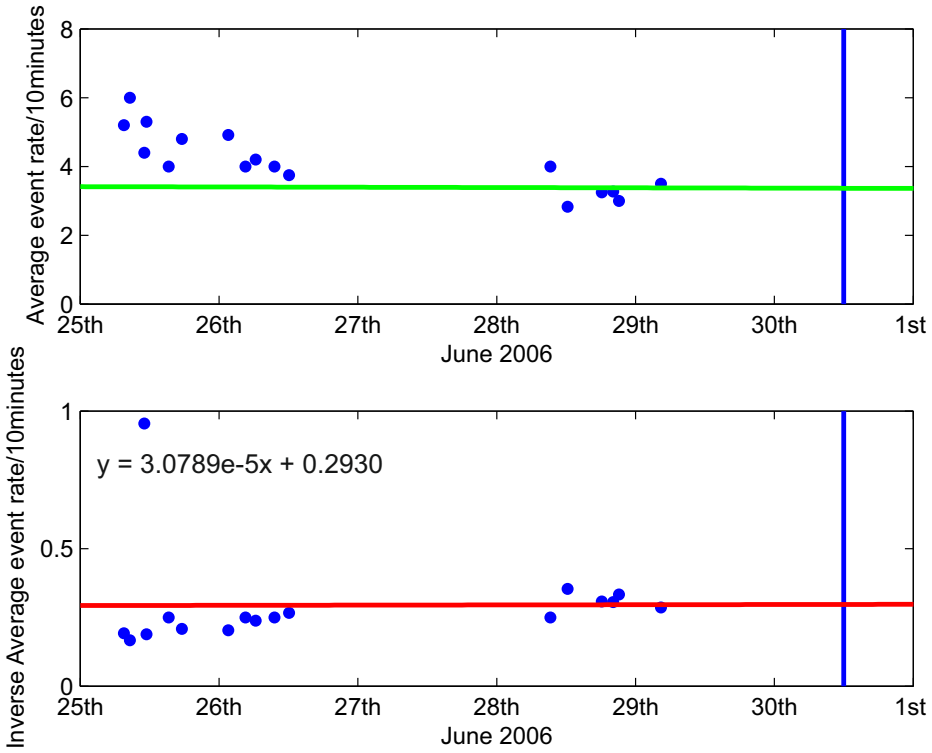

Figure 3.30: Consecutive swarm analysis: June 2006. A minor dome collapse occurred on 30 June 2006 and is represented by the vertical blue line. *Upper:* Consecutive swarms at Soufrière Hills volcano, 25 to 30 June 2006 using events identified from the MVO catalogue, station MBLG. Each data point represents one individual swarm, and the average event rate per 10 minutes within this swarm. No acceleration in the event rate is observed. *Lower:* Application of the FFM. Although a linear fit could be fitted to the data (R^2 = 0.00003), there was no regression in this. Consequently no forecast could be made for this dome collapse using consecutive swarm analysis.

in June 1997 for example (Figure 3.5). Using consecutive analysis limits the cyclicity of the seismicity, thereby avoiding forecasts due to this.

Use of RSAM, SSAM, RSEM and SSEM has proved to be useful as a forecasting tool at some volcanoes (e.g. Redoubt in the 1989-90 eruptive episode (Cornelius and Voight, 1994)). However, at Soufrière Hills volcano during the cases investigated (major dome collapses of 1997, 2003 and 2010), none of these tools provided accurate forecasts, and in fact often suggested no change in the seismicity during the precursory periods. One of the major problems with RSAM and RSEM is the averaging over all seismicity, which can therefore be made up of multiple sources generated by a number of mechanisms. Whilst most of the time these may all be volcanic sources, it is possible that anthropogenic sources and other noise become mixed up in this signal, and then therefore used in the forecast. This approach has a good chance of success only if one event type completely dominates the seismicity. For this reason, methods

which can separate source mechanisms should be favoured, such as SSAM and SSEM, even though they also may not always provide an accurate forecast. For example Figure 3.7 and 3.13 do not necessarily provide any useful information in order to make a forecast since clear accelerations in SSAM are not seen prior to the collapses. However, based on prior interpretations of low frequency seismicity, it is thought that SSAM shows fluctuations in magmatic fluid movement at depth.

False forecasts will always be part of forecasting volcanic eruptions since nature does not always follow patterns. Therefore in order to generate as many successful forecasts as possible, a deeper understanding of the underlying process is needed. For example, is it certain that the ongoing precursory seismicity forms a causal relationship to an impending eruption? Is it forecasting failure at depth i.e. fracturing to facilitate the movement of magma at depth? Or is it forecasting failure at the surface? It is essential, therefore, that when using the FFM, which does assume a causal relationship between the accelerating precursor and failure, that direct links can be made between the precursors and the ensuing eruption. Use of RSAM and RSEM do not isolate a single mechanism at depth which could be linked to failure at the surface, and even all low frequency seismicity may not be a true representation of a single process. Waveforms which are similar in frequency content and waveform shape however can be thought of as originating from the same source mechanism and same source location at depth, and therefore from a single active system. Concentrating on a single active system at depth may allow a better and more direct link between seismicity occurring at depth and the eruption at the surface. This idea shall be investigated thoroughly in Chapter 4.

3.6 Summary

Three large dome collapses were investigated at Soufrière Hills volcano in hindsight (June 1997, July 2003 and February 2010) using the FFM. Input observations of seismic event rate, seismic amplitude and seismic energy were used, which have all been proven to be used successfully with the FFM at other volcanoes, and are currently in operation within volcano observatories around the world. For the three dome collapse investigated, RSAM, SSAM, RSEM and SSEM were all unsatisfactory as forecasting tools, and in many cases failed to identify any accelerating seismic behaviour prior to collapse. Although successful elsewhere, these tools do not appear to be reliable as a method of forecasting at Soufrière Hills volcano, at least in their

current format.

Instead, the most simple method for identifying unrest (event counts per unit time) appears to be more successful as a forecasting tool, although it is still unreliable and often inaccurate. Analysis of low frequency seismicity only should ensure that source mechanisms are not being mixed in the forecasting process, and therefore relate the precursory seismicity to the movement of magmatic fluid at depth and therefore to the eruption at the surface. In some cases, e.g. June 1997, an accurate forecast can be made in terms of the timing, but the fit of the linear regression to the data points is poor (Figure 3.20). In contrast, there are occasions when the fit of the linear regression to the data may be good, but the forecasted timing of failure is poor (e.g. July 2003 with only accelerating swarms, Figure 3.24). Consequently, it appears that application of the FFM with seismic event rates is not a reliable forecasting tool, in its present form.

Chapter 4

Characterisation of accelerated volcanic activity: Defining a single system

As demonstrated in Chapter 3, using the entire precursory seismic sequence as a forecasting tool for a number of dome collapses at Soufrière Hills volcano is not accurate enough to provide confident forecasts. In this chapter, a variation on the FFM is presented in which only one active seismic system at depth is used as the precursory activity. Similar seismic waveforms suggest a similar source mechanism and source location at depth (Geller and Mueller, 1980, Neuberg et al., 2000) and therefore by using only similar seismic events as a forecasting tool, it is less likely that multiple sources become mixed in the forecast. The technique is tested upon the dome collapses of June 1997, July 2003 and February 2010. Furthermore, the impact of using a simple least squares linear regression is analysed, and other potential forecasting models are evaluated. Despite some mathematical short comings assuming a least squares linear regression, it appears that in conjunction with only using one family of similar seismic events it provides the most accurate and confident forecast to the timing of a dome collapse.

4.1 Classification of Events by Waveform Similarities

Applying the FFM to all triggered low frequency seismicity can lead to variable results in the forecasting of dome collapses at Soufrière Hills volcano. This suggests that classification by similar frequency characteristics alone is not appropriate when applying the failure forecast method, and thus a further classification scheme should be considered. The FFM was first developed as a tool for identifying accelerating material creep and relating this to a slope fail-

ure; a cause and consequence of one single active system generating failure (Fukuzono, 1985). However, a volcanic system is inherently more complex, and it is unlikely that the input into the FFM in this instance is a single active system clearly related to the slope failure at the surface. Therefore, in order for only one system to be analysed by the failure forecast method it is necessary to focus only on one "family" of low frequency waveforms which originate from the same source mechanism and location, and therefore represent a single system. A family is defined as a group of seismic waveforms which have similar frequency content and a similar waveform shape (e.g. Thelen et al. (2011)). Classification by waveform similarity in addition to frequency content allows low frequency seismicity of a single source and depth to be exclusively analysed. In order to find low frequency events which satisfy this criterion, a cross correlation technique is applied:

$$r_{xy}(i, i-l) = \frac{\sum_{i=1}^{n}(x_i - \bar{x})(y_{i-l} - \bar{y})}{\sqrt{\sum_{i=1}^{n}(x_i - \bar{x})^2}\sqrt{\sum_{i=1}^{n}(y_{i-l} - \bar{y})^2}} \tag{4.1}$$

where *r* is the cross correlation coefficient, *x* and *y* represent the two traces in the correlation, and therefore x_i is the *i*th sample of the signal *x* and y_{i-l} is the *i-l*th sample of the signal *y*. The overbar represents the mean value of the signal and *l* is the lag between the two signals. Identical waveforms will result in a cross correlation function of 1 or -1 dependent upon the polarity of the signal. r_{xy} is a measure of similarity in waveform shape only, since events are normalised prior to calculation. Consequently, the cross correlation function gives no information on the amplitude ratios of the events.

Events which are statistically similar to one another are also known as multiplets, and are grouped together into a family. Many authors have shown that it is possible to further sort multiplets into a number of families of highly similar waveforms using a cross correlation technique, which therefore isolates a single system at depth. Stephens and Chouet (2001) investigated a 23 hour swarm of low frequency seismic events prior to the eruption of Redoubt volcano, Alaska in December 1989, finding that the events could be sorted into 3 distinct families which evolved with time, of which the majority of events were correlated (cross correlation coefficient ≥ 0.68) with just one distinctive family. Later analysis of the 2009 Redoubt eruption by Buurman et al. (2013) also suggested the presence of multiplets, in particular prior to explosion events. Petersen (2007) suggested that a dominant family of multiplets exists within the low frequency

seismic swarms at Shishaldin volcano, Alaska, although the dominant family is different within each swarm studied between 2002 and 2004. Thelen et al. (2011) suggest that the occurrence of multiplets at Mount St. Helens, Washington and Bezymianny volcano, Russia are related at least in part to the viscosity of the magma, and therefore are more prominent during dome building eruption events. Highly correlated high frequency events were observed at Mt. Unzen, Japan during significant endogenous growth of a lava dome between 1993 and 1994 and were classified into over 100 families (Umakoshi et al., 2003). Families of similar low frequency events have also been identified and studied at SHV in relation to tilt cycles by Voight et al. (1999) and Green and Neuberg (2006), who identified 9 multiplet families containing more than 45 similar events each over a time period of 6 days in June 1997, although not all of the families were active during each of the seismic swarms. In addition, Ottemöller (2008) found that 7100 hybrid events generated in the days prior to a large scale dome collapse at SHV in July 2003 all belonged to the same multiplet family.

4.1.1 Choice of Cross Correlation Threshold

A threshold must be chosen which demonstrates that waveform events are similar to one another. The threshold is extremely important: if it is too low there is a risk of placing events which are not similar into the same family, if it is too high however, many similar events may be missed due to poor signal to noise ratios. In addition, if the threshold is too high events may be divided into a number of families which are actually statistically similar to one another. Green and Neuberg (2006) and Thelen et al. (2011) suggest using 0.7 as a correlation threshold since it is significantly above the upper limit for random correlation between waveforms and noise. Therefore on a logarithmic plot of the frequency of occurrence, cross correlations which sit away from a normally distributed curve for the data are deemed to be similar. Similarly Stephens and Chouet (2001) use a cross-correlation threshold of 0.68 to identify similar events. Caplan-Auerbach and Petersen (2005) use a cross correlation threshold of 0.9 which sorted the waveforms into families of nearly identical events. Petersen (2007) noted that this is probably not appropriate at most stations within a volcanic environment, and therefore to account for events with poorer signal to noise ratios chose a cross correlation coefficient of 0.8.

The cross correlation coefficient threshold was chosen as 0.7, in agreement with Green and Neuberg (2006) and Thelen et al. (2011) since above this value the cross correlation coefficient appears to deviate from a Gaussian distribution curve (Figure 4.1), which can therefore

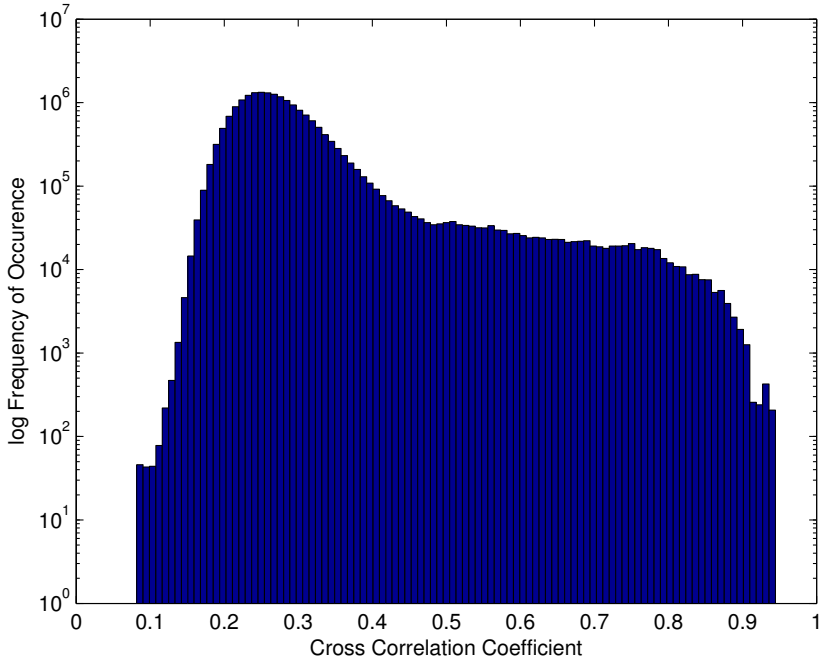

Figure 4.1: The distribution of cross correlation coefficients from 22 to 24 June 1997 at station MBLG when correlated with the dominant master event identified during this time period. At the point where the cross correlation coefficients deviate from a normal distribution curve is considered to be an ideal threshold limit to identify similar events, approximately 0.7 in this example.

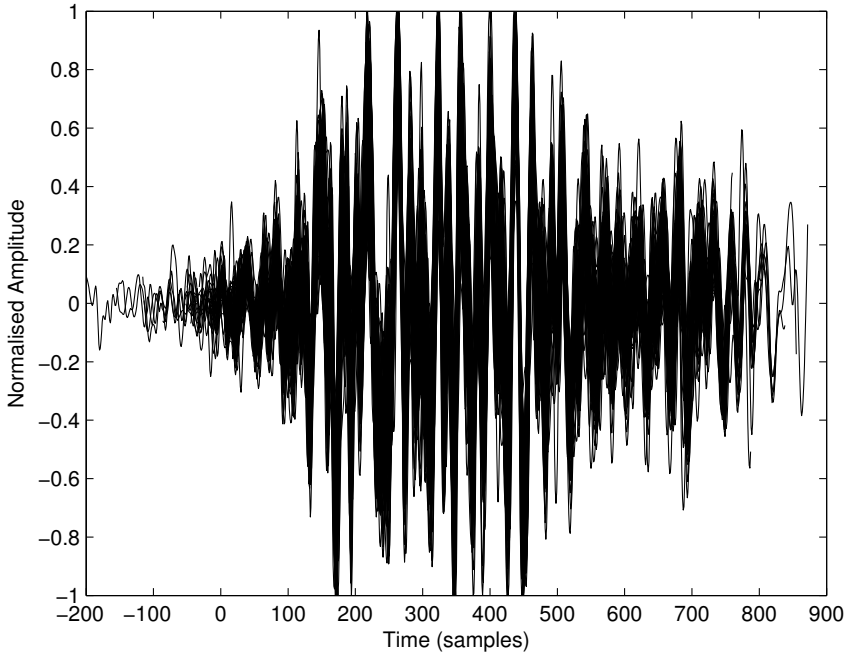

Figure 4.2: Stack of events with correlation coefficient threshold of 0.7 with identified dominant master event on 24 June 1997 at 11:18-53s, station MBLG. A total of 82 triggered events are included in the stack. Each event has been aligned at the peak correlation coefficient.

be deemed as significant. Visual inspection of the stacked waveforms also confirmed that 0.7 was an appropriate choice and captured the majority of similar events with limited scatter of the waveforms once aligned (Figure 4.2). Stacking the waveforms on top of one another at the point of maximum correlation allows an average of the stack to be taken, which is thought to be representative of all of the included waveforms. Setting the cross correlation coefficient threshold at 0.6 created a large amount of scatter amongst the aligned waveforms (Figure 4.3a) such that it was difficult to identify an average waveform which would be representative of the entire stack. This is particularly obvious at the beginning of the waveform, where a large amount of detail is lost in the stacking as many different waveform shapes are included. A cross correlation coefficient threshold of 0.8 provided nicely aligned similar waveforms, but the family contained few events (Figure 4.3b), suggesting that some may have been missed due to signal to noise ratio issues.

4.1.2 Detection of Families

The cross correlation function (Equation 4.1) requires waveforms of the same length (a correlation window) in order to carry out its calculation. Previous studies utilizing the cross correlation technique with volcano seismicity have used a range of correlation windows from 8 seconds (Green and Neuberg, 2006, Petersen, 2007), 10 seconds (Stephens and Chouet, 2001) up to 30 seconds (Caplan-Auerbach and Petersen, 2005). Here, 10 seconds was chosen to utilize as much of the waveform as possible in the calculation, without interference from adjacent events within the continuous seismic record.

In order to determine if any similar events were present on any particular day, each 10 second event was cross correlated with every other triggered event from the same day. The maximum cross correlation coefficient of each waveform with every other waveform was determined and placed into a cross correlation matrix (an example of which can be seen in Figure 4.4 for the 24 June 1997). In theory, identical events will give a cross correlation coefficient (r) of 1 (e.g. the autocorrelation of events, as seen along the diagonal of Figure 4.4), and events which have no correlation will have a cross correlation coefficient of 0 (r=0). Events were then classified as being significantly similar to one another if the maximum cross correlation coefficient was above 0.7, and are shown on a colour spectrum in Figure 4.4. Figure 4.4 suggests distinct time periods when similar seismic events were active (coloured areas are separated

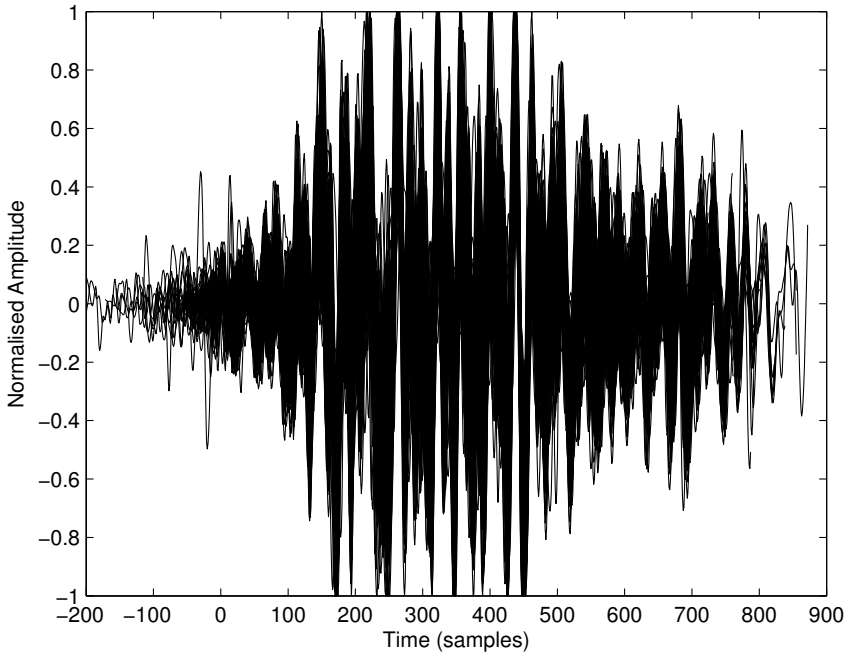

(a) Stack of events with correlation coefficient threshold of 0.6 with identified dominant master event on 24 June 1997 at 11:18-53s. A total of 179 triggered events are included in the stack and represents events identified on 24 and 25 June 1997. Each event has been aligned at the peak correlation coefficient.

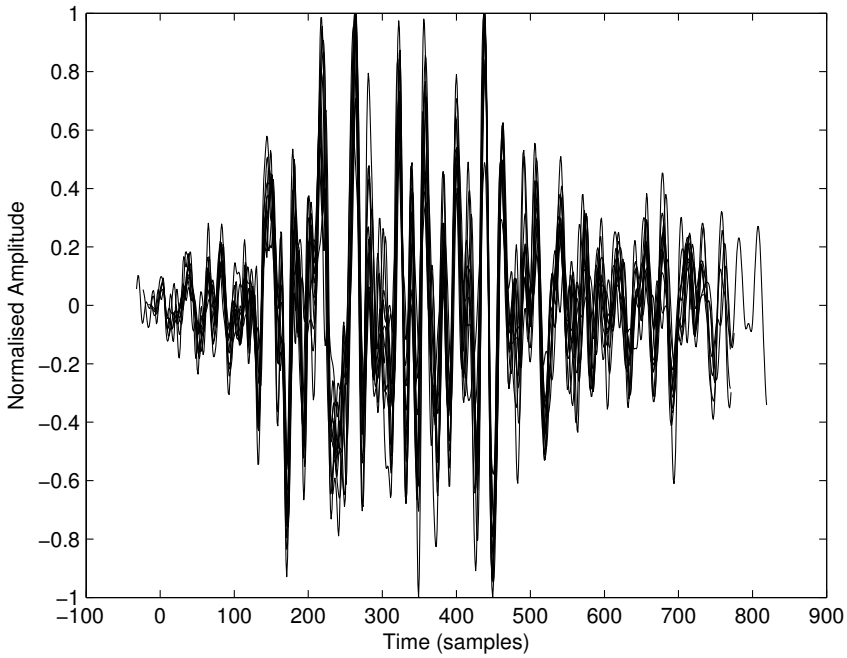

(b) Stack of events with correlation coefficient threshold of 0.8 with identified dominant master event on 24 June 1997 at 11:18-53s. A total of 11 triggered events are included in the stack and represents events identified on 24 and 25 June 1997. Each event has been aligned at the peak correlation coefficient.

Figure 4.3: Stacks of highly correlated waveforms with the dominant master event identified for the time period 22 to 25 June 1997 for different cross correlation coefficient thresholds at station MBLG.

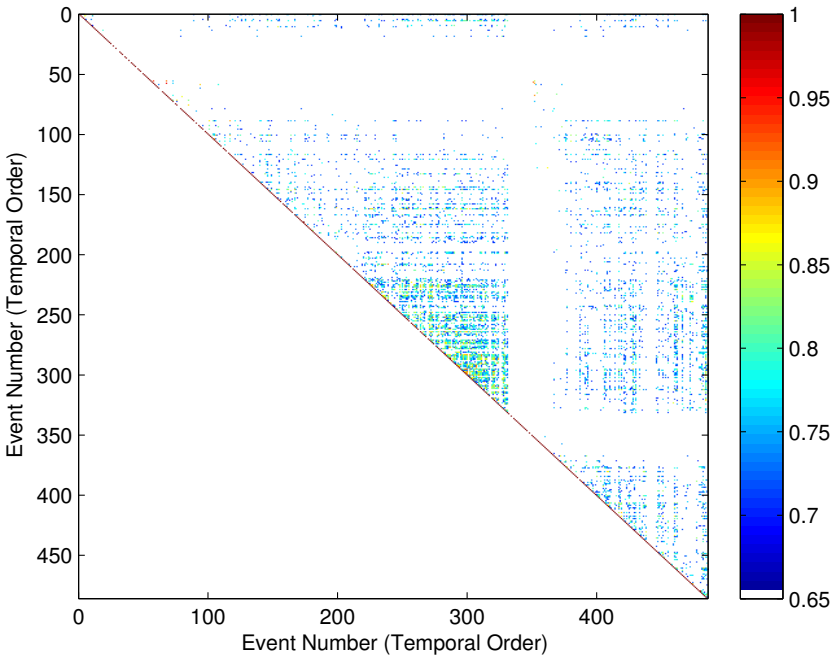

Figure 4.4: An example of a maximum cross correlation similarity matrix from station MBLG on 24 June 1997. A total of 486 triggered events were found within the 24 hour period and are represented from 1 to 486 along the x and y axis. Each row of the matrix therefore represents one triggered event compared to every other triggered event on that day. Only events with a cross correlation coefficient above 0.7 are shown on the colour spectrum and are deemed to be similar. The autocorrelation of each triggered event with itself (cross correlation coefficient equal to 1) is represented on the diagonal.

by distinctly white areas), and that a highly correlated swarm of events occurred (brighter and more concentrated colours). At this stage of the process, some events were removed after visual inspection confirmed that they were primarily composed of noise to ensure only seismic events were being cross correlated. For this reason, some events appear to have an autocorrelation of less than 1 in Figure 4.4 (the diagonal is not a solid red line), although this is an artefact of the fact that some events were removed and still cross correlated (their cross correlation would appear as zero).

Two techniques were used in order to isolate multiplets and collate them into families. Following Petersen (2007), a dominant event for each day was identified as the event correlated with the highest number of other events from that day. The mean correlation value of each event with every other event was determined from the cross correlation matrix (Figure 4.4) and the event with the highest mean was taken to be the dominant event. The second technique followed Green and Neuberg (2006) where each event in turn was correlated with every other event. Events with a cross correlation coefficient above 0.7 were subsequently grouped

together, labelled as a multiplet family and removed from the time series. This procedure was repeated across the entire investigated time period until all events had been classified into a number of different families. This has the advantage of finding all families of multiplets which may be present in the continuous data, rather than simply the dominant one, as well as finding families which may be infrequent in their repetition but still important. This procedure also allows for the identification of evolving waveforms, either by migration of their source location or change in the source process. Families which contained fewer than 10 similar individual triggered waveforms were eliminated from further analysis. To avoid selection bias, the events within a single family (i.e. all had a minimum cross correlation coefficient of 0.7 with one another) were stacked (e.g. Figure 4.2 and 4.3), and the average waveform taken. This average waveform is hereafter referred to as the Master Event of each family, and is a statistical representation of this family in terms of waveform shape.

The master events identified were then cross correlated with the continuous seismic record at MBLG using a sliding window technique and multiplets identified when the cross correlation coefficient was greater than 0.7 between the master event and the continuous seismogram. The sliding window separation of 0.01 seconds allows the maximum number of multiplets to be identified, in particular those which are too small or are overlapping in the continuous seismic record to be identified by the triggered acquisition system at MVO (STA/LTA algorithm - see Section 3.4.1). The similar events were then grouped into a multiplet family.

4.2 22nd-25th June 1997

The total number of multiplets identified using the cross correlation procedure was 7653 events from 22 to 25 June, in comparison to only 1435 events identified using the triggered algorithm at MVO over the same time period. This methodology therefore represents a five fold increase in the number of events which can be identified and used in further analysis. The dominant multiplet family identified using the technique by Petersen (2007) contained a total of 878 multiplets (Table 4.1). 10 multiplet families containing over 250 multiplets each were identified using the technique of Green and Neuberg (2006), although the dominant master and Master event 001 have a cross correlation coefficient of 0.93, suggesting that they are in fact the same family. This imitates the conclusions of Green and Neuberg (2006), who identified 9 waveform families during the same time period at station MBGA, however they did not use

Family	22nd	23rd	24th	25th	Total
Dominant	0	133	376	369	878
Master001	0	121	336	222	679
Master010	0	256	315	32	603
Master014	2	136	302	137	577
Master100	4	71	280	193	548
Master106	0	42	169	45	256
Master121	0	100	514	400	1014
Master136	3	131	483	542	1159
Master141	0	47	276	173	496
Master210	0	20	170	349	539
Master291	0	39	390	475	904

Table 4.1: Number of events within each family sorted into days from the 22 - 25 June 1997 at station MBLG.

these families as a forecasting tool. As these families of events were identified at a different station it is not possible to compare directly the results of the two studies.

For the data analysed in this example, the maximum number of triggered events that needed to be cross correlated for each day was ≤ 600. On a desktop PC the time taken to complete this calculation was just over 24 hours. Identifying a number of multiplet families using the technique of Green and Neuberg (2006) took much less time since multiplets which were correlated into one family were subsequently removed from the matrix and further cross correlations continued on the reduced subset of triggered events. Once master events had been identified, it took approximately 25 minutes to identify similar events within a six hour section of the continuous seismic record. The continuous record was split into six hour sections to optimize the computation time. Therefore although time consuming in the first instance, it should be possible for this type of system to operate in near real time since the automatic identification of master events at all times, including during periods of volcano quiescence, will mean that once unrest has been detected, the master events identified in the previous few hours/days/weeks can be immediately used in analysis, rather than having to conduct the search for master events in hindsight.

Clear differences between each of the families can be found (Figure 4.5) in terms of the onset timing of events and the waveform characteristics. In particular significant differences are noted in the expression of the waveform coda. As expected for low frequency events, mas-

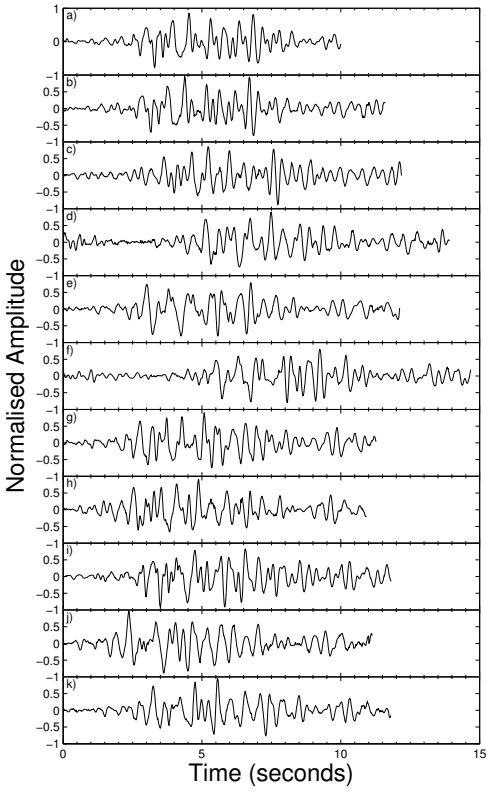

(a) Dominant master and 10 other identified master event waveform signatures

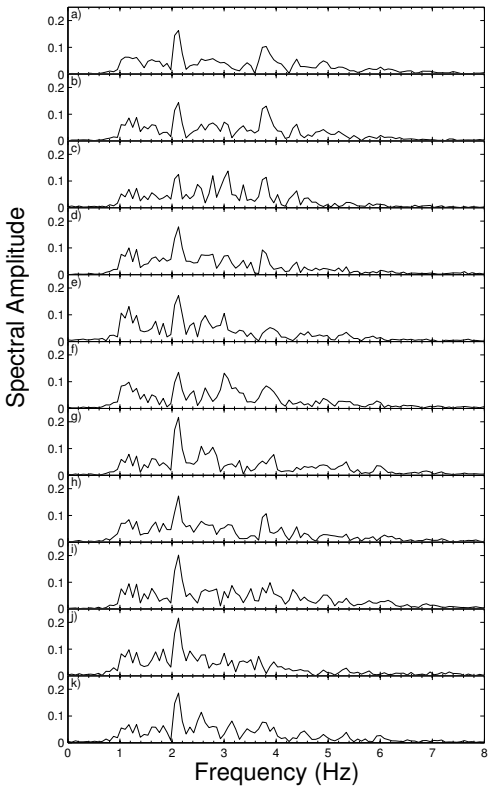

(b) Amplitude spectra of the waveforms of the dominant master and the 10 other identified master events

Figure 4.5: Comparison of all master events identified by cross correlation techniques. The waveform and amplitude spectra labelled (a) is the dominant waveform identified from the cross correlation coefficient matrix (Figure 4.4). Waveforms and corresponding amplitude spectrum labelled (b) to (k) represent the master events 001, 010, 014, 100, 106, 121, 136, 141, 210 and 291 respectively.

ter event 210 (Figure 4.5(i)) clearly decays in a harmonic manner, however this is not the case for every master event (e.g. master event 100, Figure 4.5(e)). However, very little difference is seen in the amplitude spectra (Figure 4.5). All of the low frequency master events have a dominant spectral peak at 2.1 Hz, suggesting a fundamental similarity between waveforms. A secondary spectral peak can be seen at 3.8 Hz (Figure 4.5). Variations in the amount of energy distributed from 1-5 Hz varies amongst master event waveforms, although not significantly.

Some differences are evident in the duration and timings of swarms of each master event in relation to the dome collapse on the 25 June (Figure 4.6). In particular, only three master events appear within the swarms identified on the 22 June, and these are very short lived. The beginning and ending of each swarm varies only slightly throughout the rest of the sequence

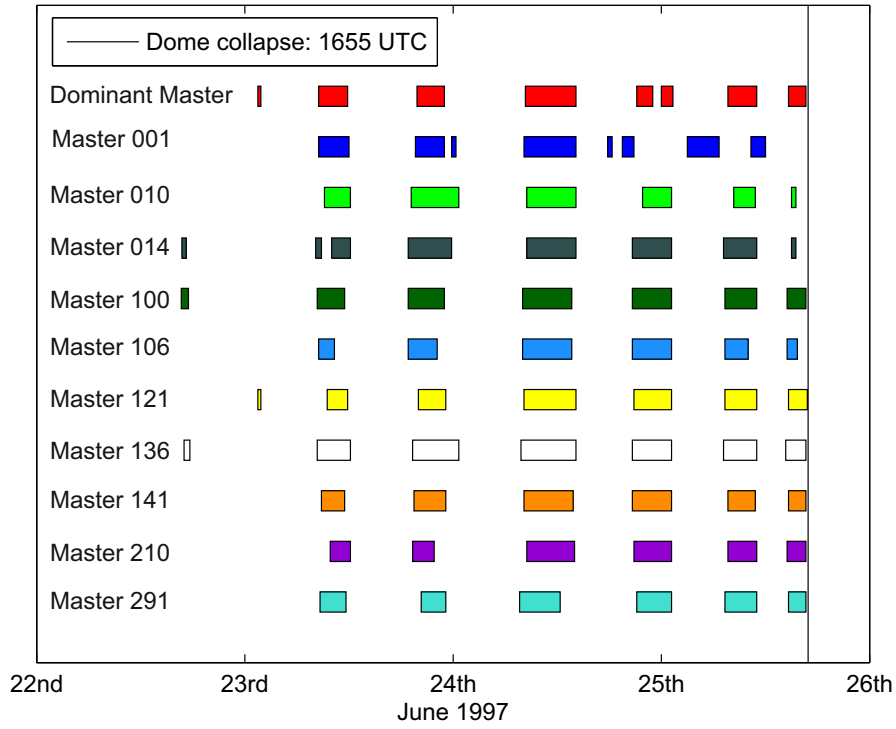

Figure 4.6: Comparison of the timing and duration of swarms related to each of the master events identified at station MBLG. The timing of the dome collapse is represented by the vertical line on the 25 June 1997. The y axis is only an indication of each of the families present separated in space for the purpose of clarity on the plot and does not represent time or dominance, each master event is simply drawn below the last so that all can be compared. Each coloured rectangular box represents the times when the master event was active during the 22 - 25 June analysis period.

from the 23 - 25 June. Since MBLG was destroyed by volcanic activity associated with the dome collapse at 16:55 UTC (Luckett, 2005), no swarms are able to be identified past this (vertical line in Figure 4.6). Each of the multiplet families are persistent across each of the six swarms which occur from the 23 June onwards, suggesting that sources at the same locations are being reactivated by the same process during this time, as was also concluded by Green and Neuberg (2006). Besides master events 010, 014 and 106, all other master events appear within swarms which are active right up to the dome collapse (Figure 4.6).

Unlike Stephens and Chouet (2001), Umakoshi et al. (2003) and Petersen (2007) the waveforms within the multiplet families observed at SHV in 1997 do not appear to significantly evolve with time, since clustering of events is not seen along the diagonal in Figure 4.4 (Caplan-Auerbach and Petersen, 2005) and each swarm appears to contain similar waveforms with limited evolution in the cross correlation coefficient with time (Figure 4.7). This suggests the waveforms are stable and persistent and therefore the trigger location and source process must

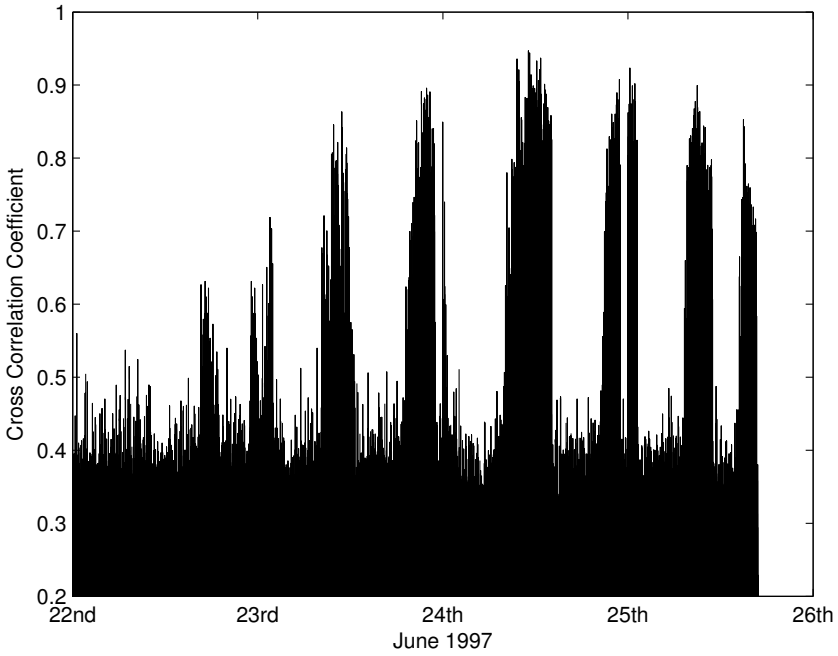

Figure 4.7: The evolution of the cross correlation coefficient with time: 22 to 25 June 1997 with the Dominant master event, station MBLG. The dome collapse occurred at the time when the seismometer stopped transmitting, as it was overrun by a pyroclastic flow. The swarms of similar seismic events are clearly demonstrated.

also be. The cross correlation coefficient can vary by up to 0.25 within each swarm, however the difference between the maximum and minimum mean cross correlation coefficient for each swarm as determined by the 11 master events only varies by ≤ 0.06, suggesting limited evolution in the waveforms.

The identification of multiplets within these swarms echo the conclusions of Green and Neuberg (2006) and Petersen (2007) that a stable source process and location must be present in generating these events, and therefore the seismic energy must travel along similar ray paths to the seismometer. This suggests that very highly correlated events can be found over sustained periods of time (hours) and indicates very little change in the source conditions over this period (Caplan-Auerbach and Petersen, 2005). Since the multiplets are repeated in swarms over a number of days, the source mechanism must be non-destructive and the trigger mechanism must be able to recharge quickly, since successive similar events occur in the continuous seismic record within seconds of one another. The identification of eleven families of multiplets each with their own waveform characteristics (Figure 4.5), suggests that a number of source mechanisms or resonating bodies must have been active at SHV in June 1997. This re-

flects the diversity of sources and physical processes which act simultaneously at SHV. Unlike Green and Neuberg (2006), no one multiplet family was more active than any other, although the families identified with Master Event 121 and 136 contained the most seismic events. This suggest that each of the source mechanisms were sustained for the duration of the precursory sequence, as can be seen in Figure 4.6.

Using the quarter wavelength hypothesis of Geller and Mueller (1980), the repeating multiplets must occur within a maximum distance of $\approx$ 300 m from one another, assuming a dominant frequency of 2.1 Hz and an average P wave velocity of 2500 ms^{-1} in the dome region as described by the current MVO velocity model for SHV. Paulatto et al. (2010), however, suggested that the upper 2.5 km of the dome at SHV could have a P wave velocity as low as 1510 ms^{-1}, therefore transforming the maximum distance between the sources to $\approx$ 178 m. Furthermore, since this hypothesis is only really applicable for general seismic body waves, Neuberg et al. (2006) have suggested that in order for low frequency events to be similar, the source location within a heterogeneous volcanic environment may vary by as little as one tenth of the wavelength. This suggests that each of the low frequency families could be located within $\approx$ 120 m (using the MVO velocity model) or $\approx$ 72 m (using the model of Paulatto et al. (2010)) of one another. This is in good agreement with De Angelis and Henton (2011) who located multiplets from this time period to a compact volume with a radius of approximately 100 m, at depths of 1100-1300 m below the dome summit.

4.2.1 Forecasting using families of LF seismicity

As detailed in Section 3.4.3, a clear acceleration in seismicity can be seen when the average event rate is taken for each swarm in a succession (e.g. Figure 4.8) as has been previously shown by Hammer and Neuberg (2009), rather than simply using the number of events within a given time period (Section 3.4.2). Using identified events from the automated triggered system at MVO, Figure 4.8a shows an initial acceleration in the average number of events per 10 minutes across swarms, although the trace of the least squares fitted curve suggests a slowing of the acceleration up to the point of dome collapse. Figure 4.8b shows the acceleration of swarms which have been identified using the dominant master event. Further classification of the low frequency seismic events into families appears to tighten the least squares fit and lead to a more convincing accelerating pattern of average number of events within 10 minutes of each

swarm. This is further verified in Figure 4.8c, 4.8d and 4.8e which all show an acceleration in the average event rate with time up until the dome collapse, using master events 121, 136 and 141 respectively.

Figure 4.9 represents the application of the FFM to each of the accelerating event rates identified in Figure 4.8. α was assumed to equal 2 so that graphical extrapolation to the forecasted timing of collapse was a simple linear regression. Inverse event rate trends were identified if at least three consecutive swarms formed an inverse trend. This was to try and eliminate spurious trends since a single decrease in the swarm event rate may be due to external factors, for example such as an increase in noise which obscures the number of events determined. Table 4.2 shows the results from the same analysis with all identified master events. When using triggered event data, although the timing of the forecasted dome collapse is within two hours of the known failure time, the fit of the linear regression (the FFM) to the data is poor. R^2 values of less than 0.65 are considered to represent a poor relationship between the observed data and the fitted FFM model.

The forecasted timing of the dome collapse was never greater than 13 hours away from the known timing of collapse when using the cross correlation technique first to identify similar events, and in most cases the collapse was forecasted early (Table 4.2). Despite increasing the difference between the known and forecasted failure times, further classification of multiplets into families consistently allows for a better fit of the linear regression to the data, as can be seen from the high R^2 values.

Since seven out of eleven master events identified had R^2 values of greater than 0.7, it can be assumed that the FFM is appropriate for this data set. The R^2 value for the dominant master is slightly lower at 0.69, however this still demonstrates a good fit between the model and the observations. Significantly, the R^2 value for using the FFM with all triggered low frequency result gives a value of 0.63, which is deemed to not be a good fit. This is confirmed by the wide discrepancy between the observed event rates and the theoretical application of the FFM (shown in Figure 4.9a).

Using amplitude as the geophysical parameter (Ω) in the FFM (RSAM) does not show an accelerating pattern up to the dome collapse (Figure 4.10a). Knowing that there is a much

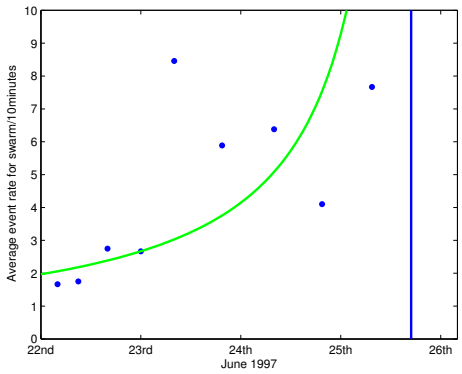

(a) All triggered low frequency seismicity

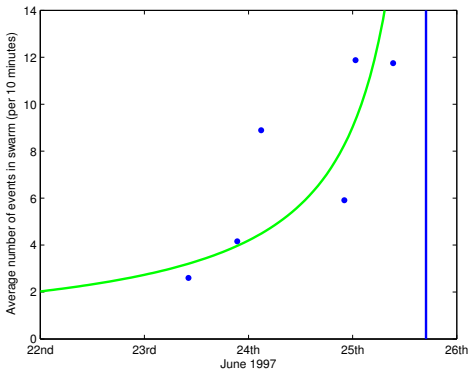

(b) Dominant master event

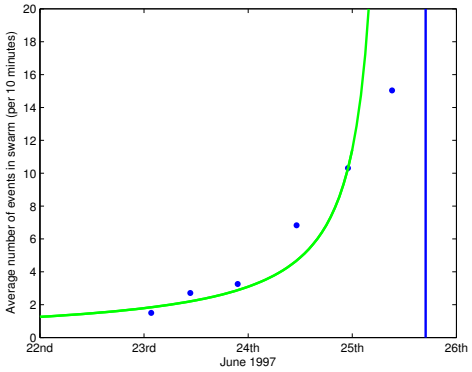

(c) Master event 121

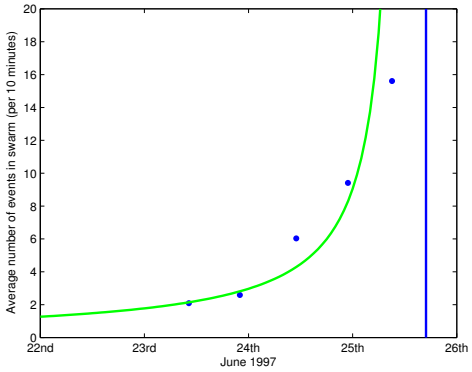

(d) Master event 136

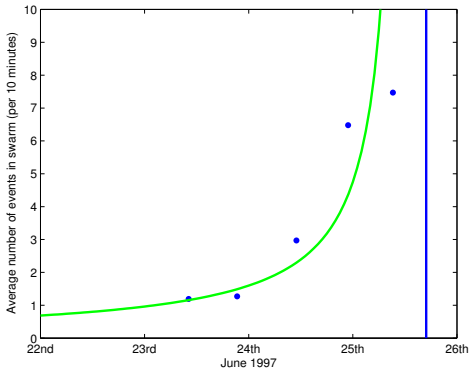

(e) Master event 141

Figure 4.8: The average event rate per 10 minutes within swarms from 22 - 25 June 1997 at station MBLG. Each data point represents the average event rate for each individual swarm. The vertical line represents the known timing of dome collapse on the 25 June 1997 at 16:55 UTC. The acceleration of these events is depicted with the curve.

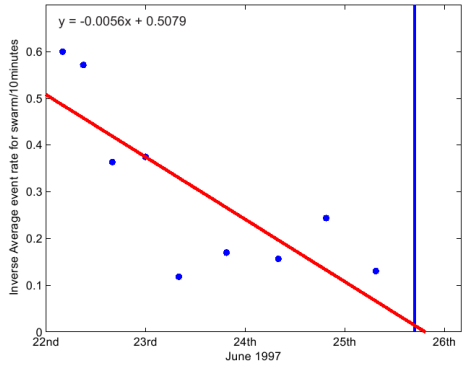

(a) All triggered low frequency seismicity

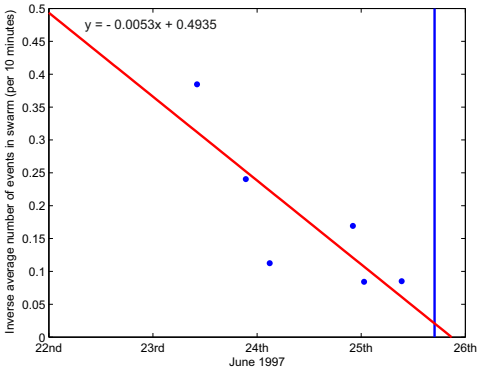

(b) Dominant master event

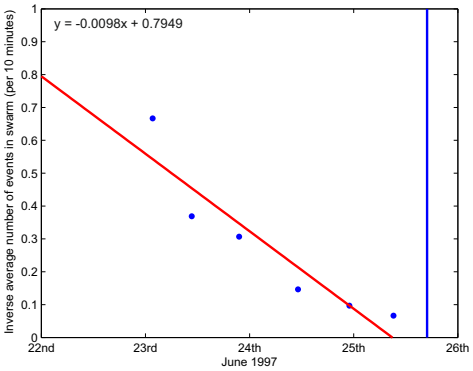

(c) Master event 121

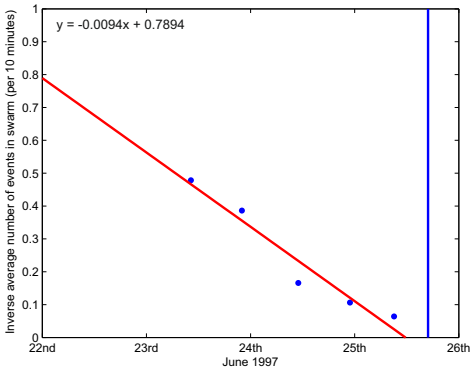

(d) Master event 136

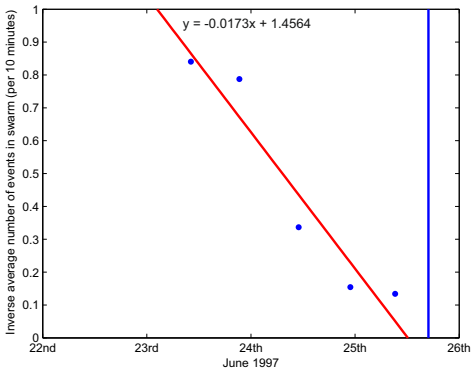

(e) Master event 141

Figure 4.9: Application of the FFM: the inverse average event rate per 10 minutes within swarms from 22 - 25 June 1997 at station MBLG. Each data point represents the inverse average event rate for each individual swarm. The vertical line represents the known timing of dome collapse on the 25 June 1997 at 16:55 UTC. The graphical representation of the FFM is depicted by the linear regression (it is assumed that $\alpha = 2$) and the forecasted timing of failure can be read off the x-axis at the point where the linear regression crosses it.

Event	Known Timing (HH:MM)	Forecasted Timing (HH:MM)	Difference (HH:MM)	Forecasted early/late	R^2
Triggered Low frequency	88:55	91:24	02:29	Late	0.63
Dominant Master	88:55	92:50	03:55	Late	0.69
Master Event 001	88:55	95:12	06:17	Late	0.73
Master Event 010	88:55	n/a	n/a	n/a	n/a
Master Event 014	88:55	77:56	10:59	Early	0.60
Master Event 100	88:55	82:29	06:26	Early	0.86
Master Event 106	88:55	85:58	02:57	Early	0.59
Master Event 121	88:55	80:54	08:01	Early	0.87
Master Event 136	88:55	83:43	05:12	Early	0.94
Master Event 141	88:55	84:10	04:45	Early	0.92
Master Event 210	88:55	82:48	06:07	Early	0.84
Master Event 291	88:55	75:55	13:00	Early	0.83

Table 4.2: Timings of forecasted failure. Timings (known, forecasted and difference) are depicted in hours and minutes. The R^2 value, as defined in the text, ranges from 0 to 1 and is the a scale of how well the model (FFM) can explain the data (event rate). Besides master events 014 and 106, each of the forecasts which were forecasted early using the FFM and a separate master event have a higher R^2 value than those who were forecasted late, or when using all low frequency seismicity. Only master event 010 was unable to be used in analysis using the FFM since no acceleration in the event rate per swarm was identified. The R^2 value for all triggered low frequency seismicity suggests that the FFM is inappropriate to describe the inverse event rates seen, since the linear regression does not fit well to the data.

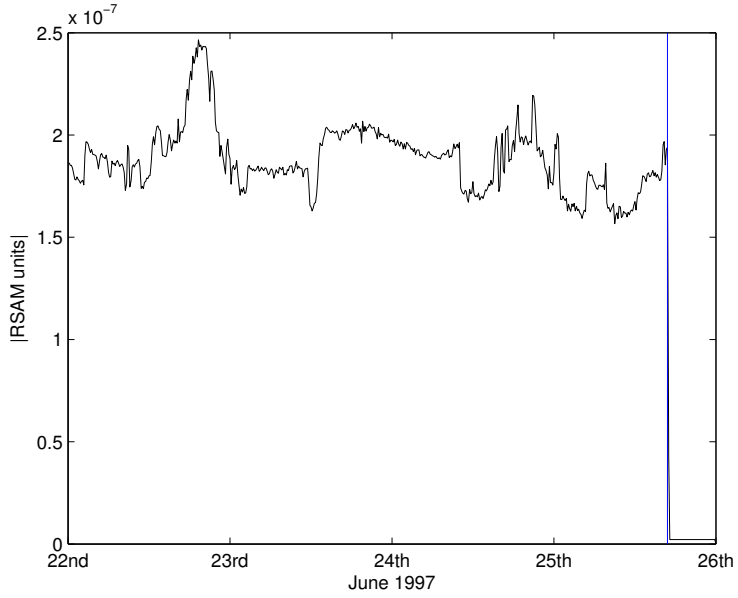

(a) RSAM for raw seismic data over the investigated period

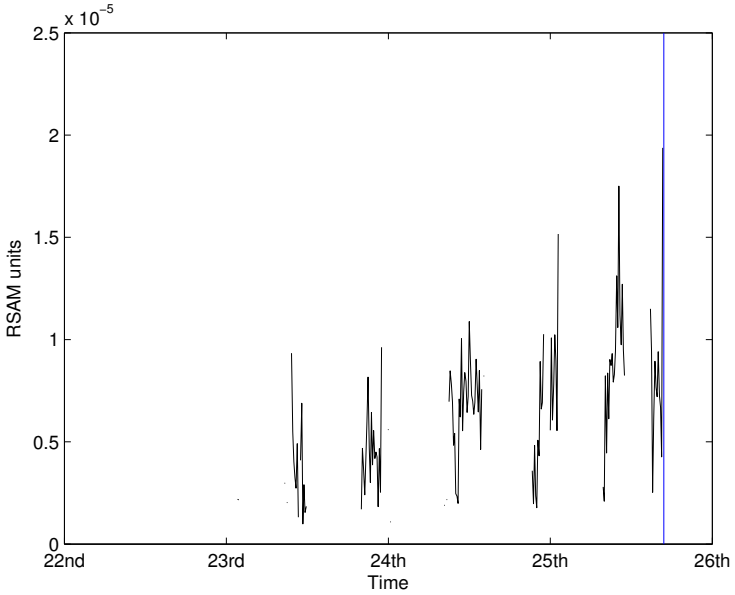

(b) RSAM for periods when the cross correlation coefficient with the Dominant Master event exceeded 0.7

Figure 4.10: RSAM for station MBLG from 22 - 25 June 1997. RSAM units are m/s. The vertical line on the 25 June represents the known timing of the dome collapse. Average amplitudes were calculated within 10 minute bins.

clearer acceleration in the seismicity when the data is separated into swarms of similar seismic events rather than taking only the raw seismic data (continuous or triggered), the RSAM calculation is performed on seismic data which only contained similar events (had a cross correlation coefficient of greater than 0.7) (Figure 4.10b). In order to do this, the continuous seismic data was separated into time periods where cross correlation coefficients were greater than 0.7 or less than this, and then the RSAM calculation was run only on the continuous data which contained similar events. Figure 4.10b suggests that there could be an acceleration trend in the maximum RSAM value within each of the well defined swarms, however it is not clear enough to rely upon as a forecasting tool since in real time it would require the entire swarm to have commenced before gaining this maximum value.

4.3 8th-12th July 2003

Using parameters identified in Section 3.4.1, a total of 520 events were identified from the continuous seismic record at station MBLG from 8 to 12 July 2003. In comparison, the total number of multiplets identified for the same time period was 2241 events, representing a four fold increase in the number of seismic events identified. However, unlike the multiplets identified in June 1997 (see Section 4.2) only one family of events could be identified since all of the similar events appear clustered together (Figure 4.11). A total of 79 events were stacked to create an average master event, shown in Figure 4.13, all of which had a cross correlation coefficient of above 0.7 to maintain a high signal to noise ratio and consequently pick the most similar events for use in the forecast. Ottemöller (2008) also identified one single dominant family of events during a similar time period from 00:00 on 9 July to 12:00 on 12 July, however suggests that a total of 7100 events could be identified. The large difference in the number of identified events from the cross correlation technique is put down to the fact that Ottemöller (2008) used a much lower cross correlation coefficient to identify events ranging from 0.6 to 0.66, whereas the event identified in this study consistently used a cross correlation coefficient threshold of 0.7 (Figure 4.12, and Section 4.1.1).

The dominant waveform has an emergent onset and it is difficult to pick out significant seismic phases (Figure 4.13). Unlike the low frequency seismicity identified in June 1997, the coda of the waveform does not decay in a smooth manner. It is evident that the peak energy is centred at approximately 4 Hz, in comparison to the June 1997 events which all had a dom-

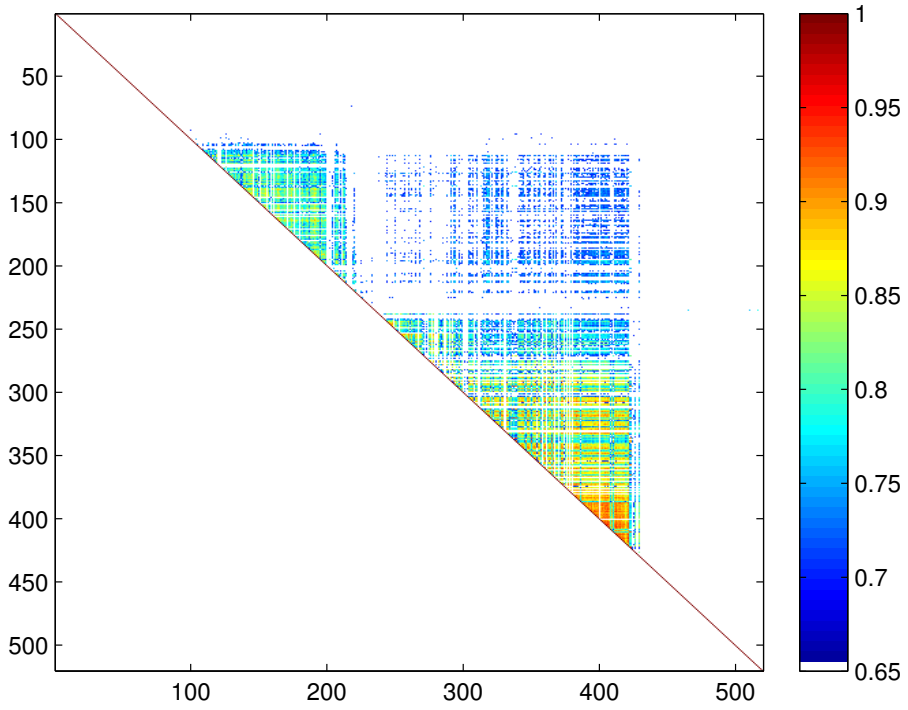

Figure 4.11: The maximum cross correlation similarity matrix from station MBLG for events identified from 8 to 12 July 2003. A total of 520 events were identified within this time period using an STA/LTA algorithm and are represented from 1 to 520 along the x and y axis. Each row of the matrix therefore represents one triggered event compared to every other triggered event. Only events with a cross correlation coefficient above 0.7 are shown on the colour spectrum and are deemed to be similar. The autocorrelation of each triggered event with itself (cross correlation coefficient equal to 1) is represented on the diagonal.

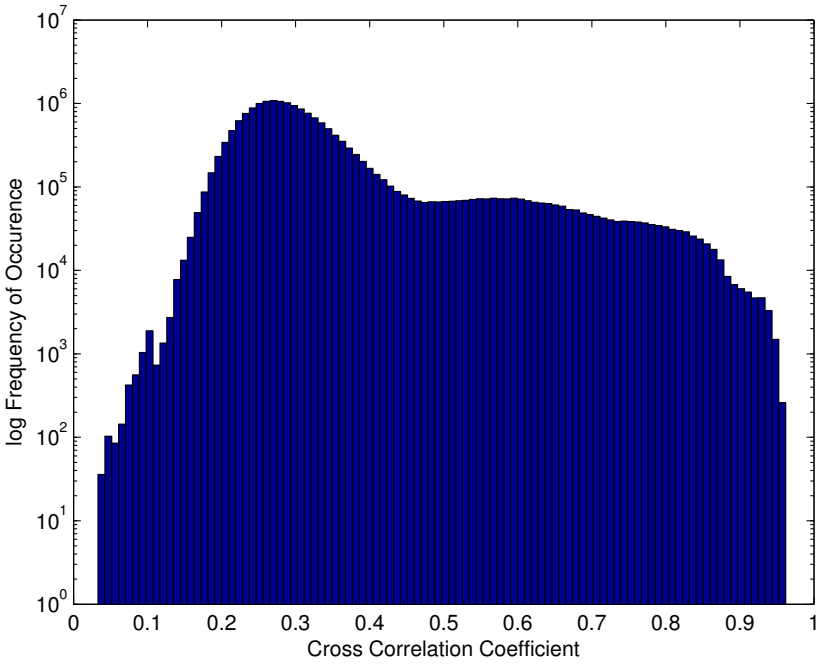

Figure 4.12: The distribution of cross correlation coefficients from 8 to 12 July 2003 at station MBLG when correlated with the dominant master event identified during this time period. At the point where the cross correlation coefficients deviate from a normal distribution curve is considered to be an ideal threshold limit to identify similar events, approximately 0.7 in this example.

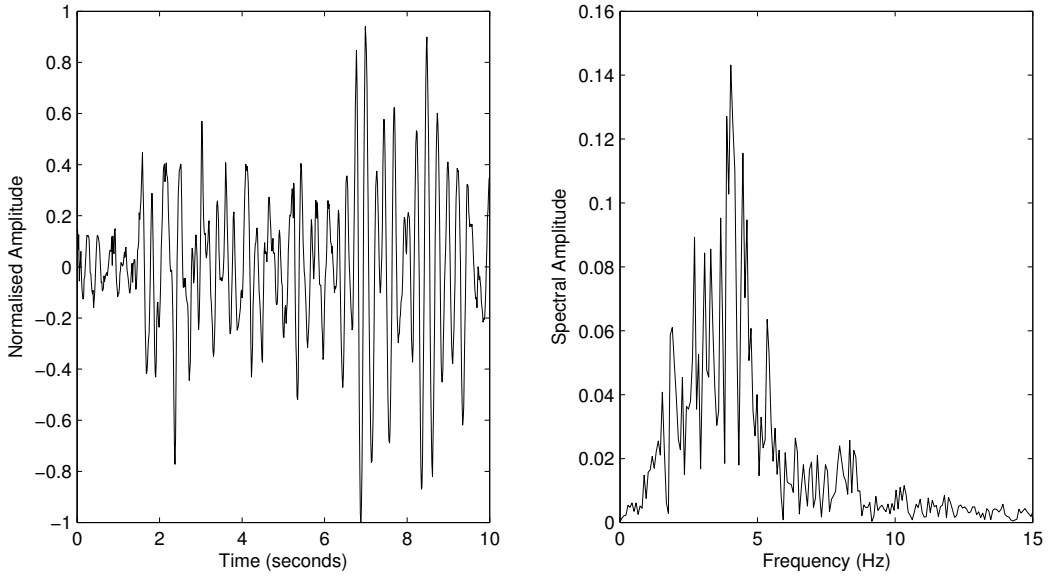

Figure 4.13: *Left*: Dominant master waveform identified by stacking similar events (cross correlation coefficient greater than 0.7) from 8 to 12 July 2003 at station MBLG. A total of 79 events were used in the stack to create the average Master event waveform. *Right*: Single sided amplitude spectrum of the dominant master waveform.

inant frequency of approximately 2.1 Hz, however it is distributed across 0 Hz to 5 Hz band. Contrary to Petersen (2007) who suggested that some multiplets can be active over a number of years, there are no similarities between the events identified in June 1997 and the dominant master event identified in July 2003, pointing to an evolving system over this time period.

Again, using the quarter wavelength hypothesis of Geller and Mueller (1980), the repeating seismicity must occur within a maximum source distance of ≈ 155 m, assuming a dominant frequency of 4.03 Hz and an average P wave velocity in the dome region of $2500\mathrm{ms}^{-1}$ using the current MVO velocity model. Following Paulatto et al. (2010), the distance between the sources is reduced further to ≈ 95 m. Even smaller distances are obtained if it is assumed that the quarter wavelength hypothesis is only valid for general seismic body waves, and that in volcanic environments the source location to produce similar low frequency seismic events may be as small as one tenth of a wavelength (Neuberg et al., 2006). This is in good agreement with Ottemöller (2008) who suggested the similar events from the precursory activity from 9 to 12 July were generated within a radius of less than 100 m, at approximately 1300 m below the dome.

Figure 4.14 suggests a clear evolution of the cross correlation coefficient with time. One possible explanation is the fact that the dominant master waveform event was identified on 11 July 2003 from the triggered seismic data since a large number of similar events occurred on this day. Therefore this may be an artefact of processing the data when taking an average waveform from events which mostly occurred on one day. However, if this was an artefact then it would not be expected to see a dip in the cross correlation coefficient on 11 July as well, as is seen. Since RSAM data suggests no significant changes in amplitudes of the seismic events with time (Section 3.2.2), it is thought that this therefore represents a slightly migrating source location. The events with a relatively lower cross correlation coefficient on the 9 and 10 July occurred further away from the dominant master event location, than those on 11 July. Perhaps more significantly, it should be noted that the similar seismic waveforms appear to stop in the hours prior to the dome collapse (vertical line in Figure 4.14), although a large amount of data is missing from this time period so it is not possible to tell the exact timing of the change from very similar events to non-similar events. This is significant because it may represent a time delay function between events occurring at depth and those at the surface as first envisaged by Voight (1988).

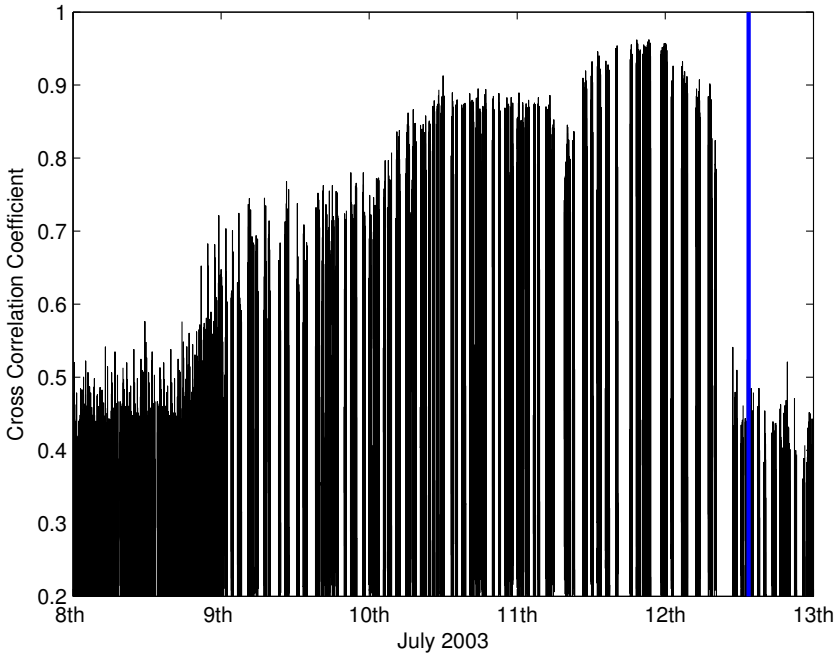

Figure 4.14: The evolution of the cross correlation coefficient with time: July 2003 with the Dominant Master Event, station MBLG. The dome collapse occurred at the time of the vertical line (13:30 on 12 July 2003). The gaps in the data represent gaps in the seismometer recordings rather than a dip in the cross correlation coefficient.

4.3.1 Forecasting using families of LF seismicity

Seismicity prior to the dome collapse in July 2003 did not take the form of well defined swarms, as occurred in June 1997. Instead, as suggested in Figure 3.8, seismicity is pulsatory which was further highlighted by many data gaps for MBLG, and therefore what appears pulsatory may in fact be continuous. In addition, Figure 4.14 suggests that the cross correlation coefficient is constantly evolving, with highly similar events occurring throughout the precursory sequence and no evidence of an acceleration in the event rate. However "swarms" of events were identified in the triggered incoming seismicity as recorded by MVO in near real time (STA/LTA parameters unknown) and therefore the timings of these swarms were used with the FFM as a forecasting tool.

A clear acceleration can be seen in the swarms which occurred from the 10 to 12 July 2003 (Figure 4.15), followed by a slight deceleration in the event rate for the final swarm before the dome collapse (vertical line). Application of the FFM to all swarms identified (i.e. if the forecast was made on 12 July 2003 after the last swarm had ended) then the forecasted timing of collapse would be on 14 July 2003 at approximately 15:00 h. However, the confidence in

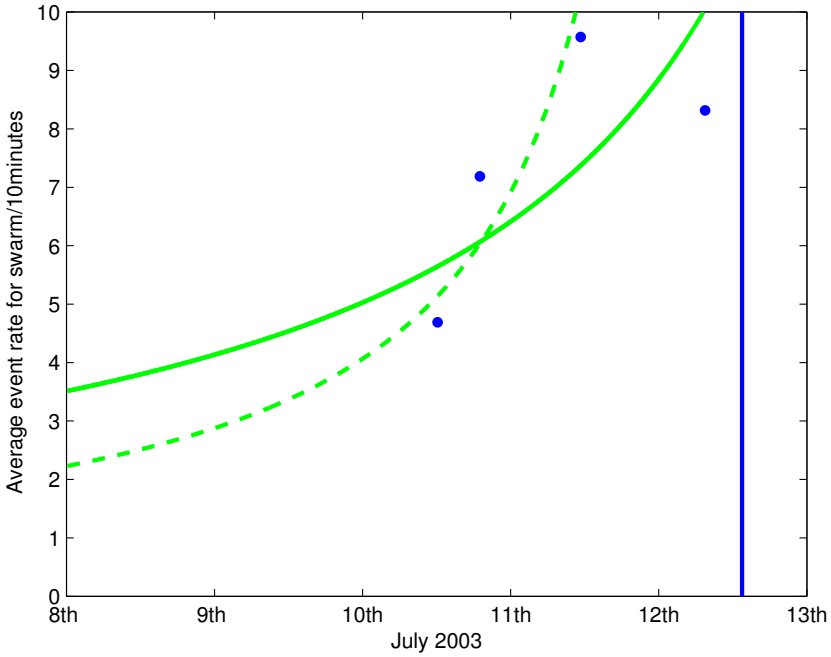

Figure 4.15: The average event rate per 10 minutes within swarms from 10 to 13 July 2003, station MBLG. Each data point therefore represents the average event rate for each individual swarm. The vertical line represents the known timing of dome collapse on the 12 July 2003 at 13:30. The acceleration of all swarms is depicted with the solid curve and only the accelerating swarms by the dotted curve.

the forecast would be low, with an R^2 value of 0.51. However, if only the first three swarms are used (i.e. only those swarms which exhibit an acceleration) then a forecast is made for 12 July at approximately 10:12 (dotted line in Figure 4.16), just over 3 hours before the known timing of failure at 13:30 on 12 July. A greater amount of confidence can also be placed on this forecast, since the R^2 value is 0.82, suggesting a significant relationship between the observed data points (event rate in each swarm) and the model (FFM).

4.4 8th-11th February 2010

Figures 3.11 and 3.12 suggest a clear cyclicity in seismicity in February 2010, which is unaffected by two small Vulcanian explosions in the days prior to the dome collapse. However, Figure 3.13 suggests that very little low frequency seismicity was occurring during the precursory phase. Stinton et al. (2014) also reported very little precursory seismic activity before the dome collapse. Figure 4.17 shows the most common waveform identified from the STA/LTA algorithm using the original parameters (Section 3.4.1). This was, however, discarded since it did not resemble a true seismic event.

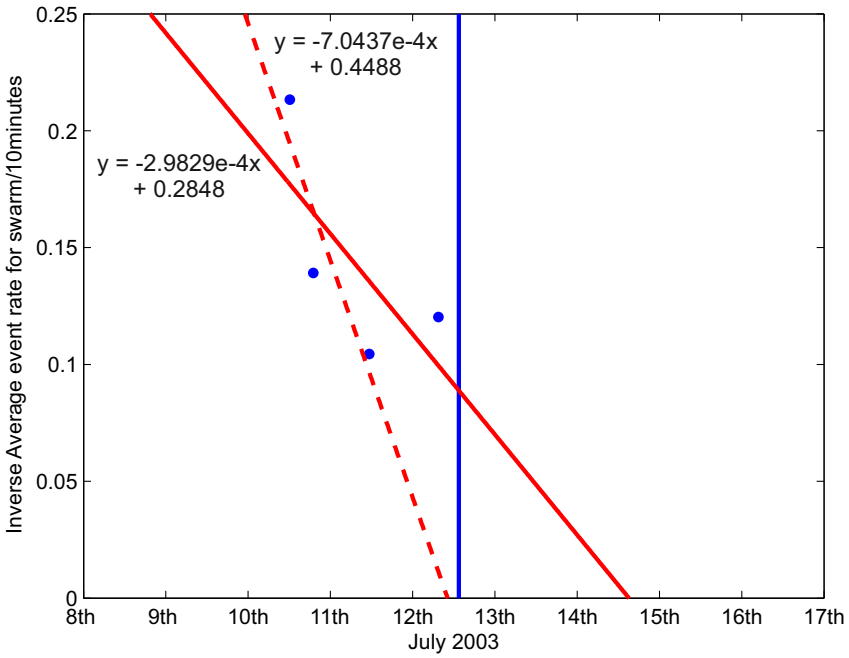

Figure 4.16: Application of the FFM: the inverse average event rate per 10 minutes within swarms from 10 to 13 July 2003, station MBLG. Each data point therefore represents the inverse average event rate for each individual swarm. The vertical line represents the known timing of dome collapse on the 12 July 2003 at 13:30. The graphical representation of the FFM is depicted by the linear regression (it is assumed that $\alpha = 2$) and the forecasted timing of failure can be read off the x-axis at the point where the linear regression crosses it. The solid regression includes data from all swarms; the dotted regression is only the swarms which were accelerating.

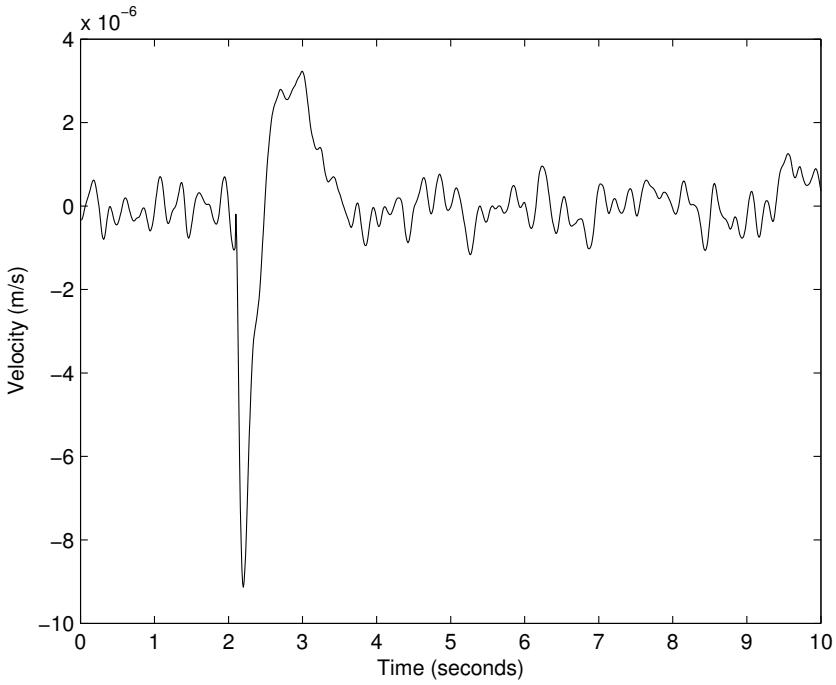

Figure 4.17: Most common waveform identified in February 2010 with original STA/LTA parameters (see Section 3.4.1 for further details of parameters used), station MBLG.

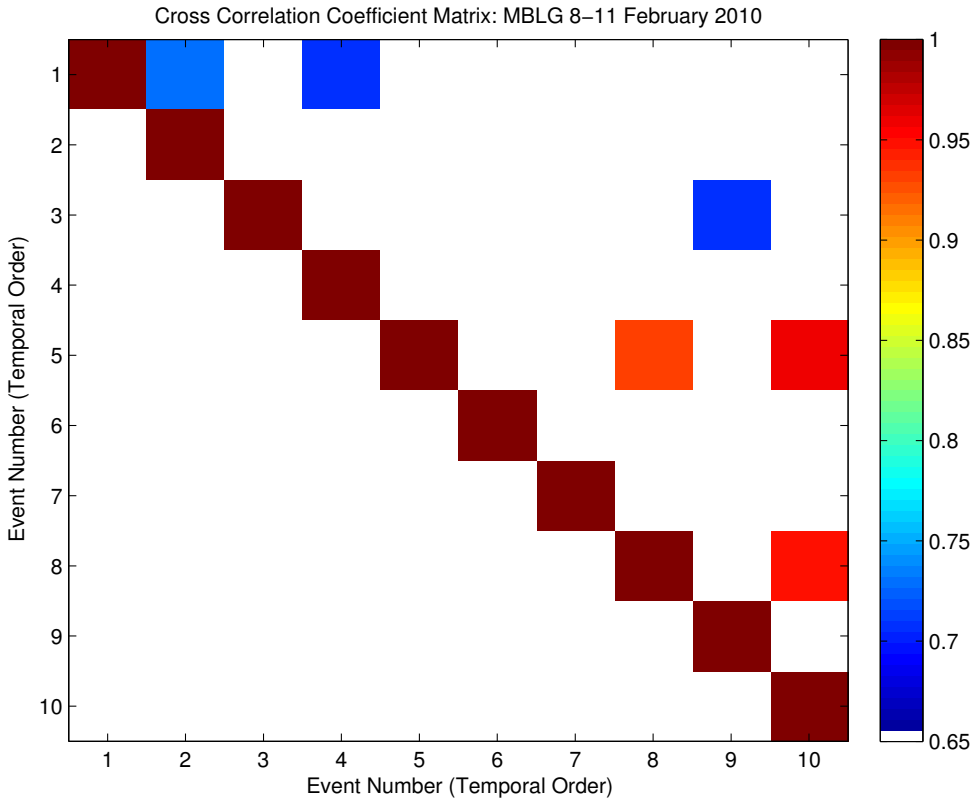

Figure 4.18: The maximum cross correlation similarity matrix from station MBLG for true seismic events identified on 11 February 2010. A total of 10 events were identified within this time period using an STA/LTA algorithm and are represented from 1 to 10 along the x and y axis. Each row of the matrix therefore represents one triggered event compared to every other triggered event. Only events with a cross correlation coefficient above 0.7 are shown on the colour spectrum and are deemed to be similar. The autocorrelation of each triggered event with itself (cross correlation coefficient equal to 1) is represented on the diagonal.

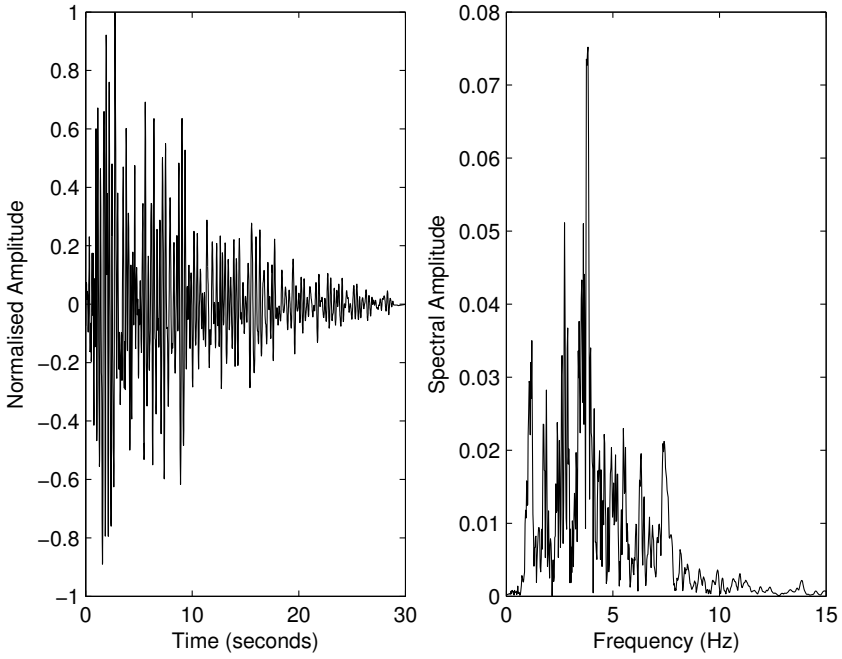

Figure 4.19: *Left*: Dominant master waveform identified by stacking similar events (cross correlation coefficient greater than 0.7) on 11 February 2010. A total of 3 events were used in the stack to create the average Master event waveform. *Right*: Single sided amplitude spectrum of the dominant master waveform.

Changing the STA/LTA parameters from those used to identify events in 1997 and 2003 (Section 3.4.1) resulted in the identification of 10 seismic events on 11 February 2010, of which 3 events were very similar to one another (Figure 4.18). These events were subsequently stacked and a Master waveform produced (Figure 4.19). The master waveform is much longer than the previous master events identified in 1997 and 2003, lasting ≈30 seconds. The distribution of energy is also very different, with energy existing over the ranges of 0 to 10 Hz, suggesting a more hybrid nature to this waveform. Hybrid events have a more prominent onset to the waveform, with a higher proportion of energy concentrated above 2 Hz (the peak frequency of the waveform is 3.83 Hz). However, on Montserrat, hybrid and low frequency earthquakes appear to occur on a continuum, with these two types bestowing the idealised end members (Neuberg et al., 2000). Therefore, although characteristically different to the master events identified prior to the 1997 and 2003 dome collapses, it is assumed that the master event for 2010 is a low frequency type earthquake related to the movement of magma at depth (Chouet, 1988, Neuberg et al., 2000).

Again, using the quarter wavelength hypothesis of Geller and Mueller (1980), the repeating

seismicity must occur within a maximum distance of ≈ 163 m from one another, assuming a dominant frequency of 3.83 Hz and an average P wave velocity in the dome region of 2500 ms^{-1} as described by the current MVO velocity model. Following Paulatto et al. (2010), the distance between sources is reduced further to within ≈ 99 m of one another. Even smaller distances are obtained according to Neuberg et al. (2006); 65 m and 40 m for the MVO and the Paulatto et al. (2010) models respectively.

4.4.1 Forecasting using families of LF seismicity

Despite changing the STA/LTA parameters in order to identify seismic events during the precursory period of 8 to 11 February 2010, no additional seismicity from the continuous seismic data was identified using the cross correlation technique. This not only suggests that there was very little precursory seismicity to the dome collapse, in terms of event counts or identified from accelerations in RSAM which simply appeared cyclic up to the collapse (Figure 3.12), but also suggests that at this time events which were detected were not similar. This is in stark contrast to both the dome collapses of 1997 and 2003 which were dominated by similar seismic events, and which showed an acceleration in seismicity prior to the collapse.

The fact that this collapse was not preceded by low frequency seismicity suggests that the collapse originated in processes unrelated to the movement of magmatic fluid at depth in the few days before the collapse or that this movement was aseismic in nature. Stinton et al. (2014) suggest that the collapse occurred due to over-steepening of the dome and talus which led to a gravitational collapse of the material. In the 4 months prior to the collapse, intensive extrusive and explosive activity had been observed, and since the collapse occurred in a piecemeal fashion over a number of hours, gravitational instability of a large dome is thought to have been a primary driving factor in collapse. Due to the gravitational collapse and removal of material from the dome surface (manifested in a number of small pyroclastic density currents), the conduit and pressurized volcanic system was unroofed, thereby creating a more explosive eruption as it continued. The possibility of this collapse being driven entirely by gravitational collapse shall be further investigated in Section 5.4.2 using Finite Element modelling.

4.5 The role of α

α in Equation 1.1 expresses the power law relationship between the rate of change of a geophysical precursor and its acceleration with time, and is therefore an important parameter describing the precursory sequence. Previous applications of the FFM to seismic data from Montserrat, including this research, has assumed that α is equal to 2 since it allows for a simple linear regression to be placed through the inverse event rate to determine a time of failure. However, although offering a simple solution for determining the timing of failure, the validity of assuming α is equal to 2 is questionable. In particular, it is often obvious that setting α to 2 results in poor correlation between data points and the plotted regression (e.g. Figure 3.20). Voight (1988) and Cornelius and Voight (1995) suggest that α lies between 1 and 2 (although typically closer to 2), and is constant for the entirety of the precursory sequence. Kilburn (2003) however has suggested that α may evolve with time from 1 towards 2 as the dominant mechanism for generating the precursory signals changes due to the dynamic and ever evolving nature of the volcanic system. When crack nucleation and initiation is the dominant process at depth generating VT seismicity, α is closer to one. However with time and as the dominant process changes from crack nucleation to crack growth and extension due to an increased density of fractures within the network, α evolves towards 2, eventually reaching stages of uncontrolled propagation and therefore failure. Furthermore, recent analysis of the VT precursory seismicity of the 1991 Pinatubo eruption suggest that α may take values of up to 3.3 ± 1.3 (Smith and Kilburn, 2010), although this appears to be an extreme value, with all other α values calculated for this eruption remaining between 1 and 2.4. Note that in these cases, the FFM was applied to VT events and therefore to the initial generation of a connection between a magma reservoir and the surface, whilst in this study it is employed to analyse low frequency events during an eruptive episode, which assumes that a connective pathway is already present.

A number of methods can be used to determine α, extensively outlined in Cornelius and Voight (1995), however the preferred method is through the optimization of α, K and the timing of the eruption, since all of these are unknown *a priori*. This can either be done graphically or through an iterative procedure to determine the constants (e.g. Cornelius and Voight (1995), Smith et al. (2007b), Boué et al. (2015)). Integration of the original formulation of the FFM proposed by Voight (1988) (Equation 1.1) means that it is possible to describe the power-law

evolution of the rate of an accelerating precursor $\frac{d\Omega}{dt}$ with time (t) such that:

$$\frac{d\Omega}{dt} = \left(K(1-\alpha)(t-t_0) + \left(\frac{d\Omega}{dt}\right)_0^{1-\alpha} \right)^{\frac{1}{1-\alpha}} \tag{4.2}$$

where t_0 is time zero of the accelerating precursor and $\left(\frac{d\Omega}{dt}\right)_0$ is the rate of the precursory sequence at time zero under the circumstances where $K>0$ and $\alpha>1$. The position of the asymptote of function $\frac{d\Omega}{dt}(t)$ is therefore:

$$t_f = -\frac{\left(\frac{d\Omega}{dt}\right)_0^{1-\alpha}}{K(1-\alpha)} + t_0 \tag{4.3}$$

with t_f being interpreted as the eruption time, or the time of failure. A combination of Equations 4.2 and 4.3 allows the calculation of the failure time (t_f) as a direct result of the rate of the accelerating precursory activity ($\frac{d\Omega}{dt}$):

$$\frac{d\Omega}{dt}(t) = k\left(1 - \frac{t}{t_f}\right)^{\frac{1}{\alpha-1}} \tag{4.4}$$

where k is a constant dependent upon the dimensions of $\frac{d\Omega}{dt}$. Consequently, given a precursory sequence of data, it is possible to optimize all three of these parameters for a least square criterion fit between the data and the model investigated (Boué et al., 2015).

An investigation into the possibility of α evolving with time was carried out for data prior to the 1997 dome collapse using Equation 4.4. k was allowed to vary between 0.1 and 15, α between 1 and 2.5 (Voight, 1988, Kilburn, 2003, Smith et al., 2007b, Boué et al., 2015) and the timing of the collapse (t_f) between time zero (i.e. the beginning of the precursory sequence) to 27 hours past the known timing of the collapse (i.e. to $\approx 14:00$ on 26th June 1997). Table 4.3 clearly shows that the use of a linear regression (assuming α = 2) should not be applicable to this data, since α does not approach this value for any of this analysis. A migration in α is perhaps seen between swarms 2 and 4, however beyond this α appears to revert to close to 1. The value of 1.001 is the lower limit of α that could be determined from this analysis and therefore must be viewed with caution.

If this method is used to determine α, k and t_f using the average event rate for each swarm identified using the dominant master event (i.e. using the data points in Figures 4.8b and 4.9b), α is equal to 1.046 and the failure time is forecast on the 22 June 1997 (Table 4.3, row 8). In

Time Series	**Number of data points used in calculation**	**Forecasted Failure Time (minutes from 00:00 22 June)**	**Time between forecasted and known failure time (minutes)**	**k**	**Alpha**
Swarm 2	19	473	4857	0.1	1.001
Swarm 3	18	1496	3839	0.1	1.126
Swarm 4	34	2499	2836	0.1	1.362
Swarm 5	10	1898	3437	0.1	1.001
Swarm 6	7	1992	3343	0.1	1.001
Swarm 7	19	2384	2946	0.1	1.001
Average Swarm Rates	6	1284	4051	0.1	1.046
All values from all swarms	107	6957	1622	0.1	1.050
Average Swarm Rates	6	5335	n/a	2.3	1.4650
All values from all swarms	107	5335	n/a	0.1	1.077

Table 4.3: Determination of key parameters in the FFM: α, k and failure time based on LF precursory seismicity identified prior to the dome collapse on 25 June 1997. The precursory seismicity is counts of events which are all similar to one another (Dominant Master event). Each swarm is analysed individually, as well as all together. Swarm 1 contained no similar events and therefore was omitted from analysis. The number of points is the number of values used in the calculation to determine the accelerating nature of the precursory seismicity. The known timing of the collapse was $\approx$ 16:55, 25 June 1997 (or at 5335 minutes after 00:00 22 June 1997). The bottom two rows (separated by a number of lines) are the determination of α and k, whilst setting t_f to the known time of failure.

comparison, fixing α to equal 2 results in a forecasted failure time of less than 4 hours away from the known timing of failure (Table 4.2). These are very different results and would suggest that caution must be used when generating forecasts using a fixed value for α since it can vary the forecast dramatically. In this case however since only 6 data points are used to determine α (one data point for every swarm identified), α is considerably under constrained, and therefore may have large errors associated with it. This may explain the large discrepancy between the forecasted failure time for the two values of α.

Determining α, k and t_f using the entire precursory sequence from 22 to 25 June 1997 (Table 4.3: All values from all swarms) does not appear to change the value of α significantly compared to using average event rates for each identified swarm. It does however largely alter the forecasted failure time to over 24 hours past the known timing of failure. When t_f is set to the known timing of failure, α and k vary significantly depending on whether the entire precursory sequence of activity is used, or simply the average event rates of each swarm (last two rows of Table 4.3). In either case however, α does not approach two, suggesting that the FFM and its current methodology of assuming α = 2, may not be mathematically correct, despite a number of accurate forecasts with this value.

Overall, when calculating α, k and t_f by optimization of Equation 4.4, it appears that large discrepancies are found between the assumed values of α = 2 and k = 1, and the calculated values. However, the calculated values do not allow for an accurate determination of the failure time, as has been found when using α = 2 for similar seismicity, as well as adding a further complication to the FFM when administering it in real-time. The problem therefore may lie in the assumption of adopting a linear least squares regression to the data to determine the failure time, which is now explored further.

4.6 Alternative parametrization of seismicity

As the FFM follows a least squares regression analysis when α is equal to 2, the residual error between the observed event rate and the mean event rate should follow a typical Gaussian distribution (Bell et al., 2011b). Greenhough and Main (2008) have suggested that since earthquake occurrence is a point process (i.e. each earthquake is a discrete isolated process occurring within a memoryless system, the rate uncertainties are best described by a Poisson distribution.

This was also suggested by Bell et al. (2011a) who determined that the daily earthquake rates at Mauna Loa preceding the 1984 eruption were consistent with a Poisson regime, within 95 per cent confidence limits. In this instance, a generalised linear model (GLM) rather than a least squares regression model may be more appropriate, since it can allow for a distribution of data that is non-Gaussian (Bell et al., 2011b).

The Generalised Linear Model (GLM) uses an iterative technique of weighted linear regression to obtain maximum likelihood estimates of parameters with observations distributed in a non-Gaussian manner (Nelder and Wedderburn, 1972, Bell et al., 2011b). Bell et al. (2011b) showed that use of the GLM for forecasting synthetic and real earthquake sequences (precursory activity to the 1989 Mt Etna eruption) considerably reduced the variances and mean error in comparison to using the standard FFM procedure with a least squares linear regression where α = 2. In this example, a GLM is used to represent a Poisson distribution of data, and therefore represents an exponential acceleration in the swarm event rate (α = 1).

However, although using a GLM as a fitting tool does provide a higher R^2 value for each of the forecasts (always > 0.8), suggesting a GLM is a better fit to the data than a least squares linear regression, it is clear from Figure 4.20 that the forecasted dome collapse in 1997 is consistently late. Moreover, forecasting using a GLM for the July 2003 collapse generated a forecast over a week from the known timing of the collapse when using all of the available data (red line in Figure 4.21). If only the accelerating swarms are used, the forecast is over 72 hours after the known timing of failure. This is in contrast to Bell et al. (2011b) who suggest that the GLM provides more accurate forecasts for the timings of eruptions than the FFM with a linear least squares regression ($\alpha = 2$) since forecasts are consistently further away from the known timing of failure using a GLM (in this case of $\alpha = 1$). Figure 4.20 however does suggest that the timing of the dome collapse in June 1997 may be related to a threshold of an inverse event rate of approximately 0.05 if employing an exponential decay function to the data (GLM with $\alpha = 1$). It is unclear as to whether this is an artefact of the data or the exponential decay, and further investigation into this potential threshold is certainly warranted.

Although the GLM solves the problem of needing to use a model which can account for the appropriate error structure, its use may not be applicable in a volcanic setting (Hammer and Ohrnberger, 2012). Forecasting volcanic eruptions using the FFM and rates of temporal seis-

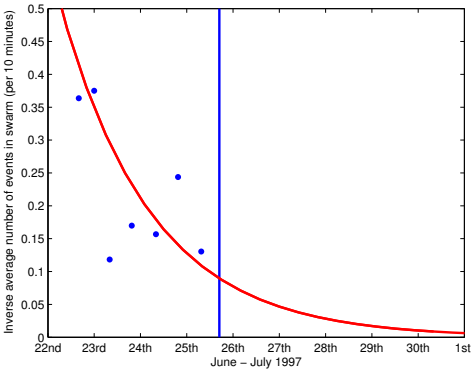

(a) All triggered low frequency seismicity
log(y) = -0.0210x - 0.5476

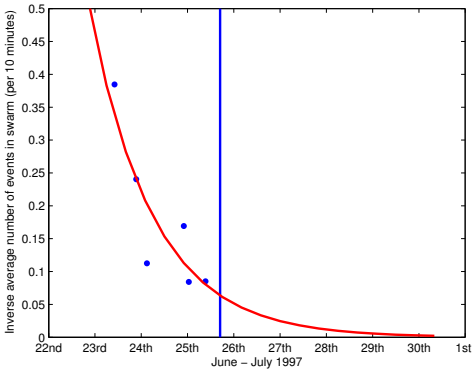

(b) Dominant master event
log(y) = -0.0305x - 0.0451

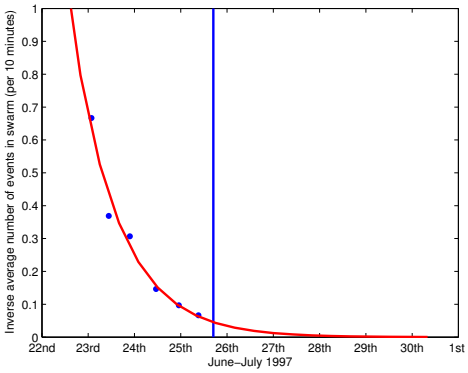

(c) Master event 121
log(y) = -0.0416x + 0.6047

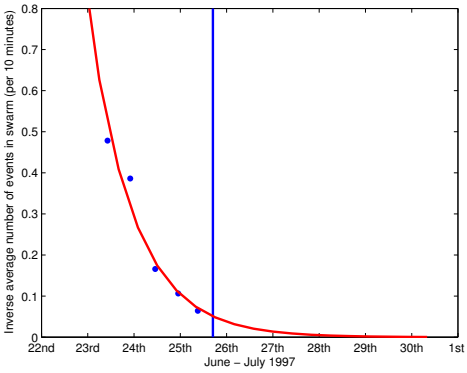

(d) Master event 136
log(y) = -0.0427x + 0.8126

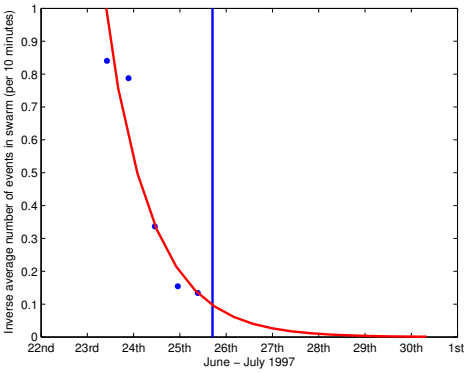

(e) Master event 141
log(y) = -0.0419x + 1.3989

Figure 4.20: Application of a GLM: the inverse average event rate per 10 minutes within swarms from 22 - 25 June 1997, station MBLG. Each data point therefore represents the inverse average event rate for each individual swarm. The vertical line represents the known timing of dome collapse on the 25 June 1997 at 16:55 UTC. The graphical representation of the GLM is depicted by the regression and the forecasted timing of failure can be read off the x-axis at the point where the regression crosses it.

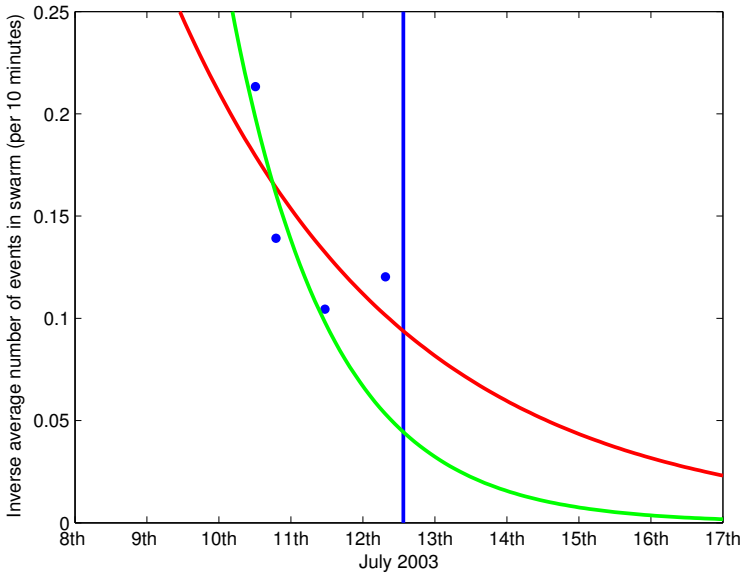

Figure 4.21: Application of a GLM: the inverse average dominant event rate per 10 minutes within swarms from 8 to 17 July 2003, station MBLG. Each data point represents the inverse average event rate for each individual swarm. The vertical line represents the known timing of dome collapse on the 12 July 2003 at 13:30 UTC. The graphical representation of the GLM is depicted by the regression and the forecasted timing of failure can be read off the x-axis at the point where the regression crosses it. The GLM is represented for all of the swarms (red, log(y) = -0.0022x - 0.9269) and only those which show an accelerating nature (green, log(y) = -0.0051x + 0.2042).

micity requires that the system has a memory, and therefore that events which have occurred before can influence the outcome in the future. A poisson process is the exact opposite to this: it requires a memoryless system, in which events evolve independently. This would therefore make the use of the GLM with $\alpha = 1$ and FFM together invalid, since one of the overriding assumptions of the FFM is that previous geophysical observables form the basis of the forecast, and therefore suggesting that the system has a memory. Analysis of a number of dome building eruptions at Mt. St. Helens in 1985 and 1986, which may be comparable to Soufrière Hills volcano, suggested that an exponential model did not adequately explain the precursory trends in earthquake event rates (Bell et al., 2013), possibly implying that an exponential model is not appropriate for forecasting at andesitic dome building volcanoes, which may be one reason as to why the forecasts using a GLM in this instance were not successful.

4.7 Operational Applicability to Volcano Observatories

One fundamental aim of this research is to develop forecasting tools that are applicable to volcano observatories for application in real time. This has partially been successful: the cross

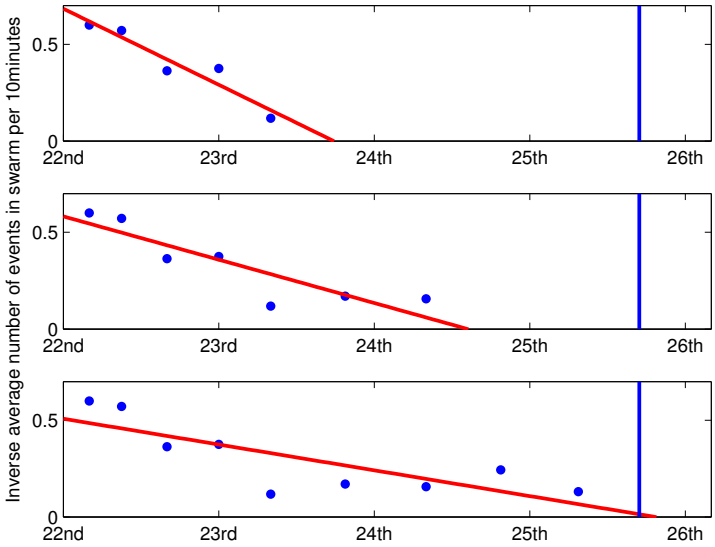

Figure 4.22: Progression of the forecasted failure time for dome collapse on 25 June 1997 using all low frequency seismicity, station MBLG. The dome collapse is marked by the vertical blue line on the 25 June. Each data point represents the average number of events per 10 minutes within identified swarms of activity. A least squares linear regression is placed through the data as described by the FFM (α=2). The forecasted timing of the eruption is the point at which this linear regression meets the x-axis. *Upper*: Forecast made on 23 June at 12:00 noon *Middle*: Forecast made on 24 June at 12:00 noon *Lower*: Forecast made on 25 June at 12:00 noon.

correlation and forecasting codes have been sent to the Instituto Geofisico in Ecuador at the request of the Director, Dr. Mario Ruiz for trial implementation at the volcano observatory in Quito. The intention is to modify the codes to allow the incoming seismicity at a number of monitoring stations to be analysed for similar seismic events, and to use these as a forecasting tool at a few specific volcanoes to test their real time applicability. However, a number of potential problems are foreseen when trying to implement the FFM in real time, fundamentally related to the accuracy of the forecasted failure times and its interpretation.

The concept of forecasting using the FFM in hindsight analysis once the eruption has occurred is common (e.g. Cornelius and Voight (1994), Kilburn and Voight (1998), De la Cruz-Reyna and Reyes-Dávila (2001), Ortiz et al. (2003), Hammer and Neuberg (2009), Smith and Kilburn (2010)). It is much less common to employ and rely upon these tactics during developing unrest as huge responsibility is placed upon generating accurate forecasts which are often simply plagued with too many uncertainties. Hindsight analysis was performed as if in "real time" for the identified dome collapses at Soufrière Hills. It is clear that an increase in the number of data points increases (i.e. as time increases), then the accuracy of the forecast increases (Bell et al., 2013). However, the failure time would not be known in a real situation

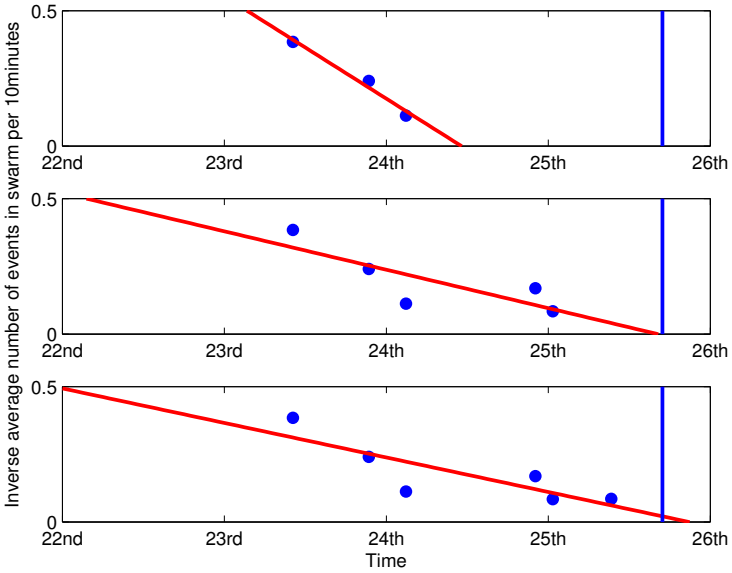

Figure 4.23: Progression of the forecasted failure time for dome collapse on 25 June 1997 using the Dominant Master event to identify seismic events, station MBLG. The dome collapse is marked by the vertical blue line on the 25 June. Each data point represents the average number of events per 10 minutes within identified swarms of activity. A least squares linear regression is placed through the data as described by the FFM (α=2). The forecasted timing of the eruption is the point at which this linear regression meets the x-axis. *Upper*: Forecast made on 24 June at 12:00 noon *Middle*: Forecast made on 25 June at 00:30 am *Lower*: Forecast made on 25 June at 12:00 noon.

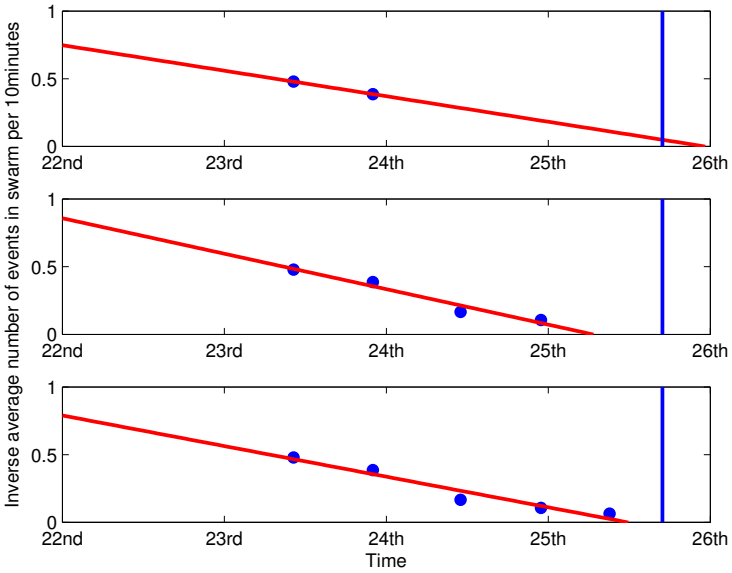

Figure 4.24: Progression of the forecasted failure time for dome collapse on 25 June 1997 using Master event 136 to identify seismic events, station MBLG. The dome collapse is marked by the vertical blue line on the 25 June. Each data point represents the average number of events per 10 minutes within identified swarms of activity. A least squares linear regression is placed through the data as described by the FFM (α=2). The forecasted timing of the eruption is the point at which this linear regression meets the x-axis. *Upper*: Forecast made on 24 June at 12:00 noon *Middle*: Forecast made on 25 June at 00:00 am *Lower*: Forecast made on 25 June at 12:00 noon.

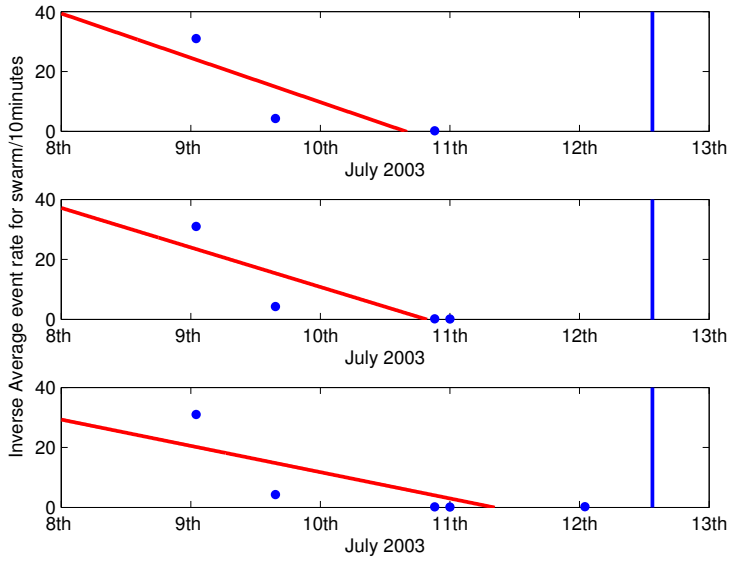

Figure 4.25: Progression of the forecasted failure time for dome collapse on 12 July 2003 using all low frequency seismicity identified in STA/LTA analysis (see Section 3.4.3). The dome collapse is marked by the vertical blue line on the 12 July. Each data point represents the average number of events per 10 minutes within identified swarms of activity. A least squares linear regression is placed through the data as described by the FFM. The forecasted timing of the eruption is the point at which this linear regression meets the x-axis. *Upper*: Forecast made on 11 July at 00:00 midnight *Middle*: Forecast made on 11 July at 12:00 noon *Lower*: Forecast made on 12 July at 00:00 midnight.

and therefore each forecast made would have an equal weight of perceived accuracy. Figures 4.23 and 4.24 suggest that using the cross correlation technique initially to identify seismicity acting from the same system not only improves the accuracy of the forecast in terms of the fit of the FFM to the data points (see Section 4.2), but also provides less change in the forecasted timing of eruption with increased data points in June 1997.

However, it is clear from Figure 4.25 that relatively little change in the position of the forecasted timing of eruption does not necessarily equate to a reliable forecast. In this instance however, it is very clear the the FFM does not fit the data well since little correlation is seen between the data points and the linear regression. Further characterization of the seismicity at depth into families does provide a more accurate forecast in terms of fitting the FFM to the data points, however the forecasted timing of failure varies wildly with time, and does not converge upon the known timing of failure when all swarms of seismicity are considered (Figure 4.26). Consequently, the application of the FFM can help to guide a forecasting process, but should not be used as a stand-alone tool.

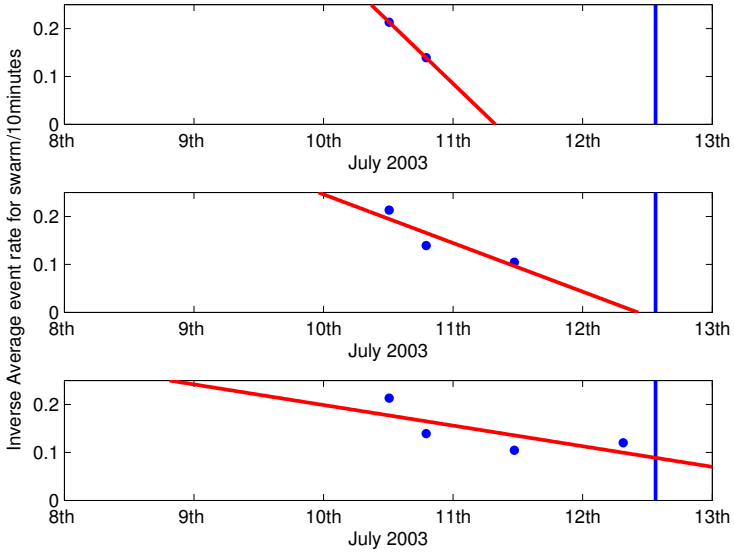

Figure 4.26: Progression of the forecasted failure time for dome collapse on 12 July 2003 using the Dominant Master event to identify seismic events. The dome collapse is marked by the vertical blue line on the 12 July. Each data point represents the average number of events per 10 minutes within identified swarms of activity. A least squares linear regression is placed through the data as described by the FFM. The forecasted timing of the eruption is the point at which this linear regression meets the x-axis. *Upper*: Forecast made on 11 July at 00:00 midnight *Middle*: Forecast made on 11 July at 12:00 noon *Lower*: Forecast made on 12 July at 00:00 midnight.

Discrepancy between the observed eruption time and the forecasted eruption time is perhaps expected, as a consequence of the time delay between the seismicity at depth and the eruption at the surface (Voight, 1988) (explored further in Chapter 6), or simply due to the stochastic nature of the earthquake event process, which means that a number of variables could fit the parameters described in the accelerating process (e.g. the values of α and k) (Bell et al., 2013). This is perhaps most evident in July 2003, when similar seismic events which had dominated the seismicity for the previous few days terminated in the hours prior to eruption (Figure 4.14). Currently, there is no solution for estimating this time delay, which appears to vary since often no apparent delay is observed (e.g. high rate of similar seismicity up to the 1997 dome collapse (Figure 4.7)). This concept shall be further explored in Chapter 6.

It is clear from Section 4.5 that α is an important parameter which is ultimately used to describe the precursory sequence of seismicity and its relationship to failure at the surface. Determination of α in real time is likely to be challenging and computationally intensive, and with some precursory data sequences being very short (up to a few hours) or having minimal data points (e.g. using the average event rate for each swarm identified), α may be poorly con-

strained anyway (Boué, 2015). Application of other models (e.g. the GLM or an exponential model - Section 4.6) may provide an adequate forecasting tool without the need to decipher α. Using the dome collapses of 1997 and 2003 as examples of the activity at Soufrière Hills volcano, it appears that the GLM and an exponential model consistently provide poorer forecasts in terms of the forecasted failure time than using the FFM with $\alpha = 2$, despite the mathematical inaccuracy.

Since many volcano observatories around the world do not have access to advanced computer software, it is essential that forecasting tools can be implemented in places with even the minimal monitoring equipment. Although initially time consuming to identify master events, the cross correlation technique could easily be adapted to work in real time at an observatory by analysing incoming seismicity against a back catalogue of "master events". These master events could be those which have featured heavily prior to eruptive activity if the events can be seen to be sustained over a long period of time. It is more likely, however, that master events will be identified from the previous few days of incoming seismicity by applying an event detection algorithm to the continuous seismicity and cross-correlating the results. This means that the master events will be continuously updating and evolving, which may also reveal patterns of the temporal and spatial distribution of seismicity, and therefore the activity of isolated areas within the volcanic system.

The overwhelming question in forecasting volcanic eruptions however still remains: how can we tell the difference between accelerating seismicity which is precursory to an eruptive event, and that which does not appear to lead to a surface expression? This is fundamental for forecasting, since the generation of false alarms can lead to deteriorating confidence in the observatory making the forecasts. False alarms are an inherent part of forecasting volcanic eruptions; the forecasts are never going to be 100% correct, 100% of the time, primarily due to the incidental nature of nature itself. However, keeping false alarms and false forecasts to a minimum is essential. Forecasting is complicated by precursory activity often having more than one acceleration event, and in particular at Soufrière Hills having cyclic acceleration events (e.g. seen in RSAM data for June 1997 collapse - Figure 3.6). The FFM does not account well for multiple accelerations within a system, which is why searching for an overall acceleration in the precursory activity (e.g. taking the average event rate of each swarm of activity, rather than per unit time) allows a more successful application. This may not always

be possible, and therefore suggests that a more holistic approach to forecasting volcanic dome collapses is needed. Rather than simply relying upon accelerating precursory signals such as seismicity, the state of the dome itself needs to be considered, and its potential for failure. This analysis forms the basis of Chapter 5.

4.8 Summary

Three dome collapses from Soufrière Hills volcano are investigated to determine whether isolating a single active seismic system at depth allows for more accurate forecasts using the FFM (α = 2) , a generalised linear model and an exponential model. The cross correlation technique allows seismic waveforms identified with a detection algorithm (e.g. an STA/LTA algorithm as is used at MVO) to be compared to other identified seismic events and their similarity determined. Events which are statistically similar to one another are likely to be generated by the same source mechanism in the same source location, and therefore can be considered to represent one active system at depth (Geller and Mueller, 1980, Neuberg et al., 2000). A threshold of similarity was chosen for events occurring at Soufrière Hills (0.7) based on previous studies (e.g. Stephens and Chouet (2001), Green and Neuberg (2006), Thelen et al. (2011)) as well as based upon the distribution of cross correlation coefficients within the investigated time periods.

In June 1997, 10 families of similar waveforms were detected, signalling a number of active sources at depth occurring at the same time. Using one of these families of seismicity as Ω in the FFM (the accelerating precursor) provided more accurate forecasts to the timing of the dome collapse, with a greater degree of confidence due to high R^2 values which suggest that the model (FFM) fits to the data well (Figure 4.9 and Table 4.2). In July 2003, only one family of events were identified. Analysis of the cross correlation coefficients suggested a slight migration of the source with time (Figure 4.14). Significantly, and in contrast to the events of June 1997, the similar seismicity ceased hours before the dome collapse, perhaps an indication of a delay function between the seismicity at depth and the collapse at the surface as first envisaged by Voight (1988). Forecasting using only the accelerating swarms in July 2003 provided an accurate forecast for the timing of the dome collapse, but proves the difficulty of using the FFM in real time, as the last swarm in the sequence led to a forecast a number of weeks from the known timing of collapse. Despite clear cyclic activity in RSAM (Figure 3.12), no families of

similar seismic events could be identified in the precursory seismicity of the February 2010 collapse. This echoes the conclusions of Stinton et al. (2014) who suggested that no acceleration in seismicity was observed prior to the collapse, and in fact, seismicity remained remarkably low.

Although it is clear that in the FFM $\alpha \neq 2$ on most occasions, alternative models for forecasting the dome collapses fail to provide as accurate a forecast. The fit of a GLM to the data is clearly better, with higher R^2 values, however the timing of the forecast is up to 5 days out in June 1997, and over 10 days out in July 2003, when using all available data. This highlights some of the main issues associated with using a forecasting method in real time at a volcano observatory, namely: which model to use, which precursory activity to use (RSAM, all event rates, swarm event rates, only accelerating swarm event rates) and how to be sure that accelerating seismicity will evolve into an eruptive event. In addition, it should be remembered that the seismicity being used as the forecasting tool occurs at depth (often a number of kilometres) and the failure actually being forecast occurs at the surface, generating a discontinuity between the two observables. This may be why accelerating seismicity may not always be observed as a precursor to eruptive events (e.g. February 2010), and that other factors need to be considered, primarily the potential for failure from the dome itself, which shall be investigated further in Chapter 5 using slope stability analysis.

Chapter 5

Modelling Dome Instability on Montserrat

In chapters 3 and 4 it was suggested that low frequency seismicity may not always be appropriate as a forecasting tool for dome collapses at Soufrière Hills volcano. One overriding assumption is made when using the FFM: that the seismicity at depth is directly related to the collapse at the surface, potentially through the movement of magma at depth. In this chapter, statistical analysis supports this assumption finding that the most important parameter influencing a dome collapse event at Soufrière Hills is the acceleration of low frequency seismicity. However, shear strength reduction stability analysis suggests that the dome complexes in 2003 and 2010 at Soufrière Hills were already at a critical state of stability at the time of the collapse, meaning that many other factors are likely to influence edifice stability. Some of these shall be further explored in this chapter. Although important, the acceleration in precursory seismicity should not be used in isolation to forecast dome collapse events, and instead, a number of other physical characteristics regarding the state of the dome itself need to be fully considered.

It is the large scale collapse of lava domes that have explosive components which are the most hazardous at Soufrière Hills, with pyroclastic flows and surges travelling for many kilometres (Loughlin et al., 2002, Calder et al., 2002, Loughlin et al., 2010). In addition, large ash clouds generated in collapse events can be hazardous to aviation (Casadevall, 1994, Guffanti et al., 2010) and therefore pose a threat not only to those living in close proximity to a volcano. Consequently it is important to understand the susceptibility of Soufrière Hills volcanic dome to collapse, and to link the accelerating precursory signals to the collapse since current forecasting tools assume such a link.

5.1 Classification of Lava Dome Collapses at Soufrière Hills

Soufrière Hills volcano has been in a cyclic state of dome building and collapse separated by periods of quiescence since 1995 (Wadge et al., 2014). Up until the time of writing (September 2015), the largest dome collapse occurred in July 2003, during which 210 million m^3 of material was displaced (Herd et al., 2005). Other significant collapses occurred on 25 June 1997 in which 19 people lost their lives (Robertson et al., 2000); 26 December 1997 (Voight et al., 2002); 29 July 2001 collapse which lowered the dome height by over 150 m (Matthews et al., 2002); 20 May 2006 event (Loughlin et al., 2010); and the most recent event on 11 February 2010 when 50 million m^3 of material was displaced (Stinton et al., 2014). A "significant" collapse is defined as one which involves a collapse material volume of greater than 40×10^6 m^3 of volume, or in which fatalities occurred.

5.1.1 Progressive Surface Failure

Progressive failure initiated at the surface, which here is taken to be the upper 50 m of the volcanic dome, is likely to be related to unloading or to changes in water pressure. Unloading is most likely achieved through surface erosion and degradation of the volcanic edifice in the form of wind or rainfall. Rainfall upon recently extruded material can cause the magmatic products to quench rapidly, and therefore fracture more readily leading to instability (Elsworth et al., 2004). Intense rainfall can lead to the remobilization of loose pyroclastic material at the base of the dome and therefore secondary lahars may occur which destabilize the dome by removing small amounts of material incrementally. It is unlikely for this type of failure at the surface to induce the large scale dome collapses observed on Montserrat because these involved failure at depths much greater than 50 m.

A number of the smaller dome collapses on Montserrat appear to be triggered by, or at least coincide with intense rainfall. Carn et al. (2004) concluded that a dome collapse event on 20 March 2000 at Soufrière Hills was the result of mechanical erosion of the dome face, the action of pressurized fluids on the potential failure surfaces within the dome, the rapid quenching of hot volcanic deposits and the degradation of the dome further by fumerolic activity. The dominant mechanism was not identified. Intense rainfall began approximately 30 minutes prior to the first pyroclastic flows (identified from continuous seismic data), and is thought to have

caused rapid degradation of the dome at the surface through mechanical erosion, and fracturing at depth through increased gas pressures from infiltrated rain. Rainfall is also believed to have played some part in the collapse on 29 July 2001, when the island had had little rain in the preceding months (Matthews et al., 2002). The larger dome collapses of 12 July 2003 and 20 May 2006 have also been identified as being influenced by intense rainfall in the hours before collapse (Herd et al., 2005, Loughlin et al., 2010). Statistically, dome collapses at Soufrière Hills are up to 10% more likely to occur on a day with greater than 20 mm of rainfall, than on a day without (Barclay et al., 2006).

5.1.2 Progressive Failure at Intermediate Depths

Processes affecting intermediate depths of the volcanic edifice (50 m to 150 m) are likely to include the infiltration of rainfall, and the exsolution of magmatic gases due to depressurization. Rainfall induced collapses may occur through the destabilization of the thermal structure of the volcanic dome through the percolation of rainwater into cracks (Thomas et al., 2004a, Simmons et al., 2004). This leads to the generation of increased pore fluid pressure as the water vaporizes upon contact with hot dome rocks, and subsequently forces the shattering of overlying dome material (Matthews and Barclay, 2004). The trapping of magmatic gases within the edifice as infiltration blocks gas escape (Elsworth et al., 2004) or the precipitation of silica rich vapour circulating through the system (Boudon et al., 1998) may also cause an increase in pressure at depth, leading to fragmentation of the volcanic dome. Rainfall induced dome collapses has been reported at a number of volcanoes, including Merapi, Central Java in November 1994 and October 1996 (Voight et al., 2000); Unzen volcano, Japan between May 1991 and November 1993 (Yamasato et al., 1998); and the explosive events at Mt St Helens between 1989 and 1991 (Mastin, 1994).

5.1.3 Progressive Deep seated Failure

Deep seated failure is defined as failure which occurs at depths greater than 150 m. The progressive loading of a volcanic dome with new material will lead to gravitational instability due to over steepening of the slopes and overloading the material at the surface (McGuire, 1996, Sparks et al., 2000). In volcanic environments surface fluid infiltrates the volcanic edifice through fracture networks, establishing a hydrothermal system upon the interaction of magmatic gas with groundwater and infiltrating fluid. The hydrothermal system provokes ex-

tensive dissolution of the surrounding rock and the precipitation of alteration minerals, such as clays, which can greatly enhance volcanic dome instability and promote collapse (Day, 1996). This is thought to have been influential in a number of collapse events since 1595 at Nevado del Ruiz, Colombia (López and Williams, 1993), and Mt Rainer during the Holocene (Reid et al., 2001), although these involved the catastrophic collapse of the entire volcanic edifice rather than only the volcanic dome.

Soufrière Hills volcano has one of the most active hydrothermal systems in the Lesser Antilles as demonstrated by the number of active fumaroles and hot springs at the surface (Boudon et al., 1998). Wadge and Isaacs (1988) partially attributed the formation of English's Crater (Figure 2.3) to the collapse of a lava dome 3950 ± 70 years before present (Roobol and Smith, 1998), weakened by hydrothermal alteration. Hydrothermal alteration of materials is thus expected to have had a significant influence on other failure episodes.

5.1.4 Deep seated fluid pressurisation

Collapses induced only at the surface are likely to be local events that involve relatively small amounts of material. In order to generate deep seated catastrophic failure either a large increase in shear stress, or a large decrease in shear strength is needed at depth. By raising pore fluid pressures, either mechanically as a direct volumetric response of an intruded medium, or by temperature differences between the host rock and an intrusion, instability can be induced resulting in flank collapse (Elsworth and Voight, 1995). In particular, temperature differences of intruding hot material into cold static host rock can lead to increased gas pressurization which may greatly enhance the likelihood of flank collapse, even if the intrusion is deep seated where local stresses and strains were previously stable. Stability depends on the hydraulic diffusivity of the host rock (Elsworth and Voight, 1996), since in very low diffusivity rock flow and expansion of gases will be inhibited and therefore high pore fluid pressures will only occur in very close proximity to the intrusion. In high diffusivity rocks, the increased pore fluid pressure will easily dissipate and be accommodated throughout the edifice. Therefore, there is a distinct permeability of rocks at which pore fluid pressures are likely to increase, identified as being between $2\text{x}10^{-18}$ m^2 and $1\text{x}10^{-15}$ m^2 (Reid, 2004). In addition, the thermal inertia of the rock masses involved will greatly affect the ability to raise pore fluid pressures within the edifice. An increase in deep seated pore fluid pressure may also be a direct result of progressive processes within the edifice, for example the closing of fractures during subsidence of the volcano or the

precipitation of hydrothermal minerals within fractures which inhibits the escape of fluid and gas (Matthews et al., 1997).

At Soufrière Hills there have been a number of collapse events which have removed not only fresh lava at the surface, but also highly crystalline material at depth, which is thought to represent older volcanic complexes. There was evidence of highly gas charged magma close to the surface between 1996 and 1997, since explosive events occurred following minor flank collapse events, pointing to increased gas and pore fluid pressures (Voight and Elsworth, 2000). Explosive events also followed or occurred during dome collapses on 12 July 2003 (Herd et al., 2005) and 11 February 2010 (Stinton et al., 2014), suggesting the presence of highly pressurized gas within the volcanic dome on these occasions.

5.1.5 The Influence of Seismicity

Shaking of the dome induced by seismicity at depth is not likely to be a dominant mechanism in causing dome collapses at Soufrière Hills volcano (Calder et al., 2002). Instead, shallow and intense earthquake swarms, such as those which have been described by Rowe et al. (2004) and De Angelis and Henton (2011) for example, may have the ability to shake the dome enough to generate a number of small rockfall events. At Soufrière Hills, rockfall events sometimes appear to be preceded by a low frequency event possibly triggered by an increased shaking of the dome, and consequently have been named long-period rockfalls (Patrick Smith, Pers. Comm., 2014). It may be therefore that the dome acts to focus the resonance from the LF event, causing a disturbance at the surface (Neuberg et al., 2000). Topographic amplification of seismic waves to induce shaking is greatest on slopes of more than than 60°, and in particular with surface waves polarised in the vertical plane (Ashford et al., 1997). However, even the steepest slopes at the vent of Soufrière Hills volcano rarely exceed 40° (Wadge et al., 2009). In addition, although amplification in the vertical plane may be heightened by the presence of a vertical conduit (Patrick Smith, Pers. Comm., 2014), the seismicity generated at volcanoes is typically less than magnitude 2 (Aspinall et al., 1998, Sparks, 2003) and it is therefore unlikely that these small seismic events would be able to trigger the large scale dome collapses that have been observed at Soufrière Hills volcano (Calder et al., 2002). For this reason, seismicity induced shaking shall not be considered as a dominant process in generating dome collapses, and shall not be included in modelling of slope stability at Soufrière Hills volcano.

5.2 Grey Incidence Analysis: Determining the importance of dome collapse triggers

Grey system theory, first introduced by Deng (1982), is the concept of utilizing a "system containing knowns and unknowns", and is a statistical methodology to determine the relative importance of parameters when information on these parameters is poor. Interactions between the many factors affecting the generation of collapse events are complex and difficult to describe statistically or in a mathematical manner (Lu and Rosenbaum, 2003). Within volcanic environments, data on the physical properties of rock masses and their geotechnical characteristics are sparse, making modelling of collapse processes and instability challenging (Thomas et al., 2004b). Consequently, traditional mathematical approaches such as discriminative analysis and multiple linear regression are not appropriate for determining the importance and interactions of parameters associated with dome collapses (Jibson and Keefer, 1989). Grey incidence analysis allows parameters with small sample sizes, of varying distributions to be compared through the similarities existing between geometric patterns in their occurrence curves (Lui and Lin, 2006). It is based upon a knowledge of the behaviour of a system, rather than knowledge of physical relations (Lu and Rosenbaum, 2003). A higher degree of incidence emulates a greater similarity, and therefore the more important the parameter in question is to the generation of the process being investigated.

A "mapping quantity" of the systems behaviour must be defined which is characteristic of the system being described (Lui and Lin, 2006). For example, the number of admissions to a hospital in a given town is thought to be representative of the overall health of the community. Determining the mapping quantity within a volcanic system that is characteristic of the likelihood of a large scale dome collapse is difficult since data for many parameters are not available, and all measurements of the magmatic system are indirect. Firstly the seismic event rate from 22 - 25 June 1997 (thought to represent the movement of magma from depth) was defined as the mapping quantity, and then tilt data from the same time period (related to the inflation of the dome complex) was defined as the mapping quantity in two separate analyses. The period of precursory activity to a dome collapse in June 1997 was chosen because data for many parameters existed for this time period e.g. deformation data, rainfall, and many parameters involving seismicity.

Following the example of Lui and Lin (2006), determining the importance of different parameters in relation to the mapping quantity is a three step process. First, the absolute degree of incidence must be determined, characterising the relationship between each of the data parameters and the mapping quantity. Secondly, the relative degree of incidence is determined which is a numerical representation of the relative rates of change of each of the parameters compared to their starting points. Finally, the synthetic degree of incidence is considered, which is a quantitative approach to describe the overall closeness of the data parameters to the mapping quantity, allowing the relative importance of each of the parameters in June 1997 to be determined.

5.2.1 Absolute Degree of Grey Incidence

The absolute degree of grey incidence determines the observed relationship between the parameters chosen to be assessed in terms of their relative importance and the mapping quantity. Both the mapping quantity and the other parameter sequences need to be the same length, with the same sampling interval and all either be following a generally increasing or decreasing pattern. The absolute degree of grey incidence between the mapping quantity and a time series parameter sequence is defined as:

$$\varepsilon_{ij} = \frac{1 + |s_i| + |s_j|}{1 + |s_i| + |s_j| + |s_i - s_j|} \tag{5.1}$$

where:

$$|s_i| = \left| \sum_{k=2}^{n-1} X_i(k) + \frac{1}{2} X_i(n) \right|, \tag{5.2}$$

and

$$|s_j| = \left| \sum_{k=2}^{n-1} X_j(k) + \frac{1}{2} X_j(n) \right|. \tag{5.3}$$

where $X_i(k)$ is the time series sequence of the mapping quantity, with k the position that value appears in the sequence. In this analysis, $k = 1$ for data from the 22 June, $k = 2$ for data from the 23 June, $k = 3$ for data from the 24 June and $k = 4$ for data from the 25 June. n is the length of the time series sequence, and therefore $X_i(n)$ represents the last value in the sequence (i.e. the value from the time series on the 25 June). $X_j(k)$ and $X_j(n)$ represent the time series sequences of the parameters being compared to the mapping quantity, and the last

value in the sequence of these parameters respectively. Each time series sequence of the parameters being compared to the mapping quantity is done so individually, so there is only ever one value for $X_i(1)$, $X_i(2)$, $X_i(3)$ and $X_i(n)$, however there can be a large number of $X_j(k)$ values. In Table 5.1, each of the time series which sits in rows three and below (average event rate per swarm using the dominant master event) represents a different $X_j(k)$ sequence, from which its relationship to the mapping quantity can be compared.

5.2.2 Relative Degree of Grey Incidence

The relative degree of grey incidence computes the relative rates of change of each of the parameters compared to their starting points. Assuming the mapping quantity (X_i) and the time series parameter sequence in question (X_j) are the same length with non-zero initial values, then the initial values of X_i and X_j are:

$$X_i' = \frac{X_i}{x_i(1)} = \left(\frac{x_i(1)}{x_i(1)}, \frac{x_i(2)}{x_i(1)}, ..., \frac{x_i(n)}{x_i(1)}\right) \tag{5.4}$$

$$X_j' = \frac{X_j}{x_j(1)} = \left(\frac{x_j(1)}{x_j(1)}, \frac{x_j(2)}{x_j 1)}, ..., \frac{x_j(n)}{x_j(1)}\right) \tag{5.5}$$

and the relative degree of incidence (r_{ij}) can be described as in equation 5.1 with X_i' substituted for X_i and X_j' substituted for X_j.

Both the relative degree of grey incidence (r_{ij}) and the absolute degree of grey incidence (ε_{ij}) lie between the values of 0 and 1, with values closer to 1 representing the time series of parameters that are more similar to the mapping quantity. The relative degree of grey incidence (r_{ij}) and the absolute degree of grey incidence (ε_{ij}) are not related in any manner and therefore, ε_{ij} can be relatively large and r_{ij} can be small within the same sequences of data, and visa versa.

5.2.3 Synthetic Degree of Grey Incidence

The synthetic degree of grey incidence is a quantitative approach to describe relative importance of each of the parameters to be determined and is defined as:

$$\rho_{ij} = \Theta\varepsilon_{ij} + (1 - \Theta)r_{ij} \tag{5.6}$$

Parameter	22 June	23 June	24 June	25 June	Reference and Notes
Average event rate per swarm (event rate per 10 minutes)	$X_i(1)$ 2.1	$X_i(2)$ 5.7	$X_i(3)$ 5.2	$X_i(n)$ 7.7	Chapter 3
Average event rate per swarm using dominant master event (event rate per 10 minutes)	$X_j(1)$ -	$X_j(2)$ 3.4	$X_j(3)$ 7.4	$X_j(n)$ 11.8	Chapter 4
Average event rate per swarm using Master event 100 (event rate per 10 minutes)	0.8	1.6	4.8	7.2	Chapter 4
Maximum Tilt (μradians)	-12	-3	5	6	Voight et al. (1998)
Difference in maximum and minimum tilt (μradians)	10	14	15	12	Voight et al. (1998)
Total Number of Triggered Earthquakes	244	569	498	165	SEISAN database at University of Leeds
Number of Rockfall Events	180	84	60	48	Montserrat Volcano Observatory (1997a)
Rainfall (mm)	8	29	1	2	NOAA (1997)
SO_2 Measurements (Kg/sec)	5.02	13.39	22.37	-	Watson et al. (2000)
Estimated volume of dome ($\times 10^6 \mathrm{m}^3$)	73.6	74.0	74.3	74.6	Loughlin et al. (2002)
Time since last dome collapse (days)	140	141	142	143	Small dome collapse registered on the 2nd February 1997 (Montserrat Volcano Observatory (2012))

Table 5.1: Time series' of parameters potentially influencing a dome collapse event in June 1997. A dash indicates no available data for this day. In this Table, the mapping quantity is defined as the average event rate per swarm (row two), but a number of other time series parameter sequences were also investigated as the mapping quantity (rows three to twelve).

where Θ lies between 0 and 1 and is usually taken as $\Theta = 0.5$, which puts equal emphasis upon both the absolute and relative degree of incidence when determining the overall closeness of

the two data sequences. The greater the value of ρ for each sequence, the greater the similarity to the mapping quantity and therefore the more important that parameter is in terms of affecting the mapping quantity.

5.2.4 Application to Volcanic Settings

Grey incidence analysis is particularly suited to identifying the relative importance of different parameters in influencing dome collapses, since many of the controlling parameters are unknown (e.g. the fracture network at depth, the detailed geology, the size and position of the conduit) and the quality of information is often poor (e.g. gas measurements which could indicate the state of the magma at depth is not continuously monitored at most locations, rainfall may have different effects on different parts of the dome depending on its steepness, stratigraphy and fracture density). In particular, it is very difficult to model the extreme heterogeneities that make up the rock and fluid masses and the controlling factors on eruption dynamics. The first major dome collapse to occur on Montserrat on 25 June 1997 was investigated for the most influencing parameters generating a collapse event using grey incidence analysis.

All the parameter time series in Table 5.1 were investigated since it is possible that each had some influence on the likelihood of dome collapses (see Section 5.1). The average event rate of LF seismic swarms is thought to be indicative of fluid movement at depth (Chouet, 1988, Neuberg et al., 2000), and therefore may induce instability by increasing the pore fluid pressure due to the temperature of the moving fluid (Elsworth and Voight, 1995), as well as increasing the load of material at the surface (Sparks et al., 2000). The average event rate per swarm was investigated using the rates of only STA/LTA identified events (see Section 3.4.1) and events identified from a single active system at depth (dominant and master event 100). The difference between maximum and minimum tilt values demonstrates the maximum inflation that the dome has seen that day. The volume of the dome influences the amount of material that is available for collapse, but also affects the stress regimes within the dome due to progressive loading. Loughlin et al. (2002) estimated that the dome size was 73×10^6 m^3 on the 20 June 1997, with an extrusion rate of $3 - 5$ $\mathrm{m}^3\mathrm{s}^{-1}$, allowing the dome volume to be calculated for the days preceding the collapse. Unfortunately no rainfall data was available directly for Montserrat for June 1997, and therefore the rainfall data is taken from Le Raizet, Guadeloupe, the nearest rainfall station situated at $16.27°$N and $-61.6°$E (NOAA, 1997), a distance of just over 80 km from Soufrière Hills volcano.

Table 5.2 shows the synthetic degree of grey incidence for seven different mapping quantities (X_i). Each mapping quantity sits in a different column. The larger the value of synthetic incidence, the more important it is expected to be in generating collapse. Each column can be placed in descending order to determine the relative importance of the parameter time series observed in the days prior to collapse (X_j, each row).

LF Seismicity as the mapping quantity

The importance of LF seismicity in generating dome collapse events related to the movement of fluid at depth has been summarised in Section 5.1. Using LF seismic event rate as the mapping quantity (column two of Table 5.2 suggests the relative importance of the parameters, from most to least important is:

Swarm Event Rate from Master Event 100 (0.83) $>$ SO_2 *Measurements (0.83)* $>$ *Tilt (max - min) (0.81)* $>$ *Rainfall (0.81)* $>$ *Maximum Tilt (0.73)* $>$ *Number of earthquakes (0.64)* $>$ *Number of Rockfalls (0.61)* $>$ *Time since last collapse (0.59)* $>$ *Amount of material available (0.57)*

The ranking suggests that if the rate of low frequency events is indeed a parameter which accurately describes the precursory activity before a dome collapse, then the most important parameters affecting the likelihood of collapse are the seismic event rate for an isolated system, gas emissions, tilt and rainfall. This is unsurprising, since it has already been identified in Section 5.1 how all of these parameters may affect the instability of the volcanic dome.

Column three of Table 5.2 depicts the use of LF similar seismic event rates, which is related to the movement of magma at depth under one specific system, and again suggests that the most important parameters influencing dome collapse on 25 June 1997 are LF seismic event rate, tilt, rainfall and gas emissions. The parameters which appear to have the least effect upon destabilizing the dome to induce collapse are the time since the previous collapse; the amount of material available for collapse; the total number of earthquakes; and the number of rockfalls. For monitoring purposes, this suggests that it is more important to have detailed monitoring of low frequency seismicity, deformation and gas emissions than counts of the number of seismic events, which is currently frequently used as a simple tool for assessing unrest at volcanoes.

Other mapping quantities

When using tilt values as the mapping quantity (column 5), the most important parameters for inducing a collapse event were SO_2 outputs, rainfall and the LF seismic event rate. If SO_2 output becomes the mapping quantity (Table 5.2, column 6), then the most important parameters for influencing instability are rainfall, the event rate of similar LF seismic event swarms, and tilt. Similarly, if using rainfall as the mapping quantity then the most important parameters influencing a dome collapse event are tilt, the LF seismic event rate and the SO_2 output (Table 5.2, column 7).

Independent of the selected mapping quantity, therefore, it is clear that tilt, LF seismic event rate, gas output and rainfall appear to be the most important parameters in terms of influencing a dome collapse event on Montserrat in 1997. A direct link between instability and tilt, gas output and seismic event rates can be established for the dome collapse event in June 1997. All three parameters can be seen to be increasing in the days prior to the collapse event (Table 5.1) and can be related to the movement of magmatic fluid towards the surface, and are therefore indicative of a single process. As the magma enters a shallow region below the dome, tilt will increase due to displacement of the overlying rock from the intruded fluid, seismicity shall be generated as the magma moves (Chouet, 1988, Neuberg et al., 2000) and new fractures are developed in both the magma itself, and the surrounding country rock (Arciniega-Ceballos et al., 2003). Gas exsolution is favoured during magma ascent by a decrease in the pressure from overlying rock and magma. In addition, heating by the intruded magma will raise pore fluid pressures surrounding rock because of thermal expansion of gases (Elsworth and Voight, 1995), which may drive instability. Deep-seated magmatic processes, rather than processes at the surface may therefore drive dome collapse at Soufrière Hills.

Despite being a surface processes, rainfall was also consistently considered a relatively important parameter to inducing dome collapse events. However, unlike the rates of LF events, gas output and tilt, the rate of rainfall did not consistently accelerate before dome collapse (Table 5.1). Instead, rainfall intensity peaked two days before the collapse on 25 June 1997, declining to almost no rainfall between 24 and 25 June. It can therefore be suggested that rainfall creating surface erosion is unlikely to be a contributing factor to the instability of the dome as a collapse event would be expected simultaneously with the peak rainfall if this were the case. The infiltration of rainwater to sufficient depths to generate increasing pore fluid

pressures will take time and therefore instability will involve a delay. It is possible that this mechanism contributed to the dome collapse on 25 June 1997 since a delay was observed between peak rainfall intensity and the collapse. However, this does not necessarily mean that heavy rainfall is needed during a period of LF seismicity to generate a collapse; but it would increase the likelihood of collapse.

5.2.5 Limitations of Grey Incidence Analysis

This is the first time that Grey Incidence Analysis has been applied to parameters in a volcanic setting. The theory was only originally developed in 1982 (Deng, 1982) and although has rapidly progressed in the following decades, is still really in its infancy of application. It is therefore difficult to compare or discuss the results obtained since there is no available comparison. With further research into the use of Grey System Analysis with volcanic parameters, this will hopefully become easier. One fundamental assumption employed in Grey System Analysis is that each of the time series sequences chosen accurately represents the system that is being described. In this case, this means that each of the time series (e.g. seismicity, gas output, rainfall) are all directly influencing the likelihood of a dome collapse at Soufrière Hills volcano, although in many cases this direct link has yet to be established. One such link between accelerating LF seismicity and a dome collapse shall be developed further in Chapter 6, and others have been linked to collapses in Section 5.1 (e.g. rainfall and the degradation of dome rocks), however many of these links are still assumed rather than definitive.

The ability to chose the right sequence of behaviour as the mapping quantity is difficult since it must most accurately reflect the characteristics of the system being described. In addition, Grey Incidence Analysis can only be applied to one simple system, which has one hierarchy of factors and one main behaviour which reflects the system (Bing-jun et al., 2005). Systems which are more complex, which may be the case in volcanic systems, are simplified into only having one hierarchy of important parameters, and only one mapping quantity which can accurately describe the systems behaviour, which may not be a true reflection of the environment. In particular for the analysis conducted for the dome collapse at Soufrière Hills volcano on 25 June 1997, the reliability of trends in the data identified from four data points (i.e. over four days) is questionable, however longer time series' of data was not available.

X_j \ X_i	Swarm Event Rate (per 10 minutes)	Swarm Event Rate: Master 100 (per 10 minutes)	Swarm Event Rate: Dominant Master (per 10 minutes)	Tilt (max-min) (μradians)	SO_2 Measurements (Kg/sec)	Rainfall (mm)
Swarm Event Rate (per 10 minutes)	-	0.83	0.58	0.81	0.78	0.81
Swarm Event Rate: Master 100 (per 10 minutes)	0.83	-	-	0.74	0.79	0.73
Tilt (max-min) (μradians)	0.81	0.74	0.84	-	0.67	0.93
SO_2 Measurements (Kg/sec)	0.83	0.71	0.636	0.74	-	0.78
Rainfall (mm)	0.81	0.73	0.72	0.93	0.92	-
Number of Rockfall Events	0.61	0.56	0.64	0.69	0.62	0.74
Total Number of Triggered Earthquakes	0.64	0.57	0.59	0.64	0.66	0.68
Amount of Material ($\times 10^6 m^3$)	0.57	0.57	0.58	0.63	0.55	0.61
Time since last collapse event (days)	0.59	0.58	0.62	0.65	0.57	0.63

Table 5.2: Synthetic degree of grey incidence (ρ_{ij}) for factors affecting a dome collapse event in June 1997. Each column represents a different mapping quantity (X_i) thought to be indicative of dome collapse, and therefore placing each value within a column into descending order determines the relative importance of each behavioural time sequence (X_j). The values in each column are relative to one another, and values cannot be compared across columns.

Parameter	Dinçer et al. (2004)	Voight and Elsworth (2000)	Voight et al. (1999)
Unit Weight (kN/m^3)	22.53	23.5	–
Youngs Modulus (GPa)	13.62	–	1-2
Tensile Strength (MPa)	–	–	4
Friction Angle (deg)	–	25 - 60	–
Peak Cohesion (MPa)	–	0 - 0.5	–

Table 5.3: Mechanical properties for Soufrière Hills volcano dome rocks. Dinçer et al. (2004) records average information for andesitic rocks; others refer directly to Soufrière Hills samples

5.3 Geological Model of the Volcanic System at Montserrat

Analysis of the stability of any slope requires accurate information about the physical and mechanical properties of the rocks and materials of the slope in question. Unfortunately, details of the strength values of large volcanic rock masses are scarce (Thomas et al., 2004b) and therefore introduces large uncertainties associated with the input parameters in slope stability analysis (del Potro and Hürlimann, 2008).

5.3.1 Rheological and Mechanical Properties of Rock Masses

The current active dome at Soufrière Hills volcano is believed to consist of a solid andesitic core, with deposits close to the summit being comprised of the fragmentation of this core material, surrounded by more distal aprons of pyroclastic deposits which extend down the slopes of the volcano (Wadge et al., 2009). Petrological investigations of lava erupted from 1996 to 1997 suggest that the lava dome consists primarily of andesite (Murphy et al., 2000), with an overall vesicularity between 5% and 20%. Melnik and Sparks (2002) have suggested with such a large volume of mass above it, the overpressure within the upper 200 m of the dome could be up to several MPa, suggesting that the exsolved gases could maintain high pressures. A layer of pyroclastic detritus, primarily block and ash flow deposits, covers the volcano to a depth of 25m (Wadge and Isaacs, 1988). In the simplest form therefore, the volcanic dome complex consists of a solid homogeneous andesitic core, overlain by pyroclastic deposits which taper towards the lower slopes.

Parameter	Reid et al. (2000)	Esposito and Guadagno (1998)	Apuani et al. (2005)
Unit Weight (kN/m^3)	19	6.1 - 7.5	–
Youngs Modulus (GPa)	–	–	0.596
Tensile Strength (MPa)	–	–	0.1
Friction Angle (deg)	15 - 27	–	15 - 23
Peak Cohesion (MPa)	0.01 - 0.5	–	0.6 - 1.4

Table 5.4: Mechanical Properties for Soufrière Hills volcano pyroclastic slope deposits. No direct data was available for Soufrière Hills. Reid et al. (2000) refers to pyroclastics at Mt St Helens, Washington, USA; Apuani et al. (2005) refers to pyroclastics at Stromboli volcano; and Esposito and Guadagno (1998) refers to pumice deposits at Mount Vesuvius.

Tables 5.3 and 5.4 outline the physical and mechanical properties for the andesitic core taken from literature, and the outlying pyroclastic deposits. These were the only relevant values, since data for volcanic environments is so scarce (Thomas et al., 2004b). It is clear that there are large uncertainties associated with some of the parameters (e.g. friction angle) which may lead to large uncertainties in the results. Table 5.5 shows the chosen mechanical properties of the andesitic dome and pyroclastic deposits used in modelling. The material properties undoubtedly vary within these units, and throughout the entire volcanic edifice due to rock and structural heterogeneity. However, since the distribution of such heterogeneity is unknown, the rock masses are simplified for conceptual modelling, therefore using static values for all parameters. For the andesitic dome properties, values relating directly to Soufrière Hills were favoured (Table 5.3). For pyroclastic deposits, data relating only to pumice were rejected (Esposito and Guadagno, 1998) since it is known that much of the pyroclastic deposits are made up of more cohesive block and ash flows (Wadge and Isaacs, 1988). Other parameters were calculated as the average of the identified values for pyroclastic deposits since no data was available directly related to Soufrière Hills volcano. Poissons' ratio was assumed to be 0.3 after Gercek (2007) who estimated it to lie between 0.2 and 0.35 for andesitic rocks. One input parameter required for slope stability calculations which is not discussed in the literature is the dilation angle, which affects the volume change of the material when it is yielding. Detailed volumetric modelling of the volume change of the materials involved is beyond the capabilities of this research, and thus constant volume conditions are applied, meaning that the dilation

Property	Andesitic Core	Pyroclastic deposits	Hydrothermally altered rock
Unit weight (kN/m^3)	23.5	19	13.36
Young's Modulus (kPa)	1,500,000	569,000	1,055,296
Poissons Ratio	0.3	0.3	0.3
Tensile Strength (kPa)	4000	100	400
Tensile Strength Residual (kPa)	4000	100	400
Dilation angle (deg)	0	0	0
Friction Angle Peak (deg)	60	25	14.68
Friction Angle Residual (deg)	25	15	14.68
Cohesion Peak (kPa)	500	500	369
Cohesion Residual (kPa)	500	500	369

Table 5.5: Chosen mechanical properties of the andesitic dome, pyroclastic deposits and hydrothermally altered rock masses used in slope stability analysis

angle is equal to zero (Griffiths and Lane, 1999).

Boudon et al. (1998) report that an upper hydrothermal alteration zone is likely to extend down to a minimum of 800 m depth at Soufrière Hills. The properties of this layer are outlined in Table 5.5 and are based upon the average values for parameters determined during a geotechnical investigation into hydrothermally altered volcanic rock at White Island, New Zealand (Moon et al., 2005). Tensile strength was estimated at 400 kPa after Arıkan et al. (2007) who found this to be the lowest calculated value for tensile strength for weathered andesite. The effective Young's modulus (Ed^*) was calculated by:

$$Ed^* = \rho^* V_p^2 \frac{(1-2v^*)(1+v^*)}{(1+v^*)} \tag{5.7}$$

where ρ is the unit weight of the rock, V_p is the p-wave velocity and v is Poissons ratio (Okubo, 2004). V_p was estimated at 1391.6 ms^{-1} by Arıkan et al. (2007) for weathered andesite. Ed^* was therefore calculated as 1.055 GPa.

In addition to a hydrothermally altered layer at the surface, a "conduit" and "reservoir" were introduced into the model (Figure 5.1). This was a conceptual addition, and was not modelled as an increase in temperature or pressure at depth, which is the likely influence of a magma chamber and conduit within the volcanic dome in reality. Instead, the conduit and reservoir were introduced as another geological boundary within the model, to assess the influence of introducing weak rock masses at the core of the volcanic dome. The conduit diameter was set at 30m following Costa et al. (2007) and is in agreement with Melnik and Sparks (2005) for Soufrière Hills volcano. Voight et al. (2006) suggest that a spherical magma reservoir may sit beneath Soufrière Hills at 6km depth with a radius of 1 km. This is supported by petrological (Murphy et al., 2000) and seismic (Aspinall et al., 1998) evidence, which suggests a magma source lies between 5.5 km and 8 km depth. It is nearly impossible to define the properties of the magma chamber and the conduit in terms of geotechnical characterization since it will be a heterogeneous body, likely to be in a number of different physical states throughout the system and to be constantly evolving. For simplicity therefore, the conduit and reservoir are represented by the weakest rock masses identified in this environment (minimum values taken from Table 5.5). In addition, PHASE^2 (Rocscience, 2011), the program used for the calculation of slope stability, is unable to accept values for fluid, other than water within the model, which may be a better representation of the conduit and reservoir however it cannot be represented.

5.3.2 Topography

Topographic models for the dome prior to collapse events at Soufrière Hills in July 2003 and February 2010 were constructed using digital photographs, in order to determine the shape of the dome (Figures 5.2 and 5.4), and the literature to identify the heights of identified peaks (Wadge et al., 2009, Stinton et al., 2014, SAC, 2010). Digital images taken from an automated camera at Windy Hill (NNW of the dome) from 1999 to 2003 (Figure 5.2) mean that a simplified dome geometry can be modelled for the dome in 2003 as shown in Figure 5.3 (Wadge et al., 2009). Slope angles are in good agreement with Wadge et al. (2009) who suggest that slopes in immediate proximity to the dome can reach angles of $40°$. The simplified dome structure for 2010 was reconstructed from photographs taken on 8 February 2010 taken from the Montserrat Volcano Observatory (Figure 5.4, (Stinton et al., 2014)) and from height information for the dome summit (SAC, 2010) and the surrounding topography (Figure 5.5, (Wadge et al., 2009)). A 40 m pyroclastic layer at the surface was modelled (Stinton et al., 2014), along with a hy-

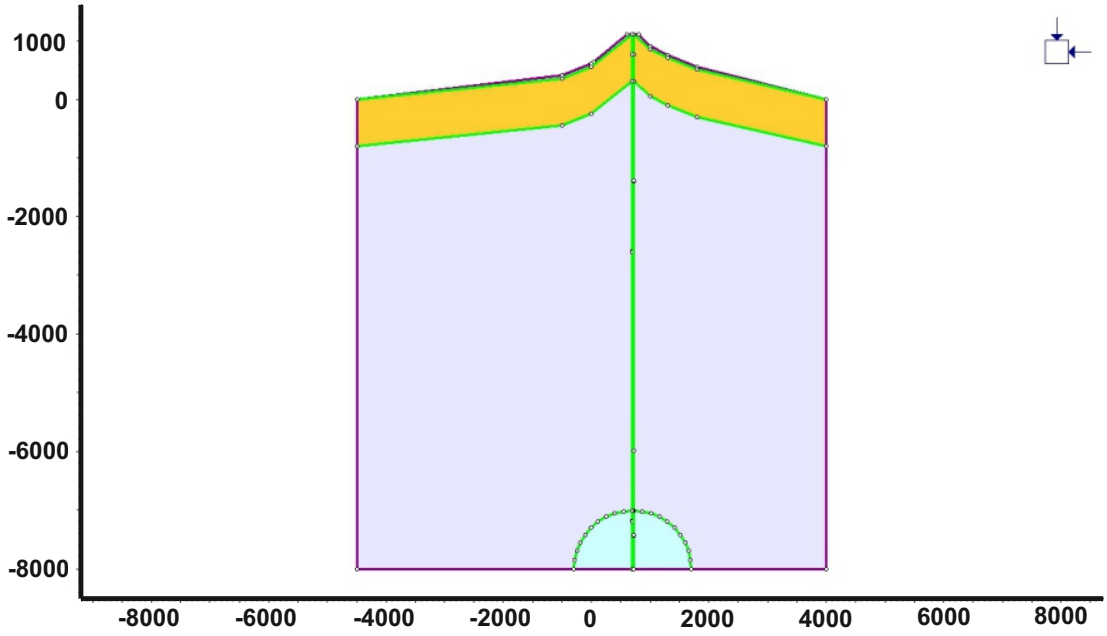

Figure 5.1: Model setup with hydrothermal layer and "reservoir" at depth (shown in blue) for Soufrière Hills in 2003. The andesitic core is represented by pale blue, and a pyroclastic layer 25 m thick at the top of the dome represents highly fractured deposits at the surface (green). The properties for each of these materials are shown in Table 5.5. Boundaries between materials are highlighted green.

drothermally altered layer extending to 800 m depth following Boudon et al. (1998).

The mechanical properties of the materials involved are detailed in Table 5.5. Boundaries within the model, defined as a change in lithology, are based on Boudon et al. (1998) who suggest a hydrothermal layer is likely to be active down to approximately 800 m below the summit, and (Wadge and Isaacs, 1988) who suggest a pyroclastic layer sits at the surface to a depth of 25 m. These deposits can be seen to taper away from the volcanic dome in Figures 5.3 and 5.5. This is because Wadge and Isaacs (1988) only describe the pyroclastic deposit layer in the area around the volcanic dome itself, and less material is likely to reach further down the talus slopes since the runout distance of pyroclastic flows can vary from less than 1 km to 7 km (Calder et al., 2002). The boundaries at depth simply follow the topography profile of the dome and surrounding talus, maintaining thickness. The boundaries are considered fixed, with no transitional qualities for model simplicity. In addition, no zones of weakness such as those envisaged which feed active fumeroles at the surface or previous collapse scars, are included in the model since the exact locations and properties of these zones are unknown.

(a) View of the dome on 5 June 2003

(b) View of the dome on 15 November 2003

Figure 5.2: View of Soufrière Hills from White's Yard by remote digital cameras before and after the July 2003 dome collapse. Images from Herd et al. (2005). Since no obvious collapse scar is seen, it must be assumed that the original failure event unroofed the highly pressurized volcanic system at depth which led to the further fragmentation of the dome, leaving little behind.

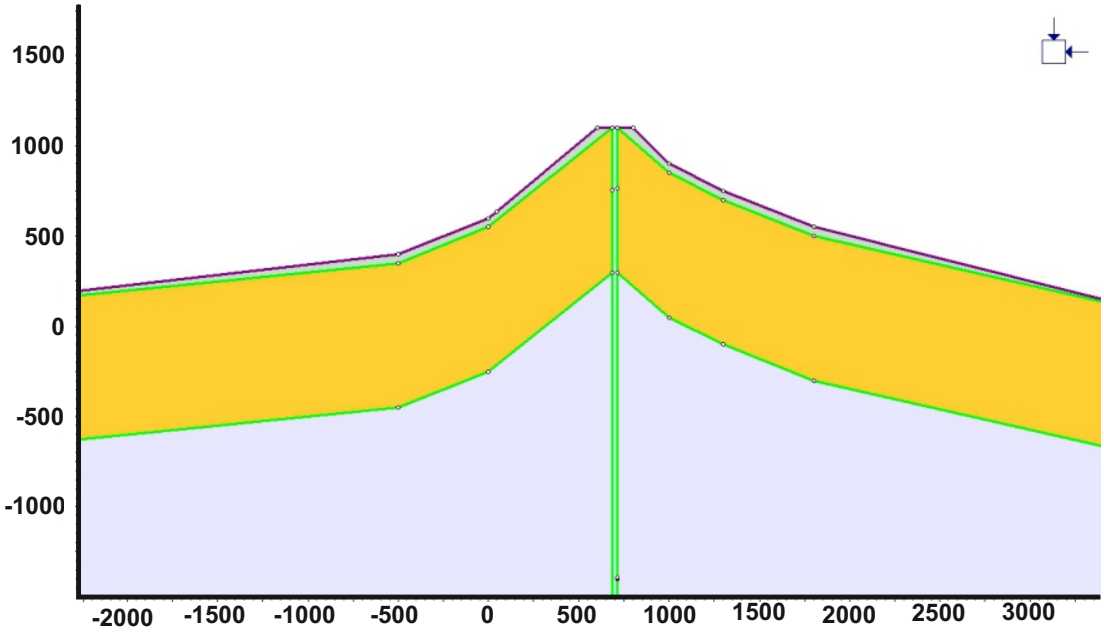

Figure 5.3: Final geological model for the dome at Soufrière Hills in July 2003. Dome shape taken from (Herd et al., 2005). A thin layer (25 m but exaggerated in this figure so can be seen) of pyroclastic material (green) sits above a hydrothermally altered layer which is 800 m deep (yellow), above the andesitic core (pale blue). Details of rock masses properties can be found in Table 5.5. A conduit of 30 m extends to 6 km depth where a circular reservoir (1 km radius) is found (shown in Figure 5.1), coloured light blue. Note the scale is with respect to the height of the volcanic dome, which in 2003 was approximately 1100 m (Wadge et al., 2009).

Figure 5.4: View of Soufrière Hills from MVO, 8 February 2010. MVO is 5.7km NW of the dome. TG is Tyers Gaunt, GM is Gages Mountain, CP is Chance's Peak. Image from Stinton et al. (2014).

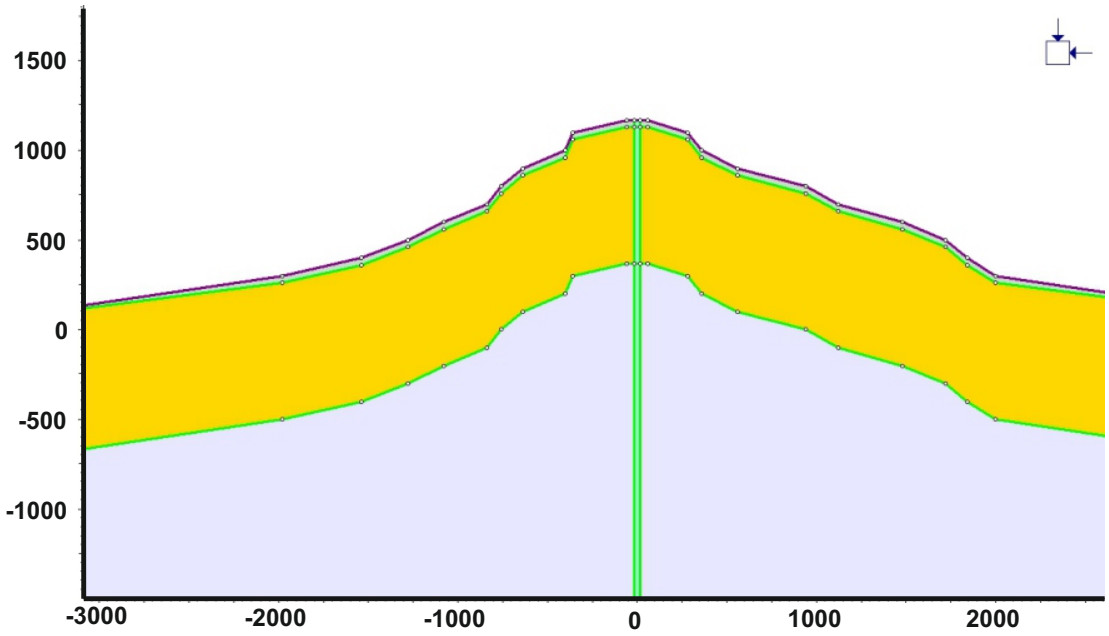

Figure 5.5: Reconstruction of the dome prior to collapse in February 2010. The andesitic core is represented in pale blue, the hydrothermally altered layer in yellow and a pyroclastic layer 40 m thick at the top of the dome is coloured green. The properties for each of these materials are shown in Table 5.5. Boundaries between materials are highlighted green. A conduit of 30 m extends to 6 km depth where a circular reservoir (1 km radius) is found, replicated from 2003. Note that the scale is with respect to the height of the volcanic dome, which in 2010 was approximately 1170 m (Stinton et al., 2014).

5.4 Slope Stability Analysis

Grey incidence analysis outlined that dome collapse events and instability at Soufrière Hills volcano is primarily a consequence of deep-seated magmatic processes as detected by low frequency seismicity. In order to investigate this further, and determine how much instability these processes could cause, an investigation into slope stability was carried out. Usually, slope stability is assessed using a Factor of Safety (F), which determines how close to failure the slope in question is, as as a ratio of the forces resisting failure and the forces driving failure and can be defined as:

$$\mathrm{F} = \frac{\tau}{\tau_{\mathrm{failure}}} \tag{5.8}$$

where $\tau = \mathrm{c} + \sigma_{\mathrm{n}}\mathrm{tan}\phi$ and $\tau_{\mathrm{failure}} = \mathrm{c}_{\mathrm{failure}} + \sigma_{\mathrm{n}}\mathrm{tan}\phi_{\mathrm{failure}}$. c is cohesion, σ_n is the normal force acting on the slope, and ϕ is the friction angle. If $F = 1$ or less, then failure is implied (Hammah et al., 2004).

Firstly, the simplest case for slope stability was investigated using Limit Equilibrium Methods to identify the most likely plane of failure within the volcanic dome. However, LEMs fail to provide any information about the mechanism of failure, and require a number of a priori assumptions (see Section 5.4.1). FEM were therefore constructed for the simple case of an andestic core with an overlying pyroclastic layer. The models were then extended to include saturation of the edifice since pore fluid pressure is thought to be important in generating instability, the introduction of a hydrothermally altered layer from the surface to 800 m depth as identified by Boudon et al. (1998), and finally the introduction of a conduit and reservoir at depth, although this was only used to suggest a difference in lithology at depth, rather than a pressure or temperature change (Section 5.4.2).

5.4.1 Limit Equilibrium Methods

Limit equilibrium methods (LEM) for calculating slope stability are popular due to their simplicity and accuracy. The methods involve splitting the slope into a number of slices, and applying appropriate equations (for forces and/or moment equilibrium) such that a failure surface can be identified (Matthews et al., 2014). A number of methods can be used to determine slope stability using LEM including: Bishop's modified method (Bishop, 1955); Janbu's generalised procedure of slices (Janbu, 1968); and Spencer's method (Spencer, 1967). Each method gen-

erates fairly similar results, with the Factor of Safety differing by no more than 12% between each method when the conditions of equilibrium are satisfied. One of the major limitations of using LEM however, is that the method provides no information on the magnitudes of the strains within the slope, or how the strain may vary along the slip surface (Duncan, 1996).

The program *SLIDE* (Rocscience, 2015) was used as a LEM to identify all possible slip planes within the models which could theoretically induce failure (using a grid search). Bishop's simplified method for calculating a Factor of Safety was used since failure in the volcanic dome is assumed to be circular which is well represented by this method, and there is little difference between this and other methods (Duncan, 1996), with a total number of 25 slices. The interslice force function used was half sine (default, which assumes that the shear forces will be higher in the middle of the slip surface than at the edges) and the failure direction was set from left to right in the models since this was the direction of failure observed at the time of collapse. The method searches for a "global minimum" slip surface, which represents the surface with the lowest Factor of Safety, and is therefore the surface that slip is most likely to occur along (Schaefer et al., 2013).

LEM analysis for both the 2003 and the 2010 domes at Soufrière Hills suggest that failure planes were most likely to develop within the pyroclastic and hydrothermal layer seen at the top of the dome (Figures 5.6 and 5.7). For July 2003 (Figure 5.6) the global minimum slip plane, which represents the failure plane with the minimum Factor of Safety given the input parameters, is shallow at several hundred meters deep at the maximum. Overall, the failure planes identified, all with a Factor of Safety of less than one, are shallow (within the hydrothermally altered layer of material which extends to a depth of 800 m) and suggest no interference with the solid andesitic core below (shown in pale blue in Figures 5.6 and 5.7). Figure 5.7 suggests that the collapse event in February 2010 was much larger than the event in 2003, removing more material if failure occurred along its global minimum slip plane. This was not the case: the July 2003 dome collapse event removed 210 million m^3 of material (Herd et al., 2005), whereas the collapse in February 2010 only involved the removal of 50 million m^3 (Stinton et al., 2014). However, the models do not allow for the additional removal of material due to explosive disintegration of dome material due to intense instantaneous pressure changes as the pressurized system at depth is unroofed with the initial removal of material in the dome collapse, which is believed to have been paramount in the July 2003 collapse (Herd et al.,

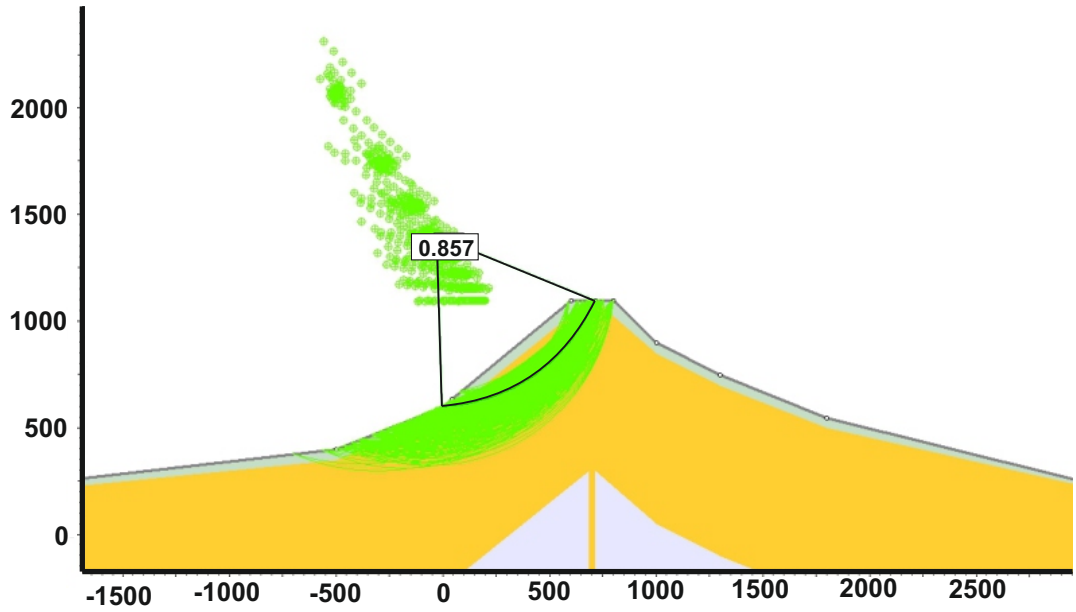

Figure 5.6: All identified slip planes for slope failure on Montserrat with a 25 m pyroclastic layer in July 2003. Each slip circle is depicted as the plane along which failure is likely to occur. Each slip plane has a corresponding pivot point above which determines the angle of the plane and extent of the surface within the modelled volcanic edifice. The slip planes and corresponding pivot points are on a colour scale dependent upon their Factor of Safety: all identified slip planes had a Factor of Safety of less than one. The global minimum slip plane is also identified, with the solid black lines connecting to its pivot point, which has a Factor of Safety of 0.857.

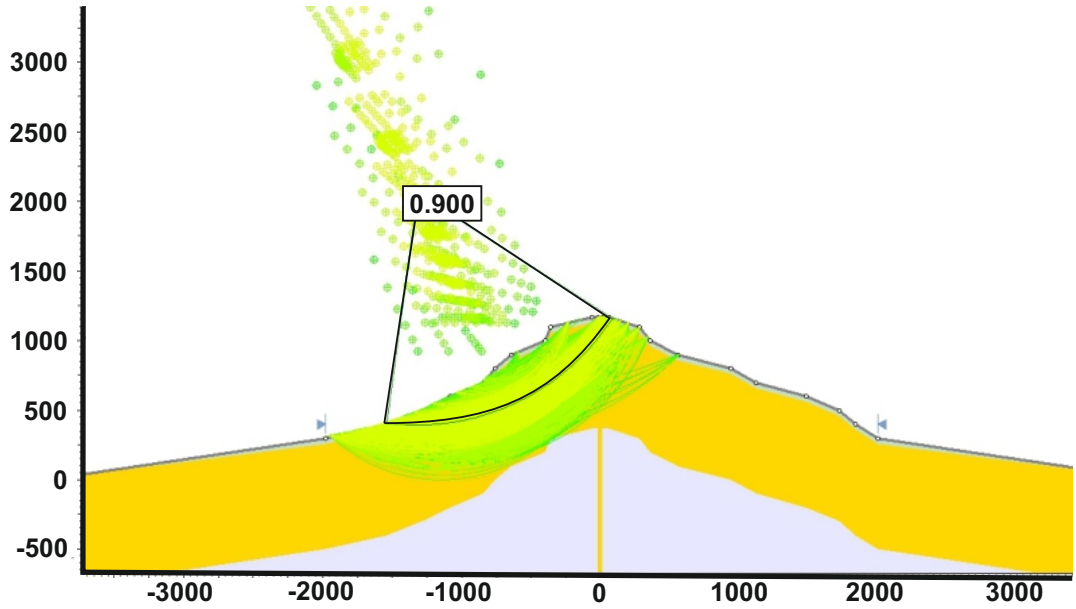

Figure 5.7: All identified slip planes for slope failure on Montserrat with a 40 m pyroclastic layer for February 2010. Each slip circle is depicted as the plane along which failure is likely to occur. Each slip plane has a corresponding pivot point above which determines the angle of the plane and extent of the surface within the modelled volcanic edifice. The slip planes and corresponding pivot points are on a colour scale dependent upon their Factor of Safety: those with a Factor of safety below one are coloured yellow and those above one are coloured green. The global minimum slip plane is also identified, with the solid black lines connecting to its pivot point, which has a Factor of Safety of 0.900.

2005).

5.4.2 Finite Element Methods

Finite Element models are now at the forefront of slope stability analysis techniques (Griffiths and Lane, 1999). One major assumption used in LEMs is that failure occurs through the sliding of a mass along a slip surface which is pre-defined (Rocscience, 2004). FEM calculations however require fewer *a priori* assumptions, in particular about the failure mechanism and location of the failure plane. FEMs also offer a more rigorous approach for defining stability in more complex slope problems such as awkward geometries (Griffiths and Lane, 1999). Griffiths and Lane (1999) state that the advantages of using FEMs over LEMs include:

1. No assumption is needed about the shape or location of the failure surface prior to analysis;

2. No assumption is needed about the interplay between inter-slice forces, since the model is analysed as a whole and not individual parts;

3. Providing realistic data is available about the failing materials, FEMs will give information about deformation at working stress levels;

4. The method is able to monitor progressive failure, rather than simply the overall shear failure;

5. Does not neglect the stress-strain behaviours of soils as LEMs do (Rocscience, 2004).

The Shear Strength Reduction Method

The program PHASE^2 (Rocscience, 2011) utilizes the FEM and analyses failure using a two-dimensional plane stress-strain method of elastic perfectly-plastic materials as defined by the Mohr-Coulomb failure criterion. Brittle failure is therefore reached when the Mohr-Coulomb failure envelope is overcome. Stresses output from the finite element analysis are compared to the Mohr Coulomb failure envelope, and if found to lie within it are assumed to remain elastic in nature. In contrast, those points in the two-dimensional model which lie on or outside of the failure envelope, are assumed to be yielding. Failure then occurs once enough elements are assumed to be yielding in order to allow a failure mechanism to develop (Griffiths and Lane, 1999). One of the main advantages of PHASE^2 is that shear strength reduction analysis can be carried out. The Shear Strength Reduction (SSR) technique undertakes a systematic search for a Strength Reduction Factor (SRF) which brings the slope being modelled to the limit of stability. In other words, the shear strength is progressively reduced until failure occurs (Rocscience, 2004), through reduction of the rock masses cohesion and the tangent to the friction angle in steps (Matthews et al., 2014). If the model fails to converge at this limit of stability within the number of iterations identified by the user (Griffiths and Lane, 1999), it is assumed that failure has occurred (Schaefer et al., 2013). The SRF is also a ratio of resisting to driving forces, however in comparison to F, it represents the value by which the forces would need to be reduced to induce failure. For example, if SRF=1.50, and failure is defined at 1, then the shear strength of the complex would need to be reduced by 50% in order to induce failure.

The shear strength at failure, assuming a Mohr Coulomb failure model, using the SSR technique can be determined by:

$$\tau_{\mathrm{failure}} = \frac{\mathrm{c_{failure}}}{\mathrm{SRF}} + \sigma_{\mathrm{n}} \tan^{-1} \frac{\tan \phi_{\mathrm{failure}}}{\mathrm{SRF}} \tag{5.9}$$

where SRF is the strength reduction factor, τ is the shear strength, c is cohesion and ϕ is the

friction angle.

The following method was used in PHASE^2 using a Gaussian elimination method to assess slope stability:

1. The initial estimate for the strength reduction factor is set to 1 which would suggest that the model is on the limits of failure;

2. Geometries are input as shown in Figure 5.3, derived from photographs, with a uniform, 6-noded triangle mesh (1500 to 5000 elements depending on x and y dimensions of the model);

3. Gravitational stress is applied to the model, so that the vertical stress above each individual finite element is based on the weight of material above it;

4. The boundary conditions of the model are set so that any boundary that does not represent the ground surface is fixed so that no slip can occur at these points;

5. Internal boundaries defined by a change in material properties to represent pyroclastic flow deposits, hydrothermally altered deposits and the conduit and reservoir are drawn;

6. Material properties are defined (Table 5.5);

7. Model is run to a maximum number of iterations of 500 to find the SRF.

The Gaussian elimination method was chosen as it produces an exact solution in a finite number of operations (LeVeque, 2006). A 6-noded triangle mesh was chosen for optimum computational in terms of time taken to compute vs. the accuracy of FEM. A greater number of elements would increase the accuracy for the identification of slip planes, but also slows the computation. Since 1500 elements was able to successfully identify slip planes in the model, no increase in accuracy was deemed essential, especially since the errors involved on the input parameters were so large, already biasing results. Gravitational stress was applied to all models to imply lithostatic pressure at depth. In FEM analysis, boundary conditions at the edges of the model are fixed in the x direction at the base of the model, and the y direction associated with this base, as indicated in Figures 5.8 and 5.9 by the small red triangles at these boundaries, meaning that no slip is able to occur at these boundaries. Interference from these boundaries (as can be seen in Figure 5.9 where pockets of yielded elements are identified at the intersection

of fixed and free boundaries) meant that the model was extended in both the x and y directions in order to avoid such boundary effects (e.g. Figure 5.14 where both the x and y axis have been extended to include the flanks of the volcano, rather than just simply the dome). Since movement was only anticipated in the volcanic dome area, other boundaries such as the flanks were set to fixed (see distribution of red triangles in Figure 5.14).

Initial FEM were constructed for the dome in July 2003 without the influence of the magma reservoir at depth, constrained by the physical properties in Tables 5.3 to 5.5. In this instance, only the dome itself was modelled, extending to limited depth (Figure 5.8). Under gravity alone, the slope of 2003 would not fail until the shear strength of the materials involved are reduced by over 50% of its original shear strength (SRF=1.51). Figure 5.8 suggests that no coherent failure mechanism would develop if this shear reduction was met, since no clear shear plane is present indicating sliding. Instead, the dome would deform under its own weight, a response known as gravitational spreading. This is unsurprising since grey incidence analysis has already suggested that the generation of a dome collapse event is manifested in deep-seated magmatic pressurization (Section 5.2.4) and therefore the raising of pore fluid pressures, which is not assessed in this model.

The percentage of yielded elements describes the percentage of finite elements within the mesh of the model which have deformed in a plastic manner (defined as a material which cannot return to its original state due to deformation applied). Figure 5.9 shows that most of the pyroclastic material which is inherently weaker deformed in a plastic manner, except for some small pockets on the flanks for the model of July 2003, thought to be induced form boundary conditions. The boundaries were then extended so that no such conditions existed. In addition, the material which sits below and within the dome at the highest point is also highly deformed since the weight of the overlying rocks is large enough to induce deformation. It is this material which has failed and therefore most likely to be involved in a dome collapse.

Finite Element Modelling in PHASE^2 for the dome at Soufrière Hills in February 2010 suggests that it was already at critical instability (SRF = 0.98), and therefore extremely vulnerable to failure. A clear failure plane has developed within the NE flank, which has maximum displacement values of 106.6 m (Figure 5.10). The Scientific Advisory Committee on Montserrat reported that the dome height had decreased from 1170 m to approximately 900 m due to the

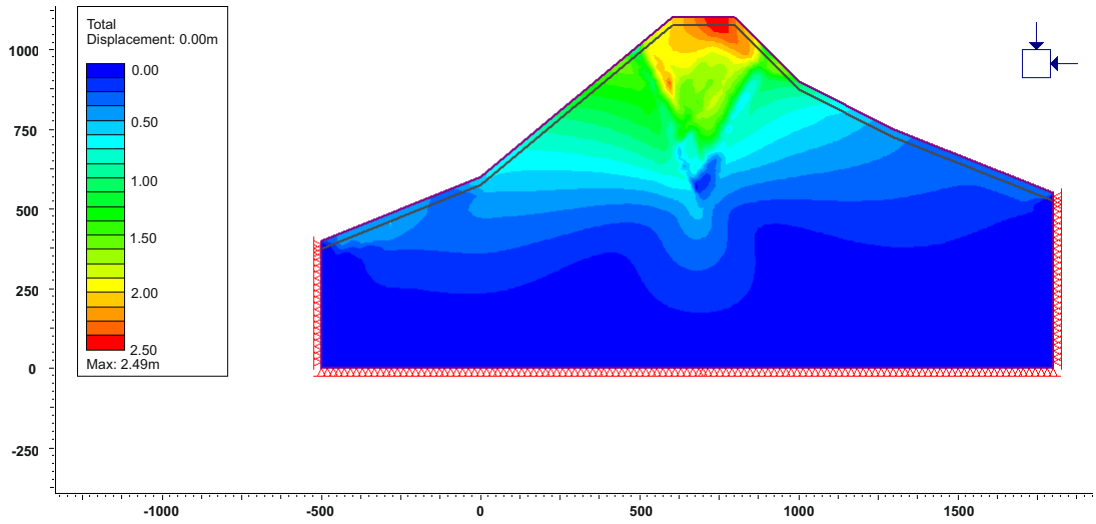

Figure 5.8: Total deformation under gravity alone for the dome in July 2003 with 25 m pyroclastic deposits. Total displacement is represented on a colour scale from 0.00 m (blue) to 3.00 m (red). Fixed boundary conditions are indicated by the small red triangles around the lower East, bottom and West of the figure. Geometry of the dome prior to collapse is indicated by the solid lines. Gravitational spreading causes the slumping of over 200 m at the top of the dome. SRF=1.51.

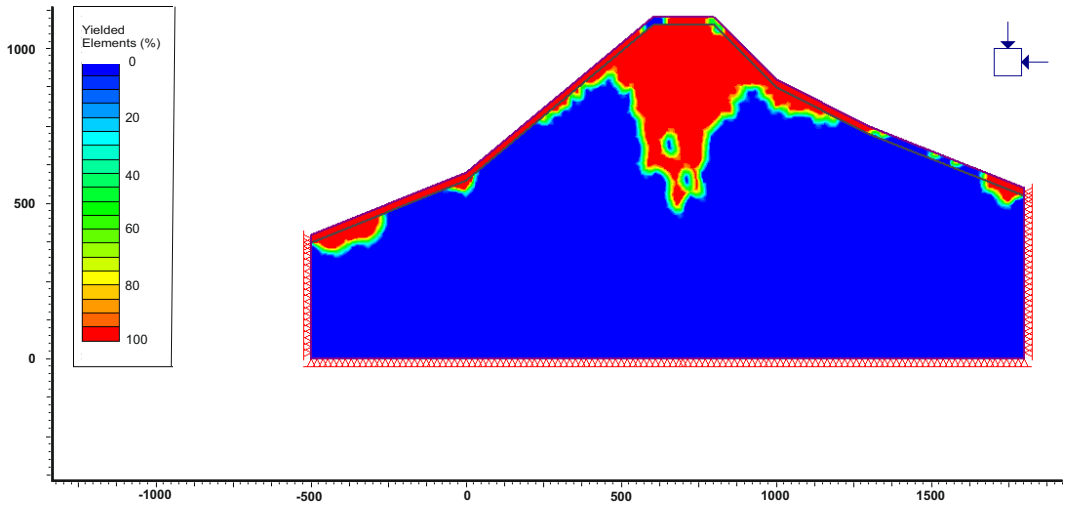

Figure 5.9: Deformation of 2003 dome showing yielded elements for 25 m pyroclastic deposits. Yielded elements are shown on a colour scale from 0% (blue) to 100% (red). Yielded elements mostly occur within the pyroclastic layer and beneath the dome itself into the andesitic core, which is caused by the overlying weight of rock due to gravity. Two smaller yielded sections are seen at the edges of the model which also affect the andesitic core. These are simply artefacts of the imposed boundary conditions.

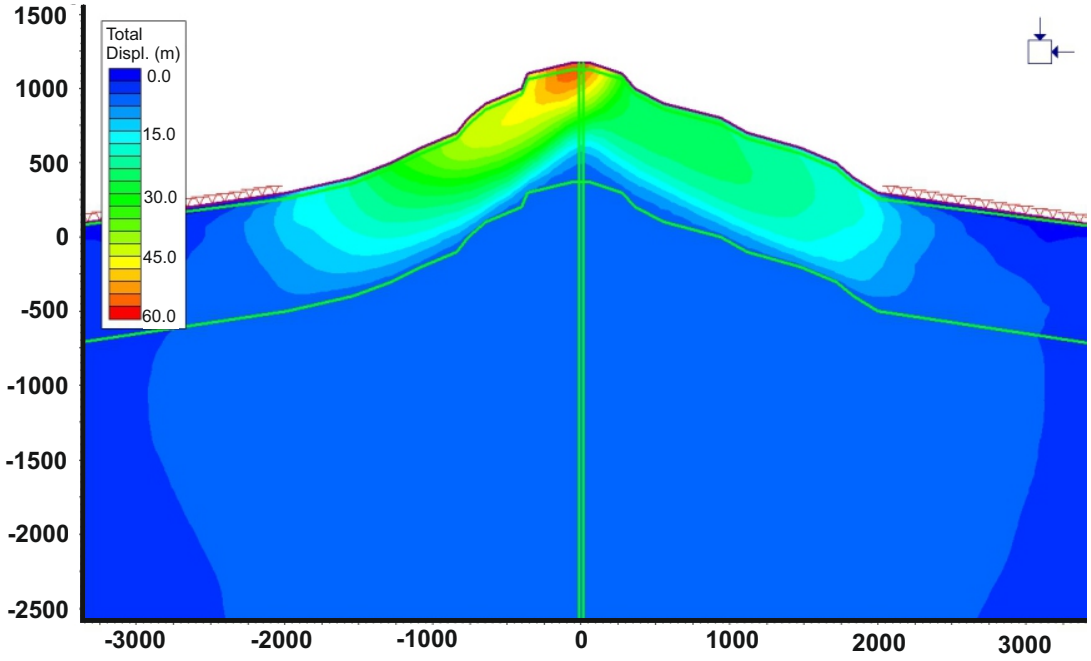

Figure 5.10: Total displacement for the 2010 Soufrière Hills dome, with deformation suggesting the lowering of the dome height by approximately 200 m. Total displacement is represented on a colour scale from 0.00 m (blue) to 60.00 m (red). Geometry of the dome prior to collapse is indicated by the solid lines, as are the internal boundaries between the andesitic core, conduit, hydrothermally altered rock and pyroclastic layer at the surface. SRF=0.98. A clear shear plane is developed, which is similar to the known failure geometry.

collapse (SAC, 2010). Displacement on the modelled dome lowers the dome height to between 800 m and 900 m, which suggests that geological spreading could have reduced the height of the dome over a long period of time based on these material parameters. It is possible that the previous vulcanian explosion events on the 5 and 8 February allowed a reduction in the rock mass cohesion, consequently inducing instability. This therefore supports the work of Stinton et al. (2014) who qualitatively suggested that the dome collapse was most likely generated by gravitational instability rather than abnormal pore fluid pressures at depth since gravity alone could have induced failure.

5.4.3 The Influence of Pore Fluid Pressure

In 2003, however, gravitational instability was unable to cause a collapse on its own, suggesting the need for other influential parameters in causing instability within volcanic domes. Numerical analysis and physical modelling using a sand heap as an analogue to represent a volcanic edifice has suggested that internal fluid pressurization may be key in promoting deep mechanical failure and instabilities (Thomas et al., 2004a). This supports the earlier conclusions of the

grey incidence analysis, where low frequency seismicity which is associated with fluid movement was the most important parameter in influencing a dome collapse event at Soufrière Hills volcano. The intrusion of magma in the far-field might be enough to raise pore fluid pressures within the volcanic edifice by infiltrating the system such that the failure envelope can be overcome, even though the intrusion and therefore the heat source driving the raised pore pressures, is spatially distant (Reid, 2004).

The brittle strength of materials containing a pressurized pore fluid (fluid within intergranular space or within small fractures) can be described as:

$$\tau_c = \tau_0 + (1 - \lambda)\mu S \tag{5.10}$$

as described by Hubbert and Rubey (1959), where τ_c is the critical shear stress required to produce a fracture or cause slip on a pre-existing fracture; τ_0 is the cohesive strength of the rock; λ is the pore pressure as a fraction of the lithostatic load; μ is the effective coefficient of friction; and S is the stress normal to the plane of the fracture. Day (1996) suggests a more useful derivative of equation 5.10 which expresses the critical angle of inclination (θ_c) upon which a block of material will begin to slide and fail as:

$$tan\theta_c = (1 - \lambda)\mu \tag{5.11}$$

Samuelson et al. (2008) cite an average co-efficient of friction (μ) of 0.67 for pyroclastic deposits at Soufrière Hills volcano which have a grain size of 0.5-1.0mm. Data already summarised in Table 5.5 does not include a co-efficient of friction, however this is intrinsically linked to the angle of repose by resolving the forces on a body on a slope through:

$$\mu = tan\theta. \tag{5.12}$$

Therefore, knowing that the maximum angle of repose for a slope made of solid andesitic core is 60° and for pyroclastic outlying deposits is 25°, the co-efficient of friction can be determined as 1.732 and 0.4663 respectively. Using these values, it can be shown that an increase in the pore fluid pressure as a fraction of lithostatic load (λ) lowers the angle of slope upon which failure will initiate (Figure 5.11). This however, assumes a planar slip surface, which is likely to be unrealistic in a volcanic setting where failure is most likely to be circular. Circular failure can be represented by individual slices in the slope creating polygons, which then follow pla-

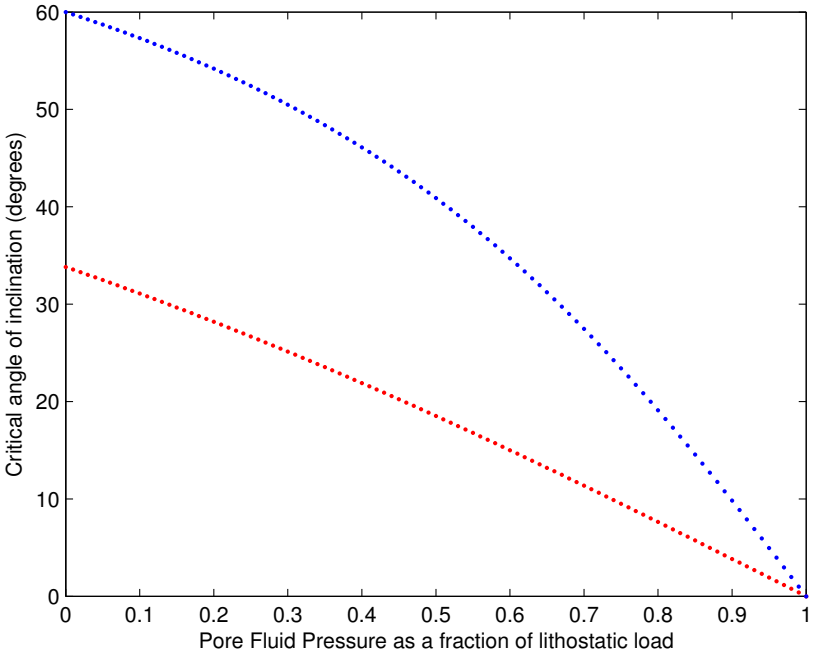

Figure 5.11: The effect of pore fluid pressure on inclination angle of repose. The upper blue curve is representative of the critical angle of inclination for the andesitic core rocks, and the lower red curve represents the pyroclastic deposits identified at Soufrière Hills.

nar failure. Therefore, it is assumed that an increase in pore fluid pressure in circumstances of circular failure will also cause failure of slopes at lower angles.

Hydrostatic pore fluid pressure (i.e. the pore fluid pressure as a result of the weight of overlying material) can be introduced in PHASE^2 through the introduction of a piezometric line (Figure 5.12). The pore water pressure is therefore equal to the depth below the piezometric line multiplied by the unit weight of water (Duncan et al., 2014) taken to be 9.81 kNm^{-3}. Rock mass below the line is therefore assumed to be saturated, and above it assumed dry. The piezometric line was modelled at 100 m arbitrary interval depths of the model to test its sensitivity, beginning at the surface and extending down to 800 m depth which is the extent of a proposed hydrothermally altered zone on Soufrière Hills (Boudon et al., 1998) (Table 5.6).

Only if the piezometric line is placed at the surface is it possible for failure to occur (SRF less than one). At all other depths, failure would only be possible with a large reduction in the shear strength of the materials. The failure geometry proposed by the model does not match the known failure geometry (Figure 5.13), with material appearing to deform under its own weight, rather than develop a clear shear failure plane at depth. Table 5.6 suggests that the SRF

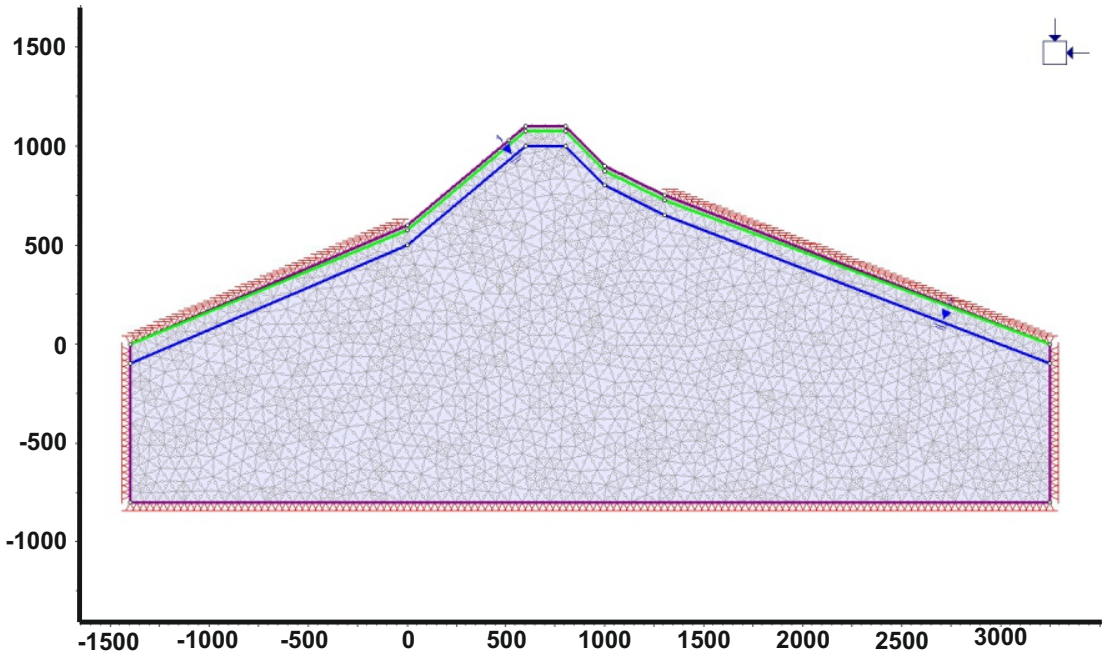

Figure 5.12: Introduction of a piezometric line to the 2003 model. Above the piezometric line is assumed to be unsaturated, whilst below the line is assumed to have an induced pore fluid pressure equal due to the weight of the water in the overlying strata. Note that the model is extended to 750 m depth to try to eliminate interference from boundary conditions of the model.

Peizometric Line (depth below surface in m)	SRF	Maximum Displacement (m)
0	0.81	16.089
100	1.45	17.732
200	1.7	15.696
300	1.75	13.658
400	1.72	12.267
500	1.72	11.235
600	1.76	10.419
700	1.73	10.100
800	1.72	9.849

Table 5.6: Changing SRF with depth of piezometric line

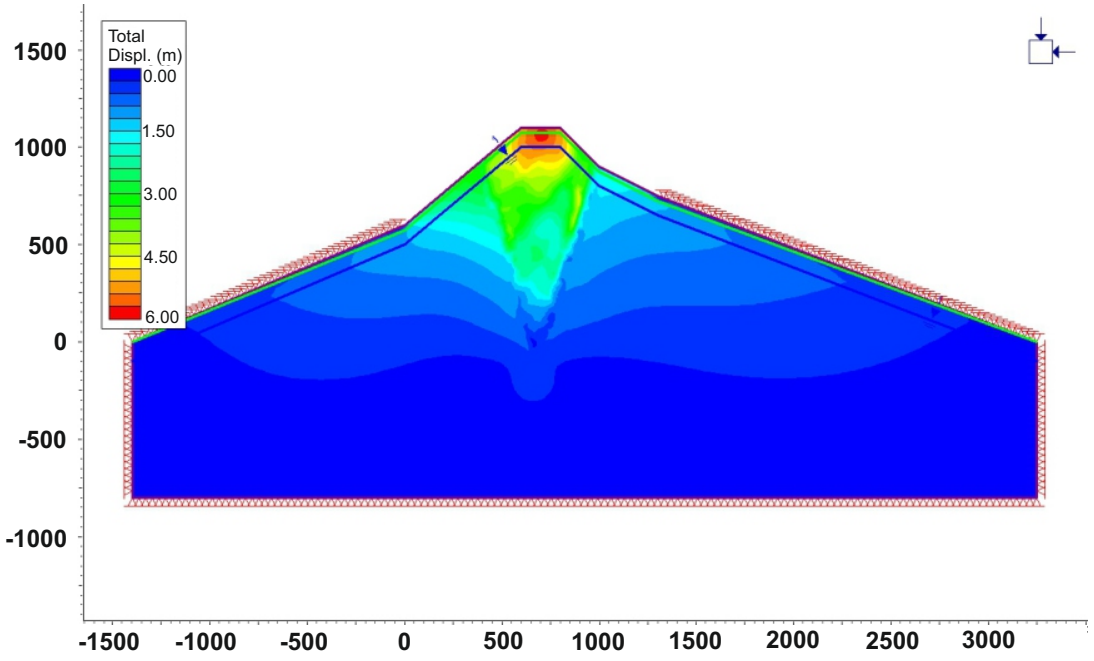

Figure 5.13: An example of the displacement generated with a piezometric line at 100 m depth, indicated by the solid line 100 m below the surface. Total displacement is represented on a colour scale from 0.00 m (blue) to 6.00 m (red). Fixed boundary conditions are indicated by the small red triangles around the lower East, bottom and West of the figure. The model is extended to 750 m depth to try to eliminate interference from boundary conditions of the model. Geometry of the dome prior to collapse is indicated by the solid lines. SRF=1.45.

stabilizes around 1.72 from 200 m depth, although the maximum displacement at the surface decreases with the depth of the piezometric line. The piezometric line is however an extremely simplified approach to include pore fluid pressures within the model. It assumes that the pore fluid pressure increases linearly with depth, and no other variation in the pore fluid pressure is taken into account. It also assumes that below the piezometric line is saturated with fluid water, which in a volcanic environment is not likely due to increase temperatures and pressures at depth. Therefore, is it unlikely that this is a true representation of the pore fluid pressures at depth within the volcanic edifice, which will be affected by the fracture network, conduit, intrusions and the movement of magmatic fluid, none of which is accounted for in this model.

Pore fluid pressure can also be introduced into the model using literature values for the saturated permeability (hydraulic conductivity) of the andesitic dome and pyroclastic flow deposits (i.e. supersaturated conditions). No specific values could be obtained for Soufrière Hills volcano directly. However Freeze and Cherry (1979) state that unfractured igneous rock has a conductivity of approximately 1×10^{-12} to 1×10^{-8} cm/sec, and that fractured igneous rock

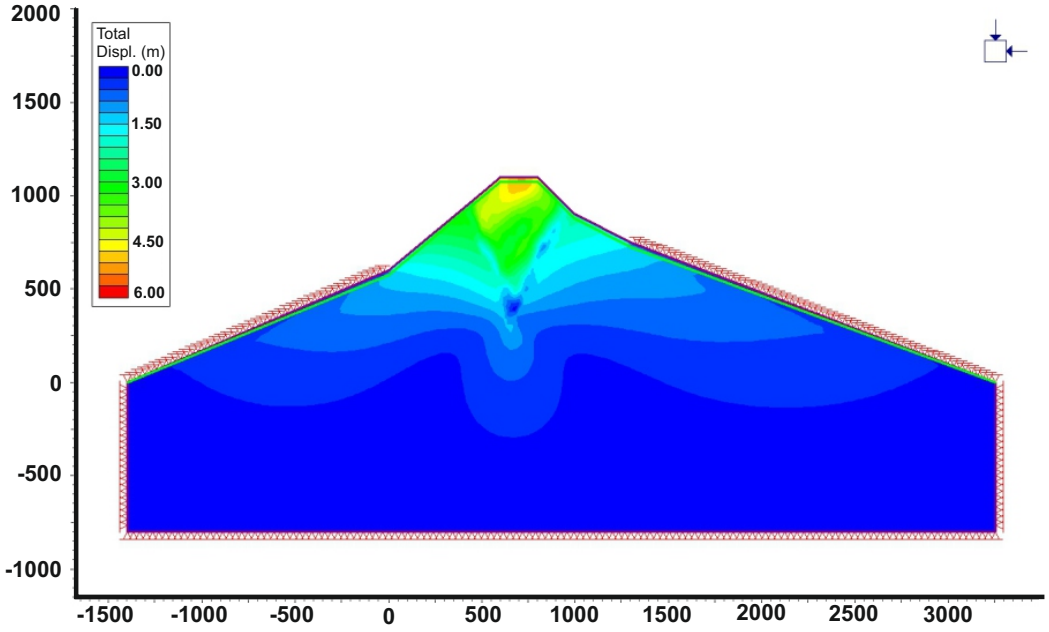

Figure 5.14: Total Displacement calculated for 2003 dome with 25 m pyroclastic deposits with saturated rock types. Total displacement is represented on a colour scale from 0.00 m (blue) to 6.00 m (red). Fixed boundary conditions are indicated by the small red triangles around the lower East, bottom and West of the figure. Geometry of the dome prior to collapse is indicated by the solid lines. The model is extended to 750 m depth to try to eliminate interference from boundary conditions of the model. Gravitational spreading due to the weight of overlying rock is clear from the deformation of material directly beneath the highest part of the dome. SRF=1.72.

has a conductivity of approximately 1×10^{-6} to 1×10^{-2} cm/sec. Therefore, the andesitic core of the dome was taken to be mostly unfractured igneous rock with an average conductivity of 1×10^{-10} cm/sec and the pyroclastic deposits were interpreted as fractured igneous rock with a conductivity of 1×10^{-6} cm/sec, and the hydrothermally altered rocks and the conduit were interpreted as a more fractured igneous rock with a conductivity of 1×10^{-4} cm/sec. The permeability function was set to "simple", which means that a permeability function is automatically assigned by the program based on the magnitude of the saturated permeability value given.

Figure 5.14 suggests that the introduction of pore water pressure equally distributed throughout the model based on the permeability of the rocks rather than simply using a peizometric line leads to the formation of a more defined failure slip plane where material would be moved from the top of the dome towards the west. The SRF is still high at 1.72 suggesting that the dome will not fail under these conditions alone. The maximum displacement is 9.9 m, with the removal of almost 200 m of material from the dome summit area. It is clear that the in-

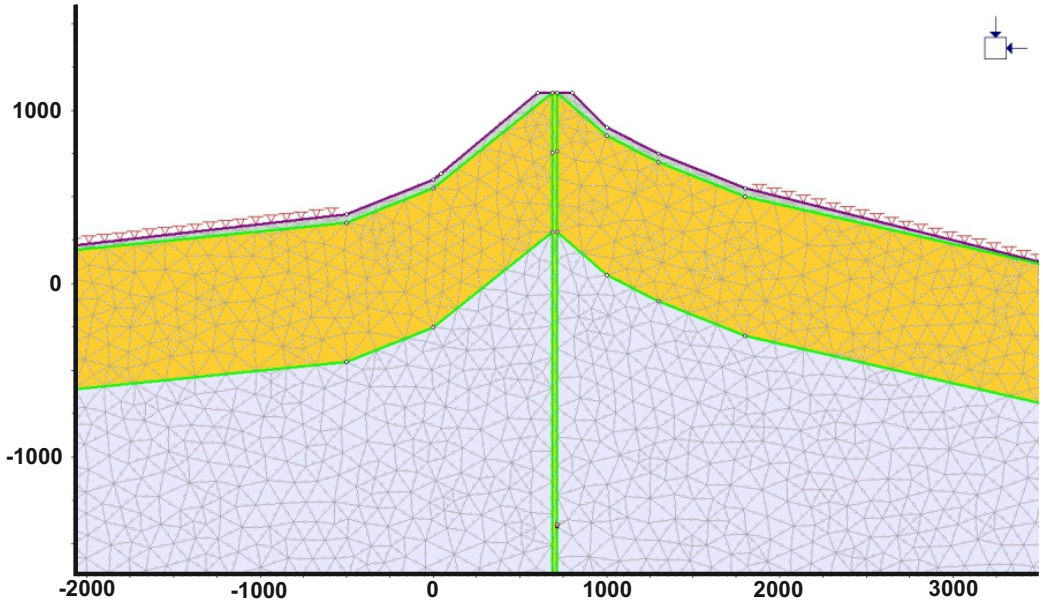

Figure 5.15: Zoom of dome structure with 25 m pyroclastic deposits and hydrothermally altered layer to 800 m for Soufrière Hills in 2003. Hydrothermally altered material is coloured yellow, the andesitic core is coloured pale blue, and a pyroclastic layer 25 m thick at the top of the dome is coloured green. The properties for each of these materials are shown in Table 5.5. The model is gridded with a uniform, 6-noded triangle mesh (5000 elements). Boundaries between materials are highlighted green. External boundaries which are fixed in the model are shown with red triangles. The position of the conduit can also be seen, but is only introduced in Section 5.4.5 and Figures 5.18 and 5.19.

troduction of pore fluid is essential in the model if it is to be as realistic as possible since it is not feasible that the rocks at depth will be completely dry, as surface evidence of pyroclastic flows generated from the fractionation of the dome rocks are highly altered by hydrothermal processes (Boudon et al., 1998).

5.4.4 The Influence of a Hydrothermally Altered Layer at the surface

Boudon et al. (1998) report that an upper hydrothermal alteration zone is likely to extend down to a minimum of 800 m depth at Soufrière Hills beneath the dome summit. This has been represented in the model as outlined in Figure 5.15, populated with the material properties found in Table 5.5. The introduction of a hydrothermally altered layer of material significantly reduces the SRF to 0.98 (Figure 5.16), suggesting that the volcanic dome is already unstable and likely to collapse. Deformation occurs within the upper layer of pyroclastic deposits and the hydrothermally altered layer only (Figure 5.17), suggesting that the andesitic core would be undisturbed. Field evidence however suggests that the collapse in July 2003 did disturb the andesitic core, parts of which were found amongst the pyroclastic flow deposits. A clear

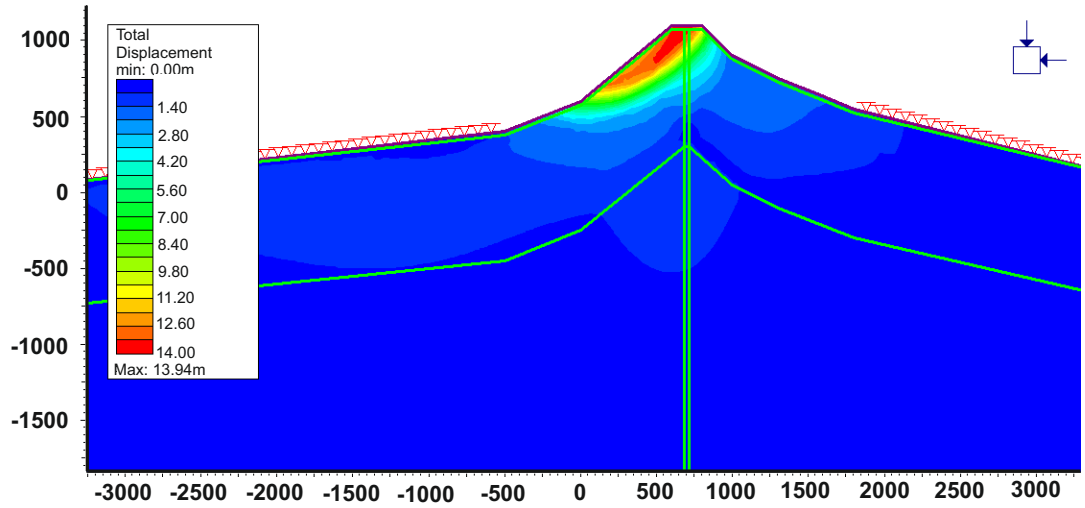

Figure 5.16: Total displacement for 2003 dome with a hydrothermal layer extending to 800 m below the dome summit. Total displacement is represented on a colour scale from 0.00 m (blue) to 14.00 m (red). Fixed boundary conditions are indicated by the small red triangles upper East and West of the figure on the external boundary. The fixed boundary continues to the base of the model, which is at 8km depth, as in Figure 5.1. Geometry of the dome prior to collapse is indicated by the solid lines, as are the internal boundaries between the andesitic core, conduit, hydrothermally altered rock and pyroclastic layer at the surface. SRF=0.87. A clear shear plane is developed, which is similar to the known failure geometry.

shear plane would have developed, which is is sharp contrast to Figure 5.8 where no such plane developed when only the pyroclastic deposits and andesitic core are modelled. The modelled failure geometry is similar to the known failure (Figure 5.2) with most material being lost towards the left hand side. In this case, SRF is equal to 0.87, which suggests that under these conditions failure would already have occurred. Since history tells us that the dome was in fact standing for a significant amount of time under such conditions suggests some fundamental problems with the interpretation of such models. This shall be discussed further in Section 5.4.6.

5.4.5 The Influence of a conduit and reservoir at depth

In this modelling, the introduction of a magma reservoir at depth and a connecting conduit to the surface is a conceptual consideration. These features do not introduce a pressure or temperature change (as would be expected in reality) and instead introduce another geological interface at depth. The reservoir and conduit have the material properties of the weakest rocks found in the volcanic environment (taken from Tables 5.1 to 5.5), since fluids cannot be represented in PHASE^2. The conduit and reservoir therefore represent zones of weakness within the andesitic core, rather than a pressurized source at depth. Modelling of a dome with a

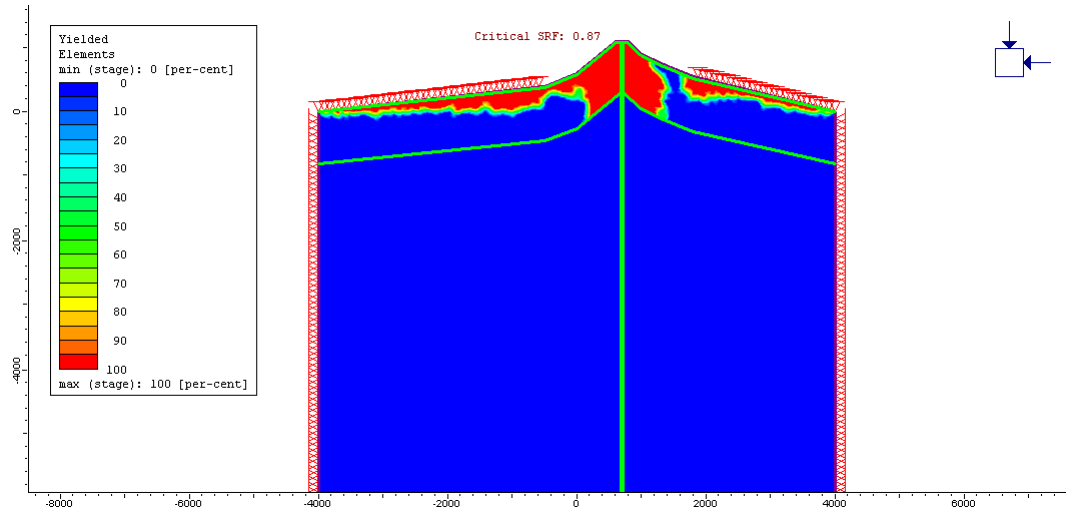

Figure 5.17: Deformation of 2003 dome showing yielded elements with 25 m pyroclastic deposits and a hydrothermally altered layer of material extending to 800 m beneath the dome summit. Yielded elements are shown on a colour scale from 0% (blue) to 100% (red). Yielded elements occur within the pyroclastic and hydrothermally altered layer, which are weaker than the andesitic core.

hydrothermally altered layer to 800 m below the summit as well as a conduit and magma reservoir at depth generates a critical SRF of 0.85 (Figure 5.18), suggesting that the dome would be in a critical state of failure under these conditions. The addition of the reservoir and conduit therefore lowers the SRF, although not significantly. Maximum displacement reaches 15.915 m with a clearly developed shear slip failure plane to the west (Figure 5.19), which is again similar to the observed failure plane in 2003 (Figure 5.2).

Using this geometry it is possible to determine the height at which the dome becomes unstable (i.e. SRF goes below one). The critical height summit for the asymmetrical geometry for the dome in 2003 is estimated at 1130 m (Figure 5.20, Upper panel). The summit of the dome ranged from 1076 m to 1116 m in the days prior to the collapse event (Herd et al., 2005), suggesting that it was very close to failure. The critical slope angles for inducing failure are estimated at 25.8° for the shallower dipping eastern flank, and 29.4° for the western flank of the volcano (Figure 5.20), which are far below the angles used at the dome summit in modelling detailed in Wadge et al. (2009) who suggest that slopes close to the vent can reach angles of 40°.

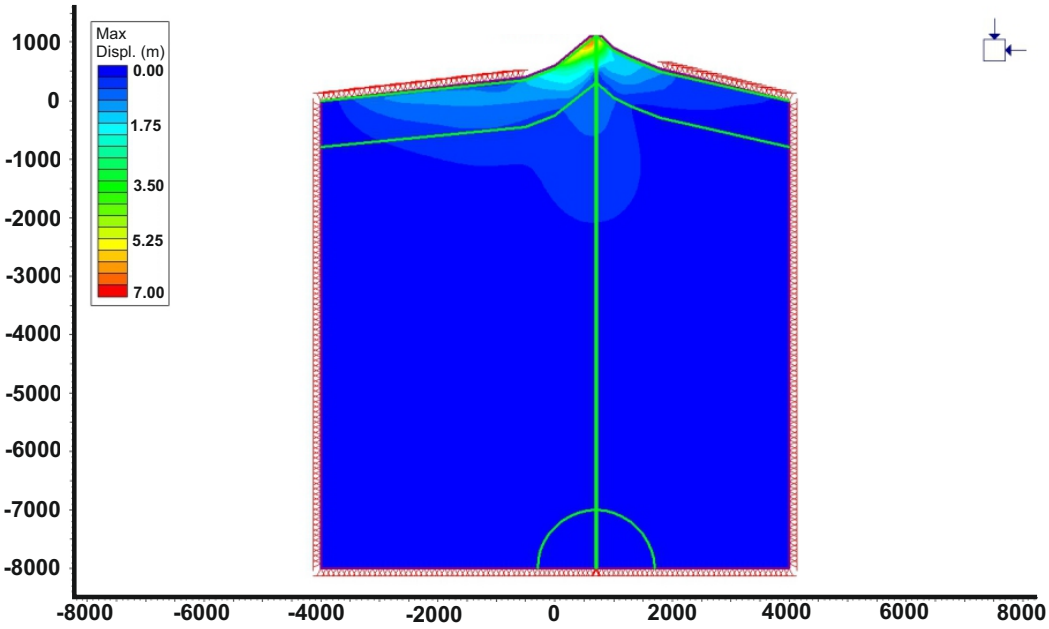

Figure 5.18: Total displacement for 2003 dome with a hydrothermal system and reservoir at depth. Total displacement is represented on a colour scale from 0.00 m (blue) to 7.00 m (red). Fixed boundary conditions are indicated by the small red triangles from the lower East, bottom and West of the figure on the external boundary. Geometry of the dome prior to collapse is indicated by the solid lines, as are the internal boundaries between the andesitic core, conduit, reservoir, hydrothermally altered rock and pyroclastic layer at the surface. SRF=0.85. A clear shear plane is developed, which is similar to the known failure geometry.

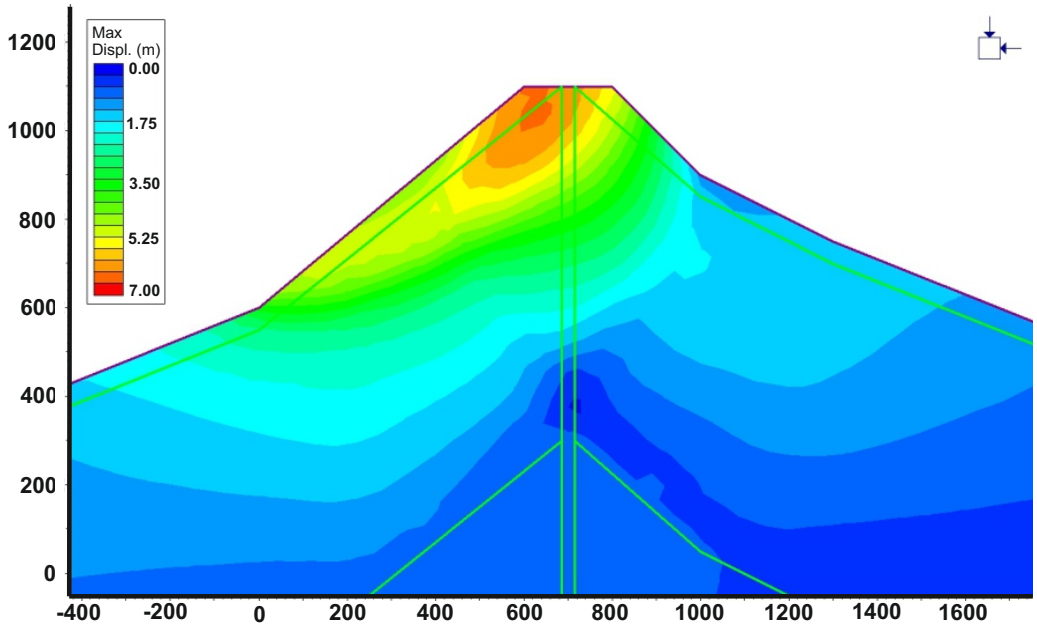

Figure 5.19: Development of a shear slip failure plane within the dome when the magmatic system at depth is introduced. Total displacement is represented on a colour scale from 0.00m (blue) to 7.00m (red). Geometry of the dome prior to collapse is indicated by the solid lines, as are the internal boundaries between the andesitic core, conduit, hydrothermally altered rock and pyroclastic layer at the surface. SRF=0.85. A clear shear plane is developed, which is similar to the known failure geometry.

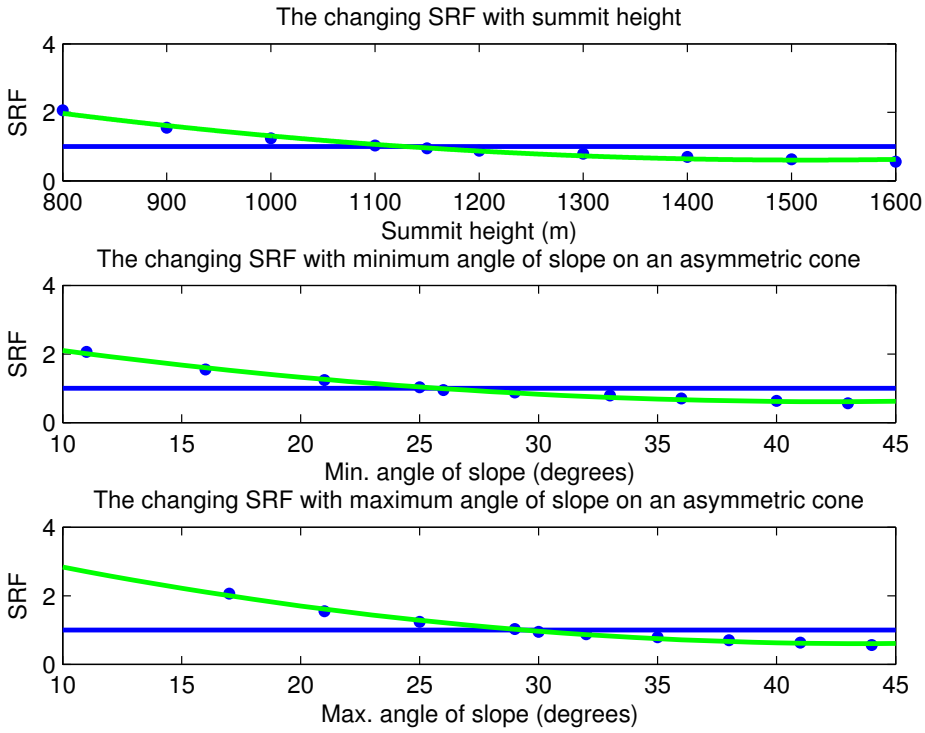

Figure 5.20: Changing SRF with increased dome height and slope angles in July 2003. The solid horizontal blue line represents a SRF of 1: above this line is stable, below is unstable and therefore represents failure. The point at which the green exponential curve crosses the line representing a SRF of 1 represents a critical value. *Upper:* Changing SRF with dome summit height *Middle:* Changing SRF with minimum angle of slope on an asymmetrical dome *Lower:* Changing SRF with maximum angle of slope on an asymmetrical dome.

5.4.6 Reliability of models

The results of FEM of the volcanic domes in July 2003 and February 2010 at Soufrière Hills volcano suggested that the domes were already in a state of failure since SRF was less than 1 (Figures 5.16, 5.19 and 5.10). This suggests that given the mechanical properties of the volcanic dome it should not have been standing for the amount of time it did, and should have failed under gravity alone. However, given the large errors associated with the mechanical input parameters it must be expected that these errors propagate through the model. Consequently, it is difficult to relate the mechanical properties to known materials at Soufrière Hills volcano in particular in relation to the interpretation of the deformed material. A dome collapse implies that material is lost from the dome, redistributed somewhere on the flanks. FEM in PHASE^2 only deforms the media and does not remove it. It is assumed that the weaker rocks included in the models (pyroclastic deposits and hydrothermally altered layer) will respond more to deformation, and therefore deform in a plastic manner, however no heterogeneities across these layers are considered in this analysis such that it is not possible to tell where such deformation is likely to be paramount. Grey Incidence Analysis suggested that low frequency seismicity, and by extension the movement of magma at depth, is important in the generation of a dome collapse (Section 5.2.4). The movement of magma at depth has not been incorporated into this modelling, and therefore no comment can be made on whether it increases instability of the dome. However, the addition of a zone of weakness at depth does increase the instability of the dome (Figure 5.19).

No heterogeneity across the layers in the complex is accounted for. In association with this, no fracture network has been incorporated, although it is likely to greatly affect instability within the complex. In addition, the complex has only been tested in two scenarios involving the presence of water: either the introduction of a water table (Figure 5.13) or under super-saturated conditions (Figure 5.14). In reality, neither of these scenarios are likely to be accurate in a volcanic environment. No clear water table is likely to be able to be defined due to the high pressures and temperatures experienced at depth, and the additional presence of a hot magma reservoir. For the same reason, the entire complex is unlikely to be super-saturated. The presence of water within the system is likely to be far more complex, with the distribution of dry and saturated conditions changing with time (as more or less magma is present, more or less material is sat within the dome complex etc.)

The simplistic nature of the modelling also means that some factors which may promote stability, and therefore could account for the volcanic domes in July 2003 and Febraury 2010 standing and remaining stable for longer than expected, are not included. For example, it has been noted that fractures within volcanic environment may be able to reheal themselves through the deposition of hot gas-particle mixtures which flow through such fractures and welds the fracture back together (Tuffen et al., 2003). This is one method in which the stability of the volcanic dome may be increased during the movement of magma, which has not been taken into account in this modelling.

5.5 Summary

The modelling of dome instability at Soufrière Hills volcano is complex, due to the number of interacting parameters which may affect the overall instability of the complex. Soufrière Hills volcano is perhaps particularly susceptible to collapse events due to its size, active hydrothermal system and fractured body which accommodates the build up of pore fluid pressures at depth. Grey system incidence analysis, which determines the relative importance of a number of parameters believed to influence the likelihood of a dome collapse is particularly suited to the volcanic environment since there is relatively little information regarding the mechanical properties of the rocks involved, which is essential for slope stability analysis. Grey incidence analysis suggested that the most important parameters in influencing a dome collapse event at Soufrière Hills volcano, based on data prior to the collapse event of June 1997, are the event rate of low frequency seismicity (indicative of magmatic fluid movement), tilt (indicative of changing slope angles), rainfall (which can infiltrate the dome complex and create instability through interaction with the magmatic reservoir) and degassing measurements (which can be indicative of increased volatiles within the magmatic body as well as increased pressurization). This would suggest that the dome collapse event of 1997 was primarily a consequence of deep-magmatic pressurization and not surface processes.

The dome collapse events of July 2003 and February 2010 were investigated using Finite Element Modelling to determine whether instability within the dome could be recognised. The model consisted of an andesitic core, a hydrothermally altered layer of andesite extending to 800 m depth, a pyroclastic layer of material sitting at the surface (ranging from 25 m to 40 m thick), and a conduit (30 m diameter) and spherical reservoir at approximately 6 km depth. The

domes in 2003 and 2010 were both at a critical stability prior to the collapse event, making them extremely susceptible to collapse (SRF <1). The dome in July 2003 was heavily influenced by an increase in pore fluid pressure, modelled by the introduction of saturated permeability of the rock masses involved. The dome in February 2010 was in a state of critical stability before the introduction of pore fluid pressures, suggesting that failure could have occurred due to gravity alone, in agreement with (Stinton et al., 2014). The models are however, extremely simplistic, only accounting for three different rock types, and ignoring the additional pressure exerted by the hot magma chamber at depth. This modelling does however highlight the use of Finite Element Modelling as a device for using slope stability as a monitoring tool for volcanic domes, in addition to routine measurements in seismicity, deformation and gas, since it may be able to indicate periods when dome collapse events are more likely.

Chapter 6

Linking depth and surface processes: A "Transfer" function

One of the fundamental assumptions of the FFM within volcanic environments is that the measured precursory signals at depth have a direct link to the failure that occurs at the surface. Here, the concept of a "transfer function" is introduced which identifies a plausible mechanism for the relationship between accelerating seismicity at depth and a dome collapse at the surface. The very nature of the transfer function means that it will have both amplitude and phase components, relating to the onset threshold and the length of time between the occurrence of the seismicity and the collapse event.

6.1 Linking the FFM from depth to surface

In order to more closely resemble the original intent of the FFM, one single active system has been used to forecast dome collapse events. This system is made up of seismicity which is generated by the same source mechanism and in the same location, and therefore can be detected by cross correlation and waveform similarity methods. This can lead to more confidence in the forecast (see Chapter 4) since sources of precursory seismicity are not mixed or averaged over time. The application of the FFM in volcanic environments is a method of describing the failure of the system at depth, with an apparent link between these processes and a failure at the surface. This "transfer function" between activity at depth and the surface was first alluded to by Voight (1988), who suggested that there is likely to be a time delay between the observed peak in precursory activity and a volcanic eruption at the surface with the application of the FFM.

The generation of low frequency seismicity has been attributed to a number of different mechanisms related to the movement of pressurized magmatic fluid at depth (e.g. a slip-stick mechanism at the conduit walls (Denlinger and Hoblitt, 1999, Iverson et al., 2006), the brittle failure of the magma itself (Webb and Dingwell, 1990, Goto, 1999, Neuberg et al., 2006) or the removal of fluid from a damage zone (Benson et al., 2008)), or may be attributed to the slow rupture failure of unconsolidated volcanic materials within the edifice (Bean et al., 2014). The acceleration in the seismicity prior to an eruption can therefore be attributed to an uncontrolled propagation of fracturing as fracture density increases (Kilburn and Voight, 1998, Kilburn, 2003, Holland et al., 2011), either within the edifice (which generates volcano-tectonic seismicity) or the magma itself (generating low frequency seismicity), or to the acceleration of the ascent rate of magma due to increased gas and crystal contents as it moves to shallower depths (Papale, 1999, Neuberg et al., 2006, Thomas and Neuberg, 2012). The acceleration in seismicity at depth needs to form a causal link with the eruption at the surface, in this case manifested as a collapse of the volcanic dome, in order for the FFM to be considered as a plausible forecasting tool, which accounts for exact processes occurring.

It would be a remarkable coincidence if all of the successful forecasts of volcanic eruptions using the FFM, whether in hindsight or real-time were chance occurrences, suggesting that some real link between the activity at depth and the surface must be plausible. If the generation of seismicity is caused by the movement of magmatic fluid (low frequency seismicity), it is possible to envisage an eruption occurring at the surface as more magmatic fluid makes it to shallower depths. This could be an explosive eruption if the top of the conduit and/or dome is blocked and therefore creates a large build up in pressure in the shallow edifice due to the intrusive body. If the seismicity is generated by the formation of fractures (high frequency seismicity), which coalesce as the fracture density increases, then new magmatic pathways may be created to the surface through which magmatic fluid can flow. Therefore both types of seismicity suggest a causal link between processes at depth, and an eruption at the surface.

6.2 A Transfer Function

Due to the complexity of each volcanic edifice, which is likely to change and evolve with time with ongoing geological processes, the transfer function is likely to be a unique value

for each volcano, despite probably being based upon common mechanisms within volcanic environments which manifest failure at depth to the surface. Here, one possible conceptual model that relates accelerating low frequency seismicity at depth to a large scale dome collapse at the surface is suggested for Soufrière Hills volcano. Since this is a repeated process at Soufrière Hills volcano, and has been for the past 20 years during its current eruptive episode, the conceptual model must be able to explain differences in precursory activity and differences in the collapse events themselves.

6.2.1 Parameters to consider

In chapters 3 and 4 it was shown that the precursory seismicity before each of these collapse events was different. In summary, low frequency seismicity prior to the June 1997 collapse occurred in distinct swarms and contained ten families of similar seismic events (Voight et al., 1998, Green and Neuberg, 2006). Using these families as forecasting tools provided accurate forecasts for the timing of the collapse event on 25 June (see Section 4.2). Seismicity prior to the dome collapses in July 2003 and February 2010 did not appear in swarms, but instead as near continuous repetitive seismic events. Only one family of events were identified in each of these cases. However the master events varied between the two cases, containing mostly energy below 5 Hz in 2003, and more significant energy from 0 to 10 Hz in 2010. In addition the length of average events of each of the families varied from $\approx$ 10 seconds in 1997 and 2003, to $\approx$ 30 seconds in 2010 (Sections 4.3 and 4.4).

Other precursors and factors likely to affect dome collapses at Soufrière Hills volcano (Section 5.1) varied prior to each of the investigated collapse events. In addition to cyclic swarms, Voight et al. (1998) noted tilt cycles related to the inflation and deflation of the dome in June 1997, with a cyclic period of 6 to 8 hours. Prior to the July 2003 collapse a pause of extrusive activity totalling one month was noted, as well as intense rainfall in the days prior to collapse (Herd et al., 2005). In direct contrast to this, the February 2010 dome collapse was preceded by over four months of intensive and explosive activity, which finally culminated in a collapse event (Stinton et al., 2014). The conceptual model for dome collapse events at Soufrière Hills volcano therefore needs to be able to explain each of these features, and why they occurred at each specific time.

Fundamentally the model must be able to explain:

1. The occurrence of LF seismicity at depth, which is repeatable - whether in swarms or not

2. The generation of families of LF seismicity which occur repeatedly at the same location over periods of hours to days, and why sometimes there is only one dominant active family and other times a greater number of families

3. The influence and significance of dome instability and rainfall, amongst other factors prior to the collapse events

6.2.2 The generation of low frequency seismicity

A number of models have been proposed to explain the occurrence of low frequency seismicity in volcanic settings. The model of Iverson et al. (2006) suggests that the generation of low frequency seismicity occurs as a magmatic plug moves incrementally upwards within a conduit due to the movement of buoyant magmatic fluid behind the plug. In this instance it would expected for seismicity to migrate with the movement of the plug, and therefore become shallower with time. This is not observed on Montserrat, where seismicity consistently occurs at $\approx$1500 m depth below the dome summit (Aspinall et al., 1998, Rowe et al., 2004, Ottemöller, 2008, De Angelis and Henton, 2011). In addition, families of similar seismic waveforms must occur within a small spatial extent in order to maintain their similarity, and single families have been observed being sustained over a number of hours and days. These observations at Soufrière Hills volcano are inconsistent with this model, since the same family of earthquakes would not be sustained over this period of time without major changes to the similarity of the waveforms. The evolution of cross correlation coefficients, such as that which were observed in July 2003, would require only a very small migration of the seismicity which would not be expected from the incremental movement of a volcanic plug, since it can still be classed as from the same family over the sustained period of time. This model also fails to explain the occurrence of a number of distinct families as observed in June 1997, which are repeatedly activated then deactivated.

The more recent model of Bean et al. (2014) suggests that slow rupture failure within unconsolidated volcanic material in the edifice can induce low frequency seismicity, whose waveform characteristics are fundamentally dependent upon the wave propagation path. It it is envisaged that families and swarms of low frequency seismicity develop due to slow defor-

mation at a number of points within the upper edifice where the stress is reduced which could be induced by gas influx, gravity or magma migration. On Montserrat, the seismicity systematically occurs at the same depth such that it would require the stress drop to be maintained at the same location over a number of years. In addition, no explanation is given for the clear acceleration in seismicity which has been observed prior to the dome collapse events studied.

The generation of low frequency seismicity has also been attributed to the brittle failure of the magma itself (Webb and Dingwell, 1990, Goto, 1999) through an increase in viscosity of the melt and/or high strain rates (Lavallée et al., 2008) as the melt enters a glass transition stage. In volcanic environments, conditions which may induce this glass transition stage may include: changes in crystal and/or bubble content of the magma (Goto, 1999); an increase in the ascent rate of magma (Neuberg et al., 2006); or through the introduction of a restriction in the conduit (Thomas and Neuberg, 2012). The brittle failure model allows for the acceleration in LF seismicity observed at Soufrière Hills prior to dome collapses, since accelerations in magma ascent has been shown to increase the strain rate within a volcanic conduit simulation, and therefore instigate the brittle failure of the melt (Neuberg et al., 2006). A much simpler way to induce an increased strain rate is to introduce a constriction within the conduit (Thomas and Neuberg, 2012). Such a constriction fits with observations at Soufrière Hills that LF seismicity consistently occurs at ≈ 1500 m below the dome summit (Aspinall et al., 1998, Rowe et al., 2004, Ottemöller, 2008, De Angelis and Henton, 2011), as well as the fact that multiple LF sources (i.e. families of similar seismic events) may be active at any given time, since a number of locations may exist where the strain rate threshold for brittle failure is overcome.

6.2.3 Preferred Conceptual Model

One possible conceptual model to explain the relationship between accelerating LF seismicity at depth and dome collapses at Soufrière Hills volcano is presented in Figure 6.1, which is primarily based upon the model of Thomas and Neuberg (2012). Low frequency seismicity is generated at depth due to the ascent of magma through a constriction in the conduit at ≈ 1500 m below the dome summit at Soufrière Hills volcano, which induces increased shear strain, in particular in proximity to the conduit walls. An increase in the shear strain rates induces brittle failure of the magma itself and therefore generates low frequency seismicity. Resonance within the conduit itself of the seismicity generated through the brittle failure of magma is able to produce the low frequency waveform content of the events observed (Ferrazzini and Aki,

1987, Jousset et al., 2003, Collier and Neuberg, 2006). As magmatic fluid ascends through the conduit, an acceleration in the number of earthquakes is generated as greater amounts of material pass through this constriction, and therefore a greater proportion of the magma column overcomes the brittle failure criterion. In addition, the coalescence of fractures within a small spatial extent is likely to become a runaway effect, as more join up to create fluid flow pathways (Main, 1991, Main et al., 1993, Main, 2000, Kilburn, 2003), adding to the acceleration in event rates observed. Since any number of geometric changes may occur at depth for the conduit, it is possible to activate a number of seismic sources at depth, and therefore to generate a number of families of similar seismic waveforms at any one time (Thomas and Neuberg, 2012). In addition, the reactivation of seismic sources over a number of days (i.e. the generation of swarms) suggests that the source of inducing seismicity is stationary, as a constriction in the conduit would be.

The coalescence of fractures will favour an increase in gas escape (Figure 6.1b) which causes the bulk magma viscosity to increase and depressurization of the magma column, and therefore slows the ascent rate. This leads to a deceleration in event rate. Hammer and Neuberg (2009) suggest this is the mechanism through which a number of swarms of the same earthquakes are repeated over a number of days, since analysis of individual swarms of activity suggest an initial acceleration in event rate followed by a deceleration (Section 3.4.2). As the fractures reheal within the magmatic column, for example through the precipitation of hot fluid within the fractures (Tuffen et al., 2003, Tuffen and Dingwell, 2005), shear strain can once again begin to build in the same location where fracturing and seismicity were occurring previously. This cycle can be repeated a number of times in order to generate a number of swarms at the same location, as was observed in June 1997.

However, the intensification of fractures around the conduit circumference may also generate a damage zone made up of highly fractured material. This may facilitate magma acceleration through the conduit, which may progress into aseismic frictional sliding (Scholz, 1998, Molina et al., 2004, Tuffen and Dingwell, 2005). The occurrence of aseismic movement may be related to a threshold in the proportion of the damage zone created to the rest of the magma column (Molina et al., 2004, Tuffen and Dingwell, 2005), suggesting the potential for the identification of such a threshold within the seismic event rate. This threshold forms the amplitude component of the transfer function. This is concurrent with observations at Soufrière

Hills, where some dome collapses are immediately preceded by a period of quiescence or of a decreased LF seismic event rate (e.g. July 2003: Figures 3.23 and 4.14). No explanation has been given for a cyclic change between seismic and aseismic movement (i.e. the generation of swarms) through the generation of a damage zone at the conduit circumference, and since the generation of a damage zone is time dependent it is envisaged that this mechanism is only responsible for the final period of quiescence seen immediately prior to dome collapses at Soufrière Hills.

This seismicity is related to the dome collapse at the surface since the ascent of magma raises pore fluid pressures within the volcanic dome due to thermal expansion of fluid close to the intrusion, as well as facilitating gas escape through newly generated fractures which causes a rise in the far-field pore fluid pressures. Accelerations in seismicity are often accompanied by cyclic inflation and deflation of the dome (measured by tilt) at Soufrière Hills, which suggests changing pressurization due to degassing magma at depth (Voight et al., 1998). An increase in gas flux at the surface during the precursory seismicity to dome collapses (Watson et al., 2000) is a reflection of the increase in the volume of the gas being exsolved at depth, and the increased volume of the fracture network at depth, facilitating its release. An increase in pore fluid pressure inherently increases instability within the volcanic dome since it lowers the overall effective lithostatic pressure (Simons et al., 2001). As magma migrates through the fracture network within the dome, it is likely to come into contact with water, whether in the form of hydrothermally altered materials, or infiltration from rainfall percolating through fractures from the surface, thereby adding to the increase in pore fluid pressure (Figure 6.1c). Eventually this leads to the volcanic dome becoming critically pressurized. The time taken for this to occur will depend upon the development of the fracture network at depth, the original pressures within the dome and the rate of magmatic fluid movement. It will also be dependent upon the connectivity of the fracture network to the surface. Once the threshold of pressurization is overcome and a pathway to the surface from the reservoir has been created, a collapse may occur (Figure 6.1d.

This conceptual model supports the most likely dome collapse scenario for the three collapses investigated: deep seated magmatic fluid causing increases in pore fluid pressures which generates instability of the volcanic dome. Rapid decompression due to the sudden removal of magma and rock will further induce fracturing and disaggregation of the dome rocks, in particular close to the parts of the conduit which have recently been excavated and weaker layers in

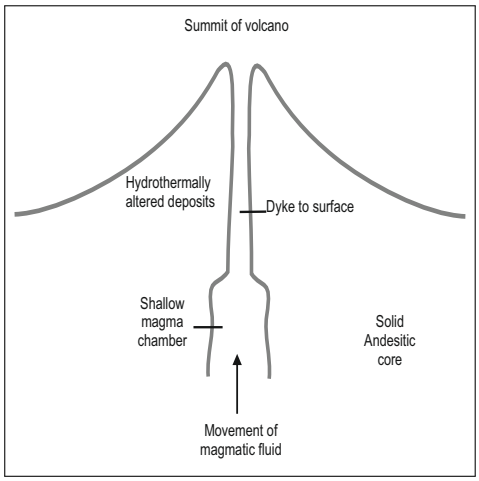

(a) Prior to magmatic intrusion

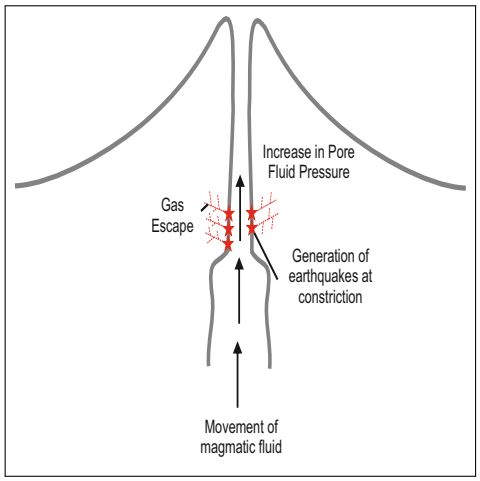

(b) Initial generation of seismicity due to the movement of magmatic fluid to the surface

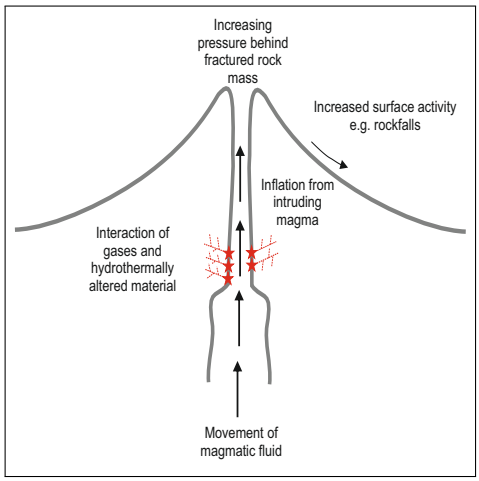

(c) Acceleration of seismicity as dome reaches critical pressure

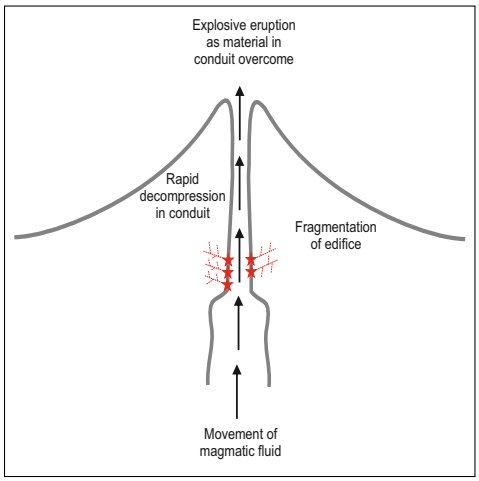

(d) Generation of a dome collapse event

Figure 6.1: Conceptual model linking accelerating seismicity at depth to a dome collapse at the surface for Soufrière Hills volcano. See Section 6.2.3 for full explanation.

the dome (such as those affected by hydrothermal weathering). This may add further volume to the collapse event.

6.3 Summary

Low frequency seismicity is generated at 1500 m depth below the dome summit repeatedly over a number of years due to a change in the geometry of the conduit at this depth (most likely a constriction) which causes an increase in the shear strain rate and therefore the brittle failure of magma at this point in the conduit. The generation of these fractures accelerates with time as more fractures coalesce creating a runaway effect, and as magma ascends through the conduit allowing a greater proportion to overcome the brittle failure criterion. Gas escape is enhanced through these fractures, especially as the magmatic fluid becomes shallower, leading to an increase in pore fluid pressures in this vicinity. This is further enhanced by the infiltration of rainwater if it occurs, and the interaction of the moving magmatic fluid with more saturated, hydrothermally altered rocks within the volcanic dome. Once the critical pressure within the volcanic dome can no longer be sustained, an explosive eruption occurs due to the continued ascent of magmatic fluid.

Chapter 7

Monitoring developing unrest: The case of Chiles-Cerro Negro

This chapter presents the application of the previously developed cross correlation method and forecasting using the FFM from Chapter 4 to Chiles-Cerro Negro volcano, which sits on the boarder of Ecuador and Colombia in South America. Very little information is known about the volcanic complex of Chiles-Cerro Negro which has had no confirmed eruptions in historic times, except for an active hydrothermal system expressed through active hot springs (Section 2.3). This chapter outlines how the cross correlation techniques can be used in another volcanic setting, and in particular used when unrest is still ongoing and the outcome is unknown.

Accelerated VT seismicity in October 2014, and in particular its relationship to a large high frequency seismic event on 20 October with M5.8 which occurred approximately 10km beneath the volcanic complex, has been investigated to determine whether similar seismic events were present during this unrest period, and analyse if there is any temporal or spatial migrations. Analysis of the acceleration of the event rate has drawn on principles of the FFM to determine the potential of generating false forecasts for volcanic events during the onset of this unrest. Similar VT seismic events have been identified during the analysis period (15 to 23 October 2014), with similar events becoming clearly organised into distinct temporal and spatial clusters on the 20 October, the day of the M5.8 earthquake. The accelerating similar VT seismicity prior to the large M5.8 earthquake could have acted as a forecasting tool, and the dominance of VT seismicity suggested little fluid movement at depth, and therefore lack of movement of magma towards the surface.

7.1 Data

Continuous seismic data for three stations (two broadband and one short period) over a period of 7 days (15 to 22 October 2014) were kindly provided by the Instituto Geofisico (IG-EPN) in Ecuador (Figure 7.1). This period was chosen for initial analysis as it sits right at the beginning of the unrest scenario, and includes the large M5.8 tectonic earthquake which occurred at an estimated depth of 10 km, less than 10 km south-east of the volcanic complex. The data were provided in February 2015, so although this analysis was not done in real time, it was done at a time of continuing unrest at a volcano where very little prior geological and geophysical information was known, and consequently the future unrest scenarios and their likelihood were uncertain at this volcano.

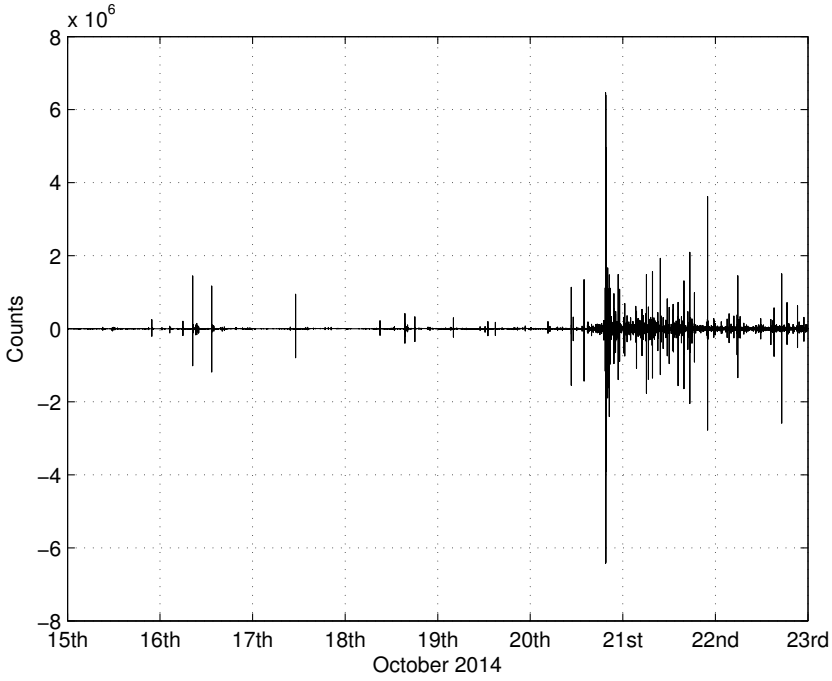

Figure 7.1: Continuous Seismogram from Station CHL1: 15 to 22 October 2014. Data has been low pass filtered between 0.5 Hz and 5 Hz to highlight low frequency seismicity. The M5.8 earthquake on 20 October can clearly be seen by the largest spike.

CHL1 and CHL2 are both three-component broadband seismometers, whereas ECEN is a short period, one component seismometer located on the Ecuadorian (south) side of the border (Figure 7.12). As discussed in Section 2.3, an increase in seismicity initially occurred in 1991, and was assumed to be related to the active hydrothermal system at depth. In July 2013 seismicity once more increased, and has remained elevated since. However, the sudden

rapid acceleration in the number of identified seismic events in October 2014 caused concern amongst scientists of the Instituto Geofisico and Ecuadorian authorities (Figure 7.2).

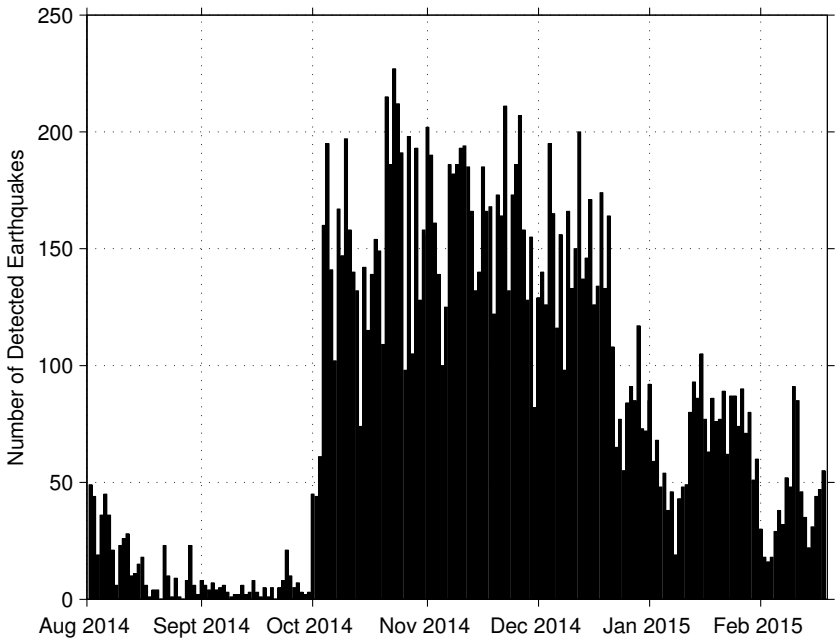

Figure 7.2: The number of events counted by an short-term average/long-term average detection algorithm between August 2014 and February 2015 at Chiles-Cerro Negro which could be located. Events were considered to be related to volcanic processes if within Latitude $0.75°$N to $0.9°$N and Longitude $-78.05°$E to $-77.85°$E. The summit of Chiles is located at $0.84°$N and $-77.9°$E and Cerro Negro at $0.84°$N and $-77.95°$E. The events had to be detected on a minimum of three stations in order to be located. This plot includes data from seismic stations in Colombia, for which continuous data was not made available.

On 20 October at 19:33:23 UTC a M5.8 earthquake occurred to the SE of the volcanic complex at a distance of ≈ 10 km. The earthquake was extremely shallow at a depth of 4.6 km (Pers. Comm. D. Sierra, IG-EPN, April 2015), although according to the USGS, it could have occurred at a depth of up to 14 km. The moment tensor solution suggests a thrust earthquake with a small component of strike slip, with nodal planes dipping $\approx 50°$ (Figure 7.3) (GFZ-Potsdam, 2014). On the previous day (19 October) approximately 1400 seismic events were detected by the Instituto Geofisico, and approximately 100 could be located (located events only shown in Figure 7.2). On 20 October, over 6000 events were detected with approximately 200 being locatable, suggesting a potential change in stress conditions at depth related to the M5.8 seismic event (Pers. Comm. S. Hernandez, IG-EPN, March 2015).

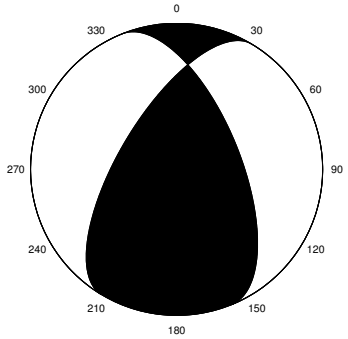

Figure 7.3: GFZ Moment Tensor Solution: M5.8 earthquake: 20 October 2014 at 0.79 N -77.89 E, depth 14 km. Solution estimated from information at 58 seismic stations. Nodal plane 1 = strike 211, dip 54, slip 128, Nodal plane 2 = strike 338, dip 51, slip 50

7.2 Picking Events from the Continuous Record

Seismic events are routinely picked from the continuous seismic record at the Instituto Geofisico using a detection algorithm, although the parameters of this were not made available. The number of waveforms identified by the Instituto Geofisico was available, but not the actual waveform signatures. Consequently, a simple STA/LTA algorithm (for general details of STA/LTA see Section 3.4.1) was applied to the continuous seismic data in order to detect individual waveforms (Figure 7.4). Waveforms are detected through a short term average (STA, 0.33 seconds) to long term average (LTA, 60 seconds) ratio triggering algorithm, which tries to identify peaks in amplitudes (STA) of the seismicity above the background (LTA). The parameters used for this algorithm are shown in Table 7.1. When the ratio between the short term average and the long term average amplitude of events exceeded 10 (i.e. the short term average was at least ten times the amplitude of the long term (background) amplitude), an event was "triggered" in the continuous data. The end of the seismic event was determined as when the ratio dropped below 5 again. If the ratio was below this value, the signal was considered to be mostly noise (confirmed by visual inspection of the continuous data). Two seconds were added to the beginning of the signal, and 10 seconds to the end, to ensure the entire triggered event had been captured.

The Instituto Geofisico recorded 114 seismic events using their detection algorithm on 15 October 2014. Using the STA/LTA parameters in Table 7.1, 51 seismic events were identified. Significantly fewer events were detected using this algorithm compared to that used by the Instituto Geofisico, however lowering the ratio value at which events would be detected only

resulted in significant increases in noise, and not in waveform identification.

Parameter	Value given	Units
Sampling Interval	1/100	Seconds
Beginning time of signal	0	Seconds
End time of signal	Dependent on length of input signal	Seconds
Short term averaging window length	0.333	Seconds
Long term averaging window length	60	Seconds
Value of STA/LTA ratio that triggers	10	
Value of STA/LTA ratio that detriggers	5	
Time buffer added before triggering time	2	Seconds
Time-buffer added after detriggering time	10	Seconds
Minimum window length of any triggered section	10	Seconds
Time between trigger and detrigger that must be exceeded in order for the triggered section to be reported	10	Seconds

Table 7.1: STA LTA parameters for detecting events at Chiles-Cerro Negro

Date (2014)	CHL1	CHL2	ECEN
15 October	51	9	-
16 October	66	26	-
17 October	21	2	664
18 October	55	38	944
19 October	49	33	479
20 October	597	219	687
21 October	820	234	-
22 October	604	322	-

Table 7.2: The number of events identified from 15 to 22 October 2014 at Chiles-Cerro Negro using an STA/LTA algorithm. Only 4 days of continuous data was made available for station ECEN during the investigated time period.

The total number of events identified with the parameters identified in Table 7.1 through an STA/LTA algorithm is presented in Table 7.2. At stations CHL1 and CHL2 a dramatic increase occurred in the number of events on the 20 October 2014. Figure 7.4 (lower panel) suggests that the majority of these events were detected after 15:00, 4 hours prior to the M5.8 earthquake that was felt in the area. This may be indicative of stress changes at depth as a result of this

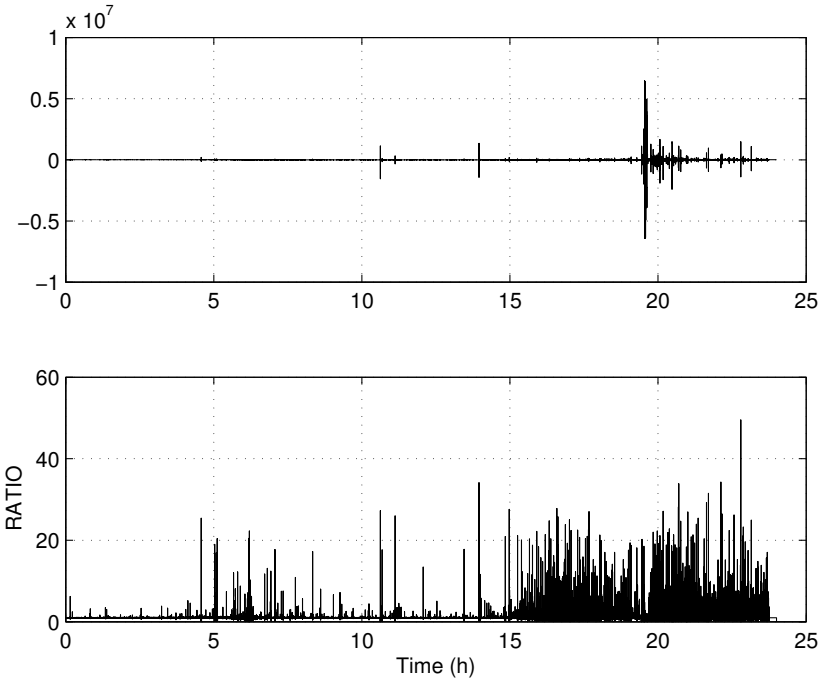

Figure 7.4: STA/LTA event detection algorithm for 20 October 2014, Station CHL1. *Upper*: Continuous seismogram (24 hours) from CHL1 on 20 October 2014. The y-axis is Counts since the calibration factors and poles and zeros are not known for the sensor. The M5.8 event at approximately 19:30 can easily be distinguished. *Lower*: Ratio of the STA to the LTA value with time. When the ratio value reaches over 10, an event is "triggered", represented by the spikes, which is then extracted from the continuous seismogram as an individual event.

large tectonic event. The increase in event numbers is less obvious at Station ECEN, which appears to have a fairly constant number of events recorded each day during the observation period (Table 7.2). Station ECEN sits upon much steeper land at a higher elevation compared to CHL1 and CHL2, and is also in much closer proximity to the dome summits than either of the broadband stations (Figure 7.12). For this reason, it is possible that ECEN identifies a greater number of events which are smaller and occurring in the dome summit region, and therefore attenuated by the time the seismic waves reach the stations further away.

7.3 Detection of Similar Events

The events identified using the STA/LTA trigger algorithm were cross correlated using the method presented in Section 4.1. Each day was individually cross correlated with every other event on that day. An example of the resulting cross correlation matrix is shown in Figure 7.5 which represents all of the seismic events identified on 19 October 2014 cross correlated with

one another. Those which are significantly similar (have a cross correlation coefficient above 0.7) are shown in colour.

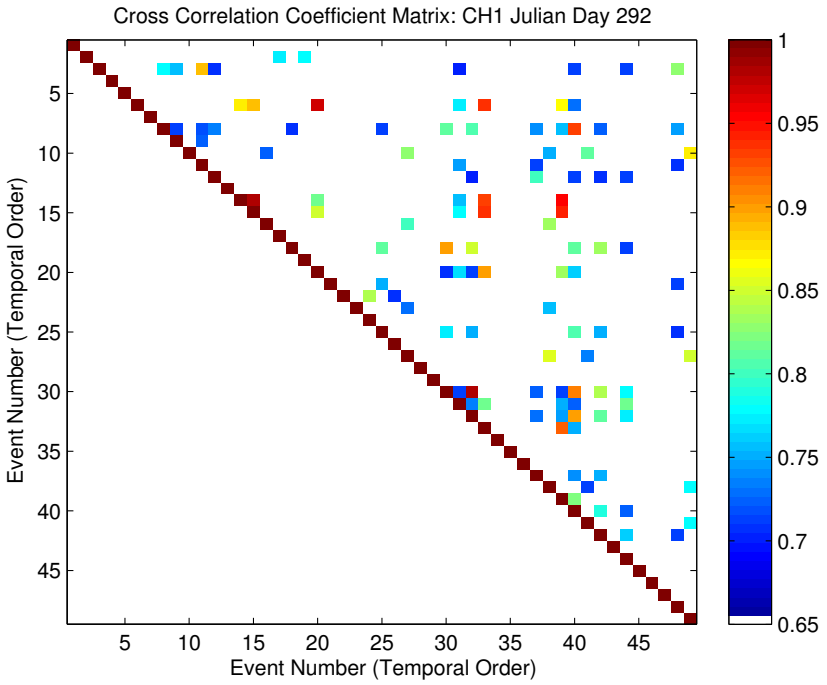

Figure 7.5: Cross Correlation Matrix of events identified using the STA/LTA algorithm: 19 October 2014, CHL1. A total of 49 events were identified and are shown in temporal order along the x and y axis. Events with a cross correlation coefficient of greater than 0.7 are shown on a colour scale, with those close to one being more similar. The autocorrelation of each event with itself is shown in dark red along the diagonal and is equal to a cross correlation coefficient of 1.

A distinct difference is seen in the cross correlation matrix for the 20 October 2014 (Figure 7.6) which is the day of the M5.8 earthquake, compared to the correlation matrix of the day before (Figure 7.5). In addition to the day containing many more identified seismic events (over a twelve-fold increase in the number of events), the similar seismicity is distinctly organised. Similar seismicity is clustered around the diagonal in a number of groups indicative of an evolving cross correlation coefficient, which may suggest an evolving source at depth either in space or with mechanism (Caplan-Auerbach and Petersen, 2005), for example a change in the trigger mechanism or frequency content of the waveform induced from rheological changes in the magma.

Using the technique of Green and Neuberg (2006) to identify families of similar events and then remove them from the matrix such that all events become grouped into different families,

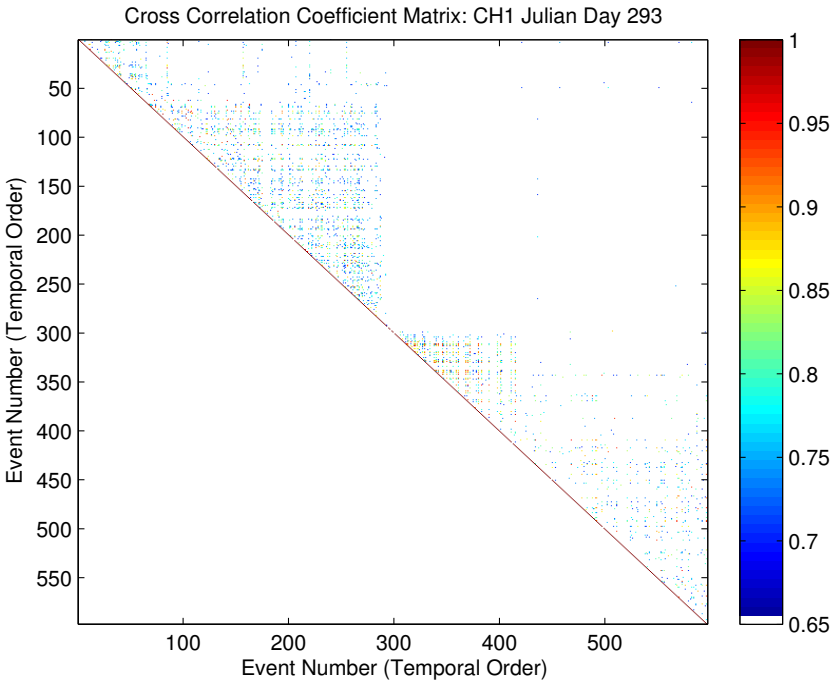

Figure 7.6: Cross Correlation Matrix of events identified using the STA/LTA algorithm: 20 October 2014, CHL1. A total of 597 events were identified and are shown in temporal order along the x and y axis. Events with a cross correlation coefficient of greater than 0.7 are shown on a colour scale, with those close to one being more similar. The autocorrelation of each event with itself is shown in dark red along the diagonal and is equal to a cross correlation coefficient of 1. Distinct clusters of similar events can be identified, thought to suggest a temporal evolution in the dominant similar seismicity.

45 families of events were identified on 20 October alone. Each of these families contained significantly different waveforms from other families. The number of events within each family ranged from a minimum of 5 up to a maximum of 46 events, which all had a cross correlation coefficient greater than 0.7 with one another. The stacks of these events and the average master events generated from the stack of these two end members (small and large numbers of events in the family) are shown in Figures 7.7 and 7.8. Clear differences can be seen in the waveform shapes, although both stacks suggest a fairly clear P- wave onset. Spectral analysis revealed that these events did contain a significant amount of energy between 5 and 15 Hz, which is more characteristic of volcano-tectonic earthquakes which are generated through the brittle failure of the country rock (Lahr et al., 1994, Arciniega-Ceballos et al., 2003) (see Section 1.2). Families which contained three or less events were discarded due to their infrequent temporal nature. Five to seven families of events were identified on each day from 15 to 19 October, significantly lower than the number detected on 20 October. Similar seismic events at other Ecuadorian volcanoes appear to not have been reported thus far in the literature, and this is certainly the first time that similar seismic events have been identified at Chiles-Cerro Negro.

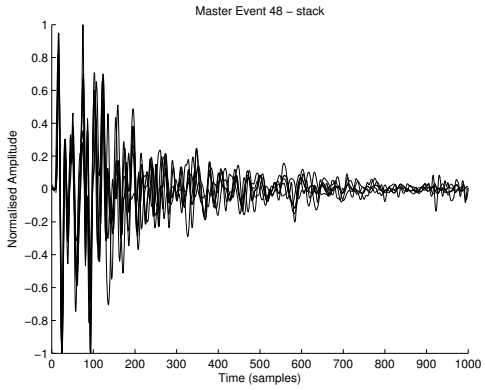

(a) Stack of similar events identified from STA/LTA ratio algorithm on 20 October 2014. Each event has a cross correlation coefficient of greater than 0.7 with one another. Each event is aligned at the point of maximum cross correlation. A total of 5 events were used in the stack.

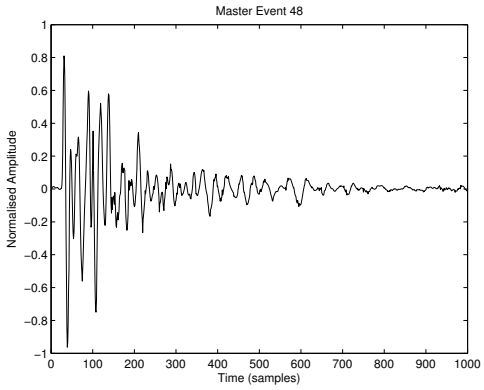

(b) Average waveform taken from stack of events in order to minimize noise and bias

Figure 7.7: Stack and Master Event 48 identified from triggered events on 20 October 2014. Master event 48 was identified in cluster 1 (Table 7.3), before the M5.8 earthquake occurred.

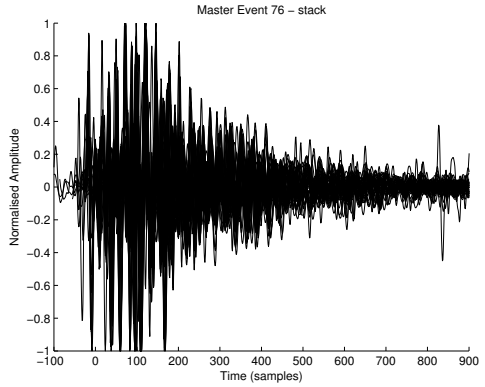

(a) Stack of similar events identified from STA/LTA ratio algorithm on 20 October 2014. Each event has a cross correlation coefficient of greater than 0.7 with one another. Each event is aligned at the point of maximum cross correlation. A total of 46 events were used in the stack

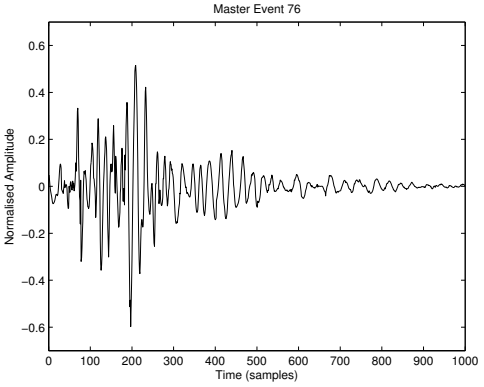

(b) Average waveform taken from stack of events in order to minimize noise and bias

Figure 7.8: Stack and Master Event 76 identified from triggered events on 20 October 2014. Master event 76 was identified in cluster 2 (Table 7.3), before the M5.8 earthquake occurred.

Cluster	Corresponding Temporal Event Numbers on Fig. 7.6	Number of Similar Events in Cluster	Corresponding time (UTC)
1	1 to 50	18	00:08 to 15:23
2	51 to 300	137	15:24 to 19:42
3	301 to 420	43	19:43 to 21:13
4	421 to 597	52	21:14 to 23:44

Table 7.3: Timings and number of similar seismic events within each cluster identified on 20 October 2014: CHL1

7.4 20 October 2014

The 20 October 2014 is clearly significant in terms of the elevated seismicity at Chiles-Cerro Negro, as a twelve fold increase in the number of seismic events was reported (Table 7.2). Furthermore, a distinct change in the similar seismicity can be observed, as the similar events go from randomly distributed throughout the day to distinct temporal patterns (Figures 7.5 and 7.6). It can be seen that this organisation of seismicity begins at $\approx$ 15:00 UTC, approximately 4 hours prior to a M5.8 earthquake approximately 10 km from the summit of Chiles-Cerro Negro (Figure 7.4, Table 7.3). As already suggested, this may relate to a changing or moving source location or mechanism at depth. Therefore the seismicity on 20 October 2014 is investigated for temporal and spatial evolution of similar seismic waveforms, and the influence of the M5.8 event on the same day.

7.4.1 Temporal Evolution of Families

Using the techniques of Petersen (2007) a dominant waveform for each cluster of events in Figure 7.6 was identified, in which the dominant event is identified as the event that has the greatest average cross correlation coefficient with every other similar event in that cluster. Each dominant waveform is an average of the stack of all of the similar waveforms with a cross correlation coefficient of greater than 0.8 with this dominant event (Figure 7.9). The average waveform from each stack and their spectral characteristics are shown in Figure 7.10, along with the dominant waveforms identified on the 19 and 21 October 2014. It is clear that the shape of each waveform varies significantly, in particular in the definition of onset, and the length of coda. Moreover in terms of spectral content, the third cluster of events (from 19:43 to 21:13 on 20 October) shows a significantly higher proportion of energy between 5 and 10 Hz,

and the last cluster (from 21:14 to 23:44) shows an important spike in energy around 10 Hz, which is not seen with any of the other identified waveforms. The presence of higher frequency seismicity suggests that the source mechanism is predominantly brittle failure of the edifice and surrounding country rock due to increased stress (Lahr et al., 1994, Arciniega-Ceballos et al., 2003), although the less dominant low frequency component of the waveforms may be indicative of fluid movement (Chouet, 1996a). The changing relative combination of high and low frequency components within each waveform identified in Figure 7.10 suggests a potential temporal change in the pressurization system at depth. If pressurization and the source mechanism of the seismicity remain the same, it would be expected for the spectral characteristics also to remain constant.

In order to identify a migration in the seismic source, as suggested by the clustering of the similar seismic events around the diagonal in Figure 7.6, each dominant event in Figure 7.10 was cross correlated together, resulting in the similarity matrix shown in Figure 7.11. If the source was migrating, it would be expected that events close to one another in time would have higher cross correlation coefficients than those further separated in time. For example, events 1 and 2 would have a high cross correlation coefficient indicating a high degree of similarity, and the cross correlation coefficient of event 1 with events 3 to 6 would systematically lower with each event. Figure 7.11 shows no such migration, and instead further supports the idea that each of the identified dominant waveforms are significantly different from one another, with their cross correlation coefficients all being below 0.45. The lack of similarity between waveforms suggests that each cluster of events on 20 October 2014 is generated at different source locations (Geller and Mueller, 1980, Neuberg et al., 2006) or that seismicity is produced by different source mechanisms for each cluster.

7.4.2 Spatial Evolution of Families

The hypothesis of each cluster of seismicity occurring at different locations can be investigated through the location of hypocentres. Similar seismic events are expected to occur within small spatial extents of a quarter of a wavelength or less (Geller and Mueller, 1980, Neuberg et al., 2006) and therefore would be expected to be located spatially very close to one another. Therefore it would be expected to find a number of distinct spatial clusters of seismicity, representing each cluster identified in Figure 7.6.

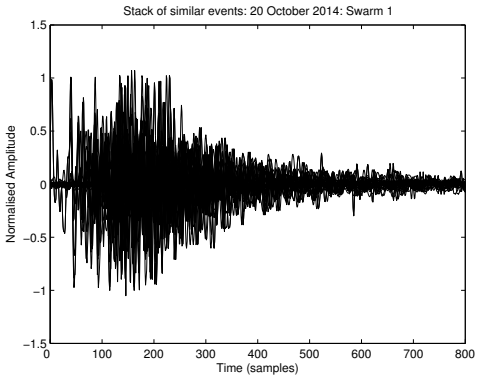

(a) Stack of similar events identified from Cluster 1 on 20 October 2014. A total of 18 events are used in the stack.

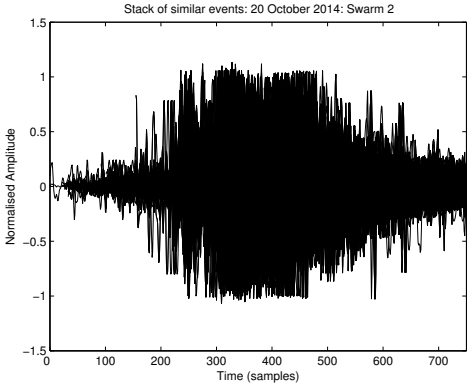

(b) Stack of similar events identified from Cluster 2 on 20 October 2014. A total of 137 events are used in the stack.

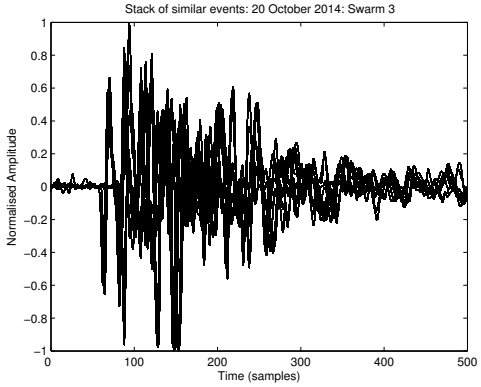

(c) Stack of similar events identified from Cluster 3 on 20 October 2014. A total of 43 events are used in the stack.

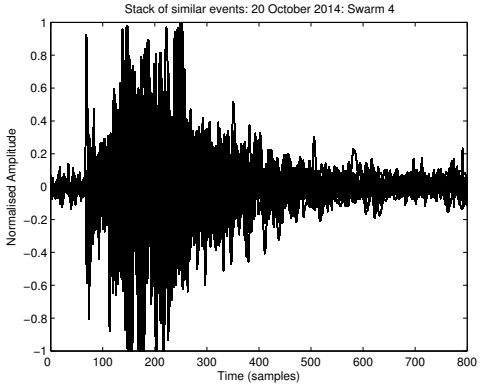

(d) Stack of similar events identified from Cluster 4 on 20 October 2014. A total of 52 events are used in the stack

Figure 7.9: Stack of dominant event identified in each cluster of events on 20 October 2014: CHL1. Clusters are as defined in Table 7.3. Clear differences can be seen in the waveforms shapes.

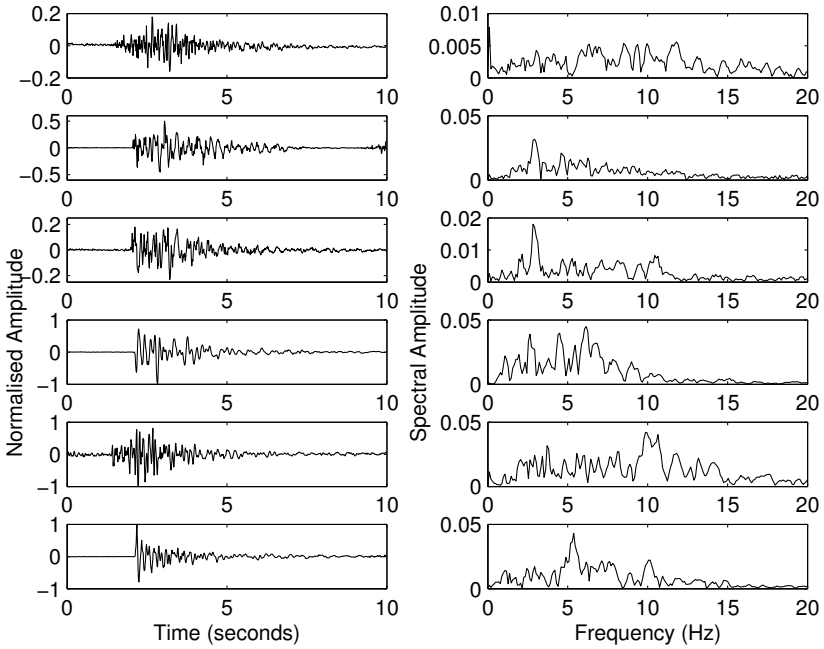

Figure 7.10: Master waveforms in the time and frequency domain for dominant similar daily events: 19 to 21 October 2014. From top to bottom: 19 October, Cluster 1 - 20 October, Cluster 2 - 20 October, Cluster 3 - 20 October, Cluster 4 - 20 October, 21 October. Clusters as defined in Table 7.3. *Left*: Normalised waveforms of dominant similar seismic events found. Note the changing scale on the y axis. *Right*: Single sided amplitude spectrum of the waveforms. Note the changing scale on the y axis.

Initial absolute locations generated by the Instituto Geofisico, Ecuador, of the events from each cluster suggests no evolution in the spatial distributions of events (Figure 7.12). The event locations to the South and South West of the summit of Chiles are similar to the locations of events in the months September 2014 to February 2015 (Figure 2.13). The locations of events provided by the Instituto Geofisico do not suggest the tight spatial clustering that would be expected from the identified similar seismic events. This may be a consequence of the error associated with the location. However, the accuracy of the location is not known because no error information was made available. It is therefore impossible to tell whether the locations are poorly constrained or not. In addition, the similar seismic events suggested by Figure 7.6 were identified using an STA/LTA algorithm whose parameters are not the same as those used to identify events at the Instituto Geofisico, which means that Figure 7.12 may include events which were not determined in Figure 7.6. Problems are also apparent with the location algorithm, since many events cluster to create a horizontal cut-off feature at 5 km depth, which is unlikely to be real.

It was not possible to locate the events identified in each cluster with any accuracy (error

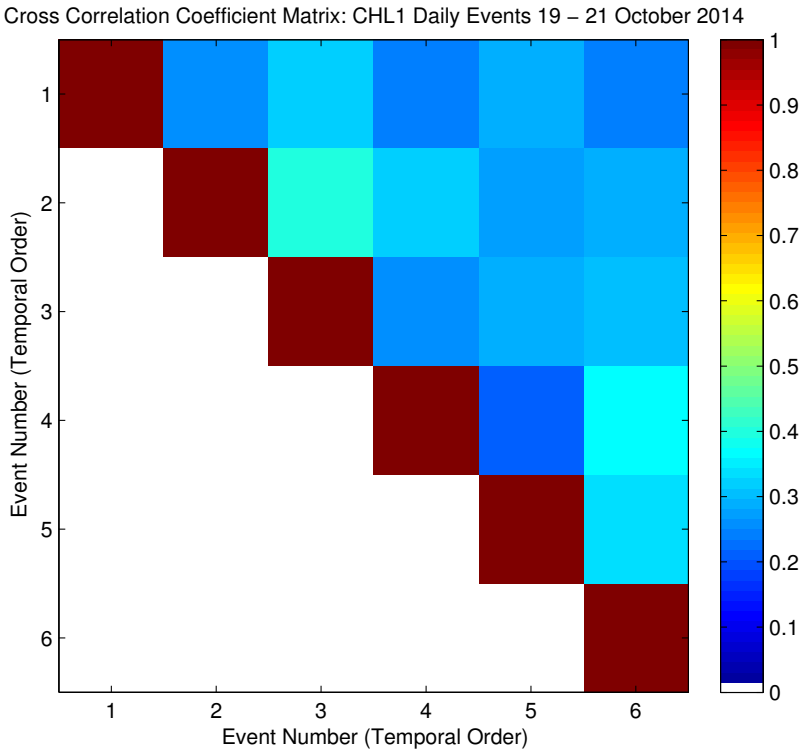

Figure 7.11: Cross Correlation Matrix of master events identified from 19 to 21 October 2014, CHL1. The first event corresponds to the daily stack of similar events identified on 19 October, events 2 to 5 are each identified cluster of events from Figure 7.6, and event number 6 is the daily stack of similar events on 21 October. The autocorrelation of each event with itself is shown in dark red along the diagonal and is equal to a cross correlation coefficient of 1.

in the location ranged up to 100 km) since data were only available from three stations (CHL1, CHL2 and ECEN), and the station configuration lacks azimuthal coverage, in particular to the south of the stations which is where the Instituto Geofisico located the majority of the seismicity (Figure 7.12). Access to the data from the other monitoring stations to the north would enable the events to be located with higher accuracy, and it is anticipated that a number of distinct clusters of similar seismicity would be identified. Using waveform similarity to aid the location of events may also reduce the error in the locations further (De Angelis and Henton, 2011). Therefore, it is not possible to confirm that the events within each cluster are located together, and in different locations to other clusters, although this is implied by the cross correlation technique.

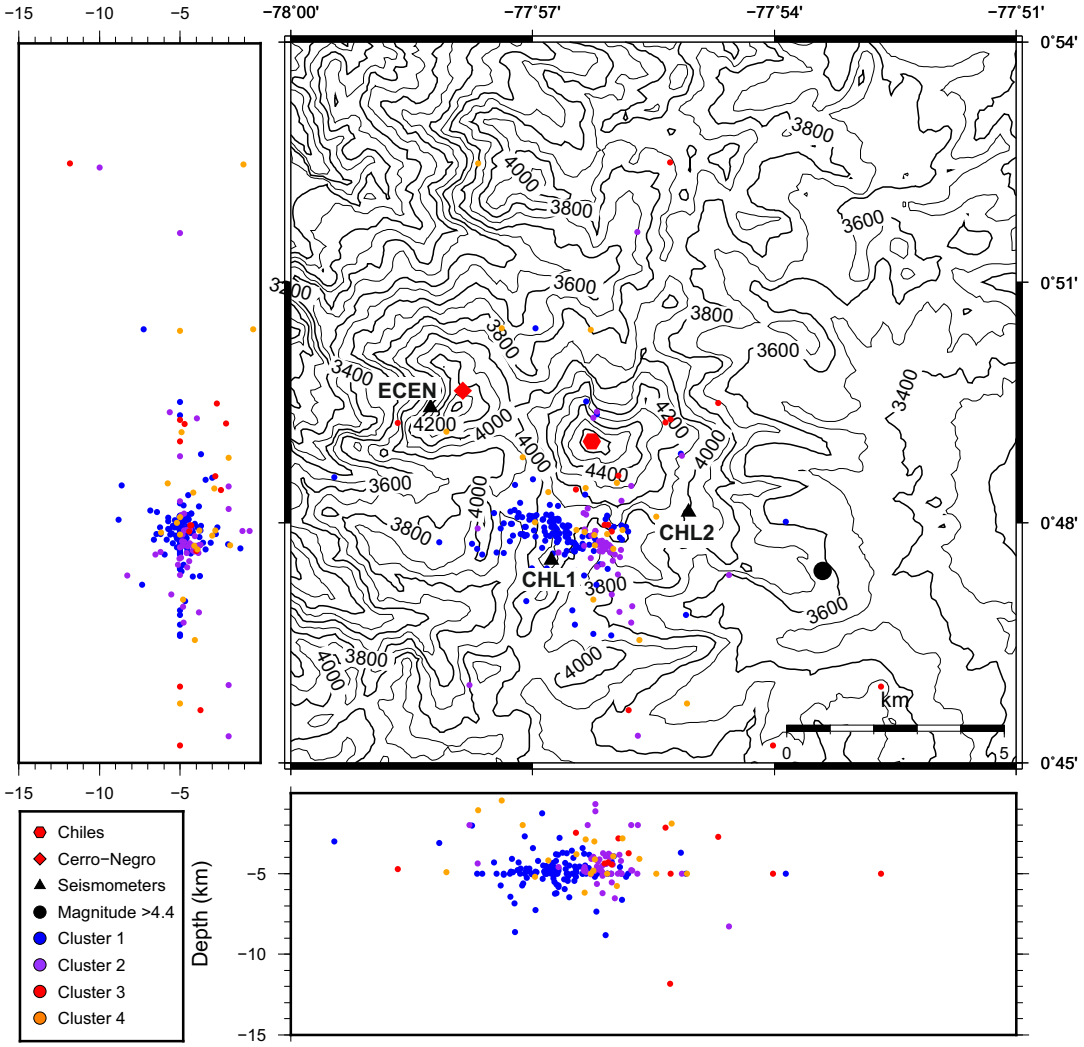

Figure 7.12: Locations of events on 20 October 2014, calculated by the Instituto Geofisico. Clusters of events, as defined in Table 7.3, are shown as different colours. Each cluster contained similar seismic events and therefore would be expected to be located within a small spatial extent. No error information is known about the event locations, however clear artefacts in the locating algorithm can be seen, with a distinct planar grouping of events around 5 km.

7.5 Applicability of technique to unfolding unrest

This cross correlation technique has previously been applied only in hindsight with the FFM to assess its potential as a forecasting tool for volcanic eruptions at Soufriere Hills volcano, Montserrat, proving useful in hindsight analysis (Chapter 4). The case of Chiles-Cerro Negro is different since analysis has been carried out on a period of unrest which ultimately did not end in an eruption. Seismicity has steadily declined in event rate since October 2014, returning to the assumed background event rate in April 2015 (Pacheco and Gomez, 2015). However, the use of the cross correlation technique to the incoming data at Chiles-Cerro Negro during

the escalation of unrest in October 2014 has offered some insight into the magmatic system at depth, which appears to be dominated by a developing fracture network rather than advancing magmatic fluid. This has been particularly useful since geological background information about this volcano is still sparse.

Continuous seismicity (upper plot, Figure 7.13) appeared to show no precursors to the unrest which began suddenly on 20 October. The usual analysis techniques of RSAM and SSAM (middle and lower plots, Figure 7.13) also gave no precursory warning of the increase in the seismicity recorded within the 0.5 to 15 Hz range following the M5.8 earthquake on 20 October. More detailed analysis of the number of events per hour on 20 October reveal a sharp acceleration in the event rate from ≈12:00 onwards (Figure 7.14), which was used in real time as an indicator of increased activity at the volcano. Application of the FFM to seismic events detected using the STA/LTA algorithm suggests a forecasted failure time on 20 October at 17:16h. Although the R^2 value suggests a reasonable fit between the data points and the FFM, visual inspection confirms that the linear regression is displaced from most of the data points (Figure 7.15).

A clear acceleration in seismic event rate was observed in the hours before the M5.8 earthquake on 20 October when using individual families of similar seismic events to identify patterns. This acceleration is perhaps most obvious when using master event 48 (Figure 7.16a), where a continuous acceleration was observed for over 18 hours. Using master event 76, an acceleration in event rate from ≈15:00 onwards was observed (Figure 7.16b). Comparing the accelerations of the master events (Figure 7.16) to the acceleration in seismicity identified using the STA/LTA detection algorithm (Figure 7.14), suggests that it might have been possible to identify the accelerating patterns of seismicity earlier in time (from $\approx 00:00$ on 20 October). If this algorithm had been implemented and used at the Instituto Geofisico on an operational level, the forecast would have been useful for the Ecuadorian authorities. However, in this case the forecast is for a high frequency earthquake rather than a volcanic eruption. Distinguishing the type of forecasted event relies upon previous knowledge of the geological history of the volcano, as well as some interpretation of the geophysical precursors. In the case of Chiles-Cerro Negro, there is very little information regarding the geological history of the complex, and therefore many events may be feasible to occur. Since the precursory activity was primarily constituted of VT events, with no evidence of fluid movement through the detection of LF

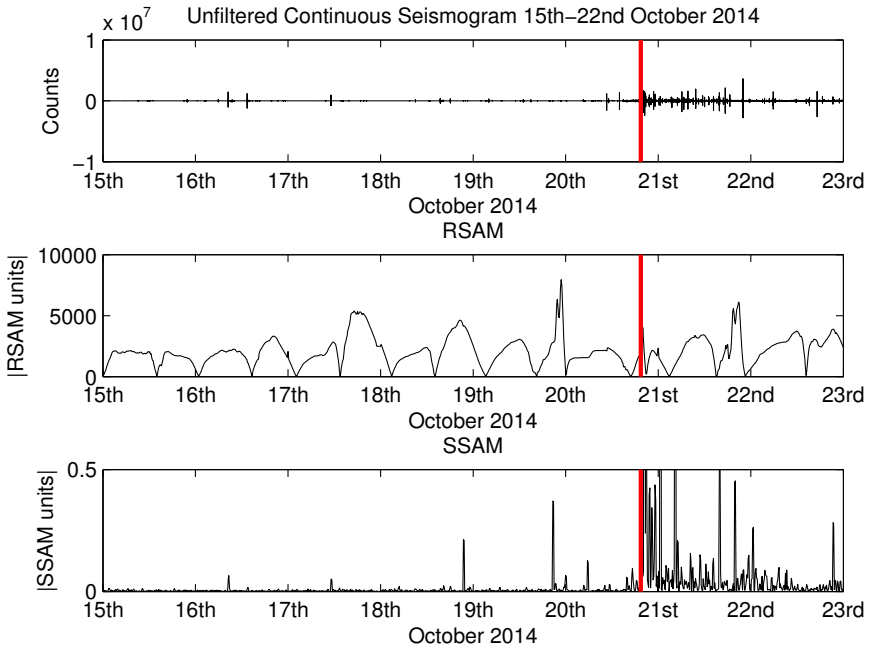

Figure 7.13: RSAM and SSAM from CHL1 15 to 23rd October 2014. The M5.8 earthquake on 20 October 2014 is represented by the vertical red line. *Upper*: Unfiltered continuous seismogram from CHL1 from 15 to 23 October 2014. Very little activity is seen prior to the M5.8 earthquake. *Middle:* RSAM appears cyclic before and after the M5.8 earthquake. RSAM units are in counts, following the units of the input seismic data. *Lower:* SSAM (data filtered between 0.5 and 15 Hz after Figure 7.10). Seismicity clearly increases after the M5.8 earthquake.

events, it may have been assumed that a volcanic eruption was less likely than a large high frequency earthquake resulting from the build up in pressure at depth.

However, since it was assumed that all of the seismicity in the area was related to volcanic processes, this acceleration in event rate may have enlisted a false alarm for an eruption to be imminent. Instead, the accelerating seismicity appears to forecast the timing of the M5.8 event at ≈19:30 (Figure 7.17). Again, although not necessarily mathematically accurate, the use of a least squared linear regression as opposed to an exponential regression appears to lead to a more accurate forecast for the timing of the failure event (Figure 7.17 even if the fit of the data to the model is often poor (Section 4.6).

The acceleration of high frequency VT earthquakes prior to failure has been observed both at the laboratory scale (Lavallée et al., 2008, Smith et al., 2009) and prior to volcanic eruptions (Kilburn and Voight, 1998, Kilburn, 2003, Bell and Kilburn, 2012). An acceleration in seismicity has also been noted prior to large regional earthquakes, thought to be representative of

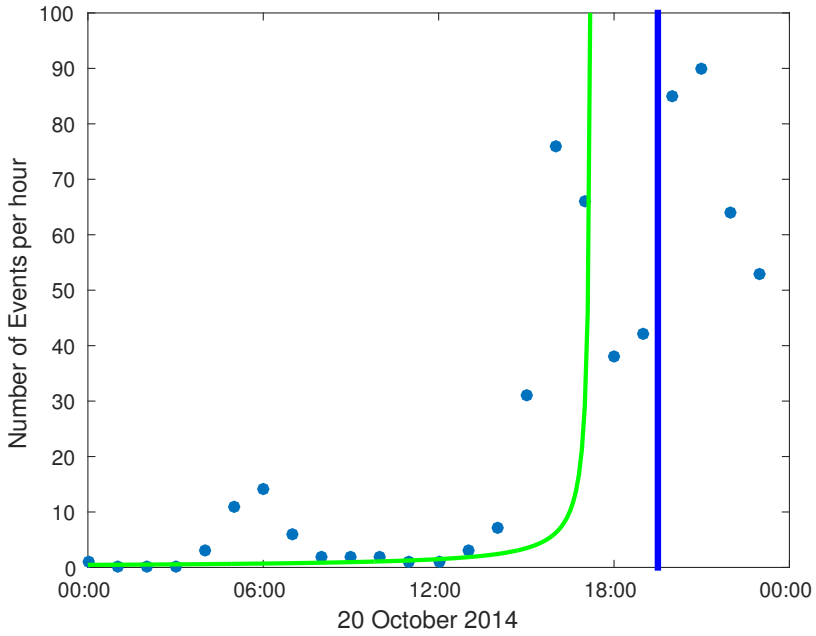

Figure 7.14: The number of events per hour extracted from the continuous seismogram using an STA/LTA detection algorithm on 20 October 2014. Each data point represents the number of events extracted during the following one hour interval. The M5.8 earthquake on 20 October is represented by the vertical blue line. The hyperbolic acceleration as described by the FFM is depicted as a solid green line.

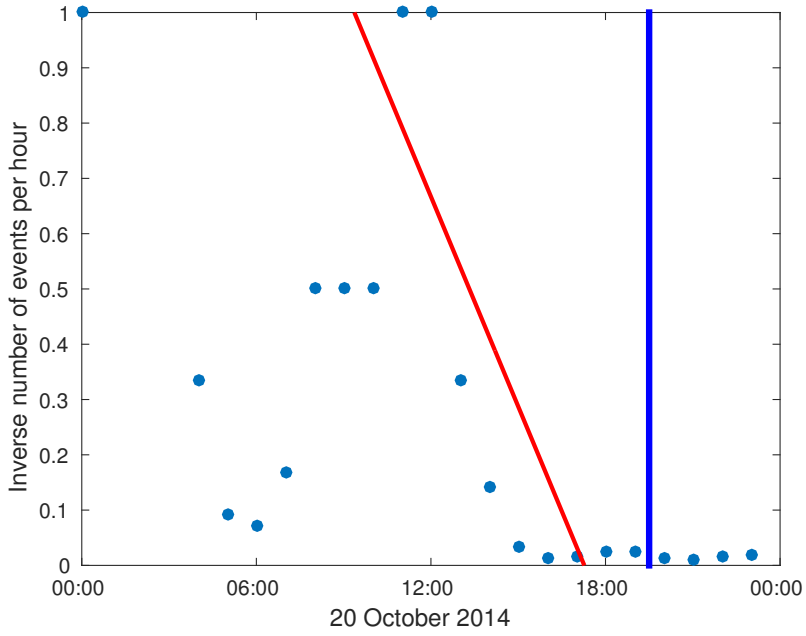

Figure 7.15: Application of the Failure Forecast Method to events detected using an STA/LTA algorithm on 20 October 2014. Each data point represents the number of events extracted during the following one hour interval. The M5.8 earthquake on 20 October is represented by the vertical blue line. A linear least squared regression is represented by the solid red line, and forecasts a failure time at 17:16h on 20 October 2014 (R^2=0.69, y = -0.1265x + 2.1854).

increasing and accumulating stress allowing greater amounts of brittle failure to occur within a distinct perturbed region (Bowman and King, 2001). Bufe and Varnes (1993) suggested that large earthquakes could be forecasted using precursory accelerating seismicity which related to the nucleation and propagation of cracks, much as Kilburn (2003) has suggested for volcanic environments. Therefore, accelerating rates of VT seismicity can potentially be used as a forecasting tool for larger main shock earthquakes. In the case of Chiles-Cerro Negro, which has had no associated magmatic activity in recent history, the acceleration of seismicity in October 2014 is likely to have been the result of an accumulation of stress at depth, resulting in the propagation of fractures. It is still unclear as to whether this stress accumulation is the direct result of magmatic processes, however analysis of the principal stresses using anisotropy suggested a bimodal distribution of stress from January to October 2014: in the E-W direction, concurrent with the regional tectonic stress in the area, but also in the N-S direction (Vaca, 2015). The bimodal distribution of principal stresses in the vicinity of volcanoes has often been attributed to the opening of a dyke or similar magmatic pathway perpendicular to the tectonic regional stress due to the coalescence of fractures created in the regional stress field (Gerst and Savage, 2004, Roman et al., 2011). This would suggest that the accumulation of stress at depth was a response to a magmatic intrusion via the opening of a dyke. This explanation would account for the mix of VT and hybrid seismic signals observed in the seismicity in October 2014, as hybrid earthquakes are more likely to be the response of the movement of fluid (Lahr et al., 1994, Chouet and Matoza, 2013) and therefore may represent magmatic fluid migration within the wider volcanic system.

Perhaps the greatest problem that faces researchers adapting the cross correlation technique to forecast volcanic eruptions at an operational level is the occurrence of false alarms generated from the data, or the possibility of no forecast being evident from the data. It is now known that the unrest at Chiles-Cerro Negro did not culminate in an eruption. However had this analysis been performed in real time, a number of forecasts could have been made. Figure 7.18 suggests that had forecasts at Chiles-Cerro Negro been made in real time in October 2014, then a number of false forecasts could have been generated, in addition to a number of days when no forecast could be achieved. False forecasts would have been generated at 12:00 on 15 October, with a forecasted time of failure on 17 October at approximately 04:24 (blue regression in Figure 7.18) and at 12:00 on 17 October, with a forecasted time of failure on 21 October at approximately 19:30 (green regression in Figure 7.18). Any other forecasts us-

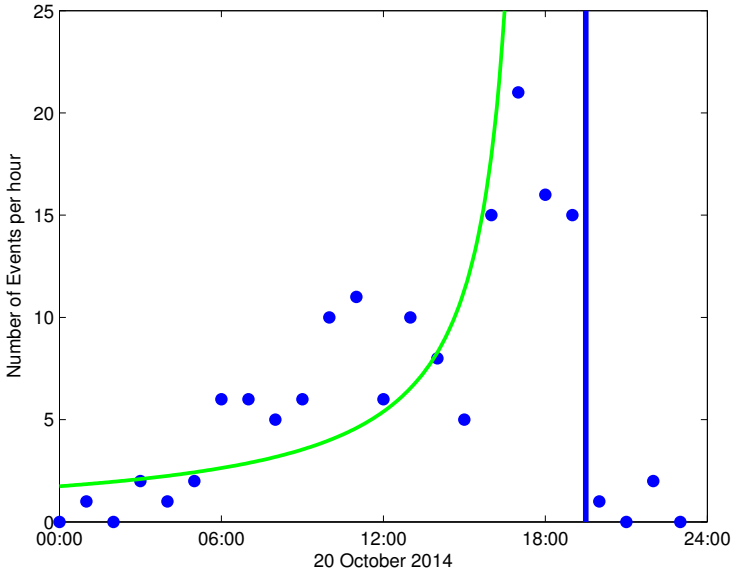

(a) Acceleration in the number of events per hour on 20 October 2014 for Master event 48 prior to the M5.8 earthquake at $\approx 19:33$. The acceleration of seismicity began over 18 hours prior to the M5.8 earthquake.

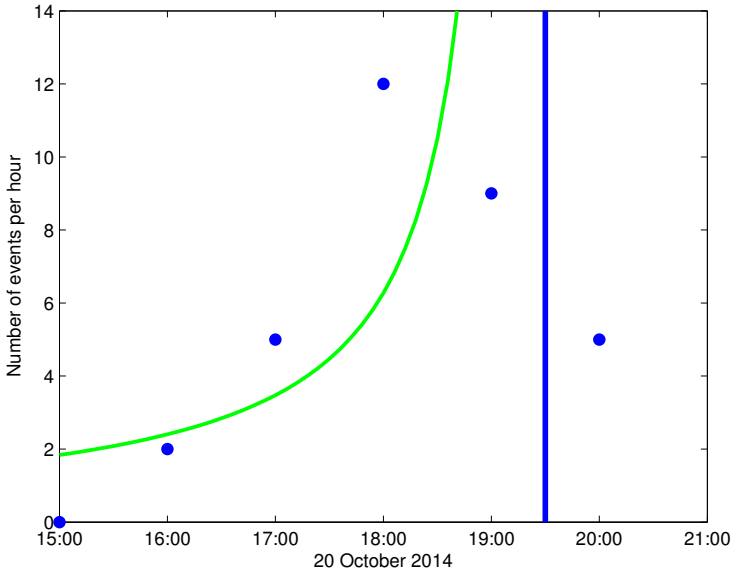

(b) Acceleration in the number of events per hour on 20 October 2014 for Master event 76 prior to the M5.8 earthquake at $\approx 19:33$. The acceleration in seismicity began 4 hours prior to the M5.8 earthquake.

Figure 7.16: Accelerations in the number of events per hour on 20 October 2014 for Master events 48 and 76. Each data point represents the number of events extracted during the following one hour interval using a cross correlation sliding window technique to identify events from the continuous record. The M5.8 earthquake on 20 October is represented by the vertical blue line. The average acceleration in these events is represented by the green curve.

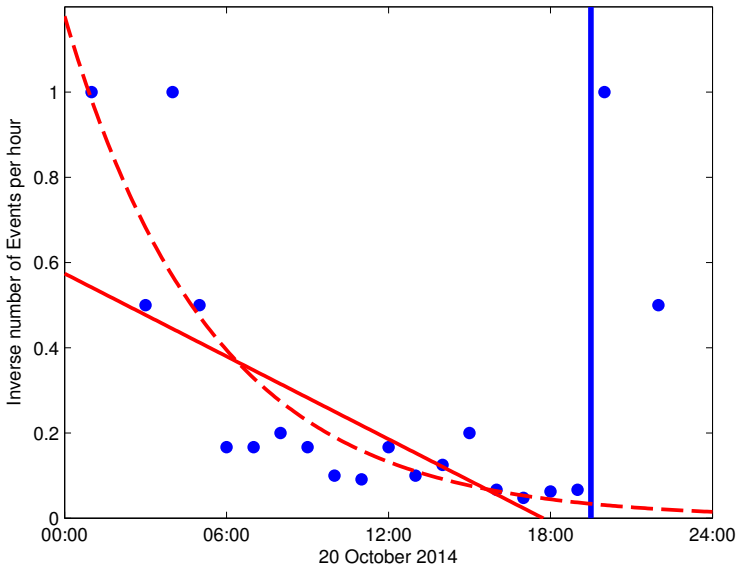

(a) Inverse event rate per hour of master event 48. Application of a least squared linear regression (solid red line, y = -0.0324x + 0.5742) suggests a forecast of a failure event approximately 2 hours before the M5.8 earthquake, but the fit of the regression to the data is poor (R^2=0.42). Application of an exponential regression (dotted red line, log(y) = -0.18228x + 0.16409) fails to make a forecast as the regression fails to cross the x-axis.

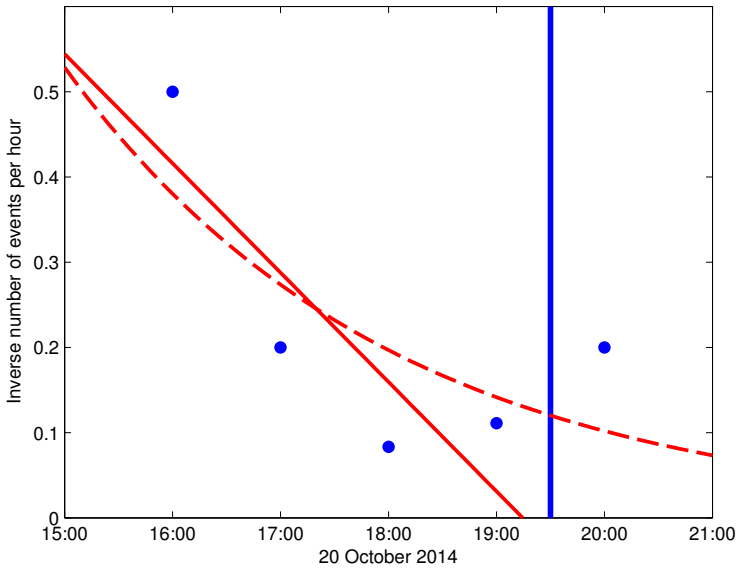

(b) Inverse event rate per hour of master event 76. Application of a least squared linear regression (solid red line, y = -0.1283x + 0.5444) suggests a forecast of a failure event approximately 30 minutes before the M5.8 earthquake. The fit of the regression to the data is reasonable (R^2=0.75). Application of an exponential regression (dotted red line, log(y) = -0.32925x - 0.6374) fails to make a forecast as the regression never crosses the x-axis.

Figure 7.17: Application of the Failure Forecast Method to the accelerating seismicity observed on 20 October 2014 prior to a M5.8 earthquake. Each data point represents the inverse number of events extracted during the following one hour interval. The M5.8 earthquake on 20 October is represented by the vertical blue line. A linear least squared regression is represented by the solid red line. Application of an exponential regression is shown by the dotted red line.

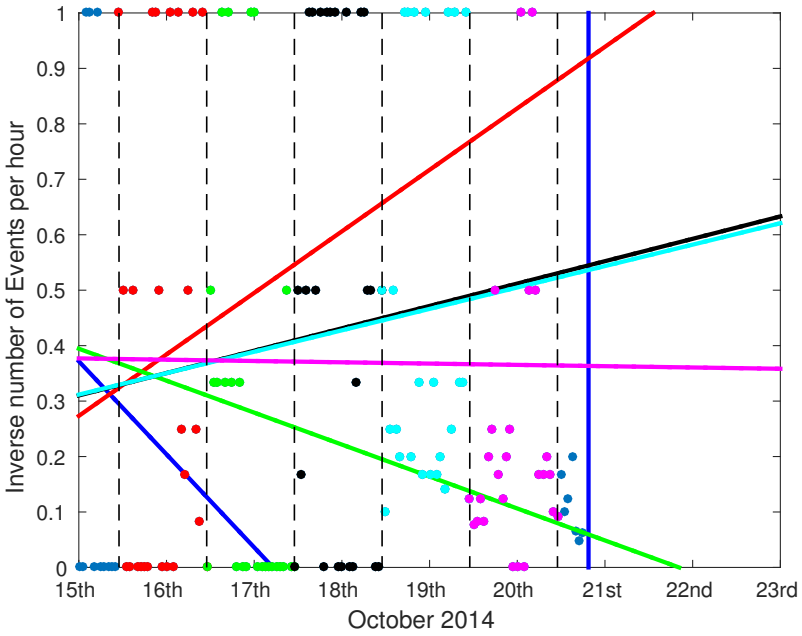

Figure 7.18: The generation of forecasts in the days prior to M5.8 earthquake using master event 48. Each data point represents the inverse number of events detected in the following one hour interval. Blue data points represent those from 00:00 to 12:00 on 15 October 2014. A forecast using these data points is made using the FFM and assuming $\alpha = 2$, and is shown by the linear least squared regression in blue. Data points in red represent those from 12:00 on 15 October to 12:00 on 16 October (24 hours), and a corresponding linear regression using these data points, and all those previously (i.e. from 00:00 on 15 October onwards) is shown in red. Data and corresponding forecasts are also shown for 12:00 on 16 October to 12:00 on 17 October (green), 12:00 on 17 October to 12:00 on 18 October (black), 12:00 on 18 October to 12:00 on 19 October (light blue) and 12:00 on 19 October to 12:00 on 20 October (pink). This represents making a forecast at 12:00 on each day using all available data (dotted vertical lines).

ing master event 48 would have been void, since the regression fails to cross the x-axis, and therefore no forecasted failure time can be anticipated. Consequently, a long range forecast in October 2014 would not have been possible, and only the final acceleration in event rate in the 24 hours prior to the M5.8 earthquake (Figure 7.17) would have led to a successful forecast.

Despite there being very little information about the geological history of the Chiles-Cerro Negro volcanic complex, it is clear from the topographic changes and amphitheatre-like depressions on the north side of Chiles, and the west side of Cerro Negro that these volcanoes have experienced dome collapses during their history (Figure 7.19). This is not unusual for volcanoes in the northern Andes, and Tungurahua (Ecuador), Cotopaxi (Ecuador) and Volcan Galeras (Colombia) have all experienced major dome collapses in their pasts (Hall et al., 1999, Hall and Mothes, 2008, Banks et al., 1997). Francis and Wells (1988) suggest a number of morphological features which can be used to identify debris avalanche deposits from volcanoes

(generated from the collapse of the volcanic edifice) from studies in the central Andes (Bolivia, northern Chile and northern Argentina) using remote sensing techniques. Namely these are: a lobate flow like morphology to the deposit; multiple surface ridges which are radial to the volcano; megablocks and hummocky terrain forming deposits; evidence of an original collapse scar or amphitheatre; and presence of unusual textural or spectral patterns, indicating the mixing of contrasting materials derived from different parts of the volcanic edifice and entrained in the collapse and flow event. All of these are clear for Chiles volcano in Figure 7.19: the original collapse amphitheatre is still visible, which is bounded by a number of sharp ridges extending radially to the volcano. Hummocky terrain is evident in the valley to the west of La Puerta, and the colouration of the surface suggests the mixing of volcanic debris and the surrounding vegetation. The lobate flow morphology is perhaps more difficult to determine, most likely because the surrounding area is already heavily mountainous, influencing the flow direction. Although not clear from Figure 7.19, Cerro Negro also boasts a clearly visible amphitheatre, hummocky terrain and radially extending ridges in the western direction.

It remains unknown whether these collapse events were caused by the volcanic system itself or external effects, but it is clearly recognised that both of these volcanoes are capable of large scale events. The morphology of the scar and the deposits at Chiles suggest that this was a deep seated failure event, since only one very large scar is seen, which can be seen to penetrate deep within the edifice, and there only appears to be one debris avalanche deposit. If this had been a progressive failure, the scar may not be so clean, and it would be expected to see a number of lobes of debris avalanche deposits, which are subject to differential weathering patterns with time. However, if this was a progressive failure, and the final collapse event was the largest then it would have overlain all of the previous deposits which would no longer be visible. Detailed mapping of the volcanic complex in future, with particular attention paid to the location, extent and characteristics of debris avalanche deposits, will make it possible to determine the mechanisms of potential failure, and therefore to postulate the possible collapse scenarios for the future.

7.6 Summary

Accelerating seismicity in October 2014 is assumed to be related to the volcanic edifice of Chiles-Cerro Negro on the Ecuador-Colombian border. For the first time, similar seismic events

Figure 7.19: Google Earth image looking from the North of Chiles and Cerro Negro volcanic complex showing evidence of past collapse events. The collapse scar on Chiles faces north. The collapse scar on Cerro Negro faces west. The yellow line represents the boarder between Ecuador (south) and Colombia (north). Settlements with any registered population are shown, with the two closest being less than 3 km away from the summit of their nearest volcano. The distance between Chiles and Cerro Negro is approximately 5 km (Google Earth 5.0, 2013).

were identified at Chiles-Cerro Negro, and appear to be particularly important in the hours preceding and following a M5.8 tectonic earthquake on 20 October 2014. The events are dominantly hybrid to high frequency (0.5 to 15 Hz) and therefore are thought to represent the nucleation and propagation of fractures at depth, possibly due to a magmatic intrusion or the opening of a dyke perpendicular to the regional principal stress. Cross correlation analysis also identified a temporal and potentially spatial migration in the similar seismicity, suggesting the movement of the source of seismicity at depth, possibly related to changing pressurization and stress as the fracture network propagates. Since a number of distinct clusters of similar seismicity have been recognised, it is likely that each cluster of similar seismicity is generated

within a small volume, which are well separated from one another. More detailed location analysis using more seismic stations would enable this hypothesis to be investigated further. The Chiles-Cerro Negro complex shows evidence of deep seated dome collapses in geologic history. However their relationship to magmatic activity is yet to be established.

Chapter 8

Discussion and Conclusions

One of the primary aims of this research was to further develop forecasting tools for volcanic dome collapses using LF seismicity, specifically focusing on similar seismic waveforms which are assumed to be generated by the same source mechanism and at the same source location. This represents a single active seismic system at depth (i.e. seismicity resulting from the same active processes), and forecasting using only one system allows correlation and causative relationships to be determined between the seismicity at depth and the forecasted event at the surface. This technique has been applied to precursory activity at Soufrière Hills volcano, Montserrat prior to a number of large scale dome collapses that have dominated the volcano's recent history. Thus a dome collapse of June 1997 and July 2003 were successfully forecasted in hindsight. However, the dome collapse of February 2010 could not have been successfully forecast using seismicity, although use of the cross correlation technique did allow other temporal and spatial patterns in the seismicity to be identified. In this instance, stability of the volcanic dome suggested that the dome complex was already unstable, and therefore the lack of seismicity prior to collapse may simply be because the system short-circuited itself and failed almost immediately upon movement of magma at depth. Hence, it is evident that this forecasting method may not always be successful, even between eruptive events at the same volcano, and that it is particularly important to consider the state of the volcanic dome during volcanic unrest scenarios in terms of its potential for collapse.

The identification of similar seismicity was also investigated for an unrest episode at Chiles-Cerro Negro, Ecuador/Colombia border, in October 2014. This offered a unique opportunity to test forecasting tools in near-real time at a volcano which was entering a period of unrest after over three thousand years of repose, as opposed to Soufrière Hills volcano, which has been

persistently active for a number of decades. Although the unrest at Chiles-Cerro Negro did not culminate in an eruption, similar seismic waveforms showed remarkably systematic patterns on 20 October 2014 and may have aided real time forecasting of a M5.8 earthquake that occurred less than 10km from the volcano, and is therefore assumed to be related to volcanic processes. The analysis also allowed an investigation into the likelihood of false forecasts based on accelerating seismicity.

Finally, this research has highlighted the need for multi-parameter forecasting tools at volcanoes. Although the level of seismicity is often the most obvious precursory signal, the event rate may not always increase significantly above background levels. In the case of Soufrière Hills and other dome building volcanoes, instability analysis of the dome based on its size, shape and mechanical properties of the rock masses may prove useful for linking seismic sources at depth to surface processes, and for identifying the most likely areas of failure.

8.1 Forecasting lava dome collapse

Use of the FFM in forecasting the collapse of volcanic lava domes relies upon the assumption that an accelerating geophysical precursor at depth, such as seismicity, is directly related to the event at the surface. It is therefore essential to quantify the stability of the volcanic dome and its likely potential for failure, as well as link any acceleration in precursory activity to the failure in any forecasting analysis.

8.1.1 Success of the FFM

Accelerating rates of geophysical precursors appear to be common in volcanic settings prior to material failure (e.g. eruptions, landslides, fracturing). For example accelerations in the number of seismic events were observed prior to the 1989/1990 eruption of Redoubt volcano (Cornelius and Voight, 1994) and the 1982, 1985 and 1986 eruptions at Mt St Helens (Voight, 1988, Voight and Cornelius, 1991, Smith et al., 2007b). The Alaskan Volcano Observatory issued a “formal warning” of an impending eruptive event on the morning of the 2 January 1990, a few hours before an eruption (Cornelius and Voight, 1994). Accelerations in seismic energy prior to the 1994 and 1998 eruption of Colima volcano (De la Cruz-Reyna and Reyes-Dávila, 2001) have also been observed as well as accelerations in seismic amplitude prior to the 2000 eruption of Villarrica volcano (Ortiz et al., 2003). After 12 days of elevated seismic energy release at Colima volcano in November 1998, forecasts were generated for the 16-18

November (De la Cruz-Reyna and Reyes-Dávila, 2001). The onset of a dome building eruption occurred on 21 November, within 48 hours of the forecasted timing (Reyes-Dávila and De la Cruz-Reyna, 2002).

Accelerating seismicity at Soufrière Hills volcano has been investigated on a number of occasions using the FFM. Kilburn and Voight (1998) showed that the FFM could be successfully used to forecast an eruption in November 1995, when magma first reached the surface, by using inverse daily VT event rates. Hammer and Neuberg (2009) used accelerating LF event rates to forecast the timing of a dome collapse on 25 June 1997 using only one family of events, as has been emulated in Chapter 4. A number of families of LF events have been detected during the precursory seismicity for the 25 June 1997 dome collapse (Green and Neuberg, 2006), and this research evaluated the use of each these different families with the FFM, rather than simply one family. This technique of defining a family of LF seismicity and using it in conjunction with the FFM to focus on a single active system at depth was also applied to precursory LF seismicity in July 2003 and February 2010, prior to dome collapses. LF seismicity in July 2003 was represented by one family of similar seismic events, and were successfully used for a forecast of the dome collapse within 4 hours of the known timing of collapse. No forecast could be generated in February 2010, which supports the findings of Stinton et al. (2014), who suggested that there was no noted increase in seismicity prior to the collapse.

This research also showed the successful use of the FFM at Chiles-Cerro Negro, Ecuador/ Colombia border, which was entering a period of unrest after a long period of repose, successfully using accelerating VT seismicity to forecast the timing of a large M5.8 earthquake, occurring within 10 km of the volcanic complex. This suggests that the FFM may be useful in other volcanic settings other than ongoing restless volcanoes experiencing dome collapses.

8.1.2 Potential for real time forecasting

Ultimately, scientists wish to be able to use real time forecasting tools with confidence. However, it appears rare that such tools are used in real time scenarios or are rarely published in the literature, primarily due to the lack of confidence in the tool. Hindsight analysis using forecasting tools is extremely important in order to verify parameters, such as α and the use of a least squares linear regression when using the FFM, and therefore should be carried out on as many accelerating sequences as is possible. Testing of forecasting tools at places such

as Soufrière Hills is ideal since large volumes of data are available covering a wide variety of possible volcanic scenarios such as dome collapse with obvious accelerating seismicity and no accelerating seismicity. In addition, Soufrière Hills volcano has experienced explosion events, which although not investigated in this research, may offer the possibility for developing forecasting tools. However, this volcano does not allow the testing of other eruptive scenarios such as awakening volcanoes after a long period of repose. In comparison, accelerating unrest at Chiles-Cerro Negro in October 2014 offers this unique opportunity for study of developing unrest from quiescence.

However, all of this research was carried out in hindsight. At the explicit request of the director of the Instituto Geofisico, the forecasting tools developed during this research, including the identification of similar seismicity are currently under investigation having been implemented for their real time application at the IG-EPN in Quito, Ecuador. Since the Instituto Geofisico is responsible for the monitoring of over 55 active volcanoes in Ecuador, it can be assumed that accelerations in seismic event rate are more likely to be seen on a regular basis here, and therefore has many opportunities to test these tools in real time. The success of such forecasting tools will need to be evaluated over the coming years as unrest scenarios unfold.

One of the biggest problems with working with real time data is that the forecast timing is likely to evolve as more data become available. Therefore the best forecast is one which remains stable even with the addition of data points, hence its stability should be taken as a measure of its reliability. One major problem therefore becomes when to issue a forecast, and the confidence one has in such a forecast. With time, greater assurance in both of these is probable. The problem of issuing false forecasts remains; not every accelerating sequence of precursors will culminate in a surface eruption.

The technique itself of utilizing similar seismic events (whether LF or VT) potentially holds problems for use in real time. Essentially, this technique is likely to be more time consuming than current forecasting practices, and will require more computational power. The codes however were developed in order to use the minimum computational power possible in order for the tools to be applicable even in volcano observatories with very limited computational and monitoring resources. The identification of similar seismic events will need to be undertaken in real time, i.e. a continuous search for similar events and defining of master events. Experience

at Soufrière Hills volcano teaches us that some similar seismic events are consistent over a number of days (e.g. June 1997, July 2003) and therefore their early identification would allow simple manipulation of the incoming seismicity. In other circumstances, the master events for similar seismicity may be short-lived, which requires the recalculation of master events more often (e.g. October 2014 at Chiles-Cerro Negro). There are also occasions when similar seismic events may not be apparent in the seismicity (e.g. Soufrière Hills, February 2010) and other forecasting methods will need to be relied upon.

The determination of α in real time is likely to be difficult, especially if the value is considered to not be static (Kilburn, 2003). A decision must be made as to whether the assumption will be maintained that α is equal to two to allow for a simple linear regression, or whether more complicated regression analysis shall be used if the value of α is not directly investigated. Secondly, it is clear that the fit of the FFM to inverse event rate data can be poor, although this appears to be somewhat improved when forecasting focuses primarily on a single active system at depth. Uncertainties and error in the fit and the forecast make the technique difficult to use in real time. Thirdly, determining an acceleration in precursory data is more simple when done in hindsight. When investigated in real time, and in particular if the incoming data has a low signal-to-noise ratio, accelerating trends can be easily overlooked.

8.1.3 Operational Challenges

As demonstrated by the monitoring capacity of different volcanoes around the world (Section 2.1), there is also not a single universal methodology for dealing with incoming data from a volcano, processing it or communicating the results with the wider community. However, there are a number of idealised practices which ensure the successful monitoring within a volcanic environment. Firstly, the data catalogue needs to be continuous, consistent and in real time. Therefore, the way in which data are recorded needs to be consistent from the beginning of the operation to present, and any updates in this should also be explicitly recorded (e.g. changes in sensors, changes in distribution). This is difficult with advancing technologies and changing personnel, but is paramount. Data gaps must be investigated as soon as possible, and details for the reason of failure should be recorded and resolved.

The uptake of new monitoring and/or forecasting practices within volcano observatories appears limited, and yet research institutes around the world are spending vast amounts of money

and vast amounts of time developing such tools. One issue may be that some of the complicated monitoring tools developed in research institutes are simply too financially and computationally expensive to run at the observatory level, and expert knowledge would be required to do so. In addition, there is such a wide variety of data formats both for the incoming monitoring data and the processing tools available that it is almost inevitable that each observatory will have favoured formats, and data not in this format are more easily disregarded.

8.1.4 Limitations of the FFM

With its application to volcanic environments (Tokarev, 1963, Voight, 1988), and in particular to forecasting dome collapses, one fundamental assumption of the FFM is that the accelerating precursor from depth (usually seismicity, deformation or gas output) has a direct causal link with the failure event at the surface. In reality, it is unlikely that the link between these two parameters is simple, and this "Transfer Function" may have currently unidentified effects upon the forecasting methodology. For example, the link may be different depending on whether their is an active open or closed system in terms of the magmatic conduit at the volcano. For a closed system, accelerating seismicity is likely to indicate the formation of a link between depth and the surface, whereas accelerating seismicity in an open system would suggest that a link already exists between depth and the surface, and the accelerating seismicity is an affect of the moving magma to the surface. The model described in Chapter 6 suggests one plausible explanation for the relationship between the depth and surface, linking the accelerating seismicity at depth to the accelerated movement of the magma column, which raises pore fluid pressures within the edifice, thus contributing to its instability and leading to failure at the surface. A more detailed understanding of the fluid and fracture network within the dome of Soufrière Hills will allow more realistic modelling of the state of stress, improving our understanding of the likely links between the two parameters. The FFM should only be used in instances when a direct link between processes at depth and the surface can be established, which means it may not always be applicable.

The FFM is most applicable to geophysical precursory data which shows a single accelerating phase (e.g. LF seismicity at Soufrière Hills volcano, June 1997). However in reality there are often a number of accelerating and decelerating phases in a precursory sequence. The FFM is not applicable to decelerating sequences of precursors, and yet a decrease in the average event rate is often observed immediately prior to an eruptive event. This deceleration was

originally noted when using STA/LTA event rates, and so was initially assumed to be a consequence of averaging the event rate for a number of active seismic systems at depth, which may not all be active at the same time. However, even when using only one single active system of seismicity as a forecasting tool, a deceleration in the event rate may still be observed immediately prior to the eruptive event (e.g. July 2003, Figure 4.15). Voight (1988) called this a "delay function", supporting the idea that seismicity at depth may not have an immediate impact upon a failure event at the surface. Further investigation into this function may enable similarities to be identified between parameters such as the length of the delay, the type of eruption, the explosivity of the eruption and the onset timing and amplitude of the delay in order to understand the cause of such a delay. This in turn may lead to a better understanding of the driving forces behind the failure mechanisms of a volcanic dome, which are currently only assumed to be linked.

In some instances there may not be a clear acceleration in the precursor activity at all (e.g. Soufrière Hills Volcano, May 2006 and February 2010). Accelerations in seismicity or deformation may also occur that do not culminate in an eruption (e.g. at Chiles-Cerro Negro, October 2014) and therefore can lead to false forecasts, although deformation has not been investigated in this study. This research has taken one step in the direction of reducing the likelihood of false forecasts by simply focusing on a single active system at depth, however they are likely to always be part of forecasting since nature is usually more chaotic than simple. It is essential for forecasters to be able to tell the difference between accelerating seismicity which may culminate in an eruption, and that which will not. Data mining of a large number of accelerating sequences of precursory activity before eruptive events, as well as those which did not erupt may expose patterns between these two which could be exploited.

Bell et al. (2011b) suggested one of the fundamental limitations of the FFM is that the assumed error structure after linearisation is not valid, and this therefore generates imprecise failure times. They suggest that a generalised linear model (GLM) may be more appropriate since it accounts for the likely Poisson distribution of errors that is incurred for seismic event rates. However, investigation into the use of a GLM did not provide more accurate forecasts for the dome collapse events at Soufrière Hills volcano, and instead consistently over-estimated the timing of failure (Section 4.6). Therefore, although the error structure is accurately accounted for, the forecast which is arguably the most important output parameter, is not accurate which makes its use inappropriate in this instance. This suggests perhaps that a GLM which assumes

a Poisson mode of error is not appropriate either. In order for the Poisson error structure to be valid, the event rate process must be a memoryless system, where each event is not influenced by any that have come before it (Greenhough and Main, 2008), however this may not be the case (Hammer and Ohrnberger, 2012).

The main reason behind the assumption that $\alpha = 2$ is that it the least squared linear regression pattern has been commonly observed in real data for forecasting volcanic processes (Cornelius and Voight, 1994, Voight, 1988, Ortiz et al., 2003, Hammer and Neuberg, 2009, Smith et al., 2009). Typically α is thought to lie between values of 1 and 2 if measured (Voight, 1988, Cornelius and Voight, 1995) and may even evolve between the two values (Kilburn, 2003), however there are cases where α has been seen to extend up to 3.3 (Smith and Kilburn, 2010), although this was using high frequency seismicity as an input parameter to the FFM and is the only case of such a high value, and therefore may represent an artefact. It may therefore be that α is a direct consequence of the input parameters, differing depending on whether it is deformation data, low frequency seismicity or high frequency seismicity used as an input, since the acceleration in any of these parameters is thought to relate to a different physical process. Perhaps more vital is gaining an understanding as to why α can vary so much, and under which circumstances it cannot assumed to equal two.

8.1.5 Multi-parameter studies for forecasting volcanic eruptions

This research has highlighted the real need for multi-parameter forecasting tools at volcanoes, since one methodology may not always be capable of producing accurate forecasts. Accelerating seismicity has been at the forefront of forecasting volcanic eruptions, primarily because any deviation from the background level is easily identifiable and forecasts can be based upon very simple measures such as event counts in a relatively short space of time. However, there are cases when the seismicity does not appear to accelerate prior to an eruptive event (e.g. Soufrière Hills volcano, February 2010) or when accelerations in seismicity do not culminate in an eruption (e.g. Chiles-Cerro Negro, October 2014). It is therefore not always appropriate to rely entirely upon seismicity to generate forecasts. Nonetheless, the use of multiple parameters as integrated forecasting tools may create added complications since the analysis of the data may not always agree in terms of the patterns of precursors or the timing of the forecast. In these instances it may be difficult to determine the forecast which is most accurate.

This research has highlighted the importance of understanding the stability of the volcanic dome complex during periods of unrest, since the movement of magmatic fluid at depth will only be able to induce collapse events if the dome is critically unstable to begin with. Currently, routine stability analysis is not conducted at many volcanic edifices. Finite Element modelling (FEM) software is generally expensive and computationally intensive. However, perhaps the biggest reason that FEM of slope stability has not yet become routine practice is because of the extremely large errors encountered in the potential stability due to lack of mechanical data about the volcanic dome. The general geometry of the surface of the dome can be estimated from digital images, or from recent digital elevation models. However, the distribution of rock masses within the volcanic complex, the properties of these and the fracture network are at best estimated or extrapolated from surface observations.

A model is always a simplified representation of reality. In the case of FEM at Soufrière Hills it has been assumed that the entire edifice is made up of only three different rock types (a solid andesitic core, a hydrothermally altered layer of andesite and a thin pyroclastic layer at the surface), and the magma chamber. These rock types are clearly separated within the stratigraphy by distinct boundaries and their mechanical properties are static and do not change, even with the migration of magma from depth. Strength value estimates for volcanic rocks are rare (Thomas et al., 2004b), which introduces large uncertainties associated with slope stability analysis (del Potro and Hürlimann, 2008). Even if recorded values do exist, they are often greatly under-constrained, resulting in large uncertainties in modelling. With further detailed research into the strength properties of volcanic rocks under different conditions (saturated, dry, hot, cold) it will be possible to further constrain these parameters and increase the accuracy of the modelling. Major problems for FEM stem from the fact that a volcanic edifice is likely to be hot at depth due to active magmatic sources, and the dynamic nature of the volcanic environment means that the mechanical and physical properties of the edifice are unlikely to be static through time and space. A heat source may raise the pore fluid pressure in its near vicinity, cause chemical alterations and is likely to migrate through existing or recently created fractures if opportunity presents. These can be difficult to represent in a FEM, particularly as they evolve with time, but a sensitivity analysis may offer some suggestion as to their importance in terms of affect upon the FEM. Therefore, upon interpretation, it should be remembered that the model represents a single static point in time, before the movement of magma has begun (i.e. during a time of quiescence).

8.2 Overview of conclusions

The use of similar seismic waveforms has been investigated to provide a more accurate forecasting tool for the timing of failure events at volcanoes compared to the current methodology using the FFM. Three large scale dome collapse events at Soufrière Hills volcano, Montserrat were investigated using precursory seismicity and instability analysis of the volcanic dome complex. Instability analysis allowed causal links between seismicity at depth and failure at the surface to be established. The techniques used to resolve similar seismicity and generate forecasts for volcanic events at Soufrière Hills were then applied to an unrest scenario at Chiles-Cerro Negro (Ecuador/Colombia) to determine the usefulness and accuracy of these techniques at an almost unknown volcano. One major outcome of this research is the implementation of forecasting codes (the identification of similar seismicity from the continuous seismic record and its use in conjunction with the FFM) at the Instituto Geofisico-EPN, Ecuador to test their applicability to real time forecasting.

The main conclusions of this research are:

1. **The identification of one single active seismic system at depth allows more accurate forecasts to be developed using the FFM**. The classification of seismicity based on spectral content allows different processes at depth to be separated (e.g. low frequency events are related to the movement of fluid, whereas high frequency events are related to fracturing of the volcanic edifice). However, further classification is needed so that the forecast utilizes one single accelerating process, rather than averaging over a larger set of accelerating phenomena, which can lead to larger discrepancies in the forecasted failure timing. A cross correlation technique applied to precursory dome collapse seismicity at Soufrière Hills volcano suggests that this technique improves the accuracy of the timing of the forecast of the dome collapse event in 1997 and 2003, in particular when considering only the accelerating pattern of seismicity, whilst also increasing the likely confidence in the forecast (model fits well to data).

2. **The FFM is not always appropriate as a forecasting tool**. Despite being the most commonly used forecasting tool for volcanic eruptions in hindsight and near real time, it appears that the FFM is not always appropriate to forecast lava dome collapse, since a clear forecast was only identified in June 1997 at Soufrière Hills volcano, and not the other dome collapse events investigated. Fundamentally, the FFM is appropriate for de-

termining the timing of a failure event from a single accelerating precursory sequence, which is directly related to the failure event at the surface. The identification of a single accelerating process may be for individual seismic event rates, or over a number of swarms of seismicity. Often, the precursory signals and the failure scenario are separated by a number of kilometres, and it is questionable whether traditional methods of using the FFM identify a causal relationship between the two. This is why identifying a single active system at depth is so fundamental, since a causal link must be established.

3. **Alternative regression analysis for forecasting the timing of a volcanic eruption does not necessarily lead to more accurate forecasts**. When applying the FFM to inverse event rate data it is usually assumed that the power law exponent α is equal to 2. The independent calculation of α in this research determines that it is rarely equal to 2 for accelerating LF seismicity prior to a dome collapse, suggesting a fundamental flaw in using this assumption. In addition, one major assumption of the FFM is that the error distribution should follow a typical Gaussian curve. However, seismic event rate is likely to be a point process and therefore be best represented by a Poisson regime, undermining the initial assumptions of the FFM. Application of a Generalised Linear Model which can account for this alternative error structure however does not appear to provide more accurate forecasts to the timing of the investigated dome collapses, consistently over predicting the timing of collapse.

4. **Identifying the stability of a volcano is important prior to the onset of unrest scenarios**. Dome material must be unstable, or close to instability in order for some precursory activity to cause collapse. Therefore, an initial analysis of the stability of the dome should be performed based on the mechanical properties of the rock masses identified. Stability analysis of the 2003 and 2010 dome prior to collapse events at Soufrière Hills suggest that on both occasions the dome was already in a critical state of instability, and therefore had a high potential for collapse. Finite element modelling even matched the known failure geometries of the two collapse events, suggesting the potential for stability analysis as a monitoring and forecasting tool if integrated with other techniques.

5. **The most influential parameter in causing a dome collapse at Soufrière Hills volcano is low frequency seismicity**. Grey incidence analysis for the June 1997 dome collapse suggested that statistically the most influential parameter affecting the likelihood of a dome collapse at Soufrière Hills volcano is the acceleration of low frequency

seismicity. Low frequency seismicity can fundamentally be related to the movement of magma at depth towards the surface, and therefore is thought of as inducing instability through the increase in pore fluid pressures at depth related to the movement of magmatic fluid. Therefore the large scale dome collapse events observed at Soufrière Hills volcano are controlled by the movement of magma at depth, which can be recognised through precursory low frequency seismicity, rather than surface processes such as rainfall and erosion of the talus slopes.

6. **Forecasting tools need to be adequate for the observatory in question and applicable in real time scenarios**. There is a clear difference in the monitoring capacity at the two investigated volcanoes: Soufrière Hills has excellent and modern monitoring equipment, and has been regularly monitored for over 20 years generating a huge wealth of data about different eruptive scenarios at this volcano. Chiles-Cerro Negro has few historical observations, limited monitoring data, and an unknown number of possible scenario outcomes to unrest. The codes developed to analyse similar seismicity and its use in potential forecasting scenarios is simple enough to be used by volcano observatories, which may not necessarily have the most modern equipment, but sophisticated enough to produce accurate forecasts if large volumes of data are available. The real time application of such forecasting codes is currently under investigation at the Instituto Geofisico for the daily monitoring of volcanoes in Ecuador.

7. **The identification of similar seismicity at Chiles-Cerro Negro may have aided understanding of temporal and spatial patterns of seismicity**. Similar seismicity was identified at Chiles-Cerro Negro for the first time during the unfolding unrest in October 2014. The similar seismicity became distinctly organised on 20 October, prior to a M5.8 earthquake less than 10 km from the volcano and therefore assumed to be related to volcanic processes, into separate temporal clusters of similar seismicity. Each cluster was significantly different from the others, indicating the activation of a new source at depth, related to the brittle failure of different parts of the edifice. It has been suggested that the opening of a dyke may have perturbed the stress field enough to generate an acceleration in seismicity. Analysis of the acceleration observed in the similar seismicity in real time may have provided an accurate forecast for the timing of the M5.8 earthquake.

8.3 Further Work

This research provides a first investigation into the use of similar seismic events as a forecasting tool at a number of eruptive events at the same volcano, Soufrière Hills, Montserrat, over a number of years. With over 20 years worth of seismic data, there is plenty of opportunity to further develop this methodology, testing it on the precursory seismicity at other dome collapse events, of a variety of sizes. Soufrière Hills has also experienced other eruptive events such as Vulcanian explosions, which could be investigated in relation to similar seismicity. Another obvious extension to this work would be to investigate the presence of similar seismicity during times of relative quiescence at this volcano, and compare it to that observed during eruptive episodes.

In relation to the similar seismicity identified at Chiles-Cerro Negro, further analysis of the temporal extent of similar events, its organisation and evolution would identify whether the use of similar seismicity to understand the magmatic plumbing system at depth is possible. With additional data from the Colombian seismometers, more accurate locations of the clustered events identified in October 2014 could be derived, which could detail the spatial evolution of the stress field at depth.

Similar seismicity has already been observed at a number of other volcanoes around the world including Redoubt, Shishaldin and Augustine in Alaska (Stephens and Chouet, 2001, Caplan-Auerbach and Petersen, 2005, Buurman and West, 2010) both in relation to eruptive and non-eruptive events. Previous research has already concluded that the FFM could be used successfully as a forecasting tool at Redoubt (Cornelius and Voight, 1994), therefore the further development of forecasting tools based on similar seismicity in this region appears to hold a high degree of merit.

Despite these forecasting tools already being sent for implementation at the Instituto Geofisico, a full review of its success is needed in the near future. This review should report the ease of implementation, specific parameters that had to be changed due to the codes being implemented on a number of volcanoes, and analysis of its success for determining similar seismicity during accelerating precursory patterns in real time. The additional implementation of cross correlation codes which are optimized for real time analysis with large volumes of data

(e.g. the *"peakmatch"* program, Rodgers (2013)) may aid the initial time and computationally intensive stage of identifying similar seismic events.

Slope stability modelling has yet to become routine monitoring within volcano observatories, most likely because the results to date are simply too uncertain to have real confidence in. Finite Element Models are only as accurate as the input data. More realistic models will therefore benefit from: more detailed and extensive rock strength experiments on volcanic rocks under a number of different conditions (e.g. saturated, dry, hot, fractured), the introduction of heterogeneity into the stratigraphy of the edifice, the introduction of a realistic fracture network at depth and the transformation of the models into three dimensions (e.g. using programs such as FLAC3D (ITASCA Consulting Group, Inc., 2015)).

References

Aiuppa, A., Moretti, R., Federico, C., Giudice, G., Gurrieri, S., Liuzzo, M., Papale, P., Shinohara, H., and Valenza, M. (2007). Forecasting Etna eruptions by real-time observation of volcanic gas composition. *Geology*, 35(12):1115–1118.

Apuani, T., Corazzato, C., Cancelli, A., and Tibaldi, A. (2005). Physical and mechanical properties of rock masses at Stromboli: a dataset for volcano instability evaluation. *Bulletin of Engineering Geology and the Environment*, 64(4):419–431.

Arciniega-Ceballos, A., Chouet, B., and Dawson, P. (2003). Long-period events and tremor at Popocatepetl volcano (1994-2000) and their broadband characteristics. *Bulletin of Volcanology*, 65(2):124–135.

Arıkan, F., Ulusay, R., and Aydın, N. (2007). Characterization of weathered acidic volcanic rocks and a weathering classification based on a rating system. *Bulletin of Engineering Geology and the Environment*, 66(4):415–430.

Ashford, S. A., Sitar, N., Lysmer, J., and Deng, N. (1997). Topographic effects on the seismic response of steep slopes. *Bulletin of the Seismological Society of America*, 87(3):701–709.

Aspinall, W., Miller, A., Lynch, L., Latchman, J., Stewart, R., White, R., and Power, J. (1998). Soufrière Hills eruption, Montserrat, 1995-1997: Volcanic earthquake locations and fault plane solutions. *Geophysical Research Letters*, 25:3397–3400.

Banks, N., Williams, S., et al. (1997). 14 C ages and activity for the past 50 ka at Volcán Galeras, Colombia. *Journal of Volcanology and Geothermal Research*, 77(1):39–55.

Barclay, J., Johnstone, J. E., and Matthews, A. J. (2006). Meteorological monitoring of an active volcano: implications for eruption prediction. *Journal of Volcanology and Geothermal Research*, 150(4):339–358.

Barrett, J. P. (1974). The coefficient of determinationâsome limitations. *The American Statistician*, 28(1):19–20.

Bean, C. J., De Barros, L., Lokmer, I., Métaxian, J.-P., OBrien, G., and Murphy, S. (2014). Long-period seismicity in the shallow volcanic edifice formed from slow-rupture earthquakes. *Nature Geoscience*, 7(1):71–75.

Beauval, C., Yepes, H., Bakun, W. H., Egred, J., Alvarado, A., and Singaucho, J.-C. (2010). Locations and magnitudes of historical earthquakes in the Sierra of Ecuador (1587–1996). *Geophysical Journal International*, 181(3):1613–1633.

Bell, A., Greenhough, J., Heap, M., and Main, I. (2011a). Challenges for forecasting based on accelerating rates of earthquakes at volcanoes and laboratory analogues. *Geophysical Journal International*, 185:718–723.

Bell, A., Naylor, M., Heap, M., and Main, I. (2011b). Forecasting volcanic eruptions and other material failure phenomena: An evaluation of the failure forecast method. *Geophysical Research Letters*, 38:L15304.

Bell, A. F. and Kilburn, C. R. (2012). Precursors to dyke-fed eruptions at basaltic volcanoes: insights from patterns of volcano-tectonic seismicity at Kilauea volcano, Hawaii. *Bulletin of Volcanology*, 74(2):325–339.

Bell, A. F., Naylor, M., and Main, I. G. (2013). The limits of predictability of volcanic eruptions from accelerating rates of earthquakes. *Geophysical Journal International*, 194(3):1541–1553.

Benson, P., Vinciguerra, S., Meredith, P., and Young, R. (2008). Laboratory simulation of volcano seismicity. *Science*, 322(5899):249–252.

Biggs, J., Ebmeier, S., Aspinall, W., Lu, Z., Pritchard, M., Sparks, R., and Mather, T. (2014). Global link between deformation and volcanic eruption quantified by satellite imagery. *Nature Communications*, 5.

Bing-jun, L., Si-feng, L., and Bin, L. (2005). The heirarchic Grey Incidence Analysis model with fixed weights and its application to a regional scientific-technical system. In *2005 IEEE International Conference on Systems, Man and Cybernetics*, volume 2, pages 1097 – 1102.

Bird, P. (2003). An updated digital model of plate boundaries. *Geochemistry, Geophysics, Geosystems*, 4(3).

Bishop, A. W. (1955). The use of the slip circle in the stability analysis of slopes. *Géotechnique*, 5(1):7–17.

Boudon, G., Villemant, B., Komorowski, J.-C., Ildefonse, P., and Semet, M. P. (1998). The hydrothermal system at Soufriere Hills Volcano, Montserrat (West Indies): Characterization and role in the on-going eruption. *Geophysical Research Letters*, 25(19):3693–3696.

Boué, A. (2015). *Data mining and volcanic eruption forecasting*. PhD thesis, L'université de Grenoble.

Boué, A., Lesage, P., Cortés, G., Valette, B., and Reyes-Dávila, G. (2015). Real-time eruption forecasting using the material Failure Forecast Method with a Bayesian approach. *Journal of Geophysical Research: Solid Earth*, 120(4):2143–2161.

Bowman, D. D. and King, G. C. (2001). Accelerating seismicity and stress accumulation before large earthquakes. *Geophysical Research Letters*, 28(21):4039–4042.

Bufe, C. G. and Varnes, D. J. (1993). Predictive modeling of the seismic cycle of the Greater San Francisco Bay Region. *Journal of Geophysical Research: Solid Earth*, 98(B6):9871–9883.

Buurman, H., Nye, C. J., West, M. E., and Cameron, C. (2014). Regional controls on volcano seismicity along the Aleutian arc. *Geochemistry, Geophysics, Geosystems*, 15(4):1147–1163.

Buurman, H. and West, Michael, E. (2010). Seismic precursors to the volcanic explosions during the 2006 eruption of Augustine Volcano. In Power, J. A., Coombs, M. L., and Freymueller, J. T., editors, *The 2006 Eruption of Augustine Volcano, Alaska*. US Geological Survery Professional Paper 1769.

Buurman, H., West, M. E., and Thompson, G. (2013). The seismicity of the 2009 Redoubt eruption. *Journal of Volcanology and Geothermal Research*, 259:16–30.

Calder, E., Luckett, R., Sparks, R., and Voight, B. (2002). Mechanisms of lava dome instability and generation of rockfalls and pyroclastic flows at Soufriere Hills Volcano, Montserrat. *Geological Society, London, Memoirs*, 21(1):173–190.

Caplan-Auerbach, J. and Petersen, T. (2005). Repeating coupled earthquakes at Shishaldin Volcano, Alaska. *Journal of Volcanology and Geothermal Research*, 145(1):151–172.

Carn, S., Watts, R., Thompson, G., and Norton, G. (2004). Anatomy of a lava dome collapse: the 20 March 2000 event at Soufrière Hills Volcano, Montserrat. *Journal of Volcanology and Geothermal Research*, 131(3):241–264.

Casadevall, T. J. (1994). *Volcanic ash and aviation safety: proceedings of the first international symposium on volcanic ash and aviation safety*, volume 2047. DIANE Publishing.

Chastin, S. F. and Main, I. G. (2003). Statistical analysis of daily seismic event rate as a precursor to volcanic eruptions. *Geophysical Research Letters*, 30(13).

Chouet, B. (1988). Resonance of a fluid-driven crack: Radiation properties and implications for the source of long-period events and harmonic tremor. *Journal of Geophysical Research: Solid Earth (1978–2012)*, 93(B5):4375–4400.

Chouet, B. (1996a). Long-period volcano seismicity: its source and use in eruption forecasting. *Nature*, 380(6572):309–316.

Chouet, B., Dawson, P., and Arciniega-Ceballos, A. (2005). Source mechanism of Vulcanian degassing at Popocatépetl Volcano, Mexico, determined from waveform inversions of very long period signals. *Journal of Geophysical Research: Solid Earth (1978–2012)*, 110(B7).

Chouet, B., Dawson, P., and Martini, M. (2008). Shallow-conduit dynamics at Stromboli Volcano, Italy, imaged from waveform inversions. *Geological Society, London, Special Publications*, 307(1):57–84.

Chouet, B. A. (1996b). New methods and future trends in seismological volcano monitoring. In *Monitoring and Mitigation of Volcano Hazards*, pages 23–97. Springer.

Chouet, B. A. and Matoza, R. S. (2013). A multi-decadal view of seismic methods for detecting precursors of magma movement and eruption. *Journal of Volcanology and Geothermal Research*, 252:108–175.

Chouet, B. A., Page, R. A., Stephens, C. D., Lahr, J. C., and Power, J. A. (1994). Precursory swarms of long-period events at Redoubt Volcano (1989–1990), Alaska: Their origin and use as a forecasting tool. *Journal of Volcanology and Geothermal Research*, 62(1):95–135.

Christiansen, R. L. and Peterson, D. W. (1981). Chronology of the 1980 Eruptive Activity. *The 1980 Eruptions of Mount St. Helens, Washington*, (1250):17.

Christopher, T., Edmonds, M., Humphreys, M., and Herd, R. A. (2010). Volcanic gas emissions from Soufrière Hills Volcano, Montserrat 1995–2009, with implications for mafic magma supply and degassing. *Geophysical Research Letters*, 37(19).

Collier, L. and Neuberg, J. (2006). Incorporating seismic observations into 2D conduit flow modeling. *Journal of Volcanology and Geothermal Research*, 152(3):331–346.

Collier, L., Neuberg, J., Lensky, N., Lyakhovsky, V., and Navon, O. (2006). Attenuation in gas-charged magma. *Journal of Volcanology and Geothermal Research*, 153(1):21–36.

Cornelius, R. and Voight, B. (1994). Seismological aspects of the 1989–1990 eruption at Redoubt Volcano, Alaska: the materials Failure Forecast Method (FFM) with RSAM and SSAM seismic data. *Journal of Volcanology and Geothermal Research*, 62(1):469–498.

Cornelius, R. and Voight, B. (1995). Graphical and PC-software analysis of volcano eruption precursors according to the materials Failure Forecast Method (FFM). *Journal of Volcanology and Geothermal Research*, 64(3-4):295–320.

Costa, A., Melnik, O., Sparks, R., and Voight, B. (2007). Control of magma flow in dykes on cyclic lava dome extrusion. *Geophysical Research Letters*, 34(2).

Dawson, P. B., Chouet, B. A., and Power, J. (2011). Determining the seismic source mechanism and location for an explosive eruption with limited observational data: Augustine Volcano, Alaska. *Geophysical Research Letters*, 38(3).

Day, S. (1996). Hydrothermal pore fluid pressure and the stability of porous, permeable volcanoes. *Geological Society, London, Special Publications*, 110(1):77–93.

De Angelis, S., Bass, V., Hards, V., and Ryan, G. (2007). Seismic characterization of pyroclastic flow activity at Soufrière Hills Volcano, Montserrat, 8 January 2007. *Natural Hazards and Earth System Sciences*, 7:467–472.

De Angelis, S. and Henton, S. (2011). On the feasibility of magma fracture within volcanic conduits: Constraints from earthquake data and empirical modelling of magma viscosity. *Geophysical Research Letters*, 38(19).

De la Cruz-Reyna, S. and Reyes-Dávila, G. A. (2001). A model to describe precursory material-failure phenomena: applications to short-term forecasting at Colima volcano, Mexico. *Bulletin of Volcanology*, 63(5):297–308.

del Potro, R. and Hürlimann, M. (2008). Geotechnical classification and characterisation of materials for stability analyses of large volcanic slopes. *Engineering Geology*, 98(1):1–17.

Deng, J.-L. (1982). Control problems of grey systems. *Systems & Control Letters*, 1(5):288–294.

Denlinger, R. P. and Hoblitt, R. P. (1999). Cyclic eruptive behavior of silicic volcanoes. *Geology*, 27(5):459–462.

Dinçer, I., Acar, A., Çobanoğlu, I., and Uras, Y. (2004). Correlation between Schmidt hardness, uniaxial compressive strength and Youngs modulus for andesites, basalts and tuffs. *Bulletin of Engineering Geology and the Environment*, 63(2):141–148.

Donovan, A., Oppenheimer, C., and Bravo, M. (2011). Rationalising a volcanic crisis through literature: Montserratian verse and the descriptive reconstruction of an island. *Journal of Volcanology and Geothermal Research*, 203:87–101.

Draper, G., Jackson, T. A., and Donovan, S. K. (1994). Geologic provinces of the Caribbean region. *Caribbean Geology: An Introduction*, pages 3–12.

Droux, A. and Delaloye, M. (1996). Petrography and geochemistry of Plio-Quaternary calc-alkaline volcanoes of southwestern Colombia. *Journal of South American Earth Sciences*, 9(1):27–41.

Duncan, J. M. (1996). State of the art: limit equilibrium and finite-element analysis of slopes. *Journal of Geotechnical engineering*, 122(7):577–596.

Duncan, J. M., Wright, S. G., and Brandon, T. L. (2014). *Soil strength and slope stability*. John Wiley & Sons.

Dzurisin, D. (2000). Volcano geodesy: challenges and opportunities for the 21st century. *Philosophical Transactions of the Royal Society of London A: Mathematical, Physical and Engineering Sciences*, 358(1770):1547–1566.

Dzurisin, D. (2003). A comprehensive approach to monitoring volcano deformation as a window on the eruption cycle. *Reviews of Geophysics*, 41(1).

Edmonds, M., Aiuppa, A., Humphreys, M., Moretti, R., Giudice, G., Martin, R., Herd, R., and Christopher, T. (2010). Excess volatiles supplied by mingling of mafic magma at an andesite arc volcano. *Geochemistry, Geophysics, Geosystems*, 11(4).

Edmonds, M., Herd, R., Galle, B., and Oppenheimer, C. (2003). Automated, high time-resolution measurements of SO2 flux at Soufriere Hills Volcano, Montserrat. *Bulletin of Volcanology*, 65(8):578–586.

Elsworth, D. and Voight, B. (1995). Dike intrusion as a trigger for large earthquakes and the failure of volcano flanks. *Journal of Geophysical Research: Solid Earth (1978–2012)*, 100(B4):6005–6024.

Elsworth, D. and Voight, B. (1996). Evaluation of volcano flank instability triggered by dyke intrusion. *Geological Society, London, Special Publications*, 110(1):45–53.

Elsworth, D., Voight, B., Thompson, G., and Young, S. (2004). Thermal-hydrologic mechanism for rainfall-triggered collapse of lava domes. *Geology*, 32(11):969–972.

Endo, E. T. and Murray, T. (1991). Real-time seismic amplitude measurement (RSAM): a volcano monitoring and prediction tool. *Bulletin of Volcanology*, 53(7):533–545.

Esposito, L. and Guadagno, F. (1998). Some special geotechnical properties of pumice deposits. *Bulletin of Engineering Geology and the Environment*, 57(1):41–50.

Fehler, M. (1983). Observations of volcanic tremor at Mount St. Helens volcano. *Journal of Geophysical Research: Solid Earth (1978–2012)*, 88(B4):3476–3484.

Ferrazzini, V. and Aki, K. (1987). Slow waves trapped in a fluid-filled infinite crack: Implication for volcanic tremor. *Journal of Geophysical Research: Solid Earth (1978–2012)*, 92(B9):9215–9223.

Feuillet, N., Manighetti, I., Tapponnier, P., and Jacques, E. (2002). Arc parallel extension and localization of volcanic complexes in Guadeloupe, Lesser Antilles. *Journal of Geophysical Research: Solid Earth (1978–2012)*, 107(B12):ETG–3.

Francis, P. and Wells, G. (1988). Landsat Thematic Mapper observations of debris avalanche deposits in the Central Andes. *Bulletin of Volcanology*, 50(4):258–278.

Freeze, R. A. and Cherry, J. (1979). *Groundwater*. Prentice-Hall, Englewood Cliffs, New Jersey.

Fukuzono, T. (1985). A new method for predicting the failure time of a slope. In *Proceedings of the 4th International Conference and Field Workshop in Landslides, Tokyo*, pages 145–150.

Galle, B., Oppenheimer, C., Geyer, A., McGonigle, A. J., Edmonds, M., and Horrocks, L. (2003). A miniaturised ultraviolet spectrometer for remote sensing of SO 2 fluxes: a new tool for volcano surveillance. *Journal of Volcanology and Geothermal Research*, 119(1):241–254.

Geller, R. and Mueller, C. (1980). Four similar earthquakes in central California. *Geophysical Research Letters*, 7(10):821–824.

Gercek, H. (2007). Poisson's ratio values for rocks. *International Journal of Rock Mechanics and Mining Sciences*, 44(1):1–13.

Gerst, A. and Savage, M. K. (2004). Seismic anisotropy beneath Ruapehu volcano: A possible eruption forecasting tool. *Science*, 306(5701):1543–1547.

GFZ-Potsdam (2014). GFZ Event gfz2014uozp: 14.10.20 19:33:23.71: Colombia-Ecuador Border Region: Moment Tensor Solution. Online at: http://geofon.gfz-potsdam.de/data/alerts/2014/gfz2014uozp/mt.txt, Accessed: 10.08.2015.

Giggenbach, W. (1996). Chemical composition of volcanic gases. In *Monitoring and Mitigation of Volcano Hazards*, pages 221–256. Springer.

Giunta, G. and Orioli, S. (2011). *The Caribbean Plate Evolution: Trying to resolve a very complicated tectonic puzzle*, chapter 10. InTech, Rijeka, Croatia.

Google Earth 5.0 (2013). Chiles and Cerro Negro Volcanoes: 00°48' N, 77°56' W. Software Online at: http://www.google.com/earth/, Accessed: 19.08.2015.

Goto, A. (1999). A new model for volcanic earthquake at Unzen Volcano: Melt rupture model. *Geophysical Research Letters*, 26(16):2541–2544.

Green, D. and Neuberg, J. (2006). Waveform classification of volcanic low-frequency earthquake swarms and its implication at Soufrière Hills Volcano, Montserrat. *Journal of Volcanology and Geothermal Research*, 153(1):51–63.

Green, D., Neuberg, J., and Cayol, V. (2006). Shear stress along the conduit wall as a plausible source of tilt at soufrière hills volcano, montserrat. *Geophysical Research Letters*, 33(10).

Greenhough, J. and Main, I. (2008). A poisson model for earthquake frequency uncertainties in seismic hazard analysis. *Geophysical Research Letters*, 35(19).

Griffiths, D. and Lane, P. (1999). Slope stability analysis by finite elements. *Geotechnique*, 49(3):387–403.

Grösser, J. (1989). Geotectonic evolution of the Western Cordillera of Colombia: New aspects from geochemical data on volcanic rocks. *Journal of South American Earth Sciences*, 2(4):359–369.

Guffanti, M., Casadevall, T. J., and Budding, K. (2010). Encounters of aircraft with volcanic ash clouds; A compilation of known incidents, 1953-2009. Technical report, US Geological Survey.

Hall, M. and Mothes, P. (2008). The rhyolitic–andesitic eruptive history of Cotopaxi volcano, Ecuador. *Bulletin of Volcanology*, 70(6):675–702.

Hall, M. L., Robin, C., Beate, B., Mothes, P., and Monzier, M. (1999). Tungurahua Volcano, Ecuador: structure, eruptive history and hazards. *Journal of Volcanology and Geothermal Research*, 91(1):1–21.

Hammah, R. E., Curran, J. H., Yacoub, T., and Corkum, B. (2004). Stability analysis of rock slopes using the finite element method. In *Proceedings of the ISRM regional symposium EUROCK*.

Hammer, C. and Neuberg, J. (2009). On the dynamical behaviour of low-frequency earthquake swarms prior to a dome collapse of Soufrière Hill volcano, Montserrat. *Geophysical Research Letters*, 36(6):L06305.

Hammer, C. and Ohrnberger, M. (2012). Forecasting seismo-volcanic activity by using the dynamical behavior of volcanic earthquake rates. *Journal of Volcanology and Geothermal Research*, 229:34–43.

Harford, C., Pringle, M., Sparks, R., and Young, S. (2002). The volcanic evolution of Montserrat using 40Ar/39Ar geochronology. *Geological Society, London, Memoirs*, 21(1):93–113.

Harlow, D. H., Power, J. A., Laguerta, E. P., Ambubuyog, G., White, R. A., and Hoblitt, R. P. (1996). Precursory seismicity and forecasting of the June 15, 1991, eruption of Mount Pinatubo. *Fire and mud: Eruptions and lahars of Mount Pinatubo, Philippines*, pages 223–247.

Harrington, R. M. and Brodsky, E. E. (2007). Volcanic hybrid earthquakes that are brittle-failure events. *Geophysical Research Letters*, 34(6).

Hautmann, S., Gottsmann, J., Sparks, R. S. J., Costa, A., Melnik, O., and Voight, B. (2009). Modelling ground deformation caused by oscillating overpressure in a dyke conduit at soufrière hills volcano, montserrat. *Tectonophysics*, 471(1):87–95.

Hautmann, S., Witham, F., Christopher, T., Cole, P., Linde, A. T., Sacks, I. S., and Sparks, R. S. J. (2014). Strain field analysis on montserrat (wi) as tool for assessing permeable flow paths in the magmatic system of soufrière hills volcano. *Geochemistry, Geophysics, Geosystems*, 15(3):676–690.

Herd, R. A., Edmonds, M., and Bass, V. A. (2005). Catastrophic lava dome failure at Soufriere Hills volcano, Montserrat, 12–13 July 2003. *Journal of Volcanology and Geothermal Research*, 148(3):234–252.

Hidayat, D., Voight, B., Langston, C., Ratdomopurbo, A., and Ebeling, C. (2000). Broadband seismic experiment at Merapi Volcano, Java, Indonesia: very-long-period pulses embedded in multiphase earthquakes. *Journal of Volcanology and Geothermal Research*, 100(1):215–231.

Holland, A. P., Watson, I. M., Phillips, J. C., Caricchi, L., and Dalton, M. P. (2011). Degassing processes during lava dome growth: Insights from Santiaguito lava dome, Guatemala. *Journal of Volcanology and Geothermal Research*, 202(1):153–166.

Hubbert, M. K. and Rubey, W. W. (1959). Role of fluid pressure in mechanics of overthrust faulting i. Mechanics of fluid-filled porous solids and its application to overthrust faulting. *Geological Society of America Bulletin*, 70(2):115–166.

Instituto Geofisico EPN (2015). Chiles - Cerro Negro. Online at: http://www.igepn.edu.ec/chiles-cerro-negro. Accessed: 31.03.2015.

ITASCA Consulting Group, Inc. (2015). *FLAC3D, Version 5.0*. Itasca International Company.

Iverson, R., Dzurisin, D., Gardner, C., Gerlach, T., LaHusen, R., Lisowski, M., Major, J., Malone, S., Messerich, J., Moran, S., et al. (2006). Dynamics of seismogenic volcanic extrusion at Mount St Helens in 2004–05. *Nature*, 444(7118):439–443.

Janbu, N. (1968). Slope stability computations. Soil Mechanics and Foundations Engineering Report. The Technical University of Norway, Trondheim, Norway.

Jibson, R. W. and Keefer, D. K. (1989). Statistical analysis of factors affecting landslide distribution in the New Madrid seismic zone, Tennessee and Kentucky. *Engineering Geology*, 27(1):509–542.

Jimenez, G. P. C. and Velasco, M. L. C. (1997). Informe sobre la evaluacion de la amenaza volcanica del Chiles y Cerro Negro. Technical report, Republica de Colombia, Ministerio de minas y energia, Instituto de investigaciones en geociencias, mineria y quimica, Observatorio vulcanologico y sismologico de Pasto. In Spanish.

Jousset, P., Neuberg, J., and Sturton, S. (2003). Modelling the time-dependent frequency content of low-frequency volcanic earthquakes. *Journal of Volcanology and Geothermal Research*, 128(1):201–223.

Julian, B. R. (1994). Volcanic tremor: nonlinear excitation by fluid flow. *Journal of Geophysical Research: Solid Earth (1978–2012)*, 99(B6):11859–11877.

Kamo, K. and Ishihara, K. (1989). A preliminary experiment on automated judgement of the stages of eruptive activity using tiltmeter records at Sakurajima, Japan. In *Volcanic Hazards*, pages 585–598. Springer.

Kawakatsu, H., Ohminato, T., Ito, H., Kuwahara, Y., Kato, T., Tsuruga, K., Honda, S., and Yomogida, K. (1992). Broadband seismic observation at the Sakurajima volcano, Japan. *Geophysical Research Letters*, 19(19):1959–1962.

Kedar, S., Sturtevant, B., and Kanamori, H. (1996). The origin of harmonic tremor at Old Faithful geyser. *Nature*, 379:708–711.

Kilburn, C. (2003). Multiscale fracturing as a key to forecasting volcanic eruptions. *Journal of Volcanology and Geothermal Research*, 125(3-4):271–289.

Kilburn, C. (2012). Precursory deformation and fracture before brittle rock failure and potential application to volcanic unrest. *Journal of Geophysical Research: Solid Earth (1978–2012)*, 117(B2).

Kilburn, C. R. and Voight, B. (1998). Slow rock fracture as eruption precursor at Soufriere Hills volcano, Montserrat. *Geophysical Research Letters*, 25(19):3665–3668.

Lahr, J., Chouet, B., Stephens, C., Power, J., and Page, R. (1994). Earthquake classification, location, and error analysis in a volcanic environment: Implications for the magmatic system of the 1989–1990 eruptions at Redoubt Volcano, Alaska. *Journal of Volcanology and Geothermal Research*, 62(1):137–151.

Lavallée, Y., Meredith, P., Dingwell, D., Hess, K.-U., Wassermann, J., Cordonnier, B., Gerik, A., and Kruhl, J. (2008). Seismogenic lavas and explosive eruption forecasting. *Nature*, 453(7194):507–510.

Lavenu, A., Noblet, C., Bonhomme, M., Egüez, A., Dugas, F., and Vivier, G. (1992). New K-Ar age dates of Neogene and Quaternary volcanic rocks from the Ecuadorian Andes: Implications for the relationship between sedimentation, volcanism, and tectonics. *Journal of South American Earth Sciences*, 5(3):309–320.

Leet, R. C. (1988). Saturated and subcooled hydrothermal boiling in groundwater flow channels as a source of harmonic tremor. *Journal of Geophysical Research: Solid Earth (1978–2012)*, 93(B5):4835–4849.

Legrand, D., Espíndola, J., Jiménez, Z., Scolamacchia, T., Valdés-González, C., Singh, S., Lermo, J., Spica, Z., and Valenzuela, R. (2015). Comparison of the seismicity before and after the 1982 El Chichon Eruption. In *Active Volcanoes of Chiapas (Mexico): El Chichón and Tacaná*, pages 97–114. Springer.

LeVeque, R. J. (2006). Finite difference methods for differential equations. Online at: http://www.dc.uba.ar/materias/escuela-complutense/2012/FiniteDifferences, Accessed: 17.02.2016.

Linde, A. T. and Sacks, S. (1995). Continuous monitoring of volcanoes with borehole strainmeters. *Mauna Loa Revealed: Structure, Composition, History, and Hazards*, pages 171–185.

Lindsay, J., Smith, A., Roobol, M., and Stasiuk, M. (2005). Dominica. *Volcanic Hazard Atlas of the Lesser Antilles*, pages 1–18.

Lipman, P. W., Moore, J. G., and Swanson, D. (1981). Bulging of the north flank before the May 18 eruption: geodetic data. *US Geol. Surv. Prof. Pap*, 1250:143–156.

López, D. L. and Williams, S. N. (1993). Catastrophic volcanic collapse: relation to hydrothermal processes. *Science*, 260(5115):1794–1796.

Loughlin, S., Calder, E., Clarke, A., Cole, P., Luckett, R., Mangan, M., Pyle, D., Sparks, R., Voight, B., and Watts, R. (2002). Pyroclastic flows and surges generated by the 25 June 1997 dome collapse, Soufrière Hills Volcano, Montserrat. *Geological Society, London, Memoirs*, 21:191–210.

Loughlin, S., Luckett, R., Ryan, G., Christopher, T., Hards, V., De Angelis, S., Jones, L., and Strutt, M. (2010). An overview of lava dome evolution, dome collapse and cyclicity at Soufrière Hills Volcano, Montserrat, 2005–2007. *Geophysical Research Letters*, 37(19).

Lu, P. and Rosenbaum, M. (2003). Artificial neural networks and grey systems for the prediction of slope stability. *Natural Hazards*, 30(3):383–398.

Lu, Z., Mann, D., Freymueller, J. T., and Meyer, D. J. (2000). Synthetic Aperture Radar interferometry of Okmok volcano, Alaska: Radar observations. *Journal of Geophysical Research: Solid Earth (1978–2012)*, 105(B5):10791–10806.

Luckett, R. (2005). Seismic Data from the Montserrat Eruption at BGS. Technical report, British Geological Survey Open Report, OR/09/57.

Lui, S. and Lin, Y. (2006). *Grey Information: Theory and Practical Applications*. Advanced Information and Knowledge Processing. Spinger-Verlag London Limited.

Lyons, J. J., Waite, G. P., Rose, W. I., and Chigna, G. (2010). Patterns in open vent, strombolian behavior at Fuego volcano, Guatemala, 2005–2007. *Bulletin of Volcanology*, 72(1):1–15.

MacGregor, A. G. (1936). Royal Society Expedition to Montserrat, BWI: Preliminary report on the geology of Montserrat. *Proceedings of the Royal Society of London. Series B, Biological Sciences*, 121(822):232–252.

MacGregor, A. G. (1938). The Royal Society expedition to Montserrat, BWI: The volcanic history and petrology of Montserrat, with observations on Mt Pelée, in Martinique. *Philosophical Transactions of the Royal Society of London. Series B, Biological Sciences*, 229(557):1–90.

Main, I. G. (1991). A modified griffith criterion for the evolution of damage with a fractal distribution of crack lengths: application to seismic event rates and b-values. *Geophysical Journal International*, 107(2):353–362.

Main, I. G. (2000). A damage mechanics model for power-law creep and earthquake aftershock and foreshock sequences. *Geophysical Journal International*, 142(1):151–161.

Main, I. G., Sammonds, P. R., and Meredith, P. G. (1993). Application of a modified Griffith criterion to the evolution of fractal damage during compressional rock failure. *Geophysical Journal International*, 115(2):367–380.

Mastin, L. G. (1994). Explosive tephra emissions at Mount St. Helens, 1989-1991: The violent escape of magmatic gas following storms? *Geological Society of America Bulletin*, 106(2):175–185.

Matsushima, T. and Takagi, A. (2000). GPS and EDM monitoring of Unzen volcano ground deformation. *Earth, Planets and Space*, 52(11):1015–1018.

Matthews, A. J. and Barclay, J. (2004). A thermodynamical model for rainfall-triggered volcanic dome collapse. *Geophysical Research Letters*, 31(5).

Matthews, A. J., Barclay, J., Carn, S., Thompson, G., Alexander, J., Herd, R., and Williams, C. (2002). Rainfall-induced volcanic activity on Montserrat. *Geophysical Research Letters*, 29(13):22–1.

Matthews, C., Farook, Z., and Helm, P. (2014). Slope stability analysis - limit equilibrium or the finite element method? *Ground Engineering*.

Matthews, S. J., Gardeweg, M. C., and Sparks, R. S. J. (1997). The 1984 to 1996 cyclic activity of Lascar Volcano, northern Chile: cycles of dome growth, dome subsidence, degassing and explosive eruptions. *Bulletin of Volcanology*, 59(1):72–82.

McGonigle, A., Oppenheimer, C., Galle, B., Mather, T., and Pyle, D. (2002). Walking traverse and scanning DOAS measurements of volcanic gas emission rates. *Geophysical Research Letters*, 29(20):46–1.

McGuire, W. (1996). Volcano instability: a review of contemporary themes. *Geological Society, London, Special Publications*, 110(1):1–23.

McNutt, S. R. (2002). Volcano seismology and monitoring for eruptions. *International Geophysics Series*, 81(A):383–406.

McNutt, S. R. (2005). Volcanic seismology. *Annu. Rev. Earth planet. Sci.*, 32:461–491.

Melnik, O. and Sparks, R. (2002). Dynamics of magma ascent and lava extrusion at Soufrière Hills Volcano, Montserrat. *Geological Society, London, Memoirs*, 21(1):153–171.

Melnik, O. and Sparks, R. (2005). Controls on conduit magma flow dynamics during lava dome building eruptions. *Journal of Geophysical Research: Solid Earth (1978–2012)*, 110(B2).

Miller, A., Stewart, R., White, R., Luckett, R., Baptie, B., Aspinall, W., Latchman, J., Lynch, L., and Voight, B. (1998). Seismicity associated with dome growth and collapse at the Soufriere Hills volcano, Montserrat. *Geophysical Research Letters*, 25(18):3401–3404.

Molina, I., Kumagai, H., and Yepes, H. (2004). Resonances of a volcanic conduit triggered by repetitive injections of an ash-laden gas. *Geophysical Research Letters*, 31(3).

Montserrat Volcano Observatory (1997a). Scientific Report 68: 05 July 1997. Online at: http://www.geo.mtu.edu/volcanoes/west.indies/soufriere/govt/scireps/mvo_report0068.html.

Montserrat Volcano Observatory (1997b). Special report 03 - Pyroclastic flow activity on 25 June 1997. Technical report, Montserrat Volcano Observatory. Online at: http://www.geo.mtu.edu/volcanoes/west.indies/soufriere/govt/specrep/specrep03.html.

Montserrat Volcano Observatory (2012). Chronology of current eruption. Online at: http://www.mvo.ms/about-volcanoes/soufriere-hills-volcano/chronology-of-current-eruption.

Moon, V., Bradshaw, J., Smith, R., and de Lange, W. (2005). Geotechnical characterisation of stratocone crater wall sequences, White Island Volcano, New Zealand. *Engineering Geology*, 81(2):146–178.

Moore, J. (1964). Giant submarine landslides on the Hawaiian Ridge. *US Geol. Surv. Prof. Pap*, 501:D95–D98.

Morrissey, M. and Chouet, B. (2001). Trends in long-period seismicity related to magmatic fluid compositions. *Journal of Volcanology and Geothermal Research*, 108(1):265–281.

Murphy, M., Sparks, R., Barclay, J., Carroll, M., and Brewer, T. (2000). Remobilization of andesite magma by intrusion of mafic magma at the Soufriere Hills Volcano, Montserrat, West Indies. *Journal of Petrology*, 41(1):21–42.

Nakano, M. and Kumagai, H. (2005). Response of a hydrothermal system to magmatic heat inferred from temporal variations in the complex frequencies of long-period events at Kusatsu-Shirane Volcano, Japan. *Journal of Volcanology and Geothermal Research*, 147(3):233–244.

Nelder, J. A. and Wedderburn, R. W. M. (1972). Generalized linear models. *Journal of the Royal Statistical Society*, Series A(135, Part 3):370–384.

Neuberg, J., Luckett, R., Baptie, B., and Olsen, K. (2000). Models of tremor and low-frequency earthquake swarms on Montserrat. *Journal of Volcanology and Geothermal Research*, 101(1-2):83–104.

Neuberg, J., Tuffen, H., Collier, L., Green, D., Powell, T., and Dingwell, D. (2006). The trigger mechanism of low-frequency earthquakes on Montserrat. *Journal of Volcanology and Geothermal Research*, 153(1):37–50.

Neuberg, J. W. (2011). Earthquakes, Volcanogenic. In *Encyclopedia of Solid Earth Geophysics*, volume 1, pages 261–269. Springer Verlag.

Nishimura, T., Nakamichi, H., Tanaka, S., Sato, M., Kobayashi, T., Ueki, S., Hamaguchi, H., Ohtake, M., and Sato, H. (2000). Source process of very long period seismic events associated with the 1998 activity of Iwate Volcano, northeastern Japan. *Journal of Geophysical Research: Solid Earth (1978–2012)*, 105(B8):19135–19147.

NOAA (1997). Precipitation data: Le Raizet, Guadeloupe: 01.06.1997 to 30.06.1997. Online through National Climatic Data Center, http://www.ncdc.noaa.gov/cdo-web/datasets#GHCND, Data Received: 16.06.2014.

Odbert, H. M., Ryan, G. A., Mattioli, G. S., Hautmann, S., Gottsmann, J., Fournier, N., and Herd, R. A. (2014a). Volcano geodesy at the Soufrière Hills Volcano, Montserrat: a review. *Geological Society, London, Memoirs*, 39(1):195–217.

Odbert, H. M., Stewart, R. C., and Wadge, G. (2014b). Cyclic phenomena at the Soufrière Hills volcano, Montserrat. *Geological Society, London, Memoirs*, 39(1):41–60.

Ohminato, T., Chouet, B. A., Dawson, P., and Kedar, S. (1998). Waveform inversion of very long period impulsive signals associated with magmatic injection beneath Kilauea Volcano, Hawaii. *Journal of Geophysical Research: Solid Earth (1978–2012)*, 103(B10):23839–23862.

Ohminato, T., Takeo, M., Kumagai, H., Yamashina, T., Oikawa, J., Koyama, E., Tsuji, H., and Urabe, T. (2006). Vulcanian eruptions with dominant single force components observed during the Asama 2004 volcanic activity in Japan. *Earth, Planets and Space*, 58(5):583–593.

Okubo, C. H. (2004). Rock mass strength and slope stability of the Hilina slump, Kīlauea volcano, Hawai'i. *Journal of Volcanology and Geothermal Research*, 138(1):43–76.

Oppenheimer, C., Edmonds, M., Francis, P., and Burton, M. (2002). Variation in HCl/SO2 gas ratios observed by Fourier transform spectroscopy at Soufrière Hills Volcano, Montserrat. *Geological Society, London, Memoirs*, 21(1):621–639.

Ortiz, R., Moreno, H., GarcıÌ, A., Fuentealba, G., Astiz, M., Peña, P., Sánchez, N., and Tárraga, M. (2003). Villarrica volcano (Chile): characteristics of the volcanic tremor and forecasting of small explosions by means of a material failure method. *Journal of Volcanology and Geothermal Research*, 128(1):247–259.

Ottemöller, L. (2008). Seismic hybrid swarm precursory to a major lava dome collapse: 9–12 July 2003, Soufriere Hills Volcano, Montserrat. *Journal of Volcanology and Geothermal Research*, 177(4):903–910.

Owen, S., Segall, P., Lisowski, M., Miklius, A., Murray, M., Bevis, M., and Foster, J. (2000). January 30, 1997 eruptive event on Kilauea Volcano, Hawaii, as monitored by continuous GPS. *Geophysical Research Letters*, 27(17):2757–2760.

Pacheco, D. and Gomez, D. (2015). Informe del volcan Chiles-Cerro Negro n.-22: 24 de junio 2015. Technical report, Instituto Geofisico Escuela Politecnica Nacional. In Spanish.

Pagli, C., Sigmundsson, F., Pedersen, R., Einarsson, P., Árnadóttir, T., and Feigl, K. L. (2007). Crustal deformation associated with the 1996 Gjálp subglacial eruption, Iceland: InSAR studies in affected areas adjacent to the Vatnajökull ice cap. *Earth and Planetary Science Letters*, 259(1):24–33.

Papale, P. (1999). Strain-induced magma fragmentation in explosive eruptions. *Nature*, 397(6718):425–428.

Paulatto, M., Minshull, T., Baptie, B., Dean, S., Hammond, J., Henstock, T., Kenedi, C., Kiddle, E., Malin, P., Peirce, C., et al. (2010). Upper crustal structure of an active volcano from refraction/reflection tomography, Montserrat, Lesser Antilles. *Geophysical Journal International*, 180(2):685–696.

Petersen, T. (2007). Swarms of repeating long-period earthquakes at Shishaldin Volcano, Alaska, 2001–2004. *Journal of Volcanology and Geothermal Research*, 166(3):177–192.

Phillipson, G., Sobradelo, R., and Gottsmann, J. (2013). Global volcanic unrest in the 21st century: an analysis of the first decade. *Journal of Volcanology and Geothermal Research*, 264:183–196.

Pinel, V., Poland, M., and Hooper, A. (2014). Volcanology: Lessons learned from synthetic aperture radar imagery. *Journal of Volcanology and Geothermal Research*, 289:81–113.

Pingue, F., Troise, C., De Luca, G., Grassi, V., and Scarpa, R. (1998). Geodetic monitoring of Mt. Vesuvius Volcano, Italy, based on EDM and GPS surveys. *Journal of Volcanology and Geothermal Research*, 82(1):151–160.

Punongbayan, R. S., Newhall, C. G., Bautista, M. L. P., Garcia, D., Harlow, D. H., Hoblitt, R. P., Sabit, J. P., and Solidum, R. (1996). Eruption hazard assessments and warnings. *Fire and Mud: Eruptions and Lahars of Mount Pinatubo, Philippines*, pages 67–85.

Rea, W. J. (1974). The volcanic geology and petrology of Montserrat, West Indies. *Journal of the Geological Society*, 130(4):341–366.

Reid, M. E. (2004). Massive collapse of volcano edifices triggered by hydrothermal pressurization. *Geology*, 32(5):373–376.

Reid, M. E., Christian, S. B., and Brien, D. L. (2000). Gravitational stability of three-dimensional stratovolcano edifices. *Journal of Geophysical Research: Solid Earth (1978–2012)*, 105(B3):6043–6056.

Reid, M. E., Keith, T. E., Kayen, R. E., Iverson, N. R., Iverson, R. M., and Brien, D. L. (2010). Volcano collapse promoted by progressive strength reduction: new data from Mount St. Helens. *Bulletin of Volcanology*, 72(6):761–766.

Reid, M. E., Sisson, T. W., and Brien, D. L. (2001). Volcano collapse promoted by hydrothermal alteration and edifice shape, Mount Rainier, Washington. *Geology*, 29(9):779–782.

Reyes-Dávila, G. A. and De la Cruz-Reyna, S. (2002). Experience in the short-term eruption forecasting at Volcan de Colima, Mexico, and public response to forecasts. *Journal of Volcanology and Geothermal Research*, 117(1):121–127.

Ridley, W. (1971). The origin of some collapse structures in the Canary Islands. *Geological Magazine*, 108(06):477–484.

Robertson, R., Aspinall, W., Herd, R., Norton, G., Sparks, R., and Young, S. (2000). The 1995–1998 eruption of the Soufrière Hills volcano, Montserrat, WI. *Philosophical Transactions of the Royal Society of London A: Mathematical, Physical and Engineering Sciences*, 358(1770):1619–1637.

Rocscience (2004). A new era in slope stability analysis: Shear strength reduction finite element technique. *RocNews Summer 2004*.

Rocscience (2011). $Phase^2$*, Version 8.0*. Rocscience inc., Toronto, Ontario.

Rocscience (2015). Slide. Software Online at: https://www.rocscience.com/rocscience/products/slide.

Rodgers, M. (2013). *Unusual patterns of seismicity during eruptive and non-eruptive periods at the persistently restless Telica volcano, Nicaragua*. PhD thesis, Univesity of South Florida.

Rodgers, M., Roman, D. C., Geirsson, H., LaFemina, P., McNutt, S. R., Muñoz, A., and Tenorio, V. (2015). Stable and unstable phases of elevated seismic activity at the persistently restless Telica Volcano, Nicaragua. *Journal of Volcanology and Geothermal Research*, 290:63–74.

Roman, D. C., Savage, M. K., Arnold, R., Latchman, J. L., and De Angelis, S. (2011). Analysis and forward modeling of seismic anisotropy during the ongoing eruption of the Soufrière Hills Volcano, Montserrat, 1996–2007. *Journal of Geophysical Research: Solid Earth (1978–2012)*, 116(B3).

Roobol, M. and Smith, A. (1998). Pyroclastic stratigraphy of the Soufriere Hills Volcano, Montserrat-Implications for the present eruption. *Geophysical Research Letters*, 25(18):3393–3396.

Rowe, C., Thurber, C., and White, R. (2004). Dome growth behavior at Soufriere Hills Volcano, Montserrat, revealed by relocation of volcanic event swarms, 1995–1996. *Journal of Volcanology and Geothermal Research*, 134(3):199–221.

Ruiz, G., Cordova, A., Alvarado, A., and Ruiz, M. (2013a). Informe Especial No. 4 - Sismicidad en la zona fronteriza con Colombia. Technical report, IG-EPN. In Spanish.

Ruiz, G., Cordova, A., Ruiz, M., and Alvarado, A. (2013b). Informe Tecnico de los volcanes Cerro Negro y Chiles. Technical report, IG-EPN. In Spanish.

Rust, A., Balmforth, N., and Mandre, S. (2008). The feasibility of generating low-frequency volcano seismicity by flow through a deformable channel. *Geological Society, London, Special Publications*, 307(1):45–56.

SAC (2010). Assessment of the hazards and risks associated with the Soufriere Hills volcano, Montserrat: Fourteenth report. Technical report, Montserrat Volcano Observatory.

Samuelson, J., Marone, C., Voight, B., and Elsworth, D. (2008). Laboratory investigation of the frictional behavior of granular volcanic material. *Journal of Volcanology and Geothermal Research*, 173(3):265–279.

Schaefer, L. N., Oommen, T., Corazzato, C., Tibaldi, A., Escobar-Wolf, R., and Rose, W. I. (2013). An integrated field-numerical approach to assess slope stability hazards at volcanoes: the example of Pacaya, Guatemala. *Bulletin of Volcanology*, 75(6):1–18.

Scholz, C. H. (1998). Earthquakes and friction laws. *Nature*, 391(6662):37–42.

Shepherd, J., Tomblin, J., and Woo, D. (1971). Volcano-seismic crisis in Montserrat, West Indies, 1966–67. *Bulletin Volcanologique*, 35(1):143–162.

Simmons, J., Elsworth, D., and Voight, B. (2004). Instability of exogenous lava lobes during intense rainfall. *Bulletin of Volcanology*, 66(8):725–734.

Simons, N., Menzies, B., Matthews, M., Bruce, M., et al. (2001). *A short course in soil and rock slope engineering*. Thomas Telford Ltd.

Smith, A., Roobol, M., Schellekens, J., and Mattioli, G. (2007a). Prehistoric stratigraphy of the Soufriere Hills–South Soufriere Hills volcanic complex, Montserrat, West Indies. *The Journal of Geology*, 115(1):115–127.

Smith, R. and Kilburn, C. (2010). Forecasting eruptions after long repose intervals from accelerating rates of rock fracture: the June 1991 eruption of Mount Pinatubo, Philippines. *Journal of Volcanology and Geothermal Research*, 191(1):129–136.

Smith, R., Kilburn, C., and Sammonds, P. (2007b). Rock fracture as a precursor to lava dome eruptions at Mount St Helens from June 1980 to October 1986. *Bulletin of Volcanology*, 69(6):681–693.

Smith, R., Sammonds, P. R., and Kilburn, C. R. (2009). Fracturing of volcanic systems: experimental insights into pre-eruptive conditions. *Earth and Planetary Science Letters*, 280(1):211–219.

Smithsonian Institution, Global Volcanism Program (2015a). Campi Flegrei. Online at: http://volcano.si.edu/volcano.cfm?vn=211010.

Smithsonian Institution, Global Volcanism Program (2015b). Chiles - Cerro Negro. Online at: http://www.volcano.si.edu/volcano.cfm?vn=351110. Accessed: 08.04.2015.

Sparks, R. (2003). Forecasting volcanic eruptions. *Earth and Planetary Science Letters*, 210(1):1–15.

Sparks, R. S. J., Murphy, M. D., Lejeune, A. M., Watts, R. B., Barclay, J., and Young, R. S. (2000). Controls on the emplacement of the andesitic lava dome of the Soufriere Hills Volcano, Montserrat by degassing-induced crystallisation. *Terra Nova*, 12:14–20.

Spencer, E. (1967). A method of analysis of the stability of embankments assuming parallel inter-slice forces. *Geotechnique*, 17(1):11–26.

Stephens, C. and Chouet, B. (2001). Evolution of the December 14, 1989 precursory long-period event swarm at Redoubt Volcano, Alaska. *Journal of Volcanology and Geothermal Research*, 109(1):133–148.

Stephens, C. D., Chouet, B. A., Page, R. A., Lahr, J. C., and Power, J. A. (1994). Seismological aspects of the 1989–1990 eruptions at Redoubt Volcano, Alaska: the SSAM perspective. *Journal of Volcanology and Geothermal Research*, 62(1):153–182.

Stinton, A. J., Cole, P. D., Stewart, R. C., Odbert, H. M., and Smith, P. (2014). The 11 February 2010 partial dome collapse at Soufrière Hills Volcano, Montserrat. *Geological Society, London, Memoirs*, 39(1):133–152.

Stoiber, R. E. and Jepsen, A. (1973). Sulfur dioxide contributions to the atmosphere by volcanoes. *Science*, 182(4112):577–578.

Surono, Jousset, P., Pallister, J., Boichu, M., Buongiorno, M. F., Budisantoso, A., Costa, F., Andreastuti, S., Prata, F., Schneider, D., Clarisse, L., et al. (2012). The 2010 explosive eruption of Java's Merapi volcano – a 100-year event. *Journal of Volcanology and Geothermal Research*, 241:121–135.

Tárraga, M., Carniel, R., Ortiz, R., and García, A. (2008). The Failure Forecast Method: Review and application for the real-time detection of precursory patterns at reawakening volcanoes. *Developments in Volcanology*, 10:447–469.

Thelen, W., Malone, S., and West, M. (2011). Multiplets: Their behavior and utility at dacitic and andesitic volcanic centers. *Journal of Geophysical Research: Solid Earth (1978–2012)*, 116(B8).

Thomas, M. E. and Neuberg, J. (2012). What makes a volcano tick – A first explanation of deep multiple seismic sources in ascending magma. *Geology*, 40(4):351–354.

Thomas, M. E., Petford, N., and Bromhead, E. N. (2004a). The effect of internal gas pressurization on volcanic edifice stability: evolution towards a critical state. *Terra Nova*, 16(5):312–317.

Thomas, M. E., Petford, N., and Bromhead, E. N. (2004b). Volcanic rock-mass properties from Snowdonia and Tenerife: implications for volcano edifice strength. *Journal of the Geological Society*, 161(6):939–946.

Tilling, R. I. (1989). Volcanic hazards and their mitigation: progress and problems. *Reviews of Geophysics*, 27(2):237–269.

Tokarev, P. (1963). On a possibility of forecasting of Bezymianny volcano eruptions according to seismic data. *Bulletin of Volcanology*, 26(1):379–386.

Tran, M. (2013). Montserrat aid programme comes under fire from UK watchdog. The Guardian Online at: http://www.theguardian.com/global-development/2013/jul/16/montserrat-aid-dfid-icai.

Trnkoczy, A. (2002). Understanding and parameter setting of STA/LTA trigger algorithm. *IASPEI New Manual of Seismological Observatory Practice*, 2:1–19.

Tuffen, H. and Dingwell, D. (2005). Fault textures in volcanic conduits: evidence for seismic trigger mechanisms during silicic eruptions. *Bulletin of Volcanology*, 67(4):370–387.

Tuffen, H., Dingwell, D., and Pinkerton, H. (2003). Repeated fracture and healing of silicic magma generate flow banding and earthquakes? *Geology*, 31(12):1089.

Umakoshi, K., Shimizu, H., and Matsuwo, N. (2003). Seismic activity associated with the endogenous growth of lava dome at Unzen Volcano, Japan. Technical report, Abstract V10.

USGS (2013). Data files: Map showing geology, oil and gas fields, and geologic provinces of the Caribbean region. Online at: http://pubs.usgs.gov/of/1997/ofr-97-470/OF97-470K/graphic/data.html. Accessed 22.05.2015.

Vaca, D. E. S. (2015). Determinación de estado de esfuerzos tectónicos en la zona del complejo volcánico Chiles-Cerro-Negro. Master's thesis, Facultad de Ingeniería en Geología y Petroleos, Escuela Politécnica Nacional. In Spanish.

Voight, B. (1988). A method for prediction of volcanic eruptions. *Nature*, 332:125–130.

Voight, B. (1989). A relation to describe rate-dependent material failure. *Science*, 243(4888):200–203.

Voight, B. (2000). Structural stability of andesite volcanoes and lava domes. *Philosophical Transactions of the Royal Society of London A: Mathematical, Physical and Engineering Sciences*, 358(1770):1663–1703.

Voight, B. and Cornelius, R. (1991). Prospects for eruption prediction in near real-time. *Nature*, 350(6320):695–698.

Voight, B. and Elsworth, D. (2000). Instability and collapse of hazardous gas-pressurized lava domes. *Geophysical Research Letters*, 27(1):1–4.

Voight, B., Hidayat, D., Sacks, S., Linde, A., Chardot, L., Clarke, A., Elsworth, D., Foroozan, R., Malin, P., Mattioli, G., et al. (2010). Unique strainmeter observations of Vulcanian explosions, Soufrière Hills Volcano, Montserrat, July 2003. *Geophysical Research Letters*, 37(19).

Voight, B., Hoblitt, R., Clarke, A., Lockhart, A., Miller, A., Lynch, L., and McMahon, J. (1998). Remarkable cyclic ground deformation monitored in real-time on Montserrat, and its use in eruption forecasting. *Geophysical Research Letters*, 25(18):3405–3408.

Voight, B., Komorowski, J., Norton, G., Belousov, A., Belousova, M., Boudon, G., Francis, P., Franz, W., Heinrich, P., Sparks, R., et al. (2002). The 26 December (Boxing Day) 1997 sector collapse and debris avalanche at Soufriere Hills volcano, Montserrat. *Geological Society, London, Memoirs*, 21:363–408.

Voight, B., Linde, A., Sacks, I., Mattioli, G., Sparks, R., Elsworth, D., Hidayat, D., Malin, P., Shalev, E., Widiwijayanti, C., et al. (2006). Unprecedented pressure increase in deep magma reservoir triggered by lava-dome collapse. *Geophysical Research Letters*, 33(3).

Voight, B., Sparks, R., Miller, A., Stewart, R., Hoblitt, R., Clarke, A., Ewart, J., Aspinall, W., Baptie, B., Calder, E., et al. (1999). Magma flow instability and cyclic activity at Soufriere Hills volcano, Montserrat, British West Indies. *Science*, 283(5405):1138–1142.

Voight, B., Young, K., Hidayat, D., Purbawinata, M., Ratdomopurbo, A., Sayudi, D., LaHusen, R., Marso, J., Murray, T., Dejean, M., et al. (2000). Deformation and seismic precursors to dome-collapse and fountain-collapse nuées ardentes at Merapi Volcano, Java, Indonesia, 1994–1998. *Journal of Volcanology and Geothermal Research*, 100(1):261–287.

Wadge, G. and Isaacs, M. (1988). Mapping the volcanic hazards from Soufriere Hills Volcano, Montserrat, West Indies using an image processor. *Journal of the Geological Society*, 145(4):541–551.

Wadge, G., Ryan, G., and Calder, E. (2009). Clastic and core lava components of a silicic lava dome. *Geology*, 37(6):551–554.

Wadge, G., Voight, B., Sparks, R., Cole, P., Loughlin, S., and Robertson, R. (2014). An overview of the eruption of Soufriere Hills Volcano, Montserrat from 2000 to 2010. *Geological Society, London, Memoirs*, 39(1):1–40.

Waite, G. P., Chouet, B. A., and Dawson, P. B. (2008). Eruption dynamics at Mount St. Helens imaged from broadband seismic waveforms: Interaction of the shallow magmatic and hydrothermal systems. *Journal of Geophysical Research: Solid Earth (1978–2012)*, 113(B2).

Wassermann, J. (2002). Volcano seismology. *IASPEI New Manual of Seismological Observatory Practice*, 1(13):662–703.

Watson, I., Oppenheimer, C., Voight, B., Francis, P., Clarke, A., Stix, J., Miller, A., Pyle, D., Burton, M., Young, S., et al. (2000). The relationship between degassing and ground deformation at Soufriere Hills Volcano, Montserrat. *Journal of Volcanology and Geothermal Research*, 98(1):117–126.

Webb, S. L. and Dingwell, D. B. (1990). Non-newtonian rheology of igneous melts at high stresses and strain rates: Experimental results for rhyolite, andesite, basalt, and nephelinite. *Journal of Geophysical Research: Solid Earth (1978–2012)*, 95(B10):15695–15701.

Witham, C. (2005). Volcanic disasters and incidents: A new database. *Journal of Volcanology and Geothermal Research*, 148(3):191–233.

Withers, M., Aster, R., Young, C., Beiriger, J., Harris, M., Moore, S., and Trujillo, J. (1998). A comparison of select trigger algorithms for automated global seismic phase and event detection. *Bulletin of the Seismological Society of America*, 88(1):95–106.

Wylie, J. J., Voight, B., and Whitehead, J. (1999). Instability of magma flow from volatile-dependent viscosity. *Science*, 285(5435):1883–1885.

Yamasato, H., Kitagawa, S., and Komiya, M. (1998). Effect of rainfall on dacitic lava dome collapse at Unzen volcano, Japan. *Papers in Meteorology and Geophysics*, 48(3):73–78.

Young, S. R., Sparks, R. S. J., Aspinall, W. P., Lynch, L. L., Miller, A. D., Robertson, R. E., and Shepherd, J. B. (1998). Overview of the eruption of Soufriere Hills volcano, Montserrat, 18 July 1995 to December 1997. *Geophysical Research Letters*, 25(18):3389–3392.